

Interpretation of D_α Imaging Diagnostics Data on the ASDEX Upgrade Tokamak

Dissertation der Fakultät für Physik
der
Ludwig-Maximilians-Universität München

vorgelegt von Jens Harhausen
aus Würzburg

München, 1.12.2008

1.Gutachter: Prof. Dr. H. Zohm
2.Gutachter: Prof. Dr. H. Lesch

Datum der mündlichen Prüfung: 7.5.2009

Abstract

The Tokamak configuration is a promising concept for magnetic confinement fusion. Cross-field transport in the plasma core leads to a plasma flux across the separatrix into the scrape-off layer, where it is guided along field lines towards the divertor targets. A return flux of neutral particles after plasma-wall interaction is directed towards the plasma chamber. Each discharge scenario is accompanied by a characteristic recycling pattern. The dominant mechanisms of neutral-plasma interaction are ionisation and atom-ion charge exchange. The impact of neutrals on the particle-, momentum- and energy-balance of the plasma is relevant for the understanding of the properties of the edge plasma and the state of the divertor plasma. Neutrals may cause energy- and momentum-detachment, a state of reduced power and particle fluxes, at the targets, which is a prerequisite for acceptable wall loads under reactor conditions. The distribution of neutral particles in the plasma chamber can be determined by the analysis of line emission. Parameters of neutrals have been available so far only from localised measurements and it is therefore desired to extend the observation area.

At the ASDEX Upgrade Tokamak, two cameras are installed to record the Deuterium Balmer- α (D_α) emission with high spatial resolution and dynamic range in the divertor and mid-plane regions. Two methods for data deconvolution are presented. A simple profile-fit is used to resolve the radial profile of emission at the low and high field sides for low and medium density discharges. This emission profile is translated to neutral parameters by comparison to the results obtained from kinetic modelling of neutral penetration (KN1D). An algorithm for tomographic reconstruction is applied to image data of the divertor region. In general, radiance data recorded is blurred due to the impact of diffuse reflection from surfaces of the plasma facing components in the all-Tungsten machine. Therefore, the tomographic algorithm has been extended by a model for reflection based on a solid angle resolved measurement.

The sensitivity of the procedures is proven by the accurate analysis of different edge plasma configurations. Poloidally resolved neutral flux densities at the plasma edge and corresponding core fuelling rates are presented for the high field side. Underlying estimates of plasma parameters indicate a drop of static plasma pressure along the magnetic field towards the inner target. Changes of the poloidal flux density profile during a radial shift of the plasma column, indicate a correlation of plasma-wall gap and scrape-off layer parameters at the high field side. From the deconvolution of divertor view data separate emission patterns have been resolved. Besides the character of emission at the strike zones which can give a hint on the level of detachment, the occurrence of radiation above the inner target indicates that the distribution of plasma parameters is probably more complex than expected from simple radial decay lengths.

The experimental emission profiles and inferred neutral parameters display an important boundary condition for complex 2D edge modelling codes like SOLPS. The comparison of experimental and code results question the applicability of the standard recipe (concerning code settings) for arbitrary plasma scenarios. An interface to theory is required to reasonably exploit the experimental data on neutral penetration.

The essential result of this thesis is a reference frame for the quantitative analysis of video diagnostics data recorded on a Tokamak plasma, including the impact of reflecting plasma facing components.

Kurzfassung

Das Tokamak-Konzept stellt einen vielversprechenden Ansatz zur Verwirklichung der Kernfusion mittels des magnetischen Einschlusses dar. Plasmatransport senkrecht zum Magnetfeld im Kernbereich führt zu einem Plasmafluss über die Separatrix in die Abschältschicht, in der dieser entlang des Magnetfelds zu den Prallplatten des Divertors geleitet wird. Durch die Neutralisation des Plasmas an der Gefäßwand entsteht ein wiederum auf das Plasma gerichteter Fluss von Neutralteilchen. Jedes Entladungsszenario zeichnet sich durch ein bestimmtes Muster dieses Plasma-Recyclings aus. Die wesentlichen Reaktionen der Neutralteilchen-Plasma-Wechselwirkung sind Ionisation und Ladungsaustausch. Der Einfluss der Neutralen auf die Teilchen-, Impuls- und Energie-Bilanz des Plasmas ist bedeutsam für das Verständnis der Eigenschaften des Randplasmas und des Zustands des Divertorplasmas. Neutralteilchen können eine substantielle Reduzierung von Energie- und Impulsflüssen an den Prallplatten verursachen, einem Mechanismus, der als Voraussetzung für das Erreichen vertretbarer Wandbelastungen im Reaktorbetrieb gilt. Die Verteilung von Neutralen im Plasmagefäß kann durch die Auswertung von Linienstrahlung bestimmt werden. Bisher sind Daten zu Neutralteilchen nur aus lokalen Messungen verfügbar und es ist daher wünschenswert, den räumlichen Messbereich zu erweitern.

Am Tokamak-Experiment ASDEX Upgrade sind zu diesem Zweck zwei Kameras installiert, die mit hoher räumlicher Auflösung und hohem dynamischem Umfang die Balmer- α Linienemission von Deuterium (D_α) im Divertor und in der Mittelebene aufzeichnen. Es werden zwei Methoden zur Entfaltung der linienintegrierten Daten vorgestellt. Zur radialen Auflösung der Emission an der Innen- und der Aussenseite des Torus in Entladungen niedriger und mittlerer Dichte wird eine einfache Fit-Prozedur angewandt. Die so erhaltenen Emissionsprofile werden in die zugrundeliegenden Neutralparameter übersetzt, indem eine kinetische Modellierung (KN1D) des Eindringens der Neutralen am Plasmarand zum Vergleich herangezogen wird. Für die Auswertung von Bilddaten des Divertorbereichs dient ein Algorithmus zur tomographischen Rekonstruktion. Diffuse Reflektion, die von der mit Wolfram beschichteten Gefäßwand herrührt, vermindert den Kontrast der Bilddaten teilweise erheblich. Um dieser Komplikation zu begegnen, wurde der Tomographiealgorithmus um ein Reflektionsmodell erweitert, das auf einer umfassenden raumwinkelaufgelösten Messung an einer Wandkomponente beruht.

Das Auflösungsvermögen der verschiedenen Methoden wird im Vergleich der Ergebnisse zu unterschiedlichen Plasmarandkonfigurationen deutlich. Für die Torusinnenseite werden poloidale Verteilungen der Neutralzuflussdichte und der entsprechenden Zuflussraten am Plasmarand präsentiert. Die für die Auswertung der Emissionsdaten notwendigen Annahmen zu Plasmaparametern deuten auf einen Abfall des statischen Plasmadrucks entlang des Magnetfelds in Richtung des inneren Divertors hin. Die radiale Verschiebung der Plasmasäule und die dabei beobachtete Veränderung in der Neutralzuflussdichte zeigen den direkten Zusammenhang von Plasma-Wand Abstand und Plasmaparametern in der Abschältschicht bzw. die relativ weite radiale Ausdehnung des Plasmas in diesem Bereich. Mit der Entfaltung der Divertoraufnahmen werden räumlich getrennte Emissionsmuster hervorgehoben. Neben Hinweisen zum Divertorzustand, die daraus gewonnen werden können, lässt das Auftreten von Emission oberhalb des inneren Aufprallpunktes auf eine Verteilung von Plasmaparametern schließen, die komplexer sein muss, als die von einfachen radialen Abfallängen beschriebene.

Die experimentell gewonnenen Daten stellen eine bedeutende Randbedingung für aufwendige 2D Simulationsrechnungen des Plasmarandes, wie mit dem SOLPS-Code durchgeführt, dar. Der Vergleich der Simulationsergebnisse mit den experimentellen Daten zeigt eine beschränkte Aussagefähigkeit des Codes, sofern nach dem typischerweise verwendeten Rezept bezüglich der freien Code-Parameter vorgegangen wird. Eine alternative Schnittstelle zur theoretischen Beschreibung ist notwendig, um die experimentellen Erkenntnisse zum Eindringen der Neutralteilchen weitergehend verwerten zu können.

Das wesentliche Ergebnis dieser Arbeit ist die Entwicklung einer Referenz zur quantitativen Auswertung von Videodiagnostikdaten an einem Tokamak-Plasma, insbesondere unter Berücksichtigung von Reflektion an Wandkomponenten des Plasmagefäßes.

Contents

1	Introduction	1
2	Neutral-Plasma Interaction	7
2.1	Fundamental Molecular and Atomic Reactions	7
2.2	Occupation Balance of Excited States	12
2.3	Kinetic Treatment of Neutral Particles	16
2.3.1	Basic Aspects of the KN1D Algorithm	17
2.3.2	KN1D in Practise	25
3	D_α Diagnostics	31
3.1	Strike Point Observation	31
3.2	Tangential Cameras	33
4	Data Deconvolution	39
4.1	Ray-Tracing-Fit	40
4.2	Tomographic Reconstruction	46
5	Experimental Results	63
5.1	Introductory Remarks	63
5.1.1	Diagnostics Referenced	63
5.1.2	MHD Equilibrium Reconstruction	72
5.1.3	Edge Perturbation	74
5.2	Interpretation of D _α Emission	80
5.2.1	Dynamic Range of D _α Emission	80
5.2.2	Comparison of L- and H-mode Regimes at Medium Density	84
5.2.3	Recognition of Regime Change in L-mode Confinement	88
5.2.4	Impact of Geometry Parameters on HFS Fuelling	94
5.2.5	D _α Emission as Boundary Condition for SOL Modelling	107
5.2.6	Overview on Neutral Penetration Data	116
6	Summary and Conclusion	117

A The ASDEX Upgrade Tokamak	119
B Calibration of D_α Diagnostics	123
C Reflection Properties of Tungsten Surfaces	135
D Overview on Neutral Penetration Data	142
Bibliography	147
Acknowledgement	153

Chapter 1

Introduction

At the beginning of the 21st century, fossile fuels account for about 3/4 of the global primary energy consumption [1]. The issues of limitation of these resources and the impact of the massive production of greenhouse gases on the global climate demand new strategies for sustainable energy supply. With the present development status of renewable energy sources and efficient energy storage, the request for an alternative to satisfy the power base load of a globally increasing consumption is still posed. Power generation from nuclear fusion is subject to a constant research effort since the beginning of the civil use of nuclear energy in order to develop a technically safe and environmentally friendly method based on highly abundant fuels. The economically most attractive reaction is $D + T \rightarrow {}^4\text{He} (3.5 \text{ MeV}) + n (14.1 \text{ MeV})$, because of its large cross section due to the resonant character involving the unstable ${}^5\text{He}$. The maximum rate coefficient for this reaction considering Maxwellian velocity distributions for the reactants is about $\langle \sigma v \rangle \approx 9 \cdot 10^{-21} \text{ m}^3 \text{ s}^{-1}$ for particle energies (temperature) of $\sim 70 \text{ keV}$ - alternative reactions like D-D or D- ${}^3\text{He}$ are at least one order of magnitude less efficient [2]. In the energy range of interest the cross sections for Coulomb repulsion are about 2-4 orders of magnitude higher than those of the D-T fusion reaction. This requires an arrangement in which the reactants are confined sufficiently long compared to the collision time, such to ensure a high probability for a fusion reaction to occur. Confinement of highly energetic particles implies to deal with matters of high temperature plasmas.

The quality of a confinement concept can be characterised by the triple product $nT\tau$ with n the plasma density, T its temperature and τ the energy confinement time, defined as the ratio of plasma energy content and power loss. In order to achieve economic power production, $nT\tau > 5 \cdot 10^{21} \text{ m}^{-3} \text{ s keV}$ needs to be achieved, where T is restricted to a range of 10-20keV due to the temperature dependence of reaction rate coefficient and radiation losses.

The most promising progress during the last decades has been made in magnetised plasmas, in particular in so-called Tokamak devices. Values of the fusion product $nT\tau$ up to $10^{21} \text{ m}^{-3} \text{ s keV}$ could be achieved, albeit for relatively short duration in the order of several seconds [3]. Ion temperatures in the required magnitude have already been obtained and the route to a fusion reactor is set by the design of larger machines which exhibit a sufficient energy confinement time, since the ratio of plasma surface area to volume is reduced. If a magnetic configuration is to be used to confine a hot and dense plasma, its topology needs to be closed in order to avoid parallel field losses at the locations of intersection of the field lines and the surrounding walls like present in linear magnetic mirror arrangements. In the Tokamak a set of toroidally

aligned coils generates the main magnetic field component \vec{B}_t . A central solenoid is used to induce a plasma current, ie the plasma being the secondary winding of a transformer, which adds a poloidal magnetic field component \vec{B}_p . The resulting helical field structure compensates the impact of particle drifts connected to the inhomogeneity of the toroidal field. A third vertical field component \vec{B}_v , generated by external coils is required to stabilize the plasma column at the desired radial position. Using magnetohydrodynamics (MHD) to describe the plasma, the fundamental relation to characterise the Tokamak equilibrium is the stationary force equation $\nabla p = \vec{j} \times \vec{B}$, ie the plasma pressure is balanced by the Lorentz force acting on the plasma current density. This implies that $\nabla p \cdot \vec{j} = 0$ and $\nabla p \cdot \vec{B} = 0$, indicating that the plasma current density and the magnetic field span a surface perpendicular to the pressure gradient, thus building a surface of constant pressure. As $\nabla \cdot \vec{B} = 0$ the areas of different plasma pressure must be nested toroidal surfaces. The poloidal magnetic flux Ψ is used as a practical radial coordinate, according to the identity of surfaces of constant pressure and Ψ . A sketch of the magnetic configuration of the ASDEX Upgrade Tokamak is depicted in figure 1.1 and some details on this device can be found in appendix A. In order to guide losses from the core plasma to specified locations, the poloidal field is diverted by configuration of the vertical field coils such to form the so-called X-point. This divertor configuration allows to set a proper gap between the plasma edge and the wall and to keep a distance between the core plasma and the location of the target plates at which the primary plasma-wall interaction occurs as the origin of impurity fluxes. The separatrix marks the transition of closed (core plasma) to open flux surfaces which define the region of plasma transport to the material wall.

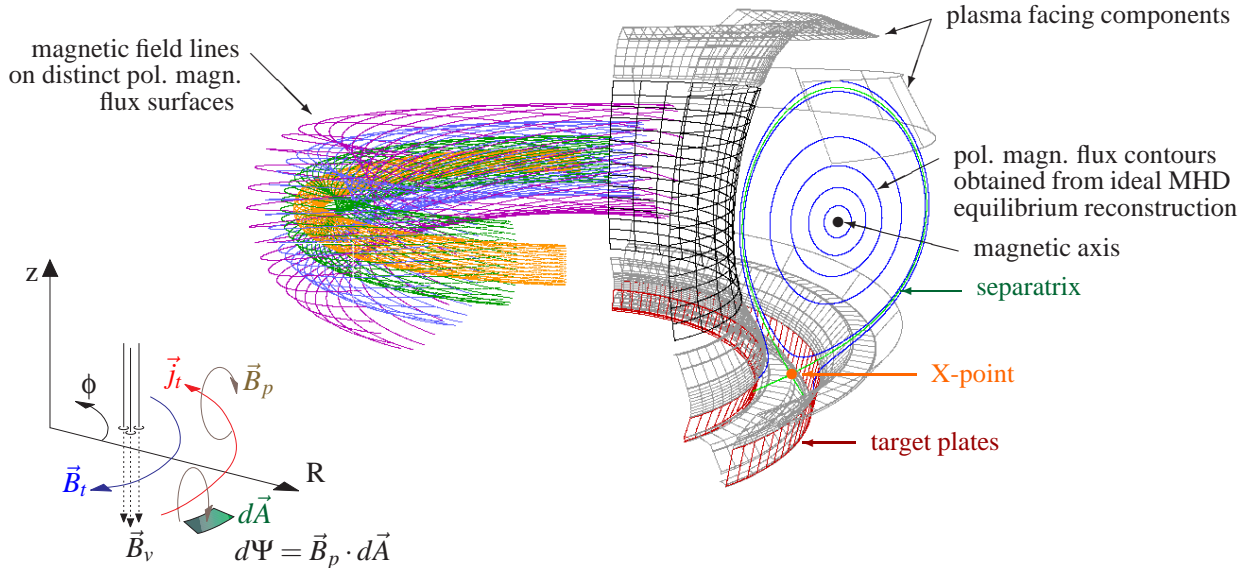


Figure 1.1: Helical orientation of magnetic field lines positioned on toroidally shaped poloidal magnetic flux surfaces. The sketch to the lower left shows the torus coordinate system, the typical orientation of various vector fields and the definition of the poloidal magnetic flux Ψ .

As an introduction to the experimental efforts to be presented in this thesis, it is useful to sketch the role of neutral particles in the plasma edge region. Throughout the chapters of this report the term neutrals is used synonymously for the molecules and atoms of the working gas Hydrogen

resp. Deuterium, impurity species are not considered. For a basic discussion, the cross section of a plasma vessel is depicted in figure 1.2. The vessel volume may be separated into three different areas: firstly the core region which is enclosed by the separatrix (transition between closed and open magnetic flux surfaces), secondly the area of open field lines which guide the plasma losses from the core to the target plates and thirdly the divertor plasma. The latter two regions display the interface, the scrape-off layer (SOL), between the main plasma and the material wall. Steady state operation is characterised by a certain circulation of plasma and neutral particles. Radial transport in the core region leads to a plasma flux to the SOL. These losses are most likely asymmetrically distributed in the poloidal plane. Diffusive losses are due to collisions with a step size related to particle trajectories determined by the magnetic field strength (gyro radius) or the helical configuration (radial excursion of mirror-trajectories). Convective losses based on micro turbulence or macro scale instabilities are related to density, temperature or pressure gradients which are larger at the low field side (LFS) than on the high field side (HFS) of the plasma column due to the magnetic flux topology. In case of interchange-type instabilities it is the radius vector of curvature of the field line opposite to the direction of the pressure gradient which makes the LFS susceptible to this kind of perturbation. Plasma which entered the SOL is predominantly transported along the magnetic field towards the divertor, since the neutralisation at the target plates leads to a pressure drop (plasma sink). Accordingly, in this basic picture, the pressure of neutral particles is highest in the divertor region and reduced in the locations further upstream, depending on the magnitude of perpendicular field transport in the SOL and penetration of neutrals to areas distant from the primary origin. This retention of neutrals in the divertor region depends on plasma parameters and vessel geometry. In order to maintain a desired particle balance, gas valves are installed at the vessel wall and a pumping duct is connected to the divertor volume. Active particle control is mandatory to compensate for the sink and source action of in-vessel components (storage and release of gas at surfaces or in the bulk material) and for removal of impurities like the Helium ash in fusion operation. It is interesting to note that the intrinsic recycling neutral flux is typically much higher than the additionally applied neutral influx.

Neutrals affect the particle-, momentum- and energy-balance of the plasma in all areas penetrated. The fundamental reaction mechanisms are molecular dissociation, atomic excitation and ionisation and atom-ion charge exchange to which details are given in section 2.1. The former three categories are predominantly induced by electron impact such that the electron species is cooled in the presence of neutrals. The electron energy is partly distributed to dissociation or ionisation products (reduced by the corresponding potentials) or lost to the line-radiation channel. With the process of charge exchange, ion momentum transport and dissipation is strongly enhanced. An ensemble of cold neutrals originating from the vessel wall interacting with a flow of hot ions, leads to a damping of the ion flow and to the creation of fast neutral particles with a random direction in the plane perpendicular to the magnetic field at the location of their origin while the parallel field velocity is maintained. Since the reaction rate for charge exchange is always higher than the rate for ionisation - typically by a factor larger than two in the range of relevant plasma parameters - charge exchange is a central mechanism to influence neutral penetration. Fast neutral particles may either enter the region of the core plasma and establish a refuelling flux, be distributed in the SOL or hit the vessel wall where they can play a significant role in terms of physical sputtering.

The distribution of neutrals is accompanied by a characteristic ion source corresponding to the local electron density and temperature. This plasma source term is a relevant component

among the processes which govern the shape of the density profile at the plasma boundary. A common ansatz found in the literature [4, 5, 6, 7] is to solve the one-dimensional (radial evolution and poloidally averaged) particle balance of ions and neutrals analytically where assumptions on the nature of neutral transport need to be made, eg using convective (average neutral velocity) or diffusive descriptions. Width and height of the density profile around the so-called edge pedestal, which is tanh-shaped in the 1D ansatz, are determined by the combined effect of neutral penetration and plasma transport. The individual importance of both mechanisms for the density profile formation is neither known from theory nor from experimental investigations. Hints have been reported for the dominance of each of both effects. Typically the ion source term is known only at a single location on the poloidal plane. The knowledge of the actual distribution of neutral particles along the whole plasma edge is obviously mandatory for the quantitative modelling of the edge density profile.

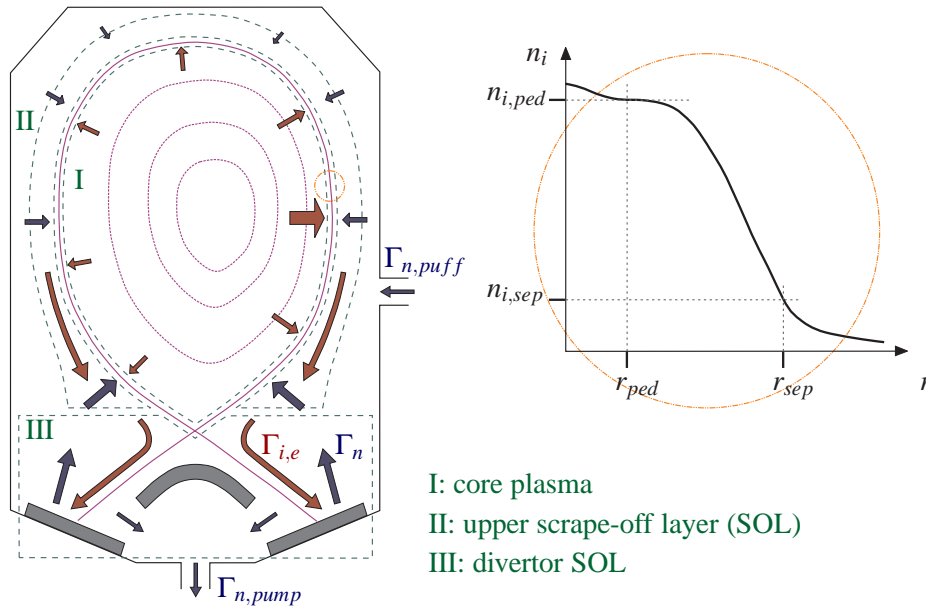


Figure 1.2: Simplified scheme of plasma and neutral fluxes projected to the poloidal plane. The axis of symmetry is to the left of the figure. Losses $\Gamma_{i,e}$ (red arrows) from the plasma core (I) are guided along the magnetic field in the SOL (II) towards the divertor (III) target plates. The main source of neutrals Γ_n (blue arrows) is at the target and neutral density decreases with increasing distance. The global particle balance is adjusted by active gas puffing and pumping, the former being the actuator for density control. The combined effect of radial plasma transport and the distribution of the ion source by the penetration of neutrals forms a pedestal like density profile shape of characteristic width and height (right part).

Theoretical investigations [8, 9] reveal the impact of neutrals on the radial ion flow profile. It is found that for a neutral to ion density ratio of $n_0/n_i \gtrsim 10^{-4}$ the neutral viscosity exceeds that of the ions and the cross field momentum flux is predicted to result in a pronounced velocity shear which in turn is suggested to play a role in the suppression of micro turbulence in certain plasma scenarios.

The divertor plasma state is influenced by the neutral density in that region. According to the particle and heat fluxes which enter the SOL from the core, very different divertor states can be established, ranging from recombining to ionising conditions. Reasonable lifetime of

plasma facing components can be achieved only if the peak power load can be restricted, a typical upper bound being $\sim 10 \text{ MW m}^{-2}$. If the ion flux entering the divertor is sufficiently high, strong interaction of the recycling neutrals and the ion flow results in a drop of particle and heat fluxes at the target. The shielding of the target by neutrals is termed energy- and momentum detachment. At least partial detachment of the separatrix strike zones is required for economic plasma operation in a future reactor. At present 2D coupled fluid plasma and kinetic neutral codes are applied to improve the understanding of the complex SOL physics. Both the interpretation of present experimental data and predictive modelling for the development of future devices are addressed.

Measurements on parameters of neutrals are highly desired for testing theoretical and numerical predictions on the properties of the edge plasma and SOL/divertor. Since neutral particles are spread throughout the plasma boundary, localised measurements, eg from spectroscopy on a few lines of sight, which are available today are not sufficient. The main purpose of this thesis is to present the efforts made on and the results obtained from the interpretation of Deuterium Balmer- α (D_α) imaging diagnostics data. Using video diagnostics, a large fraction of the plasma boundary can be recorded with high spatial resolution. Line radiation of Deuterium can directly be translated to neutral density or flux density if the local plasma parameters are known. Since the spatial coverage of the SOL in terms of plasma diagnostics is limited and the deconvolution of line integrated camera data contains several aspects of complication, a combination of measurement of D_α radiance, estimates on plasma parameters and the simulation of neutral penetration are the basis for diagnostics of neutral particles.

This thesis is organised as follows. Chapter 2 gives a view on the main aspects of neutral-plasma interaction, ie reaction mechanisms and the emission of radiation from excited species on a certain plasma background. At this place also the kinetic code KN1D is discussed which is applied for the interpretation of experimental D_α emission data.

The D_α diagnostics is described in chapter 3 which is divided into two sections for the fiber optics directed to the target plates and the video diagnostics viewing the divertor and midplane regions of the plasma tangentially. Two methods for deconvolution of the line integrated data of the D_α cameras are discussed in the sections of chapter 4. These are a relatively simple forward profile fitting procedure and a more complex inverse algorithm for tomographic reconstruction to which details of diffuse reflection at Tungsten surfaces of plasma facing components have been added.

A presentation and discussion of the experimental results is given in chapter 5. The interpretation of D_α emission is based on additional information on the plasma and a variety of simplifying assumptions. These issues include the data obtained from a number of plasma diagnostics, the accuracy of the reconstruction of the magnetic geometry of the discharge and the occurrence of perturbations of the plasma edge which cannot be resolved with the standard D_α diagnostics and data analysis employed in the framework of this thesis. In the following sections the most robust results obtained for low and medium density, mainly ohmic and L-mode discharges are presented. The survey contains information on the dynamic range of D_α emission, the details of the ion source and neutral flux density profiles at the low field and high field sides depending on the edge configuration and the position of the plasma column relative to the vessel wall. This chapter also tries to give an insight on the complex topic of scrape-off layer modelling and the benefit of the preparation of D_α emission data on the plasma cross section.

The main findings regarding the problems encountered at the operation of video based D_α

diagnostics and the corresponding data analysis and the significance and use of D_α emission and related neutral parameters data are summarised in chapter 6.

Three appended chapters (appendices A, B and C) contain additional information on the Tokamak device ASDEX Upgrade, issues regarding radiance calibration including the sensitivity of glass fibers on neutron flux and γ radiation and the construction of a reflection model for Tungsten surfaces based on a dedicated measurement. Further, appendix D gives a summary of edge plasma and neutral parameters discussed in this thesis in a condensed form.

Chapter 2

Neutral-Plasma Interaction

2.1 Fundamental Molecular and Atomic Reactions

The SOL and edge region of the confined plasma is affected by various mechanisms involving neutral particles. At this place, the most important reactions regarding the working gas Hydrogen (resp. its isotopes) shall be summarised, whereas the impact of impurity species which is a complex topic on its own is not treated. Main aspects to discuss are the origin of neutral particles, the type of reactions leading to power and momentum losses of the plasma and the area affected, ie the penetration of neutrals into the plasma volume. Table 2.1 gives a list of fundamental reactions and serves as a guideline for this section.

At first, the origin of neutral particles needs to be clarified. The standard operation of a Tokamak discharge includes permanent gas pumping and corresponding to the target plasma density a feedback controlled gas puff. Thus the intake flow of molecules is determined by external means. This displays the only contribution to which location (valve position) and magnitude of molecular flux density is precisely known. The dominant contribution to the origin of neutral particles are the manifold mechanisms of plasma-wall interaction in the framework of plasma recycling [10]. Direct reflection of ions including a recombination process at the surface represents a source of atoms with an energy distribution similar to that of the incident ions. Atoms can be released by ion impact, termed desorption if the interaction occurs at the surface or physical sputtering if atoms residing in the bulk material are ejected by momentum exchange. If atoms recombine after a diffusion process in the material, thermalised molecules at the surface can be released as such by thermal motion or desorption reactions can produce molecules with higher energies. Details of this recycling process are an important issue if the path of neutral particles is to be reconstructed in order to obtain a precise picture of neutral-plasma interaction in the SOL. The basic treatment of neutrals being released from the wall as thermal molecules like assumed in section 2.3 is supported by the work of Mertens, Brezinsek and co-workers [11]. They analysed spectroscopically the atomic and molecular Hydrogen flux from a Carbon test-limiter which can be heated independently of the plasma parameters. For limiter temperatures $T_L = 1100\text{ K}$ it was found that the major part (90% with respect to the total wall source) is released as thermal molecules and the residual fraction might be related to ion reflection processes. If the temperature is increased, it was observed that the molecular fraction is linearly decreasing until the Hydrogen influx is atomic solely at a temperature of 1700 K. These findings may serve as a hint but it has to be kept in mind that the experiments discussed in section 5.2 were performed in the Tokamak

AUG with its Tungsten covered first wall. If a different Hydrogen recycling scheme applies to Tungsten surfaces is unknown and this issue is ignored here. Concerning the wall temperature of the main chamber of AUG, $T_L \approx 300$ K is assumed. Higher values are found only at locations of large heat flux like the target plates.

molecular reactions (H_2 , threshold energy increasing)		
$e + H_2$	\rightarrow	$H + H^-$ dissociative attachment
$e + H_2$	\rightarrow	$e + H + H$ dissociation
$e + H_2$	\rightarrow	$e + H_2^* \rightarrow e + H_2 + h\nu$ excitation
$e + H_2$	\rightarrow	$e + H_2^* \rightarrow e + H + H + h\nu$ dissociative excitation
$e + H_2$	\rightarrow	$H_2^+ + e + e$ ionisation
$e + H_2$	\rightarrow	$H^+ + H + e + e$ dissociative ionisation
$e + H_2$	\rightarrow	$H^+ + H^+ + 2e + e$ dissociative ionisation
ionic molecular reactions (H_2^+ , threshold energy increasing)		
$e + H_2^+$	\rightarrow	$H + H$ dissociative recombination
$e + H_2^+$	\rightarrow	$e + H^+ + H$ dissociation
$e + H_2^+$	\rightarrow	$e + H_2^{*+} \rightarrow e + H^+ + H + h\nu$ dissociative excitation
$e + H_2^+$	\rightarrow	$e + e + H^+ + H^+$ dissociative ionisation
atomic reactions		
$e + H^+ + e$	\rightarrow	$H + e$ three body recombination
$e + H^+$	\rightarrow	$H + h\nu$ radiative recombination
$e + H$	\rightarrow	$e + H^+ + e$ ionisation
$H^+ + H$	\rightarrow	$H + H^+$ charge exchange

Table 2.1: Reactions involving neutral particles and corresponding ions [12].

Regarding the plasma parameters in the SOL, electron impact reactions display the major reaction type since heavy particle collisions, eg ionisation by proton impact, exhibit comparable cross sections at much higher energies (see eg [13]). The reason for this relation is that the relative particle velocity is the relevant parameter rather than energy and thus the magnitude of cross sections for the same reaction regarding electrons or ions often scales fairly well with the square root of the mass ratio. Reactions of dissociation, excitation and ionisation are an energy sink for the plasma electrons, energy which is transferred to reaction products like molecular ions, atomic ions or atoms, or translated to radiation if radiative deexcitation of excited states occurs. If the plasma is optically thin for the line radiation induced, this energy is lost to the walls. In the case of fast neutral particles the energy might be redeposited in the SOL or even in the edge region of the confined plasma - or otherwise distributed in neutral-wall interaction (eg physical sputtering). Figure 2.1 displays a number of electron impact reactions of molecules and molecular ions selected from [13] which already gives a basic impression about the relative importance and possible reaction chains.

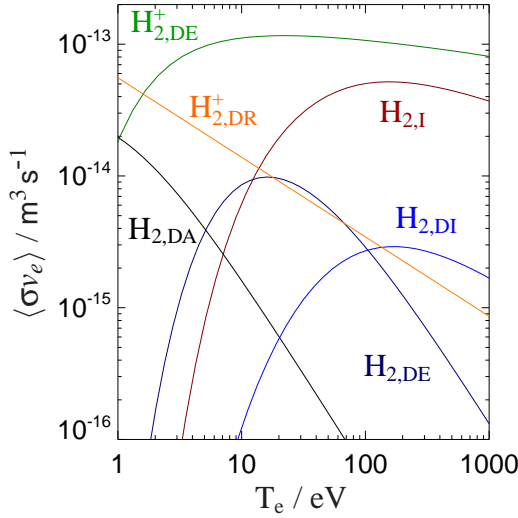
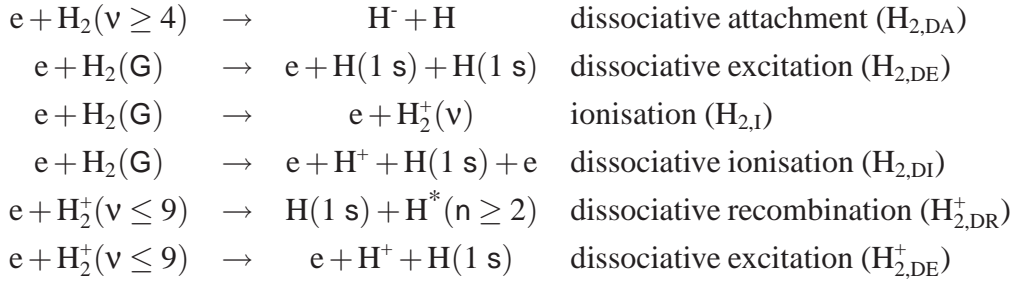


Figure 2.1: Rate coefficients for reactions listed below.



The considered molecular rate coefficients can be used to obtain an estimate of the mean free path of molecules in the SOL. For a reaction $a + b \rightarrow a' + b'$ the mean free path of reactant b is given by $\lambda_b = v_b / (n_a \langle \sigma_{ab} v_{ab} \rangle)$. This spatial parameter is shown in figure 2.2 for the molecular reactions dissociation and ionisation, where the energy of molecules was set to 0.05 eV ('thermal', $v_{H_2} \approx 2 \cdot 10^3 \text{ m/s}$) and electron densities of $n_e \in \{1 \cdot 10^{18}, 4 \cdot 10^{18}, 8 \cdot 10^{18}, 1.2 \cdot 10^{19}\} \text{ (m}^{-3}\text{)}$ respectively. These parameters were chosen to reflect the situation of thermal molecules starting from the main chamber wall of the plasma vessel somewhere distant from the divertor region (eg midplane). In the far SOL electron parameters are assumed to be in the order of $n_e \sim O(10^{18}) \text{ m}^{-3}$ and $T_e \geq 5 \text{ eV}$, closer to the separatrix density and temperature increase within a radial distance of $\sim 10 \text{ cm}$ (std. lower single null AUG operation, see appendix A) to typical values of $T_e \approx 100 \text{ eV}$ and $(1/5 - 1/3) \times \text{core density}$ ($\sim 10^{19} \text{ m}^{-3}$) at the last closed flux surface and further rise in the confined region. An example of electron density and temperature profiles is shown in figure 2.3, taken from section 5.2.2.

Regarding dissociative attachment, the cross section is significant only for vibrationally excited molecules and the distribution of vibrationally excited states requires special attention which is beyond the scope of this basic overview. However, for these molecules λ_{mfp} for dissociative attachment for low densities and temperatures is in the order of cm. The same order of magnitude is seen for dissociation and ionisation (both for the ground state molecule) at slightly elevated temperatures corresponding to the radial plasma profile in the SOL just mentioned. Ionisation of molecules becomes the dominant reaction for $T_e \geq 10 \text{ eV}$. The molecule is thus likely to be stopped radially in the SOL since it is bound to the magnetic field when ionised. Rate coefficients shown in figure 2.1 suggest that the molecular ion dissociates to H and H^+ rapidly.

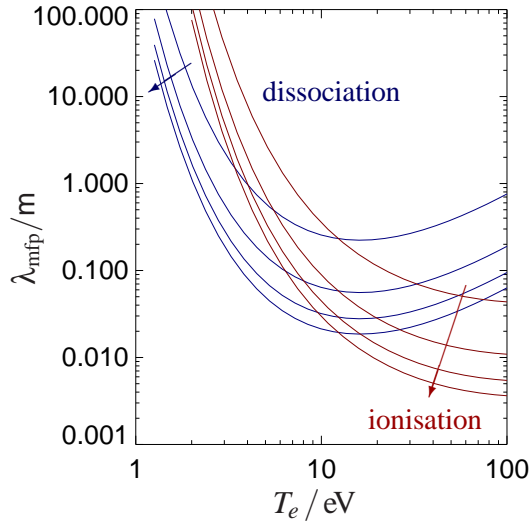


Figure 2.2: Mean free path for molecular reactions as a function of T_e for $n_e \in \{1 \cdot 10^{18}, 4 \cdot 10^{18}, 8 \cdot 10^{18}, 1.2 \cdot 10^{19}\} \text{ m}^{-3}$ (\uparrow).

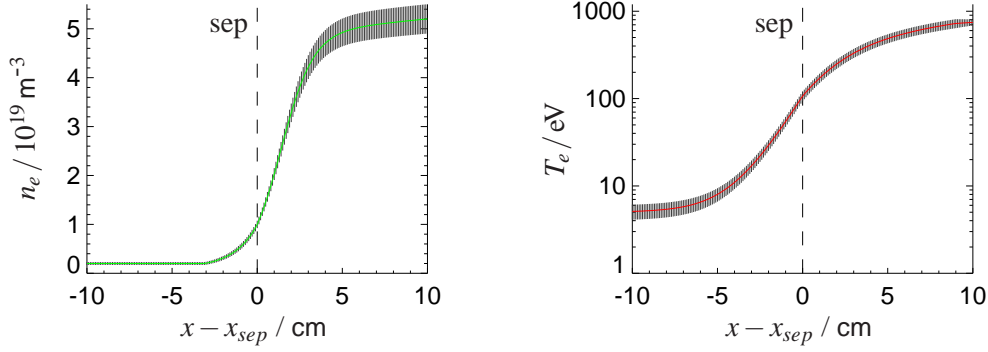


Figure 2.3: LFS midplane profiles of electron density and temperature of a medium density H-mode discharge plotted on a radial real space coordinate used in section 2.3. For a discussion on the data origin see section 5.1.1.

In order to understand the capability of neutral particles of fuelling the core plasma, the production mechanisms of atomic neutrals have to be analysed. As two important examples dissociation of H_2 and H_2^+ is briefly mentioned. Figure 2.4 displays the potential energy of molecular systems H_2 and H_2^+ as a function of the spatial separation of the nuclei for basic binding and anti-binding states. Following the Franck-Condon principle [14], changes of the electronic configuration can be treated as being largely independent of relative motion of the nuclei due to their inertia, ie the molecular vibrational state. The electronic ground state $X^1\Sigma_g^+$ might be elevated to the anti-binding state $b^3\Sigma_u^+$ by electron impact excitation. Possible potential energies of the excited state are indicated by the residence area of the ground state of the nuclei. Using the mean value as an estimate about 8.5 eV impact energy is required to excite the system to the anti-binding state from which about 4.5 eV is distributed to the reaction products (ie ~ 2.25 eV per atom) since the molecular binding has to be subtracted. The same reasoning applies for the dissociation of H_2^+ . Excitation of H_2^+ ($X^2\Sigma_g^+$) to the lowest dissociative state $\text{H}_2^+(2p\sigma_u)$ results in kinetic energy of ~ 4.5 eV per product particle. Rigorous quantum mechanical treatment of the problem provides velocity distributions of the products which are centered around the values just motivated.

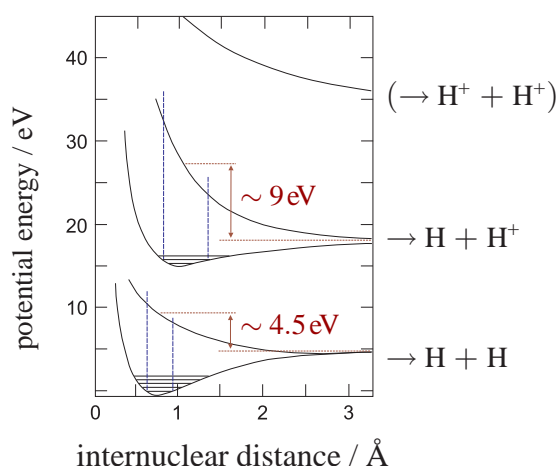


Figure 2.4: Simplified sketch of potential energy of the systems H_2 and H_2^+ [12].

Molecular reactions thus produce atoms of much higher velocity than the initial thermal molecular motion suggests. Fundamental reactions regarding the atomic species are recombination, ionisation and charge exchange. Recombination is significant only for low temperatures $T_e \leq 1\text{ eV}$ which might be the case in cold and dense divertor plasmas. Figure 2.5 shows the rate coefficients for ionisation and charge exchange for ground state Hydrogen. The charge exchange rate always surpasses ionisation, in particular below the ionisation threshold energy of 13.6 eV , indicated by the ratio. The motion of neutral particles is therefore often stated to be of diffusive character, the stepsize being determined by the local ion temperature and the charge exchange rate, and in the vicinity of higher temperatures $T_e \geq 10\text{ eV}$ the path being terminated by ionisation after a couple of steps. The mean free path for these two reactions is given in figure 2.6 for high neutral energies of $T_H \in \{2.25, 4.5, 50\}\text{ eV}$ to reflect Franck-Condon neutrals and ion temperature. In the SOL of the main chamber the mean free path obviously can become very large and the probability of neutral particles penetrating the core plasma edge increases.

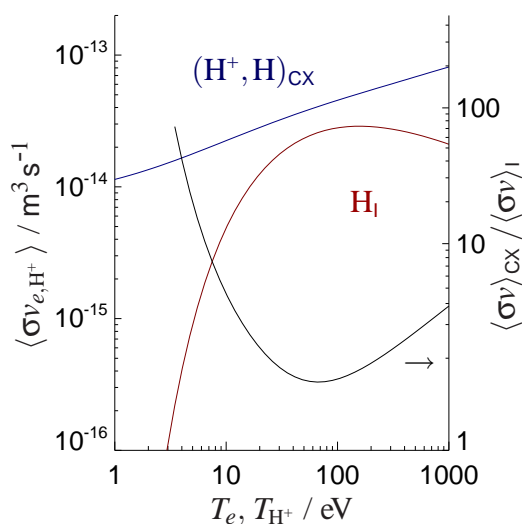


Figure 2.5: Rate coefficients for Hydrogen ionisation and charge exchange and the ratio of both.

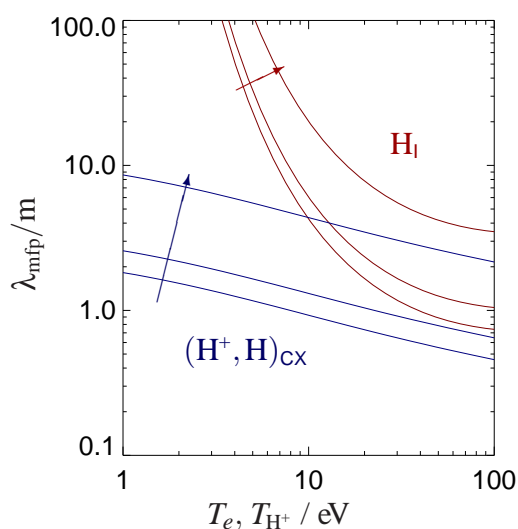


Figure 2.6: Hydrogen mean free path for reaction rates of fig. 2.5 with $n_e = 1.2 \cdot 10^{19} \text{ m}^{-3} (=n_{H^+})$ and $T_H \in \{2.25, 4.5, 50\} \text{ eV}$ (↑).

Collecting the aspects previously mentioned, the impact of neutrals might be summarized as follows. Energy distribution and therewith spatial penetration is determined by collisional cooling (gas-puff and neutral-neutral collisions) and collisional heating (Franck-Condon neutrals, charge exchange). The plasma is cooled in the electron channel by reactions of dissociation, excitation and ionisation and the ion channel is mainly affected by charge exchange reactions, displaying a possible sink for fast plasma ions and leading to friction of the parallel \vec{B} ion flow due to the loss of ion momentum to neutral particles in an arbitrary direction. A discussion of particular reactions is useful to understand basic mechanisms but gives only a strongly simplified picture. Interconnection of many collisional processes, eg collisional excitation and deexcitation lead to an increased effective ionisation energy compared to the bare threshold energy, requires the development of as complex as possible collisional-radiative models. These provide for specified plasma parameters effective rate coefficients for reaction types of interest, photon emissivity coefficients and electron cooling rates.

2.2 Occupation Balance of Excited States

The interest of plasma spectroscopy is to provide measures for interpretation of radiation from the plasma state in terms of its composition, density and temperature of its constituents [15]. Considering line radiation of some excited species a in state p (with p representing the quantum mechanical details), the emission for transition p - q per volume and solid angle is given by:

$$\epsilon_a(p, q) = n_a(p) A(p, q) h\nu / 4\pi \left[\frac{\text{W}}{\text{m}^3 \text{sr}} \right] ,$$

with $A(p, q)$ denoting the transition probability neglecting induced emission. Recording of line radiation thus gives access to the population of the emitting source in a particular state, presupposed the knowledge of $A(p, q)$. However, the character of the plasma observed remains undetermined from this single piece of information since different processes might have populated the state p , ie in general excitation and deexcitation, ionisation and recombination mechanisms. Thorough knowledge of occupation distributions among ground state and excited states of a certain ion stage is required if the species is to be characterised from a single optical measurement. The main objective of this thesis is the determination of neutral sources in the SOL and edge region of a magnetically confined plasma by the analysis of Hydrogen Balmer- α radiation. In principle, following seemingly simple relationships like

$$\epsilon_{\text{H}\alpha, \text{exc}} = n_e n_{\text{H}} \mathcal{P}EC_{\text{H}\alpha, \text{exc}}(n_e, T_e)$$

are applied, with an effective rate coefficient $\mathcal{P}EC_{\text{H}\alpha, \text{exc}}$ termed photon emissivity coefficient describing the plasma state to relate $\text{H}\alpha$ emission to the total neutral density. In this section it is tried to enlight the background of this hidden complexity. As in the previous section, reactions regarding plasma electrons besides radiative transitions are in the focus of discussion.



If the plasma is sufficiently thin ($n_e \leq 10^{18} \text{ m}^{-3}$), a balance between collisional excitation and spontaneous radiative decay can be assumed which is expressed in the framework of corona equilibrium. The balance of excited states then reads:

$$n_a(0)n_e C(0,p)(T_e) = n_a(p) \sum_{q < p} A(p,q) \quad .$$

Excitation is presumed to be dominantly from the ground state since due to the low electron density collision times are too long for multistep excitation compared to the rate of radiative decay. The excitation rate coefficient $C(0,p)$ is a function of electron temperature according to the energy dependence of the cross section for the particular reaction. Emission from a certain transition is expressed as:

$$\varepsilon_a(p,q)4\pi = n_a(p)A(p,q)h\nu = n_a(0)n_e h\nu C(0,p) \frac{A(p,q)}{\sum_{l < p} A(p,l)} = n_a(0)n_e h\nu C(0,p)B(p,q,l) \quad ,$$

with $B(p,q,l)$ termed the branching ratio characterising the structure of optically allowed transitions. The relationship between line radiation and the total density of species a is established as:

$$n_a = n_a(0) \left(1 + n_e \sum_p \frac{C(0,p)}{\sum_{q < p} A(p,q)} \right) \quad .$$

In the case of high density ($n_e \geq 10^{24} \text{ m}^{-3}$) all the reactions (a1)-(a4) are found to be equilibrated, ie forward and back reactions occur at the same rates and the system is in thermodynamic equilibrium. Excited states are found to be related as:

$$\frac{n_a(p)}{n_a(q)} = \frac{g_a(p)}{g_a(q)} \exp\left(-\frac{\Delta E_{p,q}}{kT}\right) \quad ,$$

with $g_a(i)$ denoting the statistical weight of state i and a single temperature T valid for all constituents. If thermodynamic equilibrium (TE) holds also for the reactions involving radiation, then line radiation is trapped within the plasma volume and the emitted spectrum corresponds to black body radiation. Complete TE appears as a universal description since the details of the transitions, ie reaction cross sections or transition probabilities are not required.

In an inhomogeneous plasma like encountered in magnetic confinement fusion, parameter ranges for electron density $10^{17} - 10^{21} \text{ m}^{-3}$ and temperature $1 - 10^3 \text{ eV}$ in the different areas core edge, SOL and divertor require a dedicated analysis of the plasma state and special equilibrium properties mentioned above might be applicable only partly. For all ion species and excited states the complete set of interactions has to be formulated to resolve the coupled system.

The rate equation for the excited state p reads (omitting subscript a):

$$\begin{aligned}
\frac{d}{dt}n(p) &= \sum_{q<p} C(q,p)n_en(q) && \text{collisional excitation} && \text{(a)} \\
&+ \sum_{q>p} F(q,p)n_en(q) && \text{collisional deexcitation} && \text{(b)} \\
&+ \sum_{q>p} A(q,p)n(q) && \text{spontaneous emission} && \text{(c)} \\
&+ \alpha(p)n_e^2n_z && \text{three body recombination} && \text{(d)} \\
&+ \beta(p)n_en_z && \text{radiative recombination} && \text{(e)} \\
&- \sum_{q<p} F(p,q)n_en(p) && \text{collisional deexcitation} && \text{(f)} \\
&- \sum_{q>p} C(p,q)n_en(p) && \text{collisional excitation} && \text{(g)} \\
&- S(p)n_en(p) && \text{ionisation} && \text{(h)} \\
&- \sum_{q<p} A(p,q)n(p) && \text{spontaneous emission} && \text{(i)} .
\end{aligned}$$

This description corresponds to the optically thin case, ie excitation by radiation is neglected (so is photo ionisation) - opacity has to be treated separately since considerations about the plasma geometry need to be made. Terms (a)-(e) display populating fluxes of level p of the specified types and (f)-(i) depopulating fluxes respectively. Coupling is established among excited states and via ionisation and recombination to adjacent ion stages. The standard approach is to divide the populations into two main groups which are characterised by their relaxation time. Ground state atoms and ions - and if required also metastable states - are considered separately from the group of excited states. The analysis of the various population and depopulation mechanisms reveals that typically collisional excitation to adjacent energy levels and radiative decay are responsible for a quick equilibration of excited states in relation to the ground state. Basic reason is the decreasing excitation threshold with increasing principle quantum number. For the ratio of relaxation times several orders of magnitude can be found. The system of coupled equations for the excited state populations is simplified by the assumption of quasi stationarity ($\frac{d}{dt}n(p) \approx 0$) describing the equilibrated system for particular ground state populations of involved ion stages. The set of rate equations is transformed to a set of linear equations such to relate the different groups of populations $n(p)$, $n(1)$ and n_z so that the solution takes the condensed form [15] which is based on the formulation of [16]:

$$n(p) = r_0(p)Z(p)n_zn_e + r_1(p)\frac{Z(p)}{Z(1)}n(1) \equiv n_0(p) + n_1(p) ,$$

with $Z(p) = \frac{g(p)}{2g_z} \left(\frac{h^2}{2\pi mkT_e} \right)^{3/2} \exp\left(\frac{\chi(p)}{kT_e}\right)$ the Saha-Boltzmann coefficient and the population coefficients $r_0(p)$ and $r_1(p)$ (functions of n_e and T_e , r_0 comprises the recombining branch, r_1 the ionising branch of population fluxes). $n(p)$ is the result of contributions from a recombining $n_0(p)$ and an ionising plasma component $n_1(p)$.

Except for cold and dense divertor conditions, plasma parameters in the edge and SOL determine the excited states to be in corona equilibrium at the lowest densities obtained and transiently changing with increasing density to the so-called saturation phase in which collisional deexcitation becomes stronger than radiative decay. This transition features that high lying states are

affected first by this phase transition or in other words, it exists a boundary value for the principle quantum number (Griem's boundary [17]) which is a function of density that separates lower lying states (corona phase) and higher lying states (saturation phase). Effective rate coefficients for photon emission are then expressed, eg for excitation the ionising component applies,

$$\mathcal{P}EC_{i,j,\text{exc}} = \frac{r_1(i)}{n_e} \frac{Z(i)}{Z(1)} A(i, j) \quad .$$

In the discussion of occupation balance of excited states, reabsorption of photons from spontaneous emission has been set aside so far. Opacity in general influences the intensity and spectral shape of line radiation for an observer outside the plasma and displays a populating flux mechanism for excited states which has an impact on the whole system. Strong reabsorption is in particular important for divertor conditions because the recombination rate is reduced which is not beneficial in terms of eventually desired plasma detachment. Optical thickness is determined by the absorption coefficient for a particular emission line and the size of the plasma. Transport of radiation along an arbitrary straight path is described by:

$$\frac{dL_\lambda(x)}{dx} = \varepsilon_\lambda(x) - \kappa_\lambda(x)L_\lambda(x) \quad ,$$

with the spectral emission as the source and the absorption as the sink. The solution reads:

$$L_\lambda(x) = \int_{x_0}^x \varepsilon_\lambda(x') \exp \left[- \int_{x'}^x \kappa_\lambda(x'') dx'' \right] dx' + L_\lambda(x_0) \exp \left[- \int_{x_0}^x \kappa_\lambda(x') dx' \right] \quad (*) .$$

In case of spatially constant κ_λ the exponential factors are simplified which might be employed to characterise optical transparency by $\kappa_\lambda \Delta x \ll 1$. The absorption coefficient is related to the spectral line shape P_λ and transition probability A over:

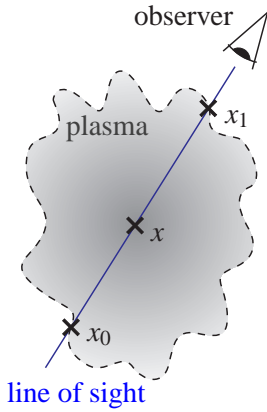
$$\kappa_\lambda = n_p \frac{g_q}{g_p} \frac{\lambda^4}{c} \frac{A(q, p)}{8\pi} P_\lambda = n_p \frac{\lambda}{c} hB(p, q) P_\lambda \quad .$$

Density and line profile are both functions of plasma parameters, the latter might be the result of various shaping effects (Stark, Doppler, Zeeman). Typically, line shapes appear as peaked functions and absorption near the line center is more probable, ie line radiation from the line wings is more likely to escape the optically thick region. Consequently, the line profile observed from outside the plasma deviates from the optically thin case.

A standard method to consider the impact of opacity on radiation and occupation balance is to introduce so-called escape factors. The line escape factor Θ_L and the population escape factor Θ_p are defined as to correct results from reasoning of the optically thin case. Following the sketch shown below, Θ_L for the observer would be expressed in the general form:

$$\Theta_L = \frac{\int_{x_0}^{x_1} \int_{line} \varepsilon_\lambda(x', \lambda) \exp \left[- \int_{x'}^{x_1} \kappa_\lambda(x'', \lambda) dx'' \right] d\lambda dx'}{\int_{x_0}^{x_1} \int_{line} \varepsilon_\lambda(x', \lambda) P_\lambda(\lambda) d\lambda dx'} \quad ,$$

where $L_\lambda(x_0)$ has been set to zero for simplicity. Interpretation of spectroscopic measurements in terms of the excited states density is possible if the experimental signal is multiplied by the inverse of Θ_L to account for all primarily emitted photons.



The change in excited states population is handled by introducing an effective probability for spontaneous emission $A_{eff}(p, q) = \Theta_p(p, q)A(q, p)$ for the collisional radiative modelling which accounts for the enhanced population of states p by reabsorption. Θ_p is defined as $\frac{u_\epsilon - u_\kappa}{u_\epsilon}$ with u_ϵ and u_κ denoting the power densities for emission and absorption:

$$\Theta_p(x) = 1 - \frac{\int_{\Omega} \int_{line} \kappa_{\lambda}(x, \lambda) L_{\lambda}(x, \lambda, \Omega) d\lambda d\Omega}{4\pi \int_{line} \epsilon_{\lambda}(x, \lambda) P_{\lambda}(\lambda) d\lambda}$$

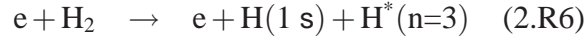
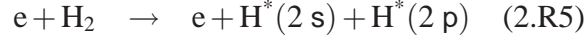
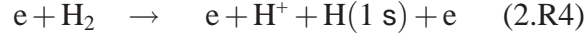
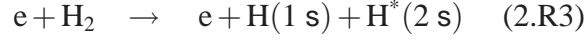
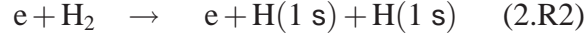
The solid angle integration implies the anisotropy of $L_{\lambda}(\Omega)$ which is described in (*) for one particular direction. Actual values for Θ_L and Θ_p may be obtained for model cases where line profile, plasma parameters and viewing geometry are prescribed. In [18] opacity for a Hydrogen plasma is discussed for divertor conditions ($n_e \gtrsim 10^{20} \text{ m}^{-3}$, $T_e \sim 1 \text{ eV}$) and certain geometry parameters. Due to the population distribution in that regime (recombining plasma, validity of Boltzmann distribution) the Lyman series is predominantly affected by opacity. Θ_L and Θ_p for Lyman- α and Lyman- β might well be in the order of 0.1 and 0.5 respectively. Optical thickness of Lyman- β directly influences the population of the ($n = 3$)-level and the emission of Balmer- α (H_{α}) is increased. Θ_L for H_{α} and higher transitions turns out to be very close to unity.

In practise the consideration of optical thickness is rather difficult because the actual plasma parameters which are usually not available throughout the volume have to be taken into account. For the plasma parameters regarding the D_{α} measurements presented in section 5.2 opacity is assumed not to be a critical issue, at least not in relation to the various systematic uncertainties of the diagnostics setup and methods applied for data analysis.

Efforts are being made to treat radiation transport with Monte-Carlo methods in modelling codes like done for neutral particles, eg EIRENE [19].

2.3 Kinetic Treatment of Neutral Particles

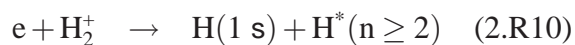
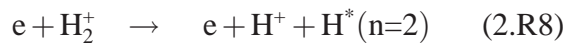
The mean free path of neutrals appears to be long compared to the spatial dimension of the SOL and edge plasma. Dissociative reactions regarding molecular species and charge exchange of plasma ions with atoms as well as elastic collisions display sources of fast neutral particles. Thus a kinetic treatment of neutral-plasma interaction is required for an appropriate description. In order to establish a picture of neutral parameters consistent with the experimental data of H_{α} emission and plasma conditions the code **KN1D** [20] is applied. This **'1D space, 2D velocity, kinetic transport algorithm for atomic and molecular hydrogen in an ionising plasma'** is provided by LaBombard and an elaborate description can be found in the reference. It computes the neutral molecular and atomic velocity distribution functions with the method of successive collision generations on a slab-like geometry with specified plasma parameters. With this expansion of the molecular and atomic velocity distribution functions and the specified boundary conditions, recursion relations for the components of the distribution (generations) on the grid can be deduced. In the following two sections the implementation and application of the algorithm are sketched.



The rate coefficients of figure 2.8 are nominal in the sense that the cross sections are averaged corresponding to the Maxwellian electron velocity distribution. If the plasma is sufficiently thin, 2.R3, 2.R5 and 2.R6 might all be treated as production terms of ground state Hydrogen (for the case of 2.R3 electron impact conversion 2s-2p is more likely than ionisation).

In the plasma environment of interest, multistep excitation processes have an impact on the electronically and vibrationally excited states population distribution and result in effective dissociation, ionisation and recombination rate coefficients, so that the numbers of fig. 2.8 might not be adequate for direct usage. Collisional radiative modelling of molecular Hydrogen in a plasma was performed by Sawada [21], considering also vibrationally excited states. Multistep excitation of molecules leads to an increased production of dissociation products and an elevated ionisation rate. The results of this study are adopted for the reactions noted here. Molecular ionisation (2.R1) is supposed to be increased by a factor of 1.85. Production of ground state atoms is increased and a dependence on n_e and T_e is also considered in KN1D; factors in the range of 1.1-1.6 are applied to the rate coefficients of 2.R2. For relevant plasma parameters, the dissociative excitation reactions 2.R3, 2.R5 and 2.R6 do not contribute significantly to the ionisation rate and these reactions are instead treated as production paths of ground state atoms. The dissociative ionisation reaction 2.R4 is considered to be increased by a factor of 1.67 independent of n_e and T_e .

Reaction 2.R1 describes the production path of molecular ions. The influence of the magnetic field which by definition is oriented perpendicularly to the x -axis is expressed in a stationarity of the ions movement in the x -direction. In the framework of rotational symmetry of the system about the x -axis there is no dedicated direction of the magnetic field. Evolution of this species is restricted to perpendicular motion which may result in limiter recycling and the reactions 2.R7-2.R10:



For the lack of availability of collisional radiative modelling of the molecular ion the reaction rates of figure 2.9 are used directly. The reactions 2.R8 and 2.R10 are interpreted as production paths of ground state atoms.

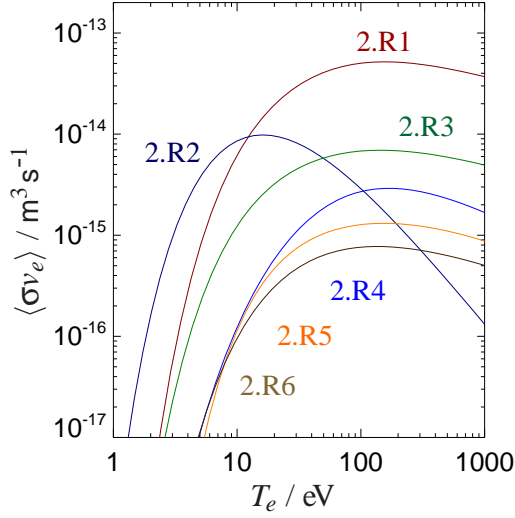


Figure 2.8: Rate coefficients for molecular neutrals reactions 2.R1-2.R6 [13].

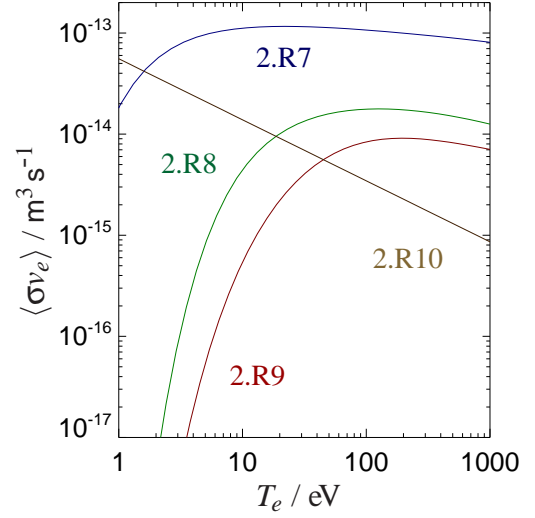


Figure 2.9: Rate coefficients for molecular ions reactions 2.R7-2.R10 [13].

Dissociative reactions of molecules and molecular ions are the origin of the velocity space source distribution of atoms. It is determined by the velocity distribution of the reaction educts and the product velocities which result from the details of the dissociation process. Table 2.2 lists the Franck-Condon energies E_{FC} of related reactions, the accompanied velocities are $v_{FC} = \sqrt{\frac{2E_{FC}}{\mu m_H}}$ ($\mu = 1$ Hydrogen, $\mu = 2$ Deuterium). The function which is employed to represent the velocity distribution f_R of the atoms is chosen as

$$f_R(v_r, v_x) \sim \exp \left[-\mu m_H \frac{\left(\sqrt{v_r^2 + v_x^2} - v_{FC} + \frac{3}{2} \frac{T_{FC}}{\mu m_H v_{FC}} \right)^2}{T_{FC} + \frac{1}{2} T_{mol}} \right]$$

with T_{FC} denoting the effective temperature of Franck-Condon neutrals which is determined by the energy spread of the dissociation and T_{mol} the temperature of the molecule or molecular ion. For T_{mol} negligible against T_{FC} , v_{FC} is returned as the most probable velocity. In the case of high molecular temperature it approaches a Maxwellian distribution for the reaction products with an average velocity of 1/2 times the one corresponding to a Maxwellian molecular distribution at T_{mol} which is supposed to be an appropriate description if the Franck-Condon energy is negligible.

Elastic scattering reactions are optionally included to simulate thermal equilibration among the particles: $(\text{H}_2, \text{H}^+)_{el}$, $(\text{H}_2, \text{H})_{el}$ and $(\text{H}_2, \text{H}_2)_{el}$. The cross sections for momentum transfer are taken from [22]. Molecular charge exchange $(\text{H}_2, \text{H}_2^+)_{cx}$ is also optionally considered in the algorithm. Rate coefficients as a function of ion temperature for several neutral energies E_n are shown in figure 2.10.

reaction	$E_{FC} = \langle E_H \rangle / \text{eV}$
2.R2	3.
2.R3	0.3
2.R4	$\frac{1}{2}(E_e - 18); 18 \leq E_e < 18.5$ $0.25; 18.5 \leq E_e < 19.$ $\frac{1}{2}(E_e - 26.); 26. \leq E_e < 41.6$ $7.8; 41.6 < E_e$
2.R5	4.85
2.R6	2.5
2.R7	4.3
2.R8	1.5
2.R10	$\frac{1}{2}(E_e - 13.58/n^2)$

Table 2.2: Franck-Condon energies of dissociation products; $E_e \approx \frac{3}{2} T_e$.

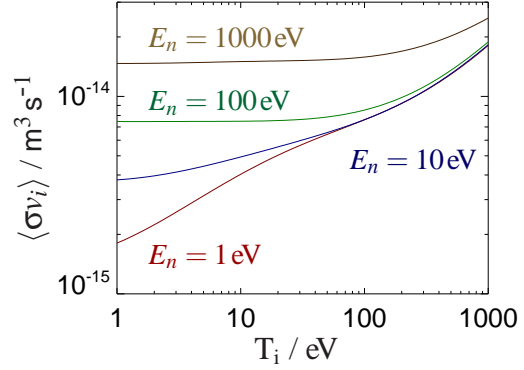


Figure 2.10: Rate coefficients for molecular charge exchange [13].

The Boltzmann equation for the molecular velocity distribution function f_{H_2} incorporating all reactions mentioned above in the actual form handled by the KN1D code reads:

$$\begin{aligned}
v_x \frac{\partial f_{\text{H}_2}}{\partial x} = & -\alpha_{\text{loss}}(x) f_{\text{H}_2} \text{ }^{(a)} + S_{\text{H}_2} \hat{f}_w \text{ }^{(b)} - \gamma_{\text{wall}} f_{\text{H}_2} \text{ }^{(c)} + \hat{f}_w \int \gamma_{\text{wall}} f_{\text{H}_2} \partial^3 v' \text{ }^{(d)} \\
& - f_{\text{H}_2} n_{\text{H}_2^+} \int f_{\text{H}_2^+}(v', x) |v - v'| \sigma_{\text{cx}}(|v - v'|) \partial^3 v' \text{ }^{(e)} \\
& + \hat{f}_{\text{H}_2^+} n_{\text{H}_2^+} \int f_{\text{H}_2}(v', x) |v - v'| \sigma_{\text{cx}}(|v - v'|) \partial^3 v' \text{ }^{(f)} \\
& + \omega_{\text{H}_2:\text{H}^+}^{\text{el}} (M_{\text{H}_2:\text{H}^+} - f_{\text{H}_2}) + \omega_{\text{H}_2:\text{H}}^{\text{el}} (M_{\text{H}_2:\text{H}} - f_{\text{H}_2}) + \omega_{\text{H}_2:\text{H}_2}^{\text{el}} (M_{\text{H}_2:\text{H}_2} - f_{\text{H}_2}) \text{ }^{(g)} \text{ }^{(*)} ,
\end{aligned}$$

where \hat{f} denotes a normalised distribution function $\int \hat{f}(v', x) \partial^3 v' = 1$. Reactions 2.R1-2.R6 lead to the destruction of molecules which is expressed in the first term $()^{(a)}$ with $\alpha_{\text{loss}} = \sum_{i=1}^6 \langle \sigma v_e \rangle_{2.Ri}$. The second term $()^{(b)}$ describes the source of molecules at wall temperature which is specified as input parameter. Loss of molecules to the wall and limiter side is characterised with the third term $()^{(c)}$ by the loss frequency γ_{wall} which is evaluated from radial velocity and perpendicular extension D of the shadowed area: $\gamma_{\text{wall}}(v_r, x) = \frac{2v_r}{D(x)}$. The following term $()^{(d)}$ displays the recycling process of molecules lost to the walls returned at wall temperature. Charge exchange of molecules with molecular ions has both the effect of a source $()^{(f)}$ and sink $()^{(e)}$ of the distribution function. Finally, the last three terms $()^{(g)}$ are used to represent the impact of elastic collisions. The latter expressions require some further remarks. These are representations, ie expressions to replace the Boltzmann binary collision terms, eg:

$$\begin{aligned}
\iint [f_{\text{H}_2}(v'', x) f_{\text{H}}(v''', x) - f_{\text{H}_2}(v, x) f_{\text{H}}(v', x)] |v - v'| \frac{\delta \sigma_{\text{H}_2:\text{H}}(|v - v'|)}{\delta \Omega} \delta \Omega \partial^3 v' \\
\longrightarrow \omega_{\text{H}_2:\text{H}}^{\text{el}} (M_{\text{H}_2:\text{H}} - f_{\text{H}_2}) .
\end{aligned}$$

Velocities involved before (v, v') and after (v'', v''') the collision are related through the scattering angles. The demanding explicit evaluation of the complex collision integral is avoided by applying a symplified kinetic model, here the BKG [23] model, as an approximation of the scattering process. The alternative expression can be constructed such that mass, momentum and energy of

the total species mixture for mixed collisions and mass, momentum and energy of each species for self-collisions are conserved. The chosen term might be described as a relaxation of the distribution function f_{H_2} to the drifting Maxwellian M on a time scale of $1/\omega^{el}$. Drift velocity and temperature characterising M are center of mass velocity and hybrid temperature of the colliding particles. Here, the momentum transfer rate is taken to obtain ω^{el} for mixed collisions, for self-collisions the temperature isotropisation rate is used. This ansatz allows to achieve relaxation rates of mass, momentum and energy close to those resulting from the Boltzmann binary collision operator.

The shorthand notation of (*) reads:

$$v_x \frac{\partial f_{\text{H}_2}}{\partial x} = S_{\text{H}_2} \hat{f}_w + s_{wall} + \beta_{cx} - \alpha_c f_{\text{H}_2} + \omega_M \quad ,$$

with $s_{wall} := ()^{(d)}$, $\beta_{cx} := ()^{(f)}$, $\alpha_c := \alpha_{cx} + \alpha_{loss} + \omega_{el} + \gamma_{wall}$ [$\alpha_{cx} := ()^{(e)}/f_{\text{H}_2}$, $\omega_{el} := \omega_{\text{H}_2:\text{H}^+}^{el} + \omega_{\text{H}_2:\text{H}}^{el} + \omega_{\text{H}_2:\text{H}_2}^{el}$] and $\omega_M := \omega_{\text{H}_2:\text{H}^+}^{el} M_{\text{H}_2:\text{H}^+} + \omega_{\text{H}_2:\text{H}}^{el} M_{\text{H}_2:\text{H}} + \omega_{\text{H}_2:\text{H}_2}^{el} M_{\text{H}_2:\text{H}_2}$ which is stated to illustrate the method of successive collision generations. The molecular distribution function is considered to be composed of a sum of subdistribution functions which are to be understood as representing an ensemble of particles after a certain number of collisions:

$$f_{\text{H}_2} = \sum_j f_{\text{H}_2 j} \quad , \quad \beta_{cx} = \sum_j \beta_{cx j} \quad , \quad \omega_M = \sum_j \omega_{M j} \quad , \quad s_{wall} = \sum_j s_{wall j} \quad .$$

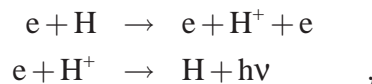
Separate Boltzmann equations for the first and subsequent collision generations are:

$$\begin{aligned} v_x \frac{\partial f_{\text{H}_2 0}}{\partial x} &= S_{\text{H}_2} \hat{f}_w && - \alpha_c f_{\text{H}_2 0} \\ v_x \frac{\partial f_{\text{H}_2 1}}{\partial x} &= && s_{wall 0} + \beta_{cx 0} - \alpha_c f_{\text{H}_2 1} + \omega_{M 0} \\ v_x \frac{\partial f_{\text{H}_2 j}}{\partial x} &= && s_{wall j-1} + \beta_{cx j-1} - \alpha_c f_{\text{H}_2 j} + \omega_{M j-1} \quad . \end{aligned}$$

Wall source S_{H_2} and all sink mechanisms characterise the evolution of the initial distribution function $f_{\text{H}_2 0}$. Following generations originate from the sink terms of the previous generation and are itself subject to attenuation.

Boundary conditions for the solution of the Boltzmann equations are $f_{\text{H}_2 0}(v_x > 0, v_r, x_a) = f_{\text{H}_2}(v_x > 0, v_r, x_a)$ specified by the flux at the wall and $f_{\text{H}_2 0}(v_x < 0, v_r, x_b) = 0$, ie no neutral flux from the plasma core region. Two hierarchically ordered iterations are involved in obtaining the desired f_{H_2} . The terms for elastic collisions require the input of a guess of f_{H_2} . Self-consistency is achieved if the zero order moment (density) of the resulting f_{H_2} does not deviate from the previous iteration step by a specified amount. Each of these iteration steps includes the expansion of successive collision generations which is followed to the point where the j th generation $f_{\text{H}_2 j}$ does not contribute to the zero order moment significantly.

From the solution of the Boltzmann equation for molecular Hydrogen the velocity space source of atomic Hydrogen is determined. Reactions contained in the algorithm which characterise the evolution of the atomic velocity distribution function are electron impact ionisation and radiative recombination, elastic scattering and charge exchange. The electron impact reactions are:



to which effective rate coefficients have to be derived from collisional radiative modelling. Here, the results from the Johnson-Hinnov CR model [24] are applied. Figure 2.11 shows the rate coefficients for different plasma parameters along with the rate coefficient determined by the cross sections without considering multistep processes. For low energies, collisional deexcitation leads to an increase in the recombination rate coefficient. The nominal recombination rate coefficients as the sum of several paths ($e + H^+ \rightarrow H[1s,2s,2p,n=3,n=4] + h\nu$) is shown with the dashed line. Although barely visible in the figure, reaction rate coefficients differ by factors of about 1 – 2 for the densities chosen. Comparing the rate coefficients for ionisation and recombination it becomes apparent that recombination might be relevant only at very low temperatures. For the parameter range typical for SOL plasmas far from the divertor region the actual recombination rate is negligible because both electron density and temperature drop strongly in the far SOL.

Cross sections for the elastic collision reactions $(H, H^+)_{el}$, $(H, H_2)_{el}$ and $(H, H)_{el}$ are taken from [22] and the treatment corresponds to that of elastic scattering of molecules. Reaction rate coefficients of atomic charge exchange $(H, H^+)_{cx}$ considered in the algorithm, taken from [13], are also depicted in figure 2.11.

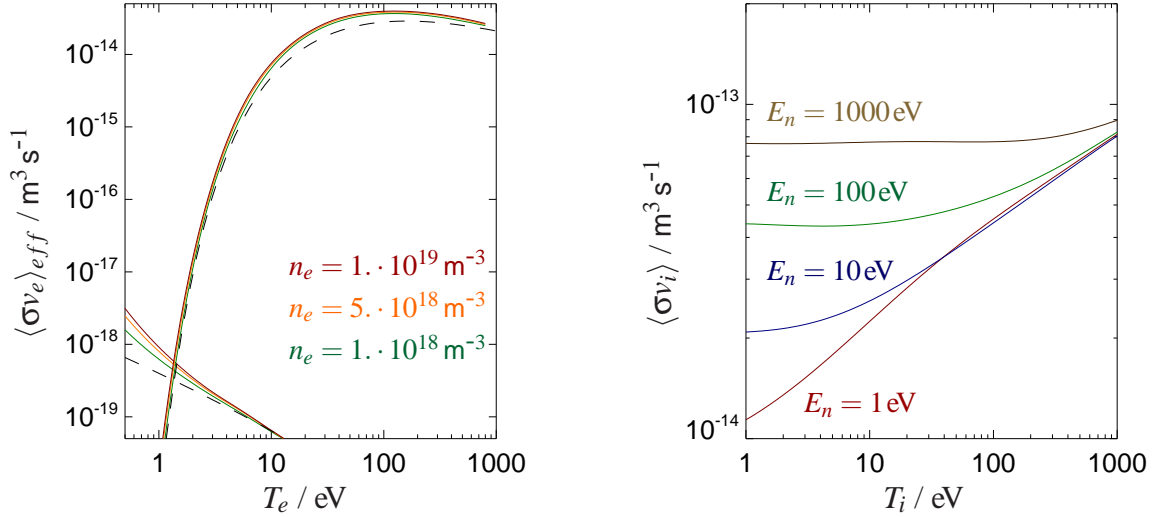


Figure 2.11: Left: Effective rate coefficients from Johnson-Hinnov CR model [24] - black dashed curves are nominal rate coefficients from radiative recombination and ground state ionisation for comparison. Right: Rate coefficients for (H, H^+) charge exchange [13].

The Boltzmann equation of the atomic velocity distribution function f_H as treated in the algorithm reads:

$$\begin{aligned}
 v_x \frac{\partial f_H}{\partial x} = & -f_H \alpha_{ion}^{(a)} + \hat{f}_i n_e n_i \langle \sigma v_e \rangle_{rec,eff}^{(b)} + S_{H^0}^{(c)} - \gamma_{wall} f_H^{(d)} \\
 & - f_H n_i \int \hat{f}_i(v', x) |v - v'| \sigma_{cx}(|v - v'|) \partial^3 v'^{(e)} \\
 & + \hat{f}_i n_i \int f_H(v', x) |v - v'| \sigma_{cx}(|v - v'|) \partial^3 v'^{(f)} \\
 & + \omega_{H:H^+}^{el} (M_{H:H^+} - f_H) + \omega_{H:H_2}^{el} (M_{H:H_2} - f_H) + \omega_{H:H}^{el} (M_{H:H} - f_H)^{(g)} .
 \end{aligned}$$

With $\alpha_{ion} := n_e \langle \sigma v_e \rangle_{ion,eff}$ the first term $()^{(a)}$ displays the atomic ionisation sink and the second term $()^{(b)}$ the recombination source. Like in the description of molecules, the reaction

rates are used directly, because the neutral velocity is small compared to that of the electrons ($|v_H| \ll |v_e|$). The third term $()^{(c)}$ includes atomic sources from molecular dissociative reactions (Franck-Condon neutrals), whereas sidewall collisions in the limiter shadow are considered in $()^{(d)}$. Terms $()^{(e)}$, $()^{(f)}$ and $()^{(g)}$ represent the impact of charge exchange and elastic collisions analogous to the molecular case. Also the solution of this equation is worked out in the same way as described for f_{H_2} with f_H being expanded in a series of collision generations.

The algorithm contains two procedures which determine the molecular and atomic velocity distribution functions f_{H_2} and f_H in a selfconsistent manner with respect to elastic collisions, some aspects of which have been mentioned above. Both parts are coupled through the atomic source originating from molecular dissociation and the molecular flux returned from the wall representing losses of molecules, atoms and ions. The net molecular flux from the wall must balance 2 times the atomic Hydrogen flux onto the wall:

$$2\Gamma_{H_2}^{net} = \Gamma_H^{w,-} \quad (**) \quad .$$

The net molecular flux can be expressed as:

$$\Gamma_{H_2}^{net} = \Gamma_{H_2}^{w,+} - \frac{\varepsilon}{2} \int S_p H_2 \partial x - \frac{\varepsilon}{2} \int S_H H_2 \partial x \quad ,$$

with $\Gamma_{H_2}^{w,+}$ being the specified molecular flux at the wall directed towards the plasma. A returned flux towards the wall is determined by the fraction $\frac{\varepsilon}{2}$ of the side wall sources of plasma $S_p H_2$ and atomic $S_H H_2$ recycling. Here, ε denotes the fraction of the molecular flux directed towards the wall which is left at the wall surface. Collecting all processes that produce atoms returning back to the wall it is obtained:

$$\Gamma_H^{w,-} = \delta(1 + \alpha) R_{dis}^{H^0} \left[\frac{2 - \varepsilon}{2} \left(\int S_p H_2 \partial x + \int S_H H_2 \partial x \right) + \Gamma_{H_2}^{w,+} \right] \quad ,$$

where δ denotes the fraction of the atomic flux towards the wall that actually reaches it and α being the fraction of initially positive directed atomic flux reflected due to charge exchange. $R_{dis}^{H^0}$ is the fraction of molecular dissociation processes resulting in atomic Hydrogen.

In order to fulfil (**), the molecular source from plasma recycling $S_p H_2$ is adjusted in an iteration including the calculation of f_{H_2} and f_H . The parameters ε and $\delta(1 + \alpha) R_{dis}^{H^0}$ can be estimated from the preceding iteration step and $S_p H_2$ refined accordingly. This procedure might be interpreted as a concession to the instance that the mechanism of plasma recycling is not rigorously specified.

An emphasis is put in the KN1D code regarding the accuracy of the numerical procedures providing the distribution functions f_{H_2} and f_H . Estimates are made on errors introduced by the discretisation of the spatial and velocity space domain, of resulting velocity moments of f_{H_2} and f_H and for the conservation of particles. Two of these estimates are stated for reference, exemplified for the molecular case. With the shorthand notation of the molecular Boltzmann equation repeated:

$$v_x \frac{\partial f_{H_2}}{\partial x} = S_{H_2}^{tot} \hat{f}_w + \beta_{cx} - \alpha_c f_{H_2} + \omega_M \quad ,$$

the representation in finite differences, termed the mesh equation, which is the basic expression for the numerical treatment, reads:

$$2v_x \frac{f_{H_2,m+1} - f_{H_2,m}}{x_{m+1} - x_m} = (S_{H_2,m+1}^{tot} + S_{H_2,m}^{tot}) \hat{f}_w + (\beta_{cx,m+1} + \beta_{cx,m}) \\ - (\alpha_{c,m+1} f_{H_2,m+1} + \alpha_{c,m} f_{H_2,m}) + (\omega_{M,m+1} + \omega_{M,m}) \quad ,$$

m denoting the spatial grid cell index. Care has been taken to use a grid spacing sufficiently small to avoid unphysical values for f_{H_2} . A closer look reveals that the grid spacing must satisfy the condition: $(x_{m+1} - x_m) < \frac{2|v_x|}{\max\{\alpha_{c,m}; \alpha_{c,m+1}\}}$, as to avoid the occurrence of negative distribution functions. The following abbreviations shall be defined:

$$T1_m = 2v_x \frac{f_{H_2,m+1} - f_{H_2,m}}{x_{m+1} - x_m} \quad , \quad T2_m = (S_{H_2,m+1}^{tot} + S_{H_2,m}^{tot}) \hat{f}_w \quad , \quad T3_m = \beta_{cx,m+1} + \beta_{cx,m} \quad , \\ T4_m = \alpha_{c,m+1} f_{H_2,m+1} + \alpha_{c,m} f_{H_2,m} \quad , \quad T5_m = \omega_{M,m+1} + \omega_{M,m} \quad .$$

The velocity moments (order M) of the Boltzmann equation should be satisfied with an appropriate f_{H_2} :

$$\iint \frac{\partial f_{H_2}}{\partial x} v_x^{M+1} \partial v_x v_r \partial v_r = \iint S_{H_2}^{tot} \hat{f}_w v_x^M \partial v_x v_r \partial v_r + \iint \beta_{cx} v_x^M \partial v_x v_r \partial v_r \\ - \iint \alpha_c f_{H_2} v_x^M \partial v_x v_r \partial v_r + \iint \omega_M v_x^M \partial v_x v_r \partial v_r \quad ,$$

to which the discretised expression reads:

$$\iint T1_m v_x^M \partial v_x v_r \partial v_r = \iint T2_m v_x^M \partial v_x v_r \partial v_r + \iint T3_m v_x^M \partial v_x v_r \partial v_r \\ - \iint T4_m v_x^M \partial v_x v_r \partial v_r + \iint T5_m v_x^M \partial v_x v_r \partial v_r \quad .$$

Using $TJ_{M,m} := \iint TJ_m v_x^M \partial v_x v_r \partial v_r$, $J \in \{1, 2, 3, 4, 5\}$ the normalised moment error for each grid cell m is defined as:

$$\eta_{M,m} := \frac{|T1_{M,m} - T2_{M,m} - T3_{M,m} + T4_{M,m} - T5_{M,m}|}{\max\{|T1_{M,m}|, |T2_{M,m}|, |T3_{M,m}|, |T4_{M,m}|, |T5_{M,m}|\}} \quad .$$

The discretisation of velocity space has to be accurate in range and resolution such that the major part of the information contained in f_{H_2} is retained. A considerable contribution to f_{H_2} outside the velocity grid would result in uncertainties of moments. In order to judge this issue, a test is performed using the velocity distribution of Franck-Condon neutrals \hat{f}_{FC} to calculate the average velocity from the discretised distribution for comparison with the analytical expression:

$$\bar{v}_{code} = 2\pi \sum_i \sum_j \sqrt{v_{r,i}^2 + v_{x,j}^2} \hat{f}_{FC}(v_{r,i}, v_{x,j}) \Delta v_{x,j} v_{r,i} \Delta v_{r,i} \quad , \\ \bar{v}_{exact} = \int |v| \hat{f}_{FC} \partial^3 v = \frac{2v_{th}}{\sqrt{\pi}} \quad .$$

The normalised expression for the deviation of the two parameters is:

$$\bar{v}_{error,m} = \frac{|\bar{v}_{code,m} - \bar{v}_{exact,m}|}{\bar{v}_{exact,m}} \quad .$$

2.3.2 KN1D in Practise

Using parameters which resemble those of a low field side midplane edge plasma profile at the AUG Tokamak, similar to a medium density, low power H-mode scenario, the results obtained from the KN1D algorithm are discussed.

The spatial grid range is set to 30 cm which is divided into three parts. The first interval is configured as the local limiter shadow, the second interval displays the SOL and the third part of the grid the edge of the core plasma region. Of the two interval boundaries the limiter edge position has an impact on the propagation of neutrals, whereas the separatrix position does not play a role in the numerical procedures but is a marker to differentiate between parameters affecting the SOL or the near core region, eg the aspect of plasma fuelling. A perpendicular extent of the shadowed area of 1 m is assumed and the limiter sides convert both impinging ions and neutral particles to molecules at wall temperature. Electron density and temperature chosen are shown in figure 2.12. In shadowed areas of short connection length, the parallel field gradients of plasma parameters are suspected to be significant and for this basic examination a pragmatic choice for the parallel field averaged profile parameters has been made which is actually not based on diagnostics data. The radial decay lengths of plasma parameters are assumed to be smaller than in regions of large connection length close to the separatrix and the base levels of density and temperature are simply estimates. As the working gas Deuterium has been chosen. The source of neutrals at the wall, which in the experiment is due to localised gas inlet, recycling of perpendicular plasma flux or divertor leakage, is expressed as the wall molecular pressure, here set to be $p_w = 10^{-3}$ Pa which corresponds to a particle flux density towards the plasma of $\Gamma_{D_2}^{w,+} = 7.7 \cdot 10^{19} \text{ m}^{-2} \text{ s}^{-1}$ at the wall temperature defined as $T_w = 293$ K. Ion temperature is not determined experimentally in the region of interest and consequently, the pragmatic choice of $T_i = T_e$ is adopted. Temperature measurements of impurity ions is not used to infer on the majority plasma ions temperature. Velocity of plasma ions in the direction perpendicular to the plasma column, ie in the x -direction of the KN1D grid, is set to zero, since this parameter is also not resolved experimentally. The set of parameters derived from the calculated velocity distribution functions selected for a basic overview contains densities (fig. 2.13), temperatures (fig. 2.14), flux densities (figs. 2.15 and 2.16), various source profiles (fig. 2.17), energy transfer to atomic neutrals and Balmer- α emission (fig. 2.18).

As to be expected from the magnitude of plasma parameters, the molecular density n_{D_2} drops monotonously with the slope being more negative at the transition of limiter shadow and SOL where the plasma parameters rise. The atomic density profile n_D is determined by the dissociation of molecules and the increased ionisation rate when approaching the separatrix with significant rise in electron temperature, which is seen in the grid range of strong drop of n_D and corresponding ionisation source S_{ion} .

Although the wall temperature of molecules is low ($T_w \approx 0.025$ eV) the impact of elastic collisions with the relatively hot plasma background results in the temperature profile of molecules in the range of $T_{D_2} \in [0.05; 2]$ eV. The atomic temperature is seen not to fall below about 4 eV which is basically due to the Franck-Condon dissociation energies and probably to some extent influenced by fast charge exchange neutrals from the core region. In general, the temperature of atomic neutrals follows the spatial evolution of the plasma temperature since elastic collisions and charge exchange reactions play the dominant role besides ionisation.

For the understanding of profiles of molecular and atomic flux densities, the consideration of the positive and negative components is useful. $\Gamma_{D_2}^+$ is determined by the boundary condition

of $\Gamma_{D_2}^{w,+}$ and the positive velocity part of recycled molecules starting from the side walls; also the rise of molecular temperature might have an impact. The negative flux density $\Gamma_{D_2}^-$ is mainly the negative velocity half of molecules from side wall recycling. From the evolution of flux density in the SOL region it can be seen that the fraction of molecules returned to the wall due to elastic collisions is obviously very small. Referring to the position of the atomic source profile S_D the large part of atomic flux in the negative direction - in the limiter shadow there is in fact nearly no positive atomic flux - is explained, since at the exit of the shadowed area dissociation of molecules sets in and the dissociation products are distributed isotropically. The closer to the core region the less negative flux density is obtained, corresponding to the constraint that there is no neutral flux from the core region and only positive directed neutrals are left before being ionised.

Magnitude and spatial range of the source profiles reveal the plasma source from the ionisation of molecules $S_{D_2^+}$ and dissociation of molecular ions S_{D^+} being relevant in the SOL but fuelling of the core region is possible only from the penetration of atomic neutrals expressed in the ionisation source profile S_{ion} .

The drain of plasma energy is documented with the energy transfer to atomic neutrals Q_D^{net} which is mainly localised at the core boundary displaying the loss of fast plasma ions due to charge exchange. This energy is lost if the resulting fast neutrals are not ionised within the core region. Negative values for this net energy transfer are obtained if the average energy of neutrals is larger than of the plasma ions in which case elastic scattering heats up the plasma at expense of fast atomic neutrals.

Emission of line radiation like $\epsilon_{D\alpha}$ is closely linked to the ionisation source profile. The similarity in shape of the profiles is explained by the roughly constant inverse photon efficiency (S/XB) which is a coefficient derived from collisional radiative modelling relating ionisation rate and photon emission [25]. If the emission profile is measured and the plasma profile is known with appropriate accuracy, KN1D can be used iteratively to estimate the neutral flux density at the plasma edge. Interestingly, plasma energy losses from radiation are shifted outwards with respect to charge exchange losses, which indicates that only a small population of neutrals has a strong impact on the edge plasma, taken the profile of ionisation source or equivalently the atomic neutral density profile into account.

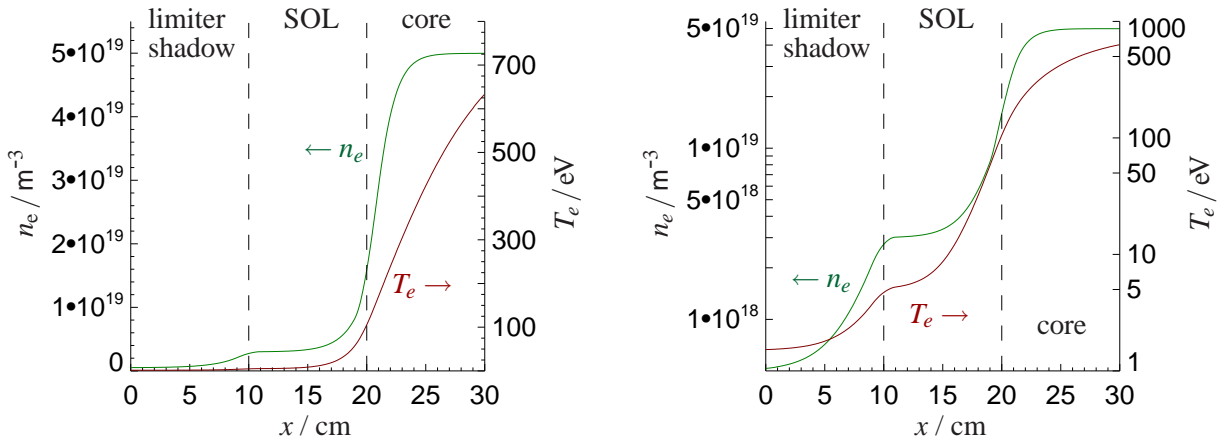


Figure 2.12: Input profile data of electron density and temperature - left linear and right logarithmic scaling to resolve the SOL.

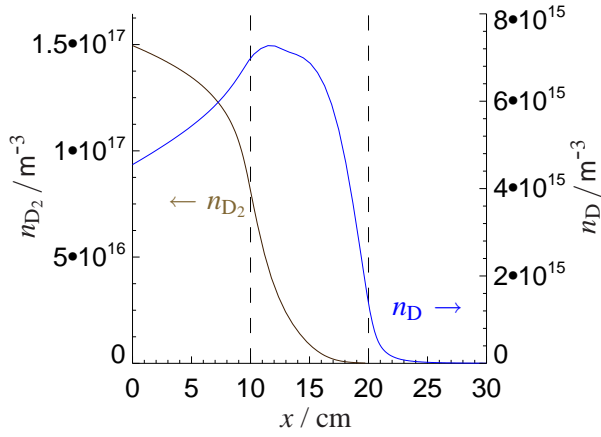


Figure 2.13: Molecular and atomic density profiles.

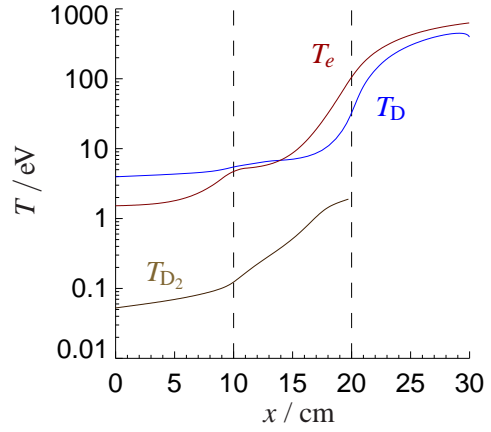


Figure 2.14: Molecular, atomic and electron temperature profiles.

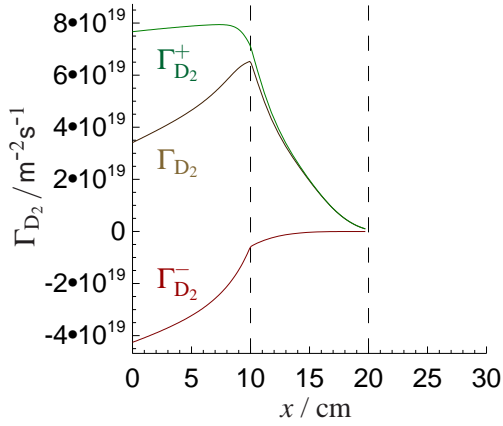


Figure 2.15: Molecular flux density: total and components.

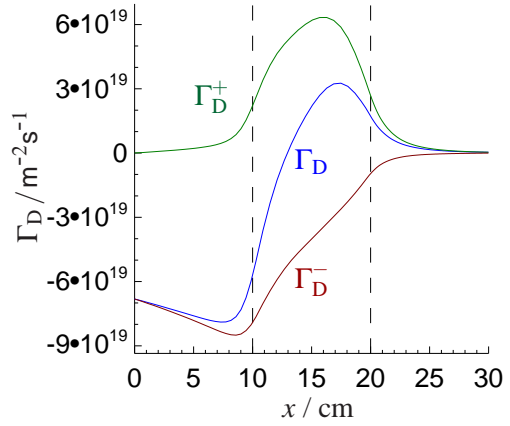


Figure 2.16: Atomic flux density: total and components.

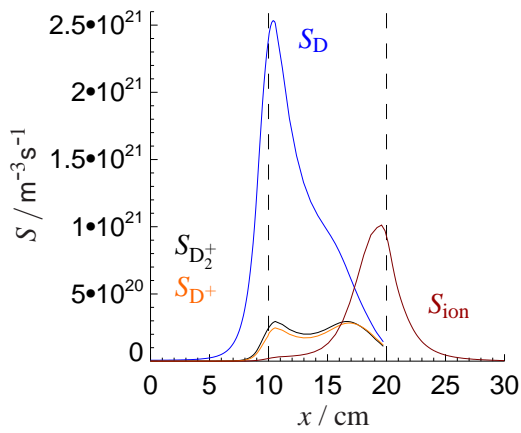


Figure 2.17: Source profiles of atoms, molecular ions and atomic ions from molecular and atomic origin.

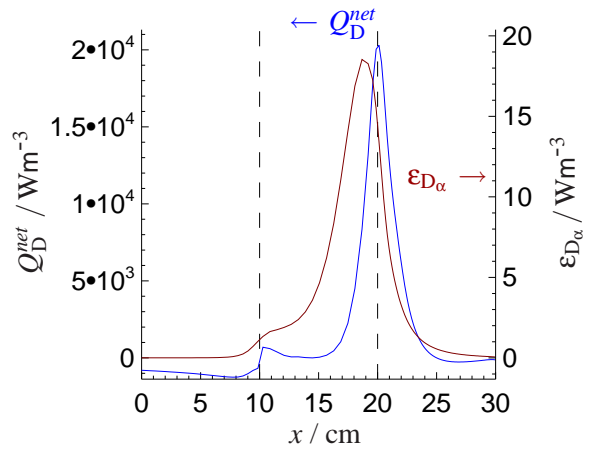


Figure 2.18: Net energy transfer to atomic neutrals and Balmer- α emission.

Figures 2.19 and 2.20 give an impression of the accuracy of the numerical procedures. The error introduced by the discretisation of velocity distribution functions \bar{v}_{error} appears to be very small, except for f_H in the limiter shadow, where a larger uncertainty is obtained. In the case of the moment errors η_M , here stated for density and flux density, numerical precision seems to be sufficient, albeit with more significant deviation in the core region. Even if errors up to $\sim 10\%$ are obtained locally in this example, the overall character of the numerics uncertainty has to be compared with those regarding experimental data of plasma parameters and Balmer- α emission and assumptions on ion temperature discussed in chapter 5.

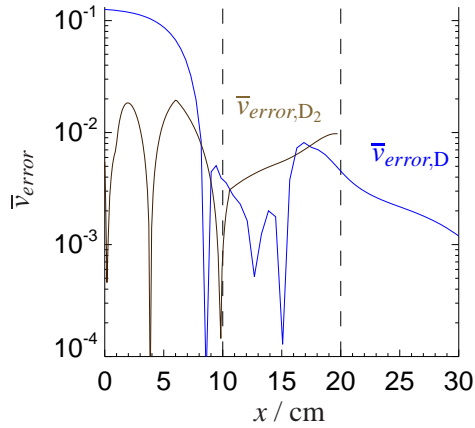


Figure 2.19: Error estimate concerning discretisation of distribution functions.

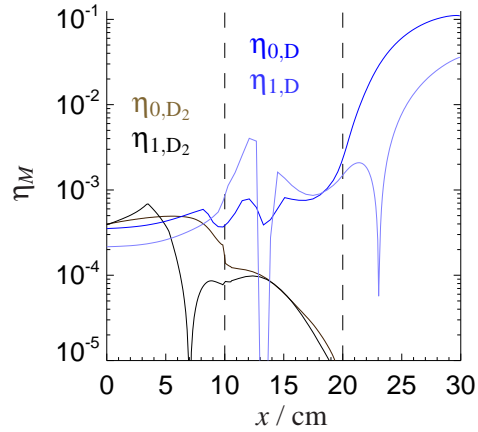


Figure 2.20: Error estimate for moments (0,1) of distribution functions.

One interesting feature of KN1D is that elastic and charge exchange collisions can be optionally excluded in the calculation, both for each reaction separately and for each of the molecular and atomic species. This is useful to judge the importance of these mechanisms with respect to the propagation of neutrals in comparison to the electron impact reactions of dissociation and ionisation. The algorithm was run with the same input parameters as described above, merely molecular and atomic elastic and charge exchange collisions were kept out. Results obtained are compared with the previous case for densities (fig. 2.21), temperatures (fig. 2.22), flux densities (fig. 2.23) and sources (fig. 2.24).

Without elastic and charge exchange processes, the particles are able to penetrate the plasma more freely and the density profiles are shifted towards the plasma and are larger in amplitude. This latter observation requires some explanation, because the volumetric sink mechanisms are the same for both cases and the integrated density profiles should give the same amount of particles, since the same wall flux of molecules is specified. The total side wall sources are indeed different for both cases, corresponding to the loss rate of particles due to elastic and charge exchange scattering. With only small wall losses of neutrals, a larger plasma recycling at the side wall needs to be assumed such to compensate the specified positive molecular flux at the wall (condition of zero net flux to wall). The two cases should therefore be compared rather in the relative radial evolution of profiles, than in magnitude. Further, there is no thermal coupling between neutral and plasma particles so that the temperature of molecules is close to the initial wall temperature without significant change along the grid. The kinetics of atoms is solely determined by dissociation processes, except in the core region, where recombination is the source of fast atoms, but nevertheless displaying a very small population, as can be seen from the atomic density profile. Corresponding to the higher densities, the accompanied flux densities and sources

are larger. However, close to the core, where all profiles decay strongly, the slopes are slightly less negative in the case of elastic and charge exchange collisions being considered, indicating the deeper penetration of a small fraction of particles due to a higher velocity.

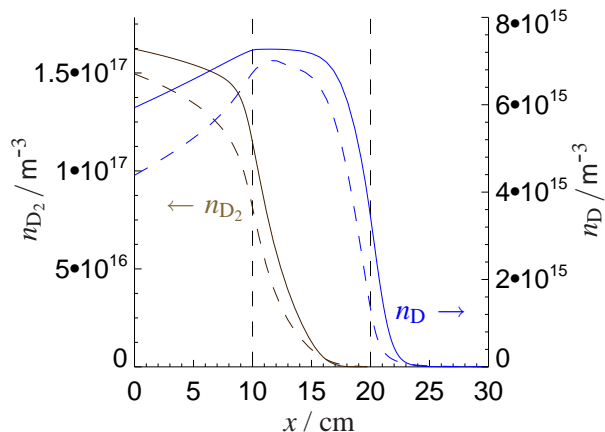


Figure 2.21: Molecular and atomic density profiles: with (dashed) and without (solid) elastic and CX collisions.

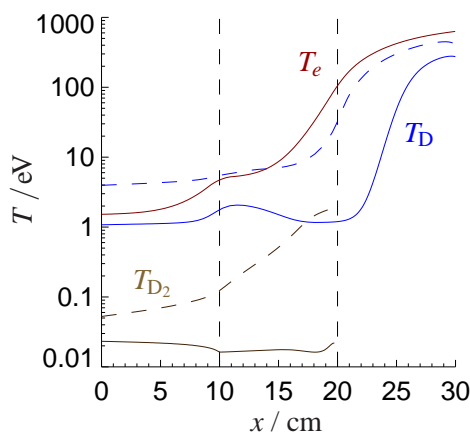


Figure 2.22: Molecular, atomic and electron temperature profiles: with (dashed) and without (solid) elastic and CX collisions.

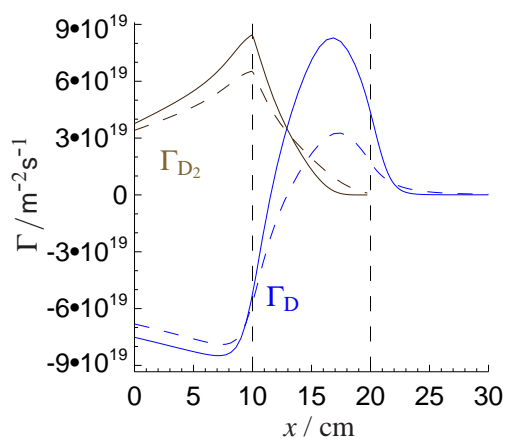


Figure 2.23: Molecular and atomic flux densities: with (dashed) and without (solid) elastic and CX collisions.

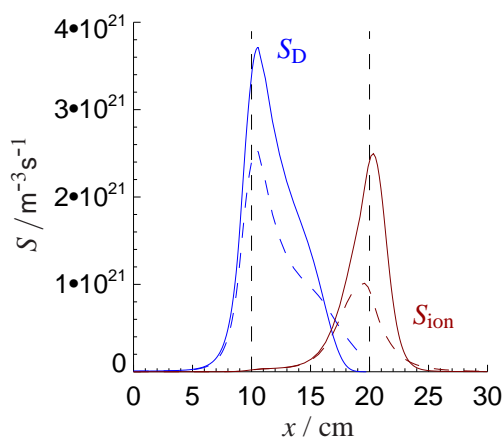


Figure 2.24: Atomic source from dissociation and atomic ionisation profiles: with (dashed) and without (solid) elastic and CX collisions.

For the interpretation of Balmer- α emission, input parameters to KNID obtained experimentally are the origin of uncertainty. Concerning the ion temperature, no data at all is available and estimates have to be made. It is assumed that heat diffusivity is larger for ions than for electrons which results in a higher ion temperature at the plasma edge if the heating power is equally distributed to the ion and electron channel in the core region. Because of the lack of better knowledge a constant factor is used to relate ion and electron temperature. For the results presented in chapter 5 the relationship $T_i = 2 \cdot T_e$ has been chosen. The impact of ion temperature on the parameters of neutrals, leaving all settings unchanged but using $T_i = 2 \cdot T_e$, are documented in figures 2.25 to 2.28.

Parameters characterising molecular penetration are hardly changed. Profiles of density, flux density and source of atoms are nearly unaffected by the increased ion temperature. A slightly elevated molecular temperature is observed which stems from the elastic collisions with plasma ions. Although the atomic source profile seems to be independent of T_i in the present example, the

higher rate coefficient for atomic charge exchange leads to a reduced atomic density, probably caused by the stronger atomic return flux to the wall. The temperature of atoms reflects the increased ion temperature and results in a slight shift of the center of the ionisation profile.

Taken the methodology and uncertainty regarding the experimental determination of the Balmer- α emission into account, the actual magnitude of ion temperature does not seem to be a matter of great concern, provided that ion and electron temperature are comparable.

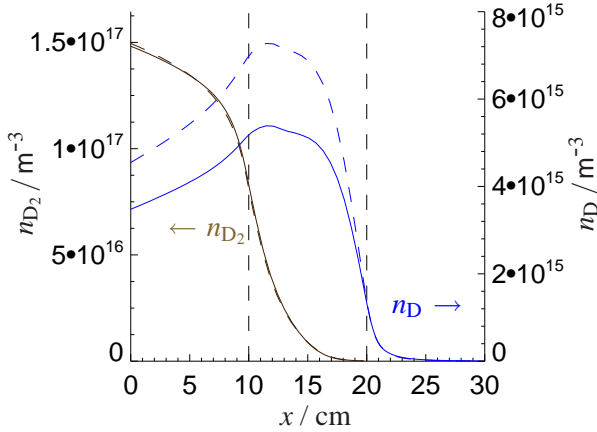


Figure 2.25: Molecular and atomic density profiles: $T_i = T_e$ (dashed) and $T_i = 2 \cdot T_e$ (solid).

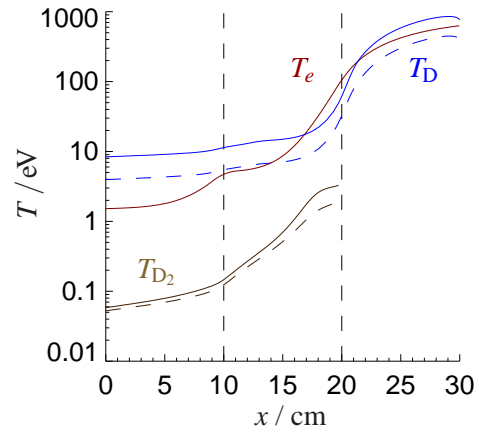


Figure 2.26: Molecular, atomic and electron temperature profiles: $T_i = T_e$ (dashed) and $T_i = 2 \cdot T_e$ (solid).

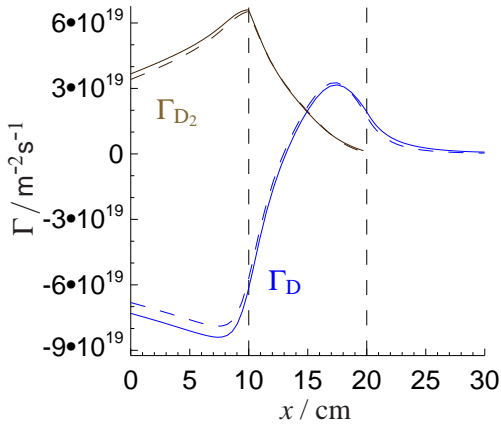


Figure 2.27: Molecular and atomic flux densities: $T_i = T_e$ (dashed) and $T_i = 2 \cdot T_e$ (solid).

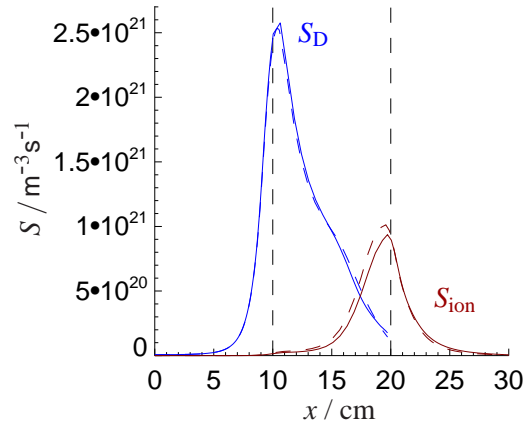


Figure 2.28: Atomic source from dissociation and atomic ionisation profiles: $T_i = T_e$ (dashed) and $T_i = 2 \cdot T_e$ (solid).

Chapter 3

D_α Diagnostics

The diagnostics instrumentation presented in this chapter is the result of preceding developments. For hints on the previous setups, the reader may refer to [26].

3.1 Strike Point Observation

Below the roof baffle of the lower divertor, two lenses are installed which map two row-aligned $100\mu\text{m}$ silica fiber arrays to the target plates. The original configuration comprised 70 fibers for the inner and 69 for the outer divertor leg. At the tile surface the maximum diameter of the lines of sight is about 3 mm at the bottom and 6 mm at the top. These are separated by 4 – 8 mm. This optical arrangement is denoted as the strike point observation (SPO) and provides a very high spatial resolution in the ASDEX Upgrade divertor.

The actual viewing geometries for the experimental campaigns 2006 and 2007 are illustrated in figure 3.1 which indicates the different viewing chords intersecting the target modules. While the fiber arrays were intact during several campaigns including 2006, one of the bundles was severely damaged in the maintenance phase before the 2007 campaign at a point of time inappropriate for repair. The fiber bundles are guided to a vacuum flange window to which relay optics and the detector are attached. This position of the detector electronics close to the plasma chamber involves the exposure to neutron flux and γ -radiation which produces some additional noise, but which can usually be clearly separated from the actual radiance recorded.

Line radiation of impurity species or of the working gas is selected by using narrow band pass interference filters (for D_α see appendix B). By introducing a dichroitic beam splitter, two different wavelength intervals can be separately transmitted to the detector (see fig. 3.2). The transmission curve of the beam splitter is shown in figure 3.2 together with the profiles of filters for the H_α/D_α lines at $\sim 656\text{nm}$ and a CIII line-triplet at $\sim 465\text{nm}$. These two lines are commonly recorded with the SPO diagnostics. In order to obtain a comparable signal-to-noise ratio for these different species, grey filters are used to adjust the brightness of each of the four arrays ($\{\text{inner, outer target}\} \times \{\text{line1, line2}\}$). A CCD sensor is installed to record this large amount of channels. With a typical exposure time of 1 ms and a readout time of 5 ms, the system monitors divertor radiation at a moderate data rate of 167 Hz. The radiance calibration is described in appendix B. Due to the impact of pitch angle on filter transmission discussed there, data from the SPO diagnostics might be underestimated by a factor as large as 2. Regarding

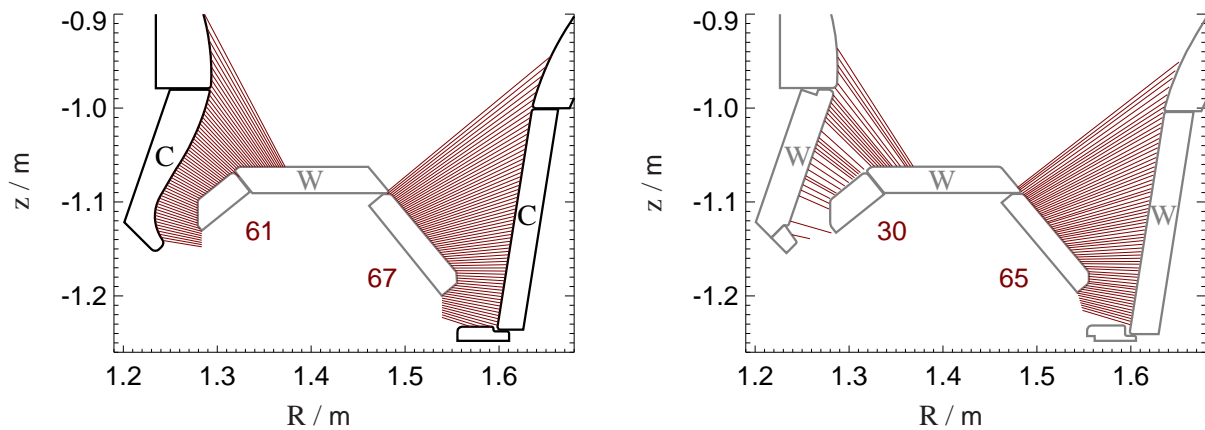


Figure 3.1: The SPO viewing geometry for the campaigns 2006 (left) and 2007 (right). The numbers indicate the chords intersecting the target modules. For data interpretation it is useful to note the type of material surfaces of the target plates: Carbon C in 2006 and Tungsten W in 2007. For reflection properties of W see appendix C.

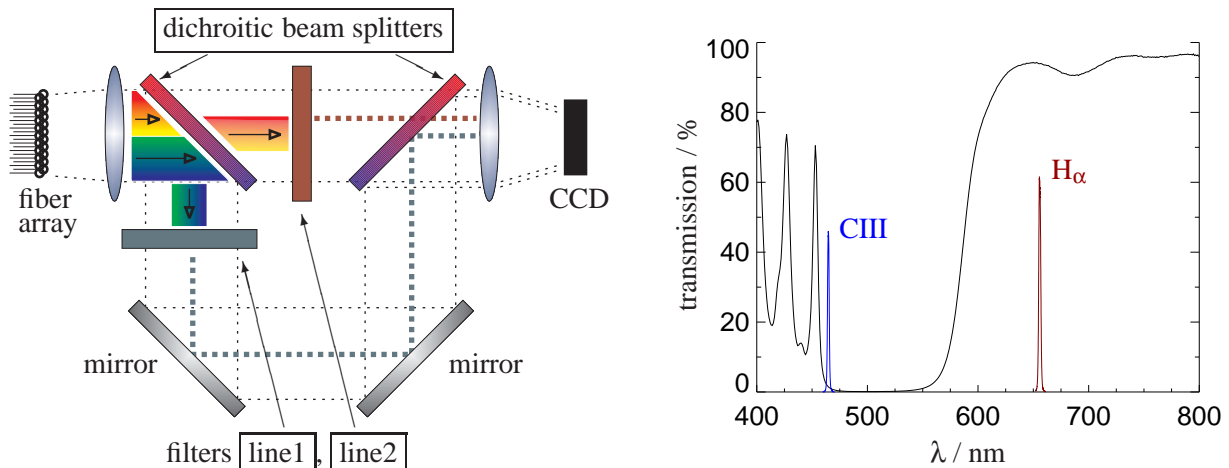


Figure 3.2: Left: Sketch of SPO optical setup. Right: Transmission curves of the dichroitic beam splitter (at 45° pitch angle) and two interference filters: with respect to the beam splitter, the H_α -filter is placed in the transmitted beam path and the CIII-filter in the reflected beam path.

systematic uncertainties, also the optical properties of the surface observed has an impact on the magnitude of radiance recorded. Until the campaign of 2006, the target modules consisted of plain graphite and interpretation of the SPO radiance data as line integration of D_α emission in the volume of the divertor leg seems appropriate. For the 2007 campaign, divertor target tiles with a Tungsten coating were installed. In view of the measured diffuse reflectivity of such Tungsten surfaces presented in appendix C, interpretation of the SPO data should consider that the actual viewing geometry is more complex than the primary lines of sight. A pragmatic point of view might be to use the aperture cone integrated value for the reflectivity as an estimate for the additionally, ie this fraction doubly counted, recorded signal which would be appropriate if the line emission from plasma recycling is due to ionising conditions close to the target surface. In fact, the radiance recorded is typically interpreted in terms of particle flux over the $S/(XB)$ -method [25, 27]. A more difficult situation arises from a recombining plasma in which the whole divertor volume might be source of line emission. Reflection properties of the observed surface also implies reception of emission from the X-point region or the HFS SOL. In this case the line

integrated data is an average piece of information of the divertor and a more distant SOL region and the interpretation is clearly hampered.

In the framework of analysis of video diagnostics data, information obtained from the SPO is added in order to improve the line of sight coverage in the divertor region, ie for tomographic reconstruction described in section 4.2. If volume emission of a certain line is prepared, the next step is to estimate or to use measured plasma parameters to translate emission to accompanied density or flux density of the species involved.

3.2 Tangential Cameras

The main purpose of this thesis is to discuss data obtained from video diagnostics which is installed to record the line emission from the SOL and divertor region at high spatial and dynamic resolution. A pair of standard CCD-cameras is attached to relay optics which contain the band pass filters for the lines of interest. These optics map the exit plane of an image guide which is connected to collecting optics placed near the plasma edge. It is possible to record the emission of two different spectral lines for one viewing geometry simultaneously using both detectors in a setup similar to that presented for the SPO diagnostics (fig. 3.2), merely by replacing the mirror optics by a mapping lense and the second detector. In the framework of this thesis it has been focussed on measuring D_α emission with a maximum coverage of the plasma cross section, so two views and detectors have been operated in parallel. Here, the basic technical aspects are summarised, whereas the physics aspects are discussed in section 5.2. The video diagnostics is abbreviated as XPMC which stands for the two views of X-point/divertor and the main chamber region.

The CCD-sensors are configured in 2×2 -binning which results in a detector resolution of 696×520 elements. In this mode of operation the time interval of recording after frame capture is about 85 ms. Using the inter-line transfer capability of the sensors (fast shift of pixel charges into temporary buffers after exposure allowing the present frame to be exposed during the readout procedure of the previous one) this time period determines a maximum frame rate of about 12 Hz. Depending on viewing geometry and plasma parameters (see section 5.2), exposure times in the range of $t_{exp} \in [0.1, 80]$ ms are chosen to ensure a sufficiently high signal-to-noise ratio, but to avoid saturation. Charges accumulated in the CCD are digitised at 14bit resolution. As can be seen on several images, eg in section 5.2, the signal-to-noise ratio is mainly determined by the readout noise appearing as stripes parallel to the large extension of the sensor. The cameras are mounted at a distance of about 3.5 m to the plasma core, restricted by the length of the image guide, and are shielded by 30cm Lithium carbonate added paraffine and 5 cm Lead to attenuate the neutron flux and the γ -radiation. However, in particular during high power plasma discharges, energetic particles may reach the detector and produce saturated pixels. Due to the hard radiation exposure during an experimental campaign, the CCD-chip is observed to deteriorate. This means that the number of pixels, which appear to be less or more sensitive or even are permanently saturated, increases. What is described as a higher sensitivity is probably in fact an increased dark current due to defects in the semiconductor structure. For compensation, an offset measurement is done before each data acquisition. Nevertheless, the deterioration of detectors during operation is of minor importance regarding the large regions of interest used for analysis, the systematic uncertainties from calibration (see appendix B) and assumptions made for physical interpretation, but indicates the limitation in lifetime of detector electronics.

The central part of the optical setup is a glass made image guide. With a transmission of $\sim 48\%$ (D_α , length 275 cm) it provides a flexible alternative to complex and mechanically sensitive periscopic arrangements. Glass fibers are sensitive to ionising radiation and therefore exhibit transiently decreasing transmission even in the radiative environment of a fusion experiment operating with Deuterium only. This aspect displays the major drawback for the use of glass fiber bundles and experience gathered at ASDEX Upgrade is outlined in appendix B. The image quality achieved with the XPMC diagnostics is basically determined by the structure of the image guide which is depicted in figure 3.3. What is suspected to be the single element of the coherent bundle when inspecting the end tip is in fact a multi-fiber composed of 5×5 $10\mu\text{m}$ diameter fibers ($8\mu\text{m}$ core, $1\mu\text{m}$ cladding). These multi-fibers are manufactured as closed loops, merged in large bundles and cemented in a short metal cylinder which is subsequently cut to obtain the end pieces of the perfectly ordered image guide. If the exit plane of the image guide is mapped properly to the detector and the front side is illuminated, either directly or by illuminating the collecting lense with a diffuse light source like done for radiance calibration, the structure of the fiber bundle becomes apparent. It is the small gaps between and displacements among the multi-fibers which sets a limitation to the image quality. Some elements which appear to be broken are actually mostly reduced in transmission probably due to roughness of the cut surface. The bundle as a whole seems to be rather insensitive to mechanical stress as far as careful handling during installation is concerned and the number of broken fibers (from manufacturing) remains constant. The detector resolution specified above is chosen such that the number of pixels is comparable to the number of imaging elements, estimated to be $N_{ie} > 300000$ based on the size of the bundle cross section ($\sim 5 \times 7 \text{ mm}^2$).

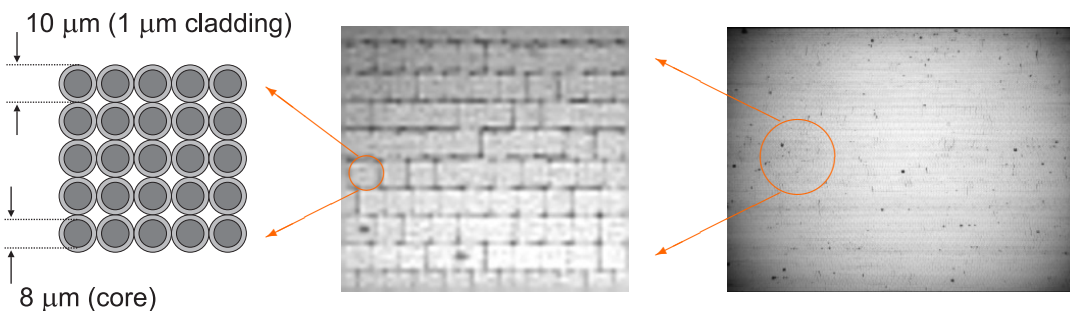


Figure 3.3: The structure of the XPMC image guide: multi-fiber (left), closeup view of image guide structure (middle) and total cross section of image guide mapped to the detector (right).

For the installation in a midsize radial entry port of the vacuum vessel, the two image guides of the XPMC diagnostics are fixed at the tilted head piece (dia.=78 mm) of an insertion mounting (fig. 3.4). A vacuum window and a protective silica pane separates the front lenses from the plasma chamber. Its position is about 30 cm below the midplane. The head piece can be replaced in order to allow a slightly different orientation of the optical axes, restricted by the space available in the narrow port. On the right part of figure 3.4 the maximum field of vision in the horizontal cross section is indicated. The orientation of the port window allows to configure one lens to be tilted towards the divertor, while the other view is directed horizontally. Figure 3.5 shows the two standard settings on the first two images. In the case of wide angle lenses, the field of vision is limited by the port size. As presented in section 5.2 the main chamber view

was exploited only on a small part on the LFS and it has been decided to magnify this area by using a larger focal length ($f=4\text{ mm} \rightarrow f=15\text{ mm}$) and adjusting the optical axis. Like mentioned in appendix C, parts of the ICRH limiter frame were replaced by Tungsten covered tiles for the 2007 campaign, coinciding with the change of the XPMC optics. Due to reflection at these surfaces, there is no data available for the enlarged view which exhibits sufficient contrast for data analysis.



Figure 3.4: Insertion mounting (left) of the tangential cameras, port window inside the vacuum vessel (middle) and horizontal cross section of maximum field of vision (right).

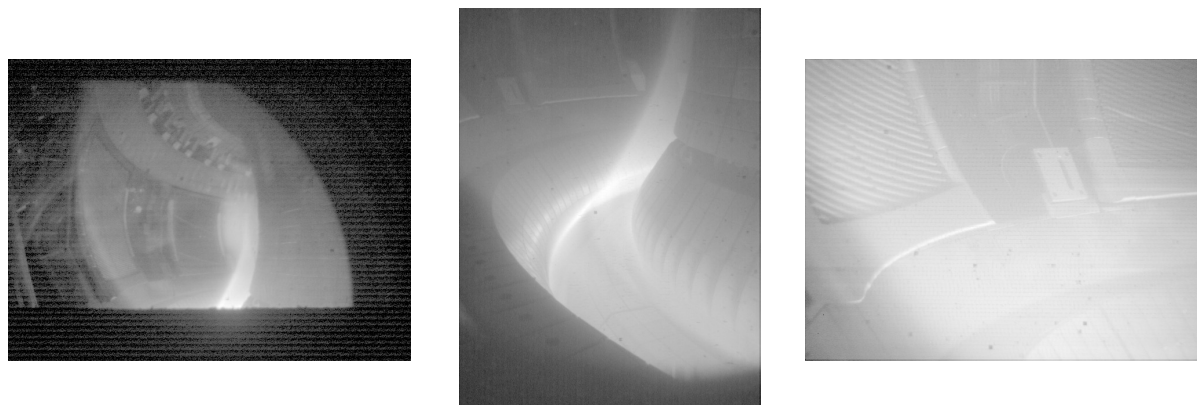


Figure 3.5: Recorded frames of ohmic discharges to indicate possible fields of vision (offset subtracted raw data in logarithmic scaling): #20901, $t \in [7.633, 7.637]\text{ s}$, $f = 4\text{ mm}$, main chamber with additional aperture to shield light from the divertor region (left); #22091, $t \in [1.785, 1.795]\text{ s}$, $f = 7.5\text{ mm}$, divertor view (middle); #22091, $t \in [1.785, 1.845]\text{ s}$, $f = 15\text{ mm}$, closeup of limiter frame of ICRH antenna #2 (right).

To obtain best results in terms of image definition, an object of high contrast is recorded with the band pass filter included in the optical setup. The empty plasma vessel can barely be illuminated to provide appropriate radiance reflected from the vessel components in a spectral interval of $\Delta\lambda \sim 1.5\text{ nm}$ (D_α filter). It is important to note that thickness and refractive index of filter glasses lead to a parallel offset of light rays passing with a tilt angle to the optical axis, ie the focal plane of the relay optics is shifted. Although this basic impact on the mapping quality is obvious, often filter wheels are used to change band pass filters remotely, but consequently image definition cannot be of the same precision for all samples. Frames from the preparation of the optics for the views shown in figure 3.5 are summarised in figure 3.6. A line pattern with different levels of line thickness and line separation has been used as a reference to judge the lateral resolution of the

diagnostics. At the given distance the smallest grid structure (5 mm/1.5 mm) seems to display the limit of lateral resolution for the wide angle view. Referring to the line thicknesses and contrast of the image, it is estimated that one imaging element represents a lateral extension of ~ 2.5 mm. For the divertor view ($f=7.5$ mm) the lateral resolution is about 2 mm per imaging element. For $f=15$ mm a resolution of 1 mm per imaging element is obtained. Aperture settings for all lenses are chosen such to achieve a large depth of focus which is found to be in the order of 1 m.

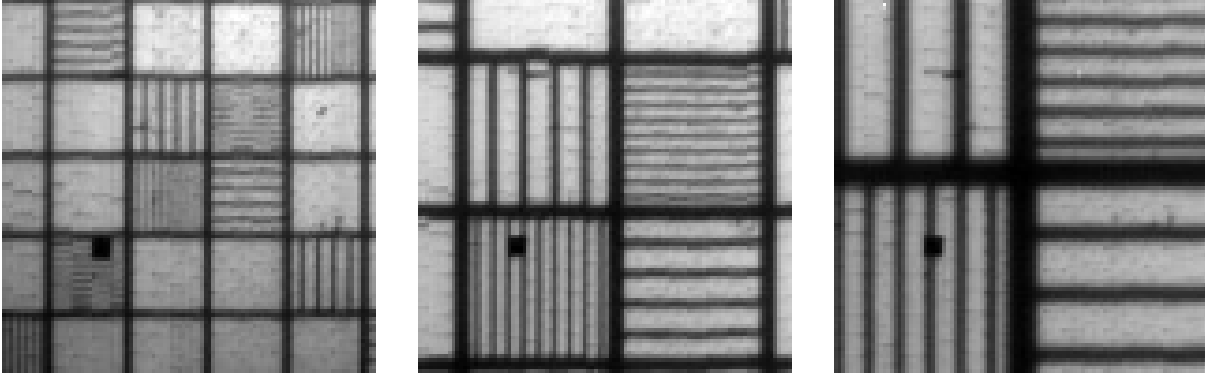


Figure 3.6: Test pattern with three steps of line thickness and line separation (50/5, 10/2.5, 5/1.5 [mm]) mapped at a distance of 100cm with different focal lengths f : $f = 4$ mm (left), $f = 7.5$ mm (middle) and $f = 15$ mm (right). The images display parts of the camera frame of size 100×100 pixels in the original resolution. The black spot in the lower left quadrant has the same size in all images, because it is due to a broken fiber of the image guide.

The full frames of the test pattern (eg fig. 3.7) indicate the impact of distortion imposed by the lenses used. A barrel like distortion is found for the present setup, being more pronounced for short focal length. In order to obtain precise information on the viewing geometry, ie the characterisation of the lines of sight corresponding to each detector element, the mapping function of the complete optical setup has to be modelled. A nonlinear mapping function is constructed by combining a vanishing point projection with a cubic polynomial to be applied on the radial displacement to the optical axis on the projection plane. This function is in fact a representation of the actual mapping and is not a simulation of the separate optical components (front lens, image guide, relay optics and filter). It is essential to use an invertible mapping function such that after the transform 'object to image plane' has been verified, the line of sight data for each image point can be calculated by employing the inverse transformation. This concept is sketched in figure 3.7.

For a given image of an object described in real space coordinates, direction of the optical axis, position of vanishing point and image plane are adjusted to achieve a satisfying agreement of simulated and real mapping. To match the size of the mapped object, the distance between vanishing point and image plane is set appropriately (linear part) and image distortion (nonlinear part) is configured referring to the mapping of a rectangular pattern. The cubic polynomial to transform radial displacement to the optical axis reads:

$$r = r' + a_2 r'^2 + a_3 r'^3 \quad , \quad (a_2 > 0 \quad , \quad a_3 > 0)$$

which describes a pillow shaped distortion. Here, r denotes the radial position of an object point on the mapping plane for an ideal pin-hole camera. It is the inverse transform to be used to obtain

the barrel shaped distortion for the mapping 'object to image plane':

$$r' = \xi - \frac{1}{\xi} \left(\frac{1}{3a_3} - \frac{a_2^2}{9a_3^2} \right) - \frac{a_2}{3a_3},$$

$$\text{with } \xi = \left[\frac{a_2}{6a_3^2} + \frac{r}{2a_3} - \frac{a_2^3}{27a_3^3} + \frac{\sqrt{3} \sqrt{4a_3 - a_2^2 + 2a_2r(9a_3 - 2a_2^2) + 27a_3^2r^2}}{18a_3^2} \right]^{\frac{1}{3}}.$$

An example of the mapping function for data analysis is shown in figure 3.8. Object coordinates are taken from the structural design of the vessel components and distinct contour lines are selected. Tiles of the divertor region and heatshield are described at high precision, whereas the limiter frames of the ICRH antennas are treated only on a basic level, ie not in the actual 3D complexity. The position of the vessel components is verified at maintenance to be accurate within $\Delta x < 2$ mm (typically) compared to the design value. Since the XPMC optics are attached to the moveable head of the carrier mounting in order to be inserted properly into the tilted port, a fixed and well defined position of the lenses cannot be assured mechanically. The optical head might be shifted slightly $\Delta x < 1$ mm, due to vibration, eg imposed by plasma disruptions caused by sudden drop of the plasma current and the loss of confinement. Consequently, the mapping function has to be checked for the discharge of interest and the brightest image is used for its configuration. Although the contrast obtained from plasma imaging for the contours of the vessel components is rather low and distributed non-uniformly, careful configuration of the mapping parameters results in a level of accuracy which is limited basically by the lateral resolution of the image.

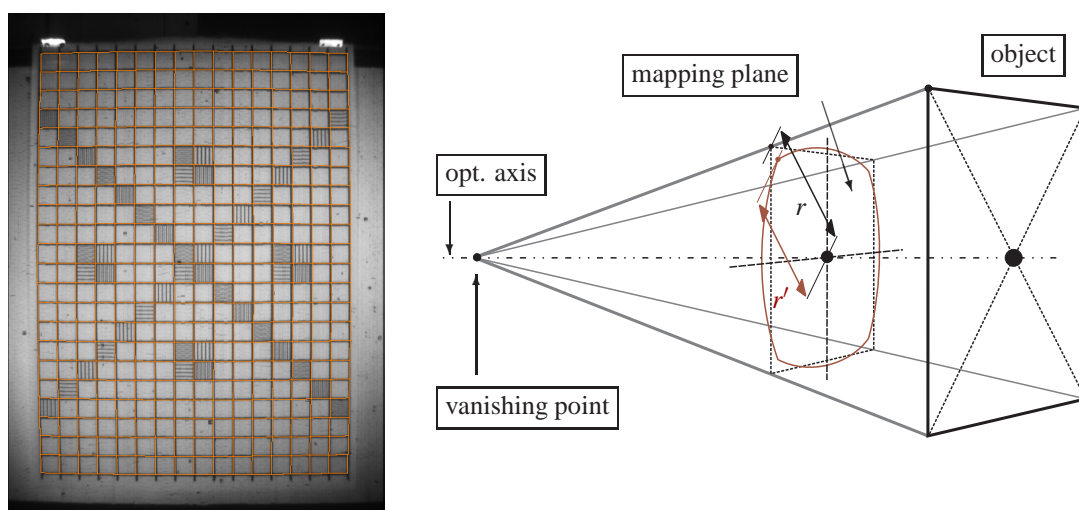


Figure 3.7: The optical setup features a barrel like distortion which can be seen on the mapping of the test pattern (left). A simple mapping function is constructed by the combination of a vanishing point projection and a radially symmetric distortion (cubic polynomial) on the mapping plane (right). The test pattern is used to determine the free parameters of the mapping function.

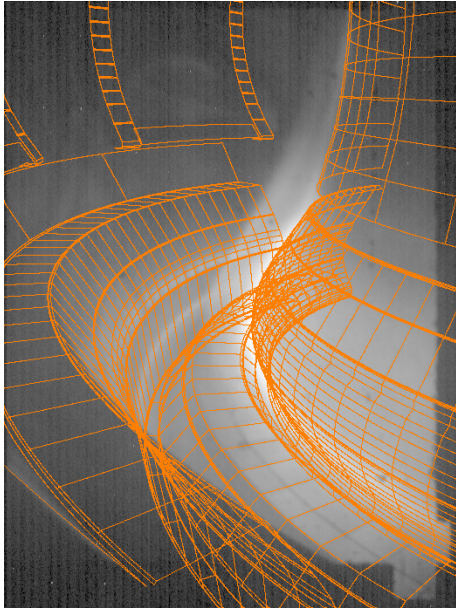


Figure 3.8: Once the linear and nonlinear parameters of the mapping function have been defined (fig. 3.7), coordinates of plasma facing components can be mapped to the image plane. Since the position \vec{x} and orientation \vec{n} of the front lens is known merely with some uncertainty ($|\vec{x} - \vec{x}'| \gtrsim 3 \text{ mm}$, $\cos^{-1}(\vec{n} \cdot \vec{n}') \gtrsim 2^\circ$), the position of the vanishing point and the optical axis for the mapping are adjusted until the lateral deviation on the image plane is in the order of the detector resolution.

Chapter 4

Data Deconvolution

The general character of video diagnostics data tempts the observer to apply the very basic method of interpretation by simply looking at one frame or a series of frames and noting what one suspects to be special or significant features. This natural approach may be adequate to recognise the global plasma behaviour on a relative scale of personal impression and experience. An example in that respect is the use of video diagnostics at AUG for the monitoring of plasma position and state and integrity of plasma facing components. Without precise knowledge of sensitivity and viewing geometry it is nevertheless obvious from strong increase of emission localised at certain wall components due to enhanced plasma recycling or even limiter glow (radiance from a surface), that plasma positioning needs to be corrected. Image data can be used for machine safety if radiance recorded from special regions of interest is compared to preset threshold levels in real-time, eg to initiate the correction of the plasma position or an active shutdown of the discharge. Taking a large amount of experiments and the data from various diagnostics into consideration, the experienced observer may obtain basic information from a video sequence such as confinement mode, density level and divertor state. Video diagnostics, in particular fast cameras, is often used to record the emission related to the dynamics of edge phenomena like turbulent transport, plasma breakdown or actively induced plasma disruptions. Here, the sole use of the primitive method has to be doubted, since it is the magnitude and location of the emission in conjunction with the plasma parameters which characterise the event observed and quantitative analysis is required. The radiance recorded obviously cannot be translated to local emission by eye easily.

In order to obtain precise information on the neutral flux density distribution and the neutral particle penetration length from D_α diagnostics, systematic and consistent data analysis of reasonable complexity needs to be developed for the deconvolution of sightline integrated emission. The difficulty is to find methods which are applicable for as many measurements as possible to provide a large set of comparable and first of all meaningful descriptions, but also to avoid presumptions which may force the results to be characterised by the method of choice while failing to notice important aspects. The appearance of ϵ_{D_α} in the plasma edge and divertor region is quite far from being described by a compact model depending on a few parameters such that image data could be inferred from. Aside from parameters of the plasma and neutral particles, the optical properties of the surfaces of the vessel components (see appendix C) determine the radiance recorded.

Two different methods are applied for data deconvolution. Firstly, in dedicated regions of interest with sufficient contrast, a ray-tracing-fit based on a model function is used to obtain a radial

emission profile which in a second step is compared to results from a kinetic model for neutral penetration (see section 2.3). Locally, a very detailed analysis is performed, albeit connected to the character of the profile model function. Secondly, data analysis without restrictions on the locations observed is done using an algorithm for tomographic reconstruction which also contains a model for diffuse reflection at Tungsten covered plasma facing components (see also appendix C). Restrictions to the emission profile are imposed by the properties of the regularisation operator which links the spatial distribution of emission to poloidal flux topology. Concerning the spatial resolution chosen such to ensure appropriate numerical efforts and the general accuracy of the approach, information on a global scale is provided. Main features displayed emphasise differences of certain discharge scenarios and are particularly useful for comparison with results from elaborate 2D SOL codes.

Both methods assume toroidal symmetry of emission. On the one hand, this assumption is necessary due to the viewing geometry of the diagnostics which does not provide adequate toroidal resolution, on the other hand, these methods are applied only to image data which are suspected to meet this requirement. In the cases of localised gas puff or recycling at toroidally separated limiting structures, applicability has to be discussed regarding expectations on data analysis in that particular case. In the following sections the two different methods are presented and restricting and beneficial aspects are summarised.

4.1 Ray-Tracing-Fit

Neutral particles penetrating the edge plasma radially are excited and ionised within a couple of centimeters due to the rapidly rising electron density and temperature. The mean free path of neutrals and the profile shape of plasma parameters result in a sheath of D_α emission which is narrow compared to the radial extension of the SOL, as far as regions of the poloidal plasma cross section are concerned which are distant from the divertor. This area is resolved best by tangential viewing chords which in addition do not integrate signal emerging from surfaces, typically reflected photons from various locations, or volume emission in the background. Corresponding to the camera views available, ie main chamber and divertor view, these regions of high contrast are indicated in figure 4.1.

To resolve the D_α emission profile at the LFS is the most difficult task given the experimental circumstances. The contrast observed at the LFS is determined by the magnitude of neutral flux density and the characteristics of the plasma profile. If the exposure time is large compared to the lifetime of macroscopic perturbations in the SOL, an emission profile broader than observed for a calm plasma edge is obtained (see also section 5.1.3). Strong emission from the divertor and HFS illuminates the whole vacuum vessel resulting in a varying background signal due to the complex arrangement of limiting structures and diagnostics components around the LFS midplane. In the left part of figure 4.1 the D_α emission is seen at the LFS plasma edge to be distributed along the poloidal circumference, but image data can be analysed with the method presented in this section only in front of the plain surface of graphite tiles which are part of the limiter frame of the ICRH antenna. Above that area contrast of the radiance data is blurred by reflection of emission from the TiZrMo-alloy rods of the Faraday-screen. For a detailed picture of the ICRH antenna see appendix C. Below the graphite tiles plasma facing components are covered with Tungsten. Following the projection of a line of fixed major radius in the SOL the radial increase of emission is still recognised, but unlike in the case of graphite, radiance recorded by the detector stays at a

high level while moving further to the right part of the image, due to light from divertor and HFS scattered towards the observer. Consequently, a ray-tracing algorithm performed on a localised grid, ie without considering reflection at surfaces, since the more distant location of emission lies outside the grid, must fail to converge. Although the reflection of emission in front of the surface could be considered, the problem lies in the fact, that the magnitude of emission from the HFS and divertor region is typically much larger.

The situation at the HFS is less complicated. For this part of the vessel cross section, data from the divertor view is preferred, because exposure times are typically one order of magnitude smaller and lateral resolution is about twice as high as in the main chamber view. The region of interest at the HFS is limited at the bottom by the contribution of emission from the divertor region and at the top by the decrease of signal-to-noise ratio. An area reaching from about 20cm distance along the separatrix with respect to the X-point position to about the midplane is covered. The complications of low contrast due to a strong background signal also occur for certain plasma scenarios, eg medium to high density L-mode plasmas exhibit very strong divertor emission and the procedure of profile fitting is not applicable.

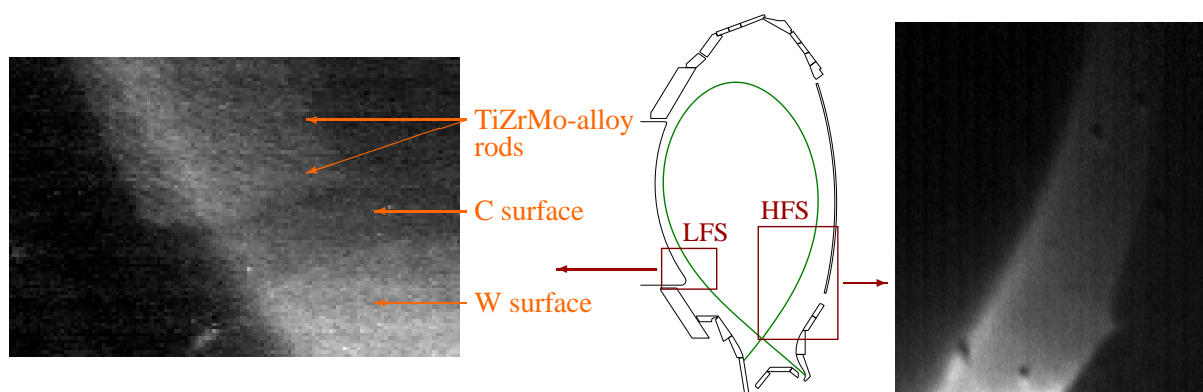


Figure 4.1: Regions of interest for the application of the ray-tracing-fit at the LFS (left, with remarks about components in the background, see also appendix C) and HFS (right); parts of radiance image data from main chamber and divertor view of low density L-mode discharge #21418 ($t \approx 3.45$ s) in linear scaling; compare to complete frames shown in section 5.2.3.

The central component of the ray-tracing-fit is the model implemented for the radial emission profile. It should be described by a small number of parameters, while being still close to the actual radial distribution. After having tested different profile functions and combinations of these, the Lorentzian shape was chosen, because it was found to match the experimental data best. Results from the 1D kinetic treatment of neutral penetration (section 2.3) indicates that an appropriate model is applied.

$$\epsilon_{D\alpha}(\rho_p) = A \cdot \frac{(w/2)^2}{(\rho_p - \rho_{p,c})^2 + (w/2)^2} (+B) \quad ; \quad w = w_i \quad , \quad \rho_p \leq \rho_{p,c} \quad ; \quad w = w_o \quad , \quad \rho_p > \rho_{p,c}$$

Amplitude A , radial center position $\rho_{p,c}$ and inward and outward decay lengths w_i , w_o are the four free parameters to be adjusted to give a modelled radiance similar to the video data. In addition, an offset parameter B is used which is understood not to be part of volume emission of interest, but to represent signal from reflections in the background or even emission in the foreground like it is the case for image data of the HFS. For the abscissa of the profile function,

the poloidal magnetic flux coordinate ρ_p is employed. Line of sight integration for a predefined part of the image (region of interest, ROI) is performed on a grid with a reasonable small parallel step size (eg 1 cm) and the grid boundaries being determined by the vessel contour and by a minimum value for ρ_p chosen to be a few cm inside the last closed flux surface. For large inclination of the sightlines towards the divertor (HFS-ROI) also the major radius is considered in order to avoid part of the grid volume to be positioned radially outwards compared to the X-point and therewith being closer to the LFS. The free parameters are inferred from a standard χ^2 -minimisation algorithm by comparing the experimental radiance data to the line of sight integrals of the model utilising the parametric dependencies. To illustrate the procedures for the LFS and HFS, two examples are given using the data of figure 4.1.

For LFS data analysis a small region of interest is chosen which covers the plasma edge in front of the bottom part of the ICRH limiter frame. Figure 4.2 illustrates the corresponding area in the specified color scale. Although the signal-to-noise ratio is rather low, the ray-tracing-fit appears as a robust method and converges in most of the cases. The result is shown in figures 4.2 and 4.3 in 2D and 1D representations. In figure 4.3 also the underlying emission profile is shown. For convenience, the poloidal flux coordinate is used as abscissa, since it is used as the radial coordinate in the fitting procedure. The more natural representation might be to follow the path of neutral particles on a real space coordinate. Therefore, the abscissa is arranged such to indicate

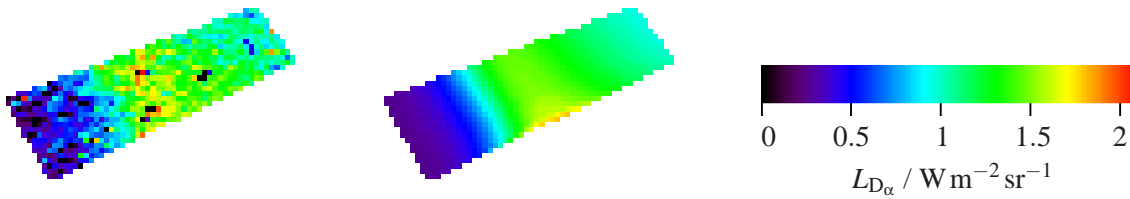


Figure 4.2: Radiance data of the small region of interest at the LFS (left) and the result of the ray-tracing-fit (middle); color scale (right).

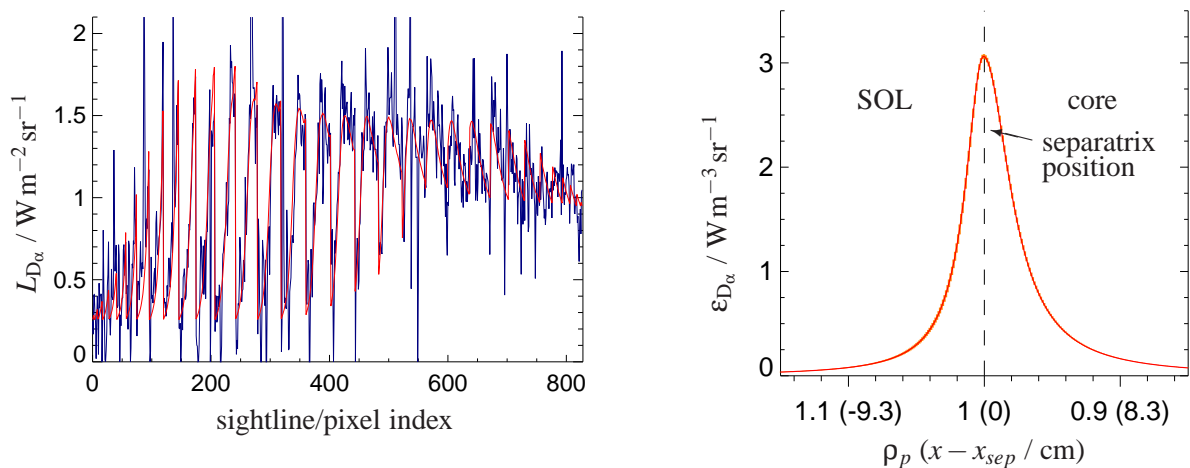


Figure 4.3: Left: 1D comparison of radiance data (blue) and fit result (red) with abscissa denoting the pixel index ordered row-wise from lower left to upper right corner of the region of interest. Right: Underlying emission profile with normalised poloidal magnetic flux as abscissa and local spatial radial position for reference.

the penetration from the SOL towards the plasma core and the local spatial separation to the last closed flux surface is noted corresponding to a straight line in the poloidal plane perpendicular to the separatrix. The uncertainty accompanying each data point inferred from preprocessing the raw data (detector offset, calibration factors) is used as a weighting factor such that applying standard fitting procedures, an error estimate for the parameters of interest can be deduced. If only a small part of the image data is examined, one single parameter set is applied and poloidal variation of the emission profile, which is hardly recognised in the region of interest, is not considered.

The poloidal variation of radiance on the HFS obviously requires a more elaborate approach than discussed for the LFS, if a large region of interest is to be examined. In order to set up a procedure which is capable of accounting for the poloidal variation of the emission profile, the ray-tracing grid has to be extended to 2D. Besides the radial coordinate, a label to indicate the poloidal position is used to characterise each grid point. A simple method has been chosen to obtain a spatial coordinate closely linked to the poloidal flux topology, but which does not imply the complications of the construction of a curvilinear coordinate system. For each grid point the corresponding point on the separatrix of smallest distance is determined, defined by the vanishing scalar product of the tangential vector of the separatrix and the vector connecting the two points (see fig. 4.4). The demanding task is to implement the poloidal variation in the fitting procedure. One idea is to introduce analytical expressions which describe the variation of parameters determining the shape of the emission profile as a function of the 'parallel separatrix coordinate' (p_{sc}). This approach seems to be impractical, because each profile parameter is replaced by several secondary parameters in form of functional dependencies which however are unknown and would have to be predefined, putting further constraints on data deconvolution. For example, the poloidal variation of the amplitude parameter could be described by a (offset-)linear or exponential function declared on the p_{sc} coordinate, with each ansatz introducing two new parameters replacing the former single one. Additionally, the numerical stability concerning a large number of free parameters is questionable. The introduction of a poloidal variation only for dedicated parameters, eg amplitude, while forcing the others to be independent of the p_{sc} coordinate, seems not to be appropriate, taking into account the results obtained from the approach presented below.

First of all, the simple answer to the problem of poloidal variation of the emission profile is to discretise the parallel separatrix coordinate, ie to sort grid points with respect to prescribed intervals. Corresponding to the inclination of sightlines against the horizontal plane, grid points belonging to one image element usually are distributed to several p_{sc} -intervals. An elegant way to meet this complication is to start the fitting procedure for a subset of data points which correspond to grid points belonging exclusively to one p_{sc} -interval, denoted as N (see figure 4.5). Lines of sight intersecting further intervals are sorted according to the maximum separation to the subset of horizontal sightlines. The parameter set of interval K would then be determined by fitting the image data by adding the integrated emission of intervals $\{N, N+1, \dots, K-1\}$ ($K > N$) or $\{K+1, K+2, \dots, N\}$ ($K < N$) and radiance depending on the free parameters. Except for intervals close to the reference interval N this algorithm turned out to be numerically unstable, even for simulated input data and initial values for the free parameters identical

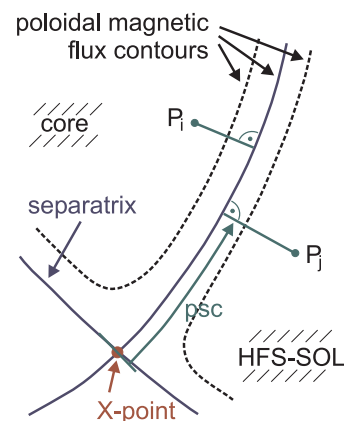


Figure 4.4: Definition of the 'parallel separatrix coordinate' p_{sc} .

to the original ones. This behaviour probably was to be expected, since small deviations of the parameters in intervals adjacent to the reference subset have to be balanced by larger variations of parameter sets in subsets more distant which results in divergence. The conclusion is thus, that the profile parameters must not change along a line of sight and the fitting procedure has to be simplified further.

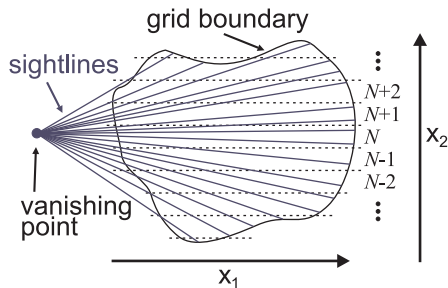


Figure 4.5: Points of each line of sight inside the grid volume are characterised by two coordinates ($x_1 \equiv \rho_p$, $x_2 \equiv psc$); poloidal variation is approached by the distribution of grid points to x_2 -intervals.

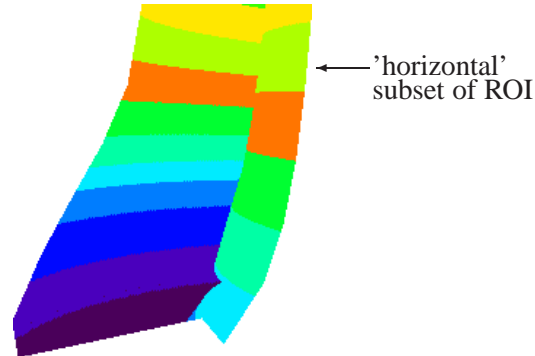


Figure 4.6: The principle sketched in figure 4.5 applied to the grid points of the HFS-ROI: the subsets highlighted by color are defined by the position regarding the psc -interval of the endpoint (vessel contour or ρ_p -boundary) of the sightlines, here $\Delta psc = 10\text{cm}$.

The pragmatic solution for the problem of considering the poloidal variation of profile parameters on the one hand and to ensure numerical stability on the other hand is to maintain the definition of ROI-subsets, but keeping only a single set of free profile parameters like this was done for the small LFS-ROI. An average value for the parallel separatrix coordinate is assigned to each parameter set by utilising the number of grid points on each sightline which are inside a certain ρ_p -interval (eg $\rho_p \in [1.0, 1.03]$, which typically includes the peak of the emission profile) as a weighting factor for the sightline-averaged psc -value. For illustration of this procedure a region of interest is defined for the HFS data of figure 4.1, depicted in figure 4.6 which also indicates the separate partitions of the image data. The corresponding radiance data of the original image and the result of the ray-tracing-fit is shown in figure 4.7.

The fit results of the separate partitions of the ROI-data in total give a fairly good description of the experimental image data, but the simplified procedure may be questioned, particularly for large inclination of sightlines towards the horizontal plane. To account for this exception, the psc -dependence of the profile parameters is described by simple functions (sum of linear and exponential terms) to obtain analytic expressions. The resulting image data based on this smoothed poloidal variation of the emission profile can then be compared to the experimental radiance data for consistency. The realisation for this example is summarised in figure 4.8.

An observation frequently made is the increase of the decay lengths and the decrease of the center parameter with rising psc . This behaviour might be attributed to the expansion of the poloidal magnetic flux surfaces which is the varying correlation of the spatial separation of two adjacent flux surfaces and the poloidal position. The vertically elongated, elliptical shape of the plasma cross section implies larger radial separation of these surfaces in the regions above and below the midplane compared to the midplane itself. Increasing decay lengths thus indicate, that the psc -dependence of the spatial width of the emission profile is less pronounced. In the same context the decreasing center parameter can be understood as the result of a slightly larger

neutral penetration length (concerning ρ_p) in the region of flux surfaces more closely placed in real space. This basic reasoning however has to be regarded critically, since the emission profile depends on the actual plasma profile. An additional remark may be to consider the decrease of the signal-to-noise ratio when approaching the midplane with increasing p_{sc} which also is probable to result in less peaked emission profiles obtained from the fitting procedure.

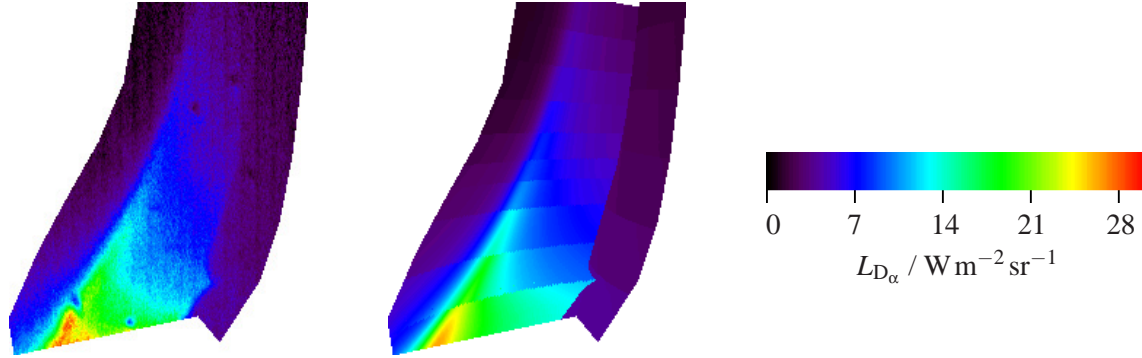


Figure 4.7: Experimental radiance data of the large region of interest at the HFS (left) and result of the ray-tracing-fit (middle); color scale (right).

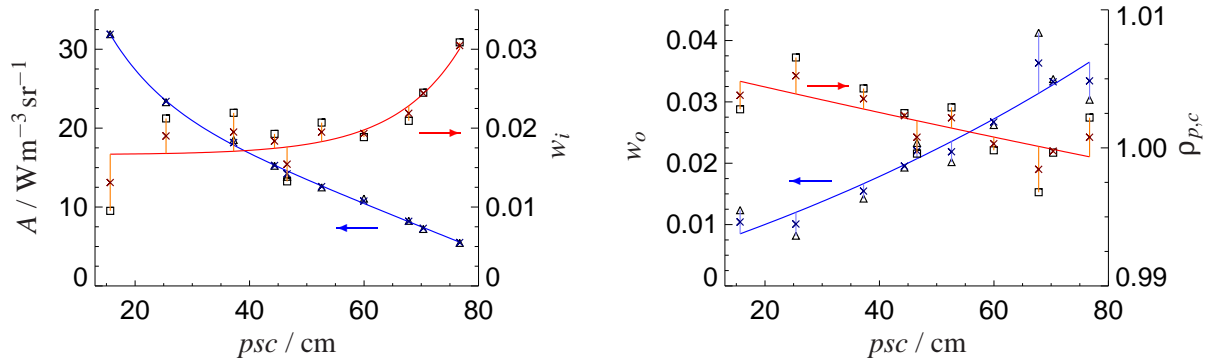


Figure 4.8: Parameters of the emission profile (amplitude A , center position $\rho_{p,c}$, inward and outward decay length w_i , w_o) as a function of p_{sc} : fit result (Δ , \square), model (solid lines) and deduced values with error estimate for further interpretation (\times).

With the analytical expressions for the profile parameters - including the offset parameter B which is not contained in figure 4.8 - emission can be calculated for each point of the grid separately. The corresponding smoothed radiance data is shown in figure 4.9 which also illustrates the relative deviation with respect to the experimental data. The general quality of the modelled radiance appears to be quite good, since the majority of image points with large deviation is found in regions of very low signal-to-noise ratio (heatshield and core). A systematically pronounced deviation is seen at the edge of the lower heatshield tiles (lower right corner) which is attributed to high reflectivity for large angles of incidence (see appendix C) rather than to discrepancy regarding the preparation of the sightline geometry. This particular feature obviously cannot be resolved by the global offset parameter. Figure 4.10 gives a 1D impression about the similarity of experimental data and results from the subset-fit and the smoothed one for a few lines of sight. Both sets of modelled data are to some extent qualified to represent the experimental observation. While the subset-fit is directly linked to the original data through the minimisation procedure, the smoothed profile parameters result in a more realistic expression of the image

data, however, using arbitrarily chosen analytical descriptions. As a compromise, the emission profile to be referred to in physical interpretation, is deduced by using the mean values of both models and considering the deviation among the two as uncertainty, implying that the resolution in p_{sc} is maintained corresponding to the subset-fit (see also figure 4.8).

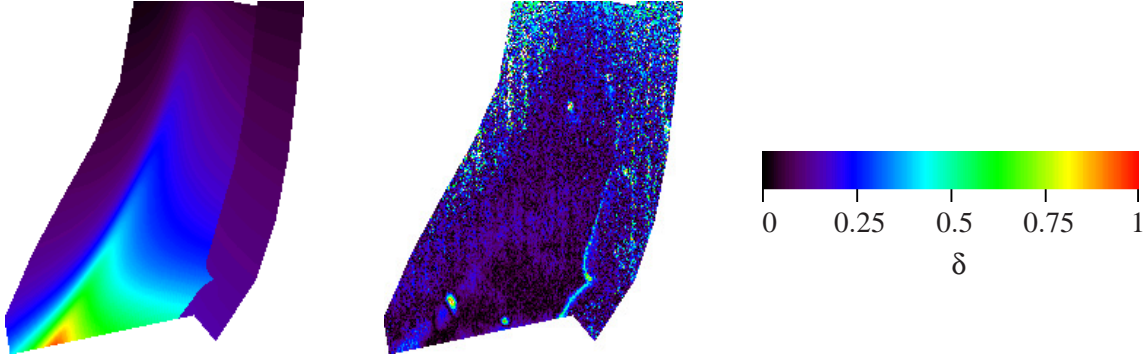


Figure 4.9: Left: Radiance obtained if model functions for p_{sc} -dependence of profile parameters are considered (color scale see figure 4.7). Middle: relative deviation of experimental and modelled radiances ($\delta = \frac{|L_{model} - L_{exp}|}{L_{exp}}$). Right: color scale for δ . The quality of the model is expressed with the distribution of δ : $\delta \leq 0.25$ for 83 % and $\delta \leq 0.1$ for still 46 % of the data points.

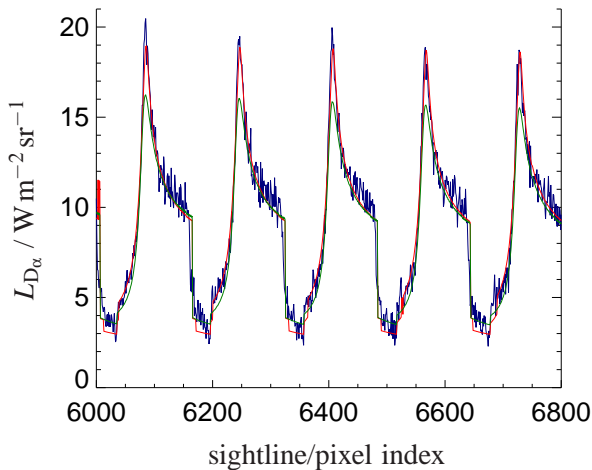


Figure 4.10: 1D representation of radiance data of a few sightlines of the HFS-ROI: experimental (blue), subset-fit (red) and with smoothed profile parameters (green); pixel index ordered row-wise from lower left to upper right corner of ROI (total number of sightlines: 31982).

4.2 Tomographic Reconstruction

The general sense of tomography is to obtain information about the internal structure of an object by applying methods of analysis to a set of measurements performed outside the object volume. Each element of the data set is characterised by a certain path of integration (emission) or attenuation (absorption) in the volume of interest. Active tomography implies the measurement of the residual intensity of probing beams which penetrate the object originating from a separate source positioned outside the object. The quantity to be determined is the local absorption coefficient. A well known example is the use of X-rays in a planar arrangement of sources and detectors to examine cross sections of technical or biological specimens. The amount of data which is needed to obtain a desired resolution in the plane of interest is provided by rotation of the probing beam array about the object. In high temperature plasma experiments it is the type of passive tomogra-

phy frequently encountered in which emission from the plasma is integrated along lines of sight or over the volume of viewing cones and recorded by detector arrays or cameras. Examples are the reconstruction of the source pattern of soft X-ray emission or large spectral range emission (bolometry) and the deconvolution of line emission. Details on diagnostics and data analysis in the field of fusion science can be found in [28] and [29]. After some basic remarks the emphasis of this section is to motivate the choice for the algorithm to be presented and to document its properties in the framework of D_α tangential camera data.

The key expression of tomographic algorithms is the Radon transform which describes the relationship between the measurement and the volumetric quantity. In an abstract notation it is:

$$f(w) = \int K(w,z)g(z)dz \equiv \mathcal{R}f \quad , \quad (4.1)$$

with $f(w)$ denoting the measurement as function of w which are the variables (or the equivalent label) to specify the geometry of the diagnostics aperture (straight or curved lines, viewing cones, see figure 4.11), $g(z)$ the quantity of interest with z the variables to span the domain of definition of g , and the kernel K characterising the details of the measurement process. In the simplest case the kernel is 1 on the path of the sightline and 0 elsewhere, but it might also contain special features like reabsorption of emission or diffuse reflection at surfaces (transition of sightlines to viewing cones of large aperture). The integral of (4.1) may be discretised to give the algebraic expression:

$$f_i = \sum_j K_{ij}g_j \quad , \quad (4.2)$$

where i and j are labels for the set of measurements and the grid cells to which the domain of g has been partitioned. K_{ij} contains the properties of the measurement process for grid cell j and sightline i ; as far as the integration volume is concerned it contains the area of cell j which is covered by the viewing aperture (length in the case of simple sightlines).

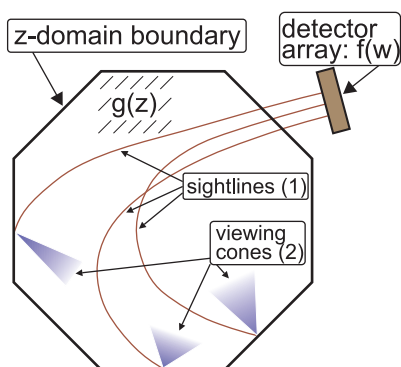


Figure 4.11: Sightlines intersecting the volume of emission. The detector signal is given by $f(w) = \int K(w,z)g(z)dz$. In the case of poloidal projection of tangential lines of sight in a toroidally symmetric arrangement, curved paths are obtained. w is the sightline index and $K(w,z)$ contains the details of the integration path on the z -domain: straight lines in primary (1) and cones in secondary (2) geometry for the example of D_α cameras at AUG.

To infer $g(z)$ from the measurement $f(w)$ obviously the inverse problem $g = \mathcal{R}^{-1}f$ needs to be solved. Despite the fact that analytic expressions for the inverse transform exist in particular cases or the discretised transform may in principle be solved by matrix inversion, these inverse problems are ill-posed. Due to the properties of analytical expressions, eg involving singularities of integrands, and the limited number of data points which corresponding paths cover the domain of g only partly, forming an underdetermined system, the solutions are bad behaved, ie these are unstable against small deviations in the initial data (eg noise). Procedures which are developed

to solve inverse problems, or more precisely to obtain approximations of the solution, therefore must include additional information, either known properties or estimates in the form of constraints to g . This formulation of varied or extended expressions closely related to the original problem is termed regularisation.

It exists a variety of methods which can be separated to different categories. Two main groups are transform methods and series expansion methods. The former are characterised by analytical inversion followed by discretisation for numerics and examples are the filtered back projection and Fourier methods. Algorithms of the latter group perform the discretisation before the inversion. The type of discretisation may be to expand f and g in a series of base functions, such that the coefficients of these are the parameters to solve for (Cormack method [30]) or to discretise the domain of g which is referred to as pixel methods like algebraic reconstruction or optimisation techniques.

The procedure discussed in the previous section denoted as ray-tracing-fit may be understood as belonging to the group of series expansion, but using only a single base function with a few degrees of freedom. Because the lines of sight are truncated and the method rather corresponds to the implementation of a strong regularisation constraint, classifying the procedure as a tomographic technique seems to be exaggerated. The actual tomographic algorithm employed for the deconvolution of tangential camera data belongs to the class of constraint optimisations and was initially developed for reconstruction of bolometric data [31]. The following optimisation problem is formulated:

$$\min \stackrel{!}{=} \underbrace{\int (div(Dgrad\varepsilon))^2 dRdz}_{\text{regularisation constraint}} + A \underbrace{\sum_{v=1}^W \frac{(\Phi_{v,rec} - \Phi_{v,meas})^2}{(\delta_v \Phi_{v,meas})^2}}_{\text{constraint of line integrals}} \equiv T_1 + A \cdot T_2 \quad , \quad (4.3)$$

with ε denoting the unknown emission profile declared on the poloidal plane defined by the variables R and z , D being a weighting tensor, $\Phi_{v,rec}$ the line integrals of the reconstructed profile, $\Phi_{v,meas}$ and δ_v the measured data and corresponding relative error, W the number of data points and A a weighting factor used to define the relative contribution of each of the two terms. Whereas the second term T_2 is recognised as a sum of weighted deviations, giving a measure of quality of the reconstructed ε -profile only in terms of line integrals, the first term T_1 is mandatory to impose a certain character on the shape of the profile, hence it displays the regularisation term.

The constraint of smoothness, ie keeping curvature at an appropriately low level, is often employed to avoid strong scatter of the quantity of interest. Using the operator $div(Dgrad\cdot)$ for regularisation implies a large freedom for demanding a certain shape of the profile. The benefit is the direct access to the level of anisotropy with respect to arbitrary directions, which may be a function of the spatial position. This option of influence on the properties of the reconstructed profile is desirable for the deconvolution of line radiation measurements on the plasma edge. As discussed in section 2.1 the mean free path of atomic neutrals is large in the SOL (compared to the vessel size) and decreases rapidly with rising electron density and temperature towards the plasma core which results in a narrow sheath of line emission due to the properties of the photon emissivity coefficient and its shape is related to those of the plasma boundary. The main features of the ε_{D_α} profile may be stated as the occurrence of large gradients perpendicular to magnetic flux surfaces, moderate gradients in the parallel direction and of largely connected areas in the toroidal and poloidal directions. Poloidal and toroidal variation of ε_{D_α} is determined by the pattern of neutral sources and the mobility of neutrals in the SOL and variations in the

plasma parameters. Radially separated structures are seldomly seen, eg in form of emission gaps between areas of ionising and recombining conditions, however, these are not contradicting the smoothness constraint, but the more separate structures are present, the larger the regularisation term adds up.

The integrand of the regularisation term T_1 is written in a form adapted to the request for alignment of emission along poloidal magnetic flux surfaces:

$$\operatorname{div}(\mathbf{D}\operatorname{grad}\varepsilon) = \operatorname{div}(\mathbf{D}_\perp \vec{n} \vec{n} \cdot \nabla \varepsilon + \mathbf{D}_\parallel \vec{t} \vec{t} \cdot \nabla \varepsilon) ; \quad \vec{n} = -\frac{\nabla \Psi}{|\Psi|} ; \quad \vec{t} = \frac{\vec{B}_p}{|\vec{B}_p|} . \quad (4.4)$$

\vec{n} and \vec{t} are unit vectors normal and tangential to the poloidal magnetic flux (Ψ) surfaces, \mathbf{D}_\perp and \mathbf{D}_\parallel denoting (scalar) weighting coefficients corresponding to the diagonal elements of the weighting tensor \mathbf{D} in the curvilinear coordinate system defined by $\vec{n}(R, z)$ and $\vec{t}(R, z)$. The formulation in cylindrical coordinates and presuming toroidal symmetry leads to:

$$\operatorname{div}(\mathbf{D}\operatorname{grad}\varepsilon) = G^{RR} \frac{\partial^2 \varepsilon}{\partial R^2} + G^{Rz} \frac{\partial^2 \varepsilon}{\partial R \partial z} + G^{zz} \frac{\partial^2 \varepsilon}{\partial z^2} + G^R \frac{\partial \varepsilon}{\partial R} + G^z \frac{\partial \varepsilon}{\partial z} , \quad (4.5)$$

with $G^{\alpha\beta}$ and G^α ($\alpha, \beta \in \{R, z\}$) known functions of $R, z, \Psi, \mathbf{D}_\perp$ and \mathbf{D}_\parallel .

In order to use algebraic algorithms to solve the optimisation problem it needs to be discretised. The emission profile is defined on a regular grid of prescribed resolution ΔR and Δz which may be set separately: $R \rightarrow R_i (i \in \{0, \dots, M\})$, $z \rightarrow z_j (j \in \{0, \dots, N\})$, $\varepsilon(R, z) \rightarrow \varepsilon_{ij} = \varepsilon(R_i, z_j)$. Partial derivatives of the regularisation term are replaced by finite differences:

$$\frac{\partial}{\partial x} f(x_i, y_j) = \frac{1}{2\Delta x} [f(x_{i+1}, y_j) - f(x_{i-1}, y_j)] , \quad \frac{\partial}{\partial y} \text{ analogous} \quad (4.6)$$

$$\frac{\partial^2}{\partial x^2} f(x_i, y_j) = \frac{1}{(\Delta x)^2} [f(x_{i+1}, y_j) - 2f(x_i, y_j) + f(x_{i-1}, y_j)] , \quad \frac{\partial^2}{\partial y^2} \text{ analogous} \quad (4.7)$$

$$\frac{\partial^2}{\partial y \partial x} f(x_i, y_j) = \frac{1}{4\Delta y \Delta x} [f(x_{i+1}, y_{j+1}) - f(x_{i-1}, y_{j+1}) - f(x_{i+1}, y_{j-1}) + f(x_{i-1}, y_{j-1})] \quad (4.8)$$

The integral expression is discretised by replacing the integrand by its linear interpolation of values of adjacent grid cells which leads to:

$$\int_{x_0}^{x_M} \int_{y_0}^{y_N} f(x, y) dx dy = \left\{ \sum_{i=1}^{M-1} \sum_{j=0}^{N-1} f(x_i, y_j) + \frac{1}{2} \sum_{i=1}^{M-1} [f(x_i, y_0) + f(x_i, y_N)] \right. \\ \left. + \frac{1}{2} \sum_{j=1}^{N-1} [f(x_0, y_j) + f(x_M, y_j)] + \frac{1}{4} [f(x_0, y_0) + f(x_0, y_N) + f(x_M, y_0) + f(x_M, y_N)] \right\} \Delta x \Delta y \quad (4.9)$$

(4.6-4.8) is used to approximate (4.5) by a linear combination of ε_{ij} . Applying (4.9) to T_1 results in \tilde{T}_1 . Considering the domain of definition of the expressions for the partial derivatives, the integration area has to be reduced appropriately. By choosing the grid boundaries sufficiently distant from the actual area of interest (inside vessel contour) the outermost grid points can be omitted. For the application of algorithms to solve for ε_{ij} to meet (4.3) it is helpful to provide expressions for the gradient of the constraint terms with respect to the unknown quantity:

$$\frac{\partial \tilde{T}_1}{\partial \varepsilon_{ij}} = \sum_{k=i-2}^{i+2} \sum_{l=j-2}^{j+2} a_{kl}^{ij} \varepsilon_{kl} \quad (4.10)$$

with the coefficients a_{kl}^{ij} being comprehensive functions of $G^{\alpha\beta}(R_k, z_l)$ and $G^\alpha(R_k, z_l)$.

T_2 is translated to a discretised expression if the line integral $\Phi_{V,rec}$ is formulated as a linear combination of the ϵ_{ij} . The line integral needs to be done in one of the spatial parameters, eg R , and the proper description of the line integral, regarding that the path of integration is tangential with an arbitrary inclination angle to the horizontal plane, is (see also fig. 4.12):

$$\Phi_{V,rec} = \int_L \epsilon(R(l), z(l)) dl \rightarrow \int_{R_M}^{\max(r_{min}, R_0)} \frac{\epsilon(r, z_0 - k\sqrt{r^2 - r_{min}^2})}{\sqrt{r^2 - r_{min}^2}} \sqrt{1 + k^2} r dr + \int_{\max(r_{min}, R_0)}^{R_M} \frac{\epsilon(r, z_0 + k\sqrt{r^2 - r_{min}^2})}{\sqrt{r^2 - r_{min}^2}} \sqrt{1 + k^2} r dr \quad (4.11)$$

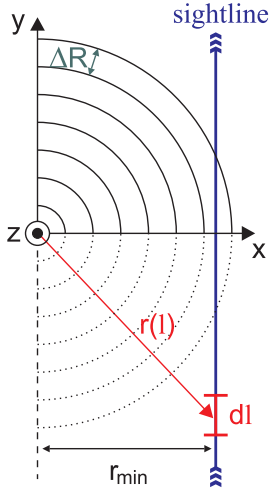


Figure 4.12: The cartesian coordinate system (x, y, z) is chosen such that x - and y -axis define the horizontal plane (midplane of the Tokamak) and the sightline lies in a plane of constant $x (=r_{min})$. The z -component of a point on the sightline is described as $z = z_0 + ky$, with $k = \tan \alpha$, α being the angle of inclination of the sightline to the horizontal plane. With these definitions it is obtained: $y = \sqrt{r^2 + r_{min}^2}$, $dl = \sqrt{1 + k^2} dy$ (consider y - z -plane), $\Rightarrow dl = \sqrt{1 + k^2} \frac{r}{\sqrt{r^2 + r_{min}^2}} dr$.

The integrands of (4.11) are discretised by replacing the profile function by its linear interpolation on the R - z -grid:

$$\epsilon(R, z) \approx \epsilon_{ij} \frac{R - R_i}{\Delta R} (\epsilon_{i+1, j} - \epsilon_{ij}) + \frac{z - z_j}{\Delta z} (\epsilon_{i, j+1} - \epsilon_{ij}) + \frac{R - R_i}{\Delta R} \frac{z - z_j}{\Delta z} (\epsilon_{i+1, j+1} - \epsilon_{i+1, j} - \epsilon_{i, j+1} + \epsilon_{ij}) \quad ,$$

where $R \in (R_i, R_{i+1})$ and $z \in (z_j, z_{j+1})$. The integral expressions obtained are solved analytically, but care has to be taken that grid cells are covered correctly ($z = z(R)$) which is done by splitting the R -area accordingly (for one ΔR -interval, several Δz -intervals might be passed through). The line integral then reads:

$$\int_L \epsilon(R(l), z(l)) dl \rightarrow \sum_{i=0}^{M-1} \sum_{j=0}^{N-1} (h_{ij}^1 \epsilon_{ij} + h_{ij}^2 \epsilon_{i, j+1} + h_{ij}^3 \epsilon_{i+1, j} + h_{ij}^4 \epsilon_{i+1, j+1}) \sqrt{1 + k^2} \quad , \quad (4.12)$$

with the coefficient matrices h^i ($\times \sqrt{1 + k^2}$, $i \in \{1, 2, 3, 4\}$) containing the contribution of each grid cell to the integration area. Using (4.12) for T_2 ($\rightarrow \tilde{T}_2$) the discretisation of (4.3) is com-

pleted. The gradient-component of \tilde{T}_2 is derived as:

$$\begin{aligned} \frac{\partial \tilde{T}_2}{\partial \varepsilon_{ij}} &= \sum_{k=0}^M \sum_{l=0}^N b_{kl}^{ij} \varepsilon_{kl} + d_{ij} \\ b_{kl}^{ij} &= 2 \sum_{v=1}^W \frac{1+k_v^2}{(\delta_v \Phi_{v,meas})^2} (h_{ij}^{1,v} + h_{i,j-1}^{2,v} + h_{i-1,j}^{3,v} + h_{i-1,j-1}^{4,v}) (h_{kl}^{1,v} + h_{k,l-1}^{2,v} + h_{k-1,l}^{3,v} + h_{k-1,l-1}^{4,v}) \\ d_{ij} &= -2 \sum_{v=1}^W \frac{\sqrt{1+k_v^2}}{\delta_v^2 \Phi_{v,meas}} (h_{ij}^{1,v} + h_{i,j-1}^{2,v} + h_{i-1,j}^{3,v} + h_{i-1,j-1}^{4,v}) \end{aligned} \quad (4.13)$$

The algorithm for tomographic reconstruction is used for data recorded from the X-point view to which the grid in the poloidal plane is sketched in figure 4.13 along with poloidal magnetic flux contours and the projections of some lines of sight. Data from the strike point observation (SPO) diagnostics is added, if available. If all coefficients regarding the constraints of regularisation and deviation of measured and modelled line integrals are prepared, the discretised optimisation problem (4.3) can be recast to the form:

$$\mathbf{t}^T \varepsilon + \varepsilon^T \kappa \varepsilon \stackrel{!}{=} \min \quad . \quad (4.14)$$

In order to use standard routines to solve for ε , the 2D formulation used to derive the numerical coefficients of each grid cell needs to be mapped to a 1D index.

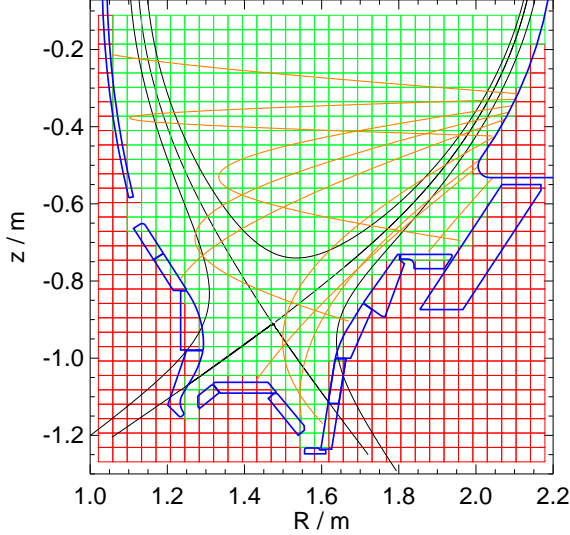


Figure 4.13: In order to reconstruct the poloidal emission profile ε from tangential camera data (specified discharge, time and viewing geometry) by solving the optimisation problem (4.3), the discretised expression $\mathbf{t}^T \varepsilon + \varepsilon^T \kappa \varepsilon \stackrel{!}{=} \min$ is approached with numerical standard methods (vector \mathbf{t} and matrix κ contain the coefficients motivated in (4.10) and (4.13) and the weighting factor A). The flux topology (Ψ -contours: black lines) is routinely available from magnetic equilibrium reconstruction. The line of sight geometry (primary: orange lines) is verified for each data set. After the coefficients regarding \tilde{T}_1 and \tilde{T}_2 are prepared for the whole grid (2D-subscription, rectangular boundary), the problem is reformulated for the area of the grid inside (green) the vessel contour (plasma facing components: blue) by introducing a 1D subscript.

The first attempt shall be to simplify the optimisation problem which is quadratic in ε by demanding a vanishing ε -gradient indicating an extremum of the constraint sum: $\nabla_{\varepsilon}(\mathbf{t}^T \varepsilon + \varepsilon^T \kappa \varepsilon) \stackrel{!}{=} 0$ which results in a system of linear equations (consider (4.10) and (4.13)). Routines provided by the *Numerical Algorithms Group NAG* [32] are applied for its solution. The pair F07MDF [33] / F07MEF [34] is used for matrix manipulation and inversion. A crucial aspect is that these algebraic routines solve the linear system without side conditions on ε . This approach has been tested on experimental data to examine the general applicability. Although some basic features of the profiles can be identified (compared to results from the more elaborate

ansatz - see next paragraph) a good match of the line integrals is actually based on the occurrence of negative values for ε in considerably large regions of the grid. The amount of negative reconstructed profile data is too large to be neglected and the approach turned out to be completely inappropriate if secondary viewing geometry (reflection) is included in the calculation of detector data, since profiles far from physical reasonability are obtained. Consequently, the simplified approach has been discarded and further documentation is omitted to be given here.

The optimisation problem (4.14) can be addressed without simplification by using the *NAG* routine E04NCF which is capable of solving convex quadratic problems where the variable is subject to linear constraints. Here, the constraint imposed to the unknown ε is formulated in the most general sense: $0 \leq \varepsilon < \infty$. Details about the algorithm and mathematical background can be found in [35] and references therein. This routine was found to converge to reasonable results for nearly all sets of input data and it is used exclusively. In the following, the complete procedure of tomographic reconstruction is sketched and the features of the resulting profiles are discussed based on modelled data (phantom data).

The very basic step is to define the boundary and resolution of the rectangular grid. While the former aspect is determined by the vessel contour and viewing geometry, the latter aspect is in principle arbitrary as long as sightlines intersect grid cells and may be subject to optimisation with respect to demands on quality of the result or limits to numerical effort. The grid resolution should be in a reasonable relationship to the detector resolution, eg such that there is a large number of grid cells which are intersected by a couple of sightlines. Since the numerical effort involving huge sets of data and high resolution grids easily results in considerable CPU-time, a pragmatic choice after some trials was made adapted to the technical equipment available. It is $\Delta R = \Delta z = 1$ cm and a detector binning of 3×3 is applied which results in a number of grid points (inside vessel contour) of ≈ 9000 and a number of sightlines of about $W \lesssim 25000$ (some regions of the original image of low signal to noise ratio are discarded). The metric coefficients $\{G^{\alpha\beta}, G^\alpha\}$ are determined by the result for the poloidal magnetic flux profile routinely available from magnetic equilibrium reconstruction, but also depend on the weighting coefficients D_{\parallel} and D_{\perp} which remain to be specified.

The flux surface oriented anisotropy of the curvature of ε is imposed by setting $D_{\parallel} = 1$ and $D_{\perp} = 0.01$ which is motivated by the spatial distribution of excited neutrals: in principle neutral sources are allocated to all vessel components, albeit with the divertor region delivering the dominant contribution, such that the vertical extension of the plasma chamber might be related to the width of the sheath of emission at the plasma edge. While this reasoning might be useful for regions far from the divertor it is more problematic close to or inside of it, where for some conditions the flux orientation of emission may be reduced or even vanish, eg for a recombining plasma. The choice of $D_{\parallel}/D_{\perp} = 100$ seems to be appropriate for a large amount of data (also different ratios like $D_{\parallel}/D_{\perp} = 10$ still lead to similar results if the weighting factor A is adjusted accordingly) but, particularly, its assignment to the entire grid displays a major simplification. The problem of specifying a reasonable value of D_{\parallel}/D_{\perp} for each grid point separately has not been tackled due to the large parameter space and numerical effort for test trials and remains to be addressed.

For each set of radiance data the line of sight geometry (starting/end point, direction) is provided for preparation of the h^i -matrices (see (4.12)). The last parameter to be specified is the weighting factor A of the line integral constraint term T_2 (\tilde{T}_2). Since the optimisation problem involves two numerically diverse terms, normalisation factors are introduced such that a similar range of A can be applied for different data sets: radiance data is normalised to its mean value and

\tilde{T}_1 and \tilde{T}_2 are normalised to the number of grid cells and the number of sightlines respectively. The task is to find a reasonable criterion for a proper setting of A . For this purpose the A -related parameter ζ is introduced by the requirement $\tilde{T}_{1,norm} \stackrel{!}{=} \zeta \cdot \tilde{T}_{2,norm}$. ζ denotes the relative size of $\tilde{T}_{1,norm}$ compared to $\tilde{T}_{2,norm}$. After a rough estimate for the solution of the ε -profile has been obtained from NAG F07MEF, an iteration using NAG E04NCF is performed in which A is changed until a predefined ζ is met within some narrow margin. Although in principle equivalent, ζ is preferred with respect to A as control parameter, because ζ relates the constraint terms directly and the actual minimisation value is secondary. The quality of reconstruction as a function of ζ is established best with the analysis of phantom data to which the underlying ε -profile is known.

An ε -profile which displays certain features often encountered in plasma operation has been constructed to examine the properties of the algorithm for data deconvolution. The profile shown in figure 4.14 is designed to represent the appearance of a predominantly ionising divertor plasma with flux surface oriented emission and the maximum emission at the strike zones (target). The retention of neutrals in the divertor region is reflected by the decrease of emission towards the midplane. In the far SOL at the HFS an additional emission zone is positioned at the wall which is useful to test the reconstruction algorithm for its ability to resolve radially separated structures. The physical background of this feature might be either a localised source of neutrals (eg from gaps between tiles) in combination with relatively hot ($T_e \gtrsim 10\text{eV}$) SOL plasma or a cold ($T_e \lesssim 1\text{eV}$) and dense recombining plasma. For the construction of the model the actual magnetic topology of a certain plasma discharge has been adopted. The model consists of a couple of simple analytical functions such that profiles of arbitrary resolution can be prepared.

An effort has been made to consider the optical properties of Tungsten surfaces (see appendix C). Either, the line of sight integration to provide $\Phi_{v,rec}$ is done on the combined primary and secondary viewing geometry, or the fraction of radiance attributed to reflection is treated as an offset to the primarily integrated emission. The behaviour of the reconstruction algorithm is examined in different configurations of the input data and the algorithm itself which are discussed in the following:

configuration	reflection on input	reflection for reconstruction
a	none	none
b	included	full line / viewing cone integration
c	included	iteration on reflection corrected input data

For all cases phantom detector data is provided in real detector resolution and the step size for line integration is chosen sufficiently small to obtain smooth images. A high resolution profile is prepared and binned for comparison to a resolution chosen for profile reconstruction which is the same as used for experimental data. Also, detector binning is done like in the experimental case (3×3) and data of the lower and upper left corners of the image is discarded. There are two aspects to be mentioned which indicate the major difference with respect to the deconvolution of experimental data. Firstly, viewing geometry on which the calculation of input data is based is identical to the geometry for line integration considered in the reconstruction algorithm. The same applies for the reflection model, if included. While the specification of viewing geometry for experimental data is believed to be very accurate, the reflection model inferred from a single measurement (appendix C) should be regarded only as an estimate used for all slightly differing Tungsten surfaces. Secondly, no simulation of noise has been included, ie each point of the data set is weighted equally. The underlying idea is to test the performance of the reconstruction algorithm in the most consistent sense possible.

In the simplest case (configuration a) the input data is obtained from ray-tracing on contour limited primary sightlines only (see figure 4.15) and also no reflection is considered in the line integration procedure performed for data deconvolution. A scan of the control parameter is done to figure out the relationship between quality of the reconstruction and ζ . As a measure of quality, the deviation of profile data $\chi_{\epsilon}^2 = \frac{1}{N_{grid}} \sum_{i=1}^{N_{grid}} [\epsilon_{model}(i) - \epsilon_{rec}(i)]^2$ as well as the line integral data $\chi_L^2 = \frac{1}{W} \sum_{i=1}^W [\Phi_{model}(i) - \Phi_{rec}(i)]^2$ is considered. The resulting $\chi_{\epsilon}^2(\zeta)$ and $\chi_L^2(\zeta)$ are depicted in figure 4.16. For illustration of the meaning of the evolution of the χ^2 parameters as a function of ζ , three characteristic examples of the profile reconstruction are collected for comparison in figure 4.17. If ζ is set to a very large value, the impact of the regularisation constraint is marginal and a very good match of line integral data may be obtained, however at the cost of physical plausibility. The more regularisation is applied by reducing ζ , the larger the deviation of line integrals, but also the smaller the deviation of the profile data develops. The benefit from the regularisation constraint is diminished if its impact is not bounded appropriately. For too low values of ζ , both the deviations of profile and line integral data increase strongly. The best result obtained for the model reconstruction exhibits all the features of the original data. Minor deviations are recognised at the HFS where the two zones of strong emission are slightly separated from the wall and in the form of artefacts in the private flux region and also reaching from the HFS edge to the core. Taking the very low magnitude of these artefacts into consideration, the algorithm may be stated as being very efficient, ie there seem to be no properties to systematically influence the resulting profile in an undesired fashion.

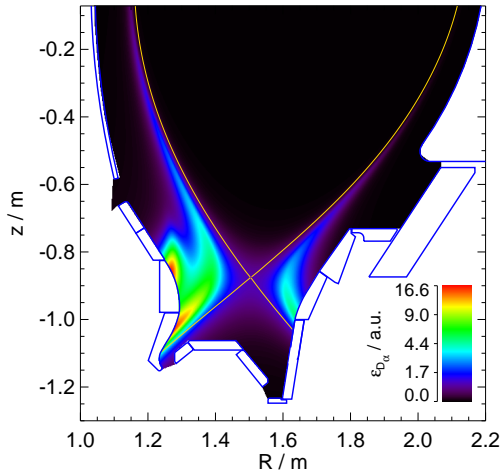


Figure 4.14: High resolution ($dR = dz = 1$ mm) model of the ϵ -profile for testing the algorithm for tomographic reconstruction.

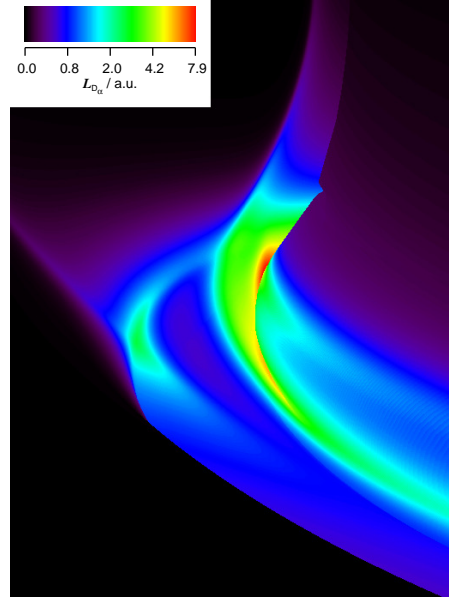


Figure 4.15: Phantom detector data to ϵ -profile of figure 4.14 for the X-point view; primary line integrals only.

The result of the ζ -scan might be referred to when choosing the presumed optimal ζ for the deconvolution of experimental data. Since only χ_L^2 can be accessed, the dependence $\chi_L^2 \propto \frac{1}{\zeta}$ serves as a guideline for a proper ζ -range: reconstructions are made for several values of ζ and the result just beyond the strong drop in $\chi_L^2(\zeta)$ is selected. The situation concerning experimental data is such that the choice for the setting of ζ is not to be overstressed, ie the resulting ϵ -profile

might be very similar for a certain interval of ζ . The reasoning of the $(\chi_L^2 \propto \frac{1}{\zeta})$ -criterion has to be checked for the case of diffuse reflection involved.

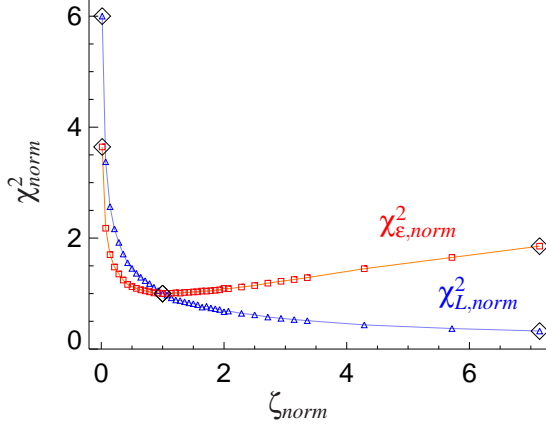


Figure 4.16: ζ -scan to indicate the optimal setting for profile reconstruction. χ_ϵ^2 , χ_L^2 and ζ are normalised to the values of best match in ϵ (minimal χ_ϵ^2); see figure 4.17 for profiles indicated by \diamond .

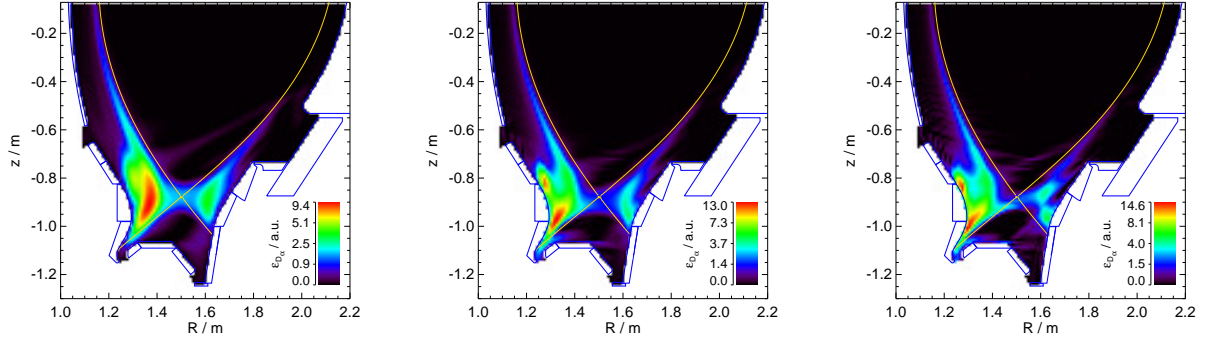


Figure 4.17: Examples for profile reconstructions (configuration a) for three different values of ζ (note logarithmic scale). Left: Low ζ leads to strong smoothing such that the features at the HFS are obscured. Middle: The result of minimal χ_ϵ^2 is actually close to the model profile concerning details on the HFS and LFS. Right: The larger ζ is chosen and the impact of smoothing is reduced the more the profile gets disturbed, in particular at the LFS

The initial step for testing the reconstruction algorithm in configurations b and c is to supply phantom detector data which includes reflection properties of Tungsten surfaces. Appendix C provides a description of the measurement of diffuse reflection of D_α -light at an original divertor tile and the construction of a parameterised reflection model which covers all possible angles of incidence and nearly all scattering angles. For ray-tracing calculations each line of sight is followed to the point of intersection at the distant vessel wall (primary sightline L_1). If the distant wall surface is covered with Tungsten, the direction of specular reflection (referring to the primary as incident direction) is determined and a pencil of separate sightlines L_2^i is prepared to cover a secondary viewing cone. With the specular direction as the reference, each of the new directions is characterised by two angles, polar angle b_1 and meridional angle b_2 (see fig. 4.18). Each of the separate rays is meant to represent a solid angle integration over $\Delta\Omega = [\cos(b_1 - \frac{1}{2}\Delta b_1) - \cos(b_1 + \frac{1}{2}\Delta b_1)] \cdot \Delta b_2$ for $b_1 \neq 0$ (for the center direction $b_1 = 0$ it is $\Delta\Omega = [1 - \cos(\frac{1}{2}\Delta b_1)] \cdot 2\pi$). The contribution of this fraction of the viewing cone is determined by the reflection coefficient R ($R \approx r\Delta\Omega$, $r = \frac{dR}{d\Omega}$) valid for light incident from the secondary direction which is scattered towards the observer (reverse primary direc-

tion). In order to apply the parameterised reflection model the angles α , β and γ (see fig. C.2) have to be provided by appropriate transformations of the coordinate systems involved: $(b_1^i, b_2^i) \rightarrow (\alpha^i, \beta^i, \gamma^i)$. The integration over the separate viewing cone VC^i is approximated: $\int_{VC^i} r(\Omega)\varepsilon(V)d\Omega dV \approx \int_{L_2^i} \varepsilon(l)dl \cdot r(\alpha^i, \beta^i, \gamma^i)\Delta\Omega(b_1^i, b_2^i)$. Due to this simplification which is anyway mandatory for numerics a reasonably high resolution in b_1 and b_2 is necessary to avoid aliasing effects for phantom detector data as well as for the ray-tracing part of the reconstruction algorithm. Regarding the limitation of the reflection model in γ ($\leq 38^\circ$) the ray-tracing procedures for phantom data and reconstruction are performed with $\Delta b_1 = 1^\circ$ and $\Delta b_2 = 10^\circ$ which results in a demanding numerical effort, since for each of the primary sightlines for which reflection is relevant a number of up to $38 \cdot 36 + 1 = 1369$ secondary sightlines are followed (depending on the angle of incidence of the primary direction and the number of resulting secondary rays pointing outside of the integration domain).

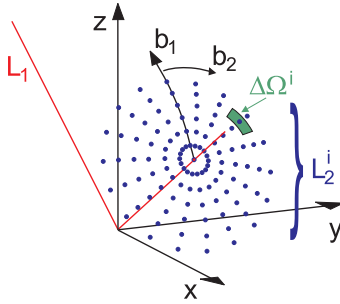


Figure 4.18: A pencil of rays (L_2^i) about the specular direction of the primary sightline (L_1) is constructed to represent the secondary viewing cone; angles b_1 and b_2 characterise each secondary sightline - dots indicate the points of intersection with a sphere centered at the point of incidence.

The resulting phantom detector data of the profile model of figure 4.14 including the model for diffuse reflection is shown in figure 4.19. As the configuration of the plasma facing components the status of the 2006 experimental campaign has been chosen. Relevant for the divertor view is the Tungsten coverage of the heatshield (central column of the torus) and divertor tiles, except for the target plates which consisted of uncoated graphite of which reflection properties are assumed to be negligible. The actual structure of the wall surface is approximated. Most of the parts do not exhibit curvature in the toroidal direction (tangential alignment) and the number of different orientations per torus-segment is maintained. If curvature in the poloidal cross section is encountered, the surface is replaced by several planes of varying poloidal tilt angle. The toroidal curvature of heatshield tiles is instead considered by referring to the local major radius. Further, gaps between tiles and off-tangential tilt ($\approx 1^\circ$) actually set for some of the divertor components is neglected and surfaces outside of the divertor region are not considered. The latter aspect is justified in the sense that the major impact of reflection emerges from surfaces close to the main sources of emission inside the divertor volume.

Although the reflection model should be regarded as an approximation for the in fact differing properties of each wall component, the appearance of the reflected emission in the simulation (based on the profile model also designed to be close to the experimental case) displays the basic features encountered in plasma operation. For the tangentially oriented observer additional contributions to the detector signal stem from regions of the large areas of the divertor sides and bottom with a characteristic toroidal distribution in contrast to an even background signal which might have been expected due to the diffuse kind of reflection. The perturbation of primary data by the reflection part can be significant, since the integral reflectivity is found to be in a range of $0.2 \leq R \leq 0.5$ (see figure C.8, extreme angles of incidence excluded) and the large dynamic range of D_α -emission. In the most problematic case a weak signal from the primary volume is exceeded in magnitude by the reflection part of a strong source in the secondary viewing cone,

eg in the 2007 campaign reflected light from the divertor volume prevents analysis of the D_α -emission sheath at the LFS, because of Tungsten coverage in the background.

In configuration b of the reconstruction algorithm the ambitious aim is to perform the ray-tracing in primary and full secondary viewing geometry in one combined step such that the model for diffuse reflection is included when providing the reconstructed detector signal for comparison with the input data, ie the line integral constraint is extended by reflection geometry. The detector data is established as (using the approximation for the viewing cone integration):

$$\Phi_{V,rec} = \int_{L_1} \varepsilon(l) dl + \sum_{s=1}^{S_{VC}} \left[\int_{L_2^s} \varepsilon(l) dl \cdot r_s \Delta\Omega_s \right] , \quad (4.15)$$

with S_{VC} the number of rays covering the secondary viewing cone. The line integral expressions are each formulated like (4.12) and the additional geometry is thus included in the optimisation problem.

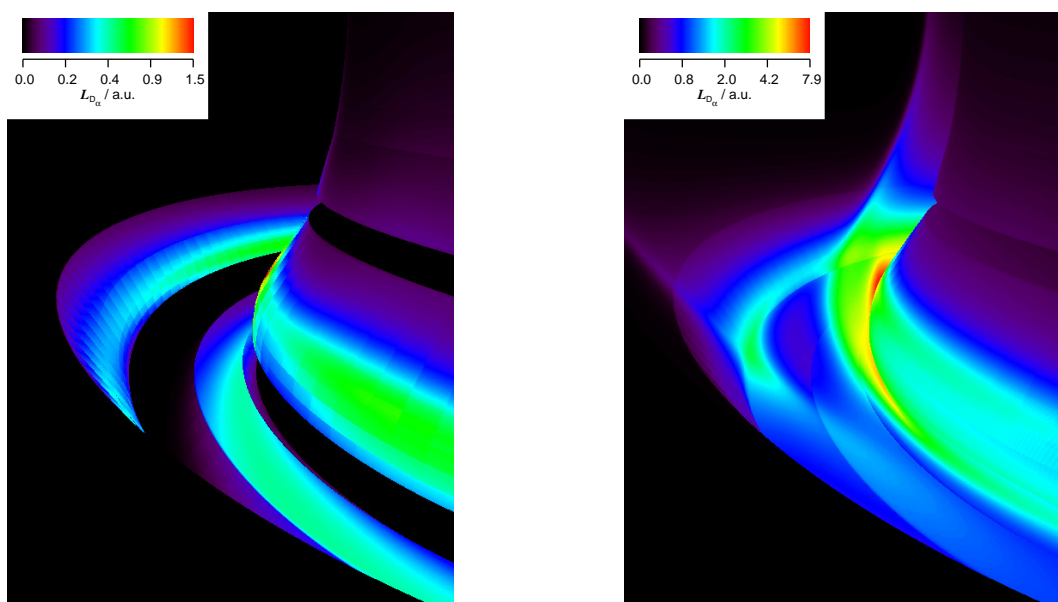


Figure 4.19: Ray-tracing based on the emission profile shown in figure 4.14 including the model for diffuse reflection at Tungsten surfaces. Left: Reflected part only (secondary viewing cone). Right: Sum of primary and secondary parts; see text for details on the specification of wall components.

While phantom detector data is based on the complete reflection model by setting $b_{1,max} = 38^\circ$, the reflection geometry for reconstruction is included stepwise by limiting b_1 to smaller values. The first drawback of this configuration is that the reconstruction algorithm fails to converge, except for $b_1 = 0^\circ$, so that in the first place it remains unclear, whether the algorithm was extended improperly or the approach is systematically unstable. In parallel to testing the algorithm on phantom data, experimental data was used to examine its behaviour. The introduction of a complex model for reflection was in fact encouraged by the promising results obtained for deconvolution of experimental data using a basic model of specular reflection, eg $R_{spec} \in \{0.1, 0.2, 0.3\}$. However, specular reflection is not realistic for the experimental situation and the secondary geometry is sharp in contrast to the large angular distribution of a secondary viewing cone which might be an aspect to influence numerical stability. Nevertheless, the algo-

rithm including diffuse reflection appears to be stable for experimental data and some conclusions about the approach can be drawn.

Figure 4.20 displays the radiance data obtained for a low density L-mode discharge which magnetic configuration and character of its ϵ -profile has been adopted for the construction of the profile model shown in figure 4.14. The distribution of reflection patterns at the lower divertor tiles (roof baffle top) and the surface at the LFS oriented towards the X-point may be stated as a confirmation of the model for diffuse reflection. The major aspect which has not been considered for phantom data is the impact of detector noise which leads to a reduction of image definition. Probably it is this blurring effect which supports the algorithms' stability for a large range of ζ and b_1 . A series of reconstructions reveals the dependence of deviation of radiance data χ_{SL}^2 on the control parameter and secondary viewing cone aperture angle (fig. 4.21). Three examples of the series are given in figure 4.22.

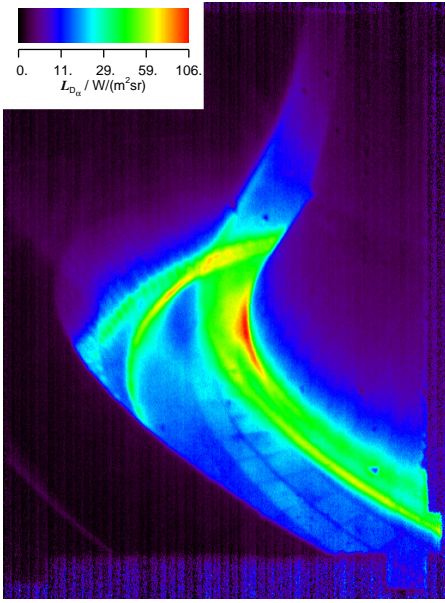


Figure 4.20: Radiance data of X-point view #20901, $t \in [4.616, 4.617]$ s.

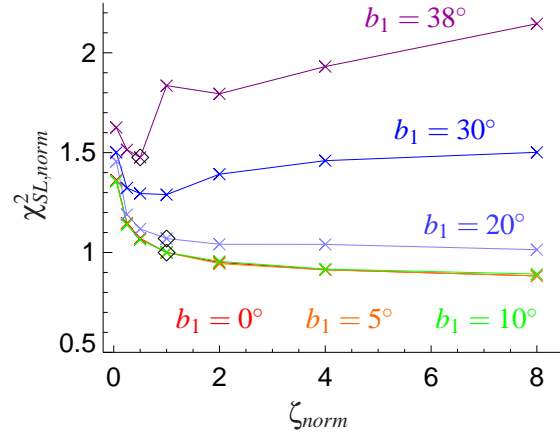


Figure 4.21: Results of tomographic reconstruction of data from figure 4.20 in configuration b: $\chi_{SL}^2(\zeta, b_1)$; ϵ -profiles corresponding to \diamond see figure 4.22.

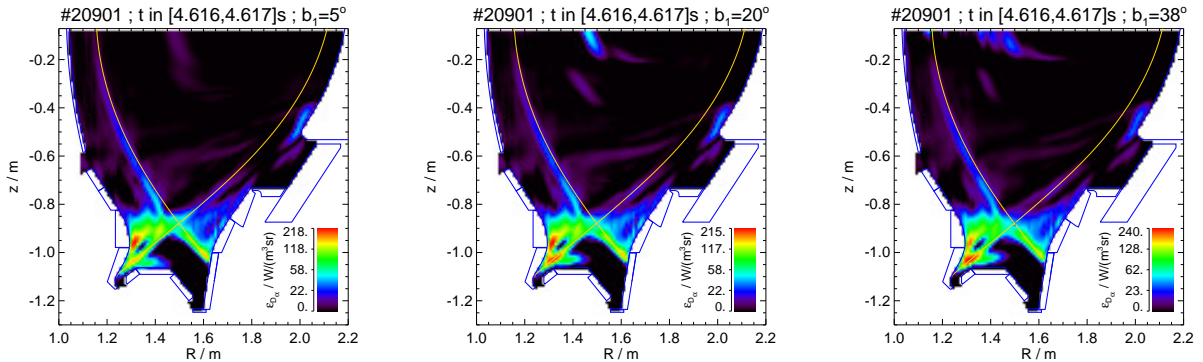


Figure 4.22: Tomographic reconstruction of experimental data in configuration b: increasing secondary viewing cone aperture angle b_1 from left to right. Astonishingly, only minor changes are observed for the different levels of diffuse reflection considered of which the strongest effect is the development of artefacts in the core region related to larger b_1 and ζ .

Against the goal of the approach, the deviation of line integrals increases with the enhanced impact of reflection imposed by the value assigned to b_1 ($\in \{0, 5, 10, 20, 30, 38\}^\circ$) which marks the second drawback. Interestingly, the resulting profile is barely dependent on b_1 at all, eg for $b_1 \in \{0, 5, 10\}^\circ$ practically the same profile is obtained (identical ζ , but slightly different A) and also the characteristics of $\chi_{SL}^2(\zeta)$ is close to the result for configuration a (see figure 4.16). For larger b_1 , $\chi_{SL}^2(\zeta)$ is seen to develop a global minimum. Although this aspect might be regarded as being useful to indicate a reasonable ε -profile, the general increase of χ_{SL}^2 is based on the development of artefacts in regions of the grid of low sightline density, eg upper part of the grid close to the heatshield and in the plasma core. The appearance of strong emission in remote areas suggests that the reflection part prescribed by the model surpasses the actual reflection in magnitude and the optimisation algorithm acts as if to remove emission from the divertor, but in the same way contradicting the idea, that a general reduction of emission should counteract a large reflection part.

In summary it has to be stated that the contribution of reflection geometry in configuration b has no beneficial effect. It is suspected that the underlying reason is the diminishment of contrast in geometrical definition imposed by the model for diffuse reflection: while the primary part of sightline data is well defined in space, the secondary part does not contain robust spatial information (viewing cone integration).

In configuration c, the aim of considering diffuse reflection is maintained, but realised in a much simpler approach. The impact of reflection can be described as an undesired piece of information from the background, ie a kind of offset to the primary part of the radiance data. Since the ε -profile is the unknown quantity, the natural ansatz is to perform an iteration on reflection corrected input data:

$$\Phi_{v,input}^{(j)} = \Phi_{v,0} - \sum_{s=1}^{S_{VC}} \left[\int_{L_2^s} \varepsilon^{j-1}(l) dl \cdot r_s \Delta \Omega_s \right] , \quad (4.16)$$

where j denotes the iteration step, $\Phi_{v,0}$ the original radiance data (experimental or modelled) and $\Phi_{v,input}^{(0)} \equiv \Phi_{v,0}$ ($\varepsilon^{(-1)}$ undefined). On the one hand the optimisation algorithm is operated only in primary viewing geometry and numerical stability is supported, but on the other hand the numerical effort is increased corresponding to the number of iteration steps. The positive aspect of this approach in contrast to configuration b is that it can be used for modelled radiance data in a wide range of ζ and b_1 such that a characterisation like done for configuration a can be made. In the present grid- and detector-resolution the algorithm was found to converge for $b_1 \leq 25^\circ$ which is the only restriction for the following description.

With increasing iteration step j the result for the profile reconstruction is observed to improve (see figs. 4.23 and 4.24). After a small number of steps the optimisation algorithm applied to altered input data approaches a self-consistent state which was found also to be the case for experimental data. The main impact of reflection on the resulting profile if secondary viewing geometry is not considered for reconstruction is recognised as emission close to the roof baffle top and in front of the LFS divertor tiles. This type of artefact is suppressed if the iteration on input correction is followed for a couple of steps. Although this behaviour seems not to illustrate a surprise, because of the simple ansatz, the onset of instability for larger b_1 ($> 25^\circ$) and ζ indicates that the optimisation problem remains numerically challenging.

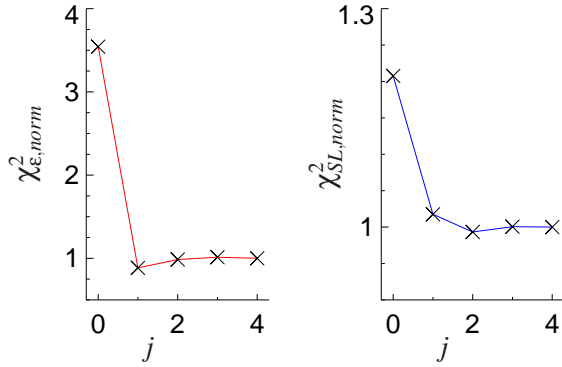


Figure 4.23: χ_{ϵ}^2 and χ_{SL}^2 for several iteration steps j from the reconstruction of phantom detector data with $b_1 = 25^\circ$ (normalised to last value of the series). Note the large drop for χ_{ϵ}^2 and the corresponding moderate change of χ_{SL}^2 . For examples of the profiles see figure 4.24.

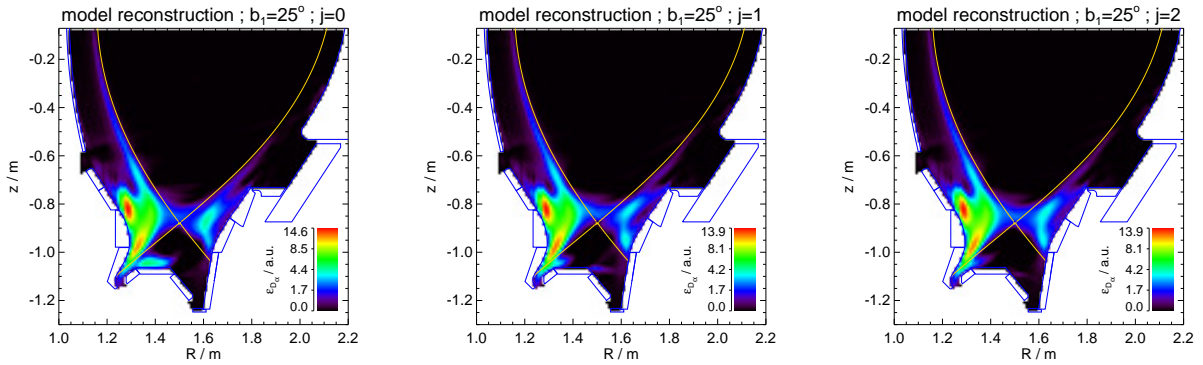


Figure 4.24: Tomographic reconstruction of phantom detector data in configuration c: for $j = 0$ parts of the ϵ -profile above the roof baffle top and at the LFS divertor tiles most probably have to be assigned to the contribution of reflection to the radiance data. The results from the subsequent iteration steps indicate that the input data is altered in a reasonable fashion (improvement in the areas just mentioned). For the profile model see figure 4.14.

A scan of the control parameter ζ has been performed for different values of b_1 to check the algorithm for consistency. Figure 4.25 gives a picture of $\chi_{\epsilon}^2(\zeta)$ and $\chi_{SL}^2(\zeta)$ similar to the one obtained for configuration a. With increasing contribution of reflection geometry (larger b_1) the deviation of reference and reconstructed profile is reduced while the deviation of line integrals nearly remains unchanged. As was motivated for the case of configuration a, the criterion for the selection of a proper value for ζ for the deconvolution of experimental data shall be to examine $\chi_{SL}^2(\zeta)$ and consider the resulting profile which is obtained in a small ζ -range between the blurring of the profile by the impact of smoothing at low ζ and the enhanced occurrence of artefacts due to large ζ . The improvement of the reconstructed profile related to the consideration of secondary viewing geometry is also depicted in figure 4.26 which shows the reduction of artefacts in the bottom and LFS part of the divertor. This representation further displays the decrease of peak emission in line with the larger reflection part.

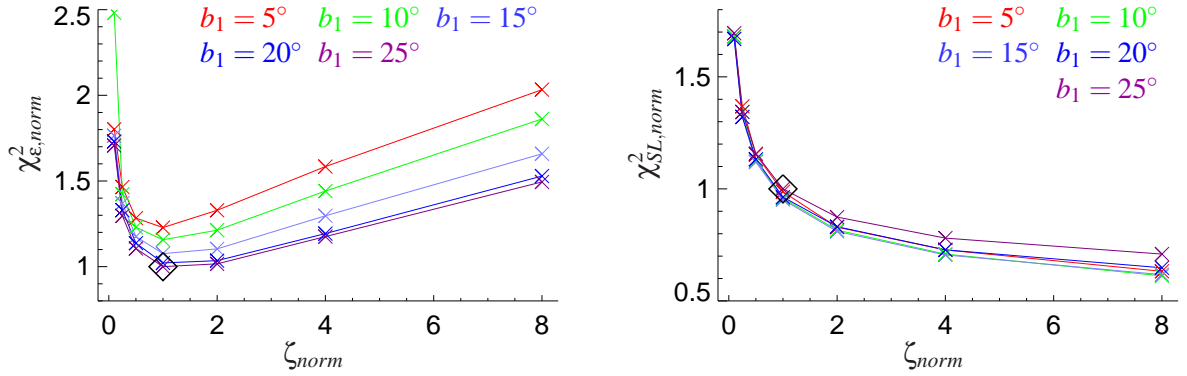


Figure 4.25: Deviation of profile and line integral data as a function of ζ for different values of b_1 . $\chi_\epsilon^2(\zeta)$ is seen to be reduced for increased b_1 (numerical stability in this ζ -range is found for $b_1 \leq 25^\circ$). The parameters are normalised to the best result (minimal χ_ϵ^2 , indicated by \diamond).

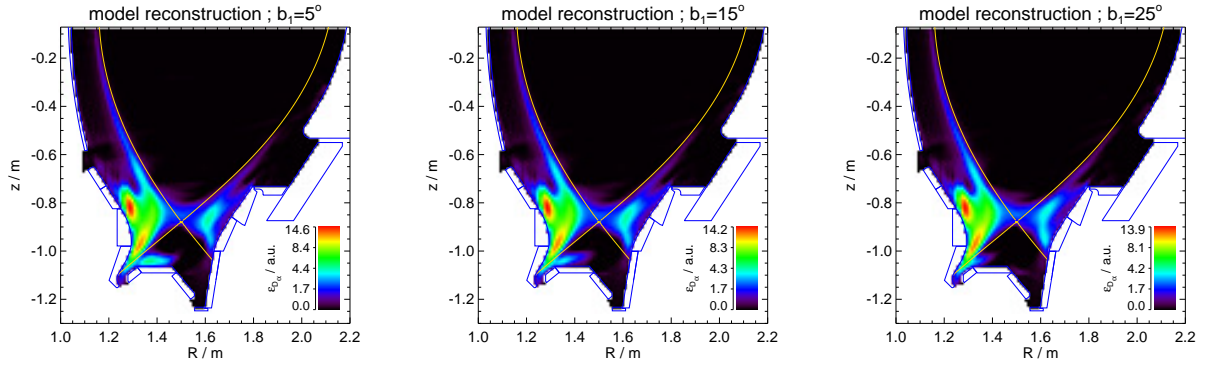


Figure 4.26: Tomographic reconstruction of phantom detector data in configuration c: the larger the contribution of reflection considered the stronger the reduction of artefacts in the divertor region and the decrease of peak emission. For the profile model see figure 4.14.

The behaviour of the reconstruction algorithm is similar for modelled and experimental radiance data. Figure 4.27 shows the result obtained for the data set which already was subject to investigation in configuration b (see fig. 4.22). In the case of experimental data, numerical stability is obtained for the full range of b_1 supported by the reflection model. Also here the reduction of artefacts by the application of secondary viewing geometry at the bottom of the divertor and at LFS tiles is observed and recognised as beneficial effect. The actual resulting ϵ -profile appears to be promising, but contains some uncertainty. Referring to the radiance data shown in figure 4.20, the emission close to the surface of the LFS tiles contained in the reconstruction is believed to be without physical support still, probably based on a deviation of actual and modelled reflection properties. The sharp contrast of the radiance data in this area is suspected to be based on a kind of reflection being more specular than expected. While the artefact above the bottom divertor tiles is strongly suppressed with increased b_1 , the pattern at the LFS wall is not changed considerably, concerning the emission located directly at the wall surface. A feature more problematic and often obtained is a band of emission reaching from the HFS radially outwards and, which is the remarkable aspect, towards the core above the X-point. The comparison of several reconstructions (section 5.2.4) reveals that this feature is independent of the magnetic configuration but related to the viewing geometry, ie radiance is distributed along a large number of sightlines

which intersect the X-point region. In this example only a few artefacts of low magnitude, eg the small zone of emission in front of the ICRH limiter frame, remain, but which are commonly ignored. Further, the resulting χ_{SL}^2 as a function of the iteration step j indicates that the reconstruction of experimental data is not as straight forward as for phantom data, due to the impact of detector noise, the actual vessel geometry and reflection properties.

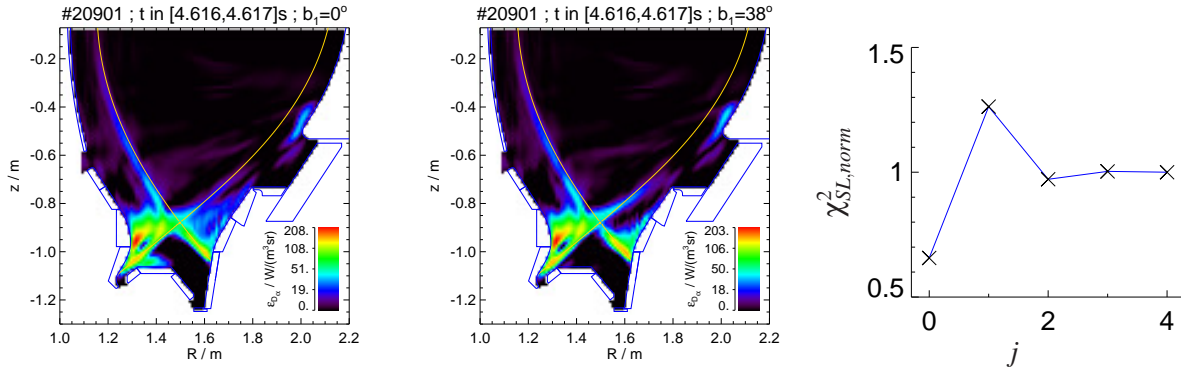


Figure 4.27: Tomographic reconstruction of experimental radiance data in configuration c: note the difference obtained for no reflection considered (left) and the application of the reflection model at full aperture angle (middle). The evolution of χ_{SL}^2 in the iteration of reflection corrected input data is quite different than obtained for the phantom data (fig. 4.23), but nevertheless converging (right).

Tomographic reconstruction in configuration c at full aperture angle of the secondary viewing cone is used for experimental data presented in section 5.2. The character of the profiles obtained suggest to utilise this method of data deconvolution for the analysis of the divertor state rather than to examine radial emission profiles at the separatrix. It is in particular the comparison of position (strike points, volume, HFS or LFS) and magnitude of emission zones which indicate the differences between distinct discharge scenarios and the occurrence of relatively weak artefacts is of minor importance.

Chapter 5

Experimental Results

5.1 Introductory Remarks

5.1.1 Diagnostics Referenced

The prerequisite for the interpretation of $\epsilon_{D\alpha}$ is the knowledge of plasma parameters, in particular n_e , T_e and T_i . These parameters are used to fetch atomic data from dedicated tables and for specification of the plasma background for the simulation of neutral-plasma interaction. In this section a brief overview is given on the set of diagnostics referenced in the analysis of $\epsilon_{D\alpha}$ and the discussion of experimental results. These diagnostics are for electron density: far infrared interferometry and alkali beam impact excitation spectroscopy, and for electron temperature: electron cyclotron emission. For comparison of different divertor conditions, the data obtained from target mounted Langmuir probes is presented and as a benchmark for the modelling results for neutral flux density, values determined with ionisation gauges are adopted. The measurement positions in the plasma vessel of the various diagnostics are sketched in figure 5.1.

One of the standard methods for the measurement of density is plasma interferometry. An electromagnetic wave may pass a plasma if its frequency ω is above the plasma frequency ω_p . for the ordinary wave ($\vec{E} \parallel \vec{B}_{plasma}$) the refractive index N is given by: $N = \sqrt{1 - \omega_p^2/\omega^2}$, with ω_p related to the electron density: $\omega_p = \sqrt{e^2 n_e / (\epsilon_0 m_e)}$. Comparing the passage through different media along a path L , a coherent light beam experiences a phase shift $\Delta\Phi$: $\Delta\Phi = 2\pi/\lambda \int_L \Delta N(l) dl$. This basic relationship can be exploited eg in the Mach-Zehnder interferometer arrangement where coherent radiation is split into a reference and a probing beam which are again superimposed and the interference signal is recorded. Presuming that the refractive index along the reference beam path, or more precisely the optical path length, is constant during the measurement, the phase shift between reference and probing beam is determined by the change in the optical path length in the intersected medium. In the case of a plasma being probed one obtains: $\Delta\Phi = [\lambda e^2 / (4\pi\epsilon_0 m_e c^2) \int_{L_p} n_e(l) dl]$, with L_p the geometrical path length in the plasma. For this phase shift to be pronounced, large wavelengths are favoured. On the other hand, since beam propagation follows a bended path by refraction, if regions of perpendicular gradient of the refractive index are passed, shorter wavelengths are preferred, because the higher the frequency compared to the plasma frequency, the less dependent the refractive index of a plasma is on its density.

For interferometry in fusion plasmas, far infrared laser radiation is used. This long wavelength radiation is emitted from transitions of vibrationally excited states of molecules. The AUG device is equipped with 5 horizontal and partly tilted channels operated with a DCN-laser (Deuterium cyanide, $\lambda = 195\mu\text{m}$) and 3 vertical chords for which a CO_2 -laser ($\lambda = 10.6\mu\text{m}$) is used. The latter is required, because of remarkable distortion imposed on the beam path, if a longer wavelength is chosen. Profile information from the line averaged density measurement can be obtained from inversion techniques including prior information on the position of plasma isobars which are commonly considered being equivalent to the poloidal magnetic flux surfaces in the region of closed topology. Profiles of electron density used in this thesis are the result of integrated data analysis combining the horizontal channels from interferometry and Lithium beam emission spectroscopy. The vertical chords are excluded, because the resolution in area density is much smaller and also the contribution of elevated density of path sections in the SOL close to the divertor region is not compatible with considerations about poloidal flux symmetry of density as a prerequisite of inversion.

An example for the technical implementation of an interferometry system can be found in [36].

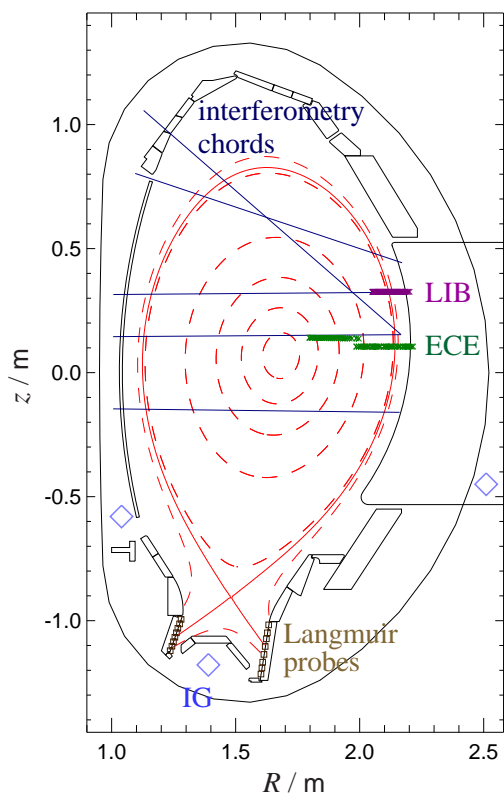


Figure 5.1: Set of diagnostics and corresponding measurement positions referenced for the analysis of $\epsilon_{D\alpha}$ and related discussion. Electron density profiles are gathered from 5 interferometer chords and 35 alkali beam excitation volumes (intersection of horizontal Lithium beam LIB and vertical sightlines). Electron cyclotron emission (ECE) is recorded for determination of T_e on 48 frequencies to which the related radii are shown for one arbitrarily chosen magnetic configuration. Langmuir probes mounted in the target plates deliver divertor parameters and ionisation gauges (IG) in three poloidal locations for neutral flux density measurements are considered.

In several fusion oriented devices, probing beams are used to infer plasma parameters from the analysis of neutral particle-plasma interaction, typically the observation of line radiation from electron impact excitation. The particles of the probing beam should be of low mass such to obtain a high velocity for a given energy, provide a strong resonance line in the visible spectral range and the excited state should be short-lived (small distance between the locations of excitation and emission at a certain velocity) in order to achieve a high spatial resolution. Although the latter aspect is not perfectly fulfilled, Lithium beams are commonly applied for the determination of electron density by recording of the line $\text{LiI}(2p-2s, 670.8\text{nm})$ [37, 38]. Lithium ions can be extracted from heated ($\sim 1300^\circ\text{C}$) Lithium aluminosilicate β -eucryptite ($\text{Li}_2\text{O} \cdot \text{Al}_2\text{O}_3 \cdot \text{SiO}_2$)

by applying an electric field (E_{ex}) in the order of $E_{ex} \sim 3 \text{ kV cm}^{-1}$. The source material allows to draw ion currents per surface area in the range of several mA cm^{-2} and after passing fields for focussing and acceleration (30-80 kV) the ion beam is neutralised penetrating a chamber of Sodium vapour. Typical neutral beam characteristics are a full width at half maximum of current density of $\sim 10 \text{ mm}$ at the plasma edge at a current of 0.5-3 mA. The resonance line emission emerging from beam-plasma interaction is recorded by fast detectors (20 kHz data rate) connected to fiber optics which define lines of sight intersecting the beam path perpendicularly with a radial resolution of 5 mm. With a total number of 35 channels the plasma edge region is covered from the SOL to the near core such to resolve the steep density gradient region.

Because of the high particle energies and the beam penetration to regions of high plasma density, collisional-radiative modelling is required to appropriately account for the processes of collisional excitation and deexcitation, ionisation and charge exchange related to the electrons and all ion species. In order to obtain the occupation density of excited states, thus a system of coupled rate equations (like sketched in section 2.2) needs to be solved. For this particular problem of beam penetration, the spatial coordinate along the beam path z is introduced as the independent variable. The basic treatment without considering impurity ions reads [39] (sum over i, j):

$$\frac{dN_i(z)}{dz} = [n_e(z)a_{ij}(T(z)) + b_{ij}]N_j(z) ; N_i(z=0) = \delta_{ij} \quad , \quad (*)$$

with i denoting the (nl)-quantum state and N the occupation density. This is a short notation with the a_{ij} rate coefficients characterising various processes: $a_{ij}(i \neq j) > 0$ excitation and deexcitation processes which lead to population of state i ; $a_{ii} < 0$ include excitation and deexcitation to other states than i as well as ionisation. Spontaneous emission is covered by the coefficients b_{ij} . A well established method to solve for $n_e(z)$ (inverse problem) with the knowledge of relative $\epsilon_{\text{Li}(2p-2s)}(z_s)$ (s the index for the measurement location) by stepwise integration of (*) is described in [39]. This ansatz introduces a proportionality constant α which relates the measured line emission and the occupation density (for brevity: $\text{Li}(2p-2s) \equiv 2$): $\alpha \cdot \epsilon_2(z) = N_2(z)$ and needs to be determined by iterative means. A difficulty arises from the inversion of (*) for n_e by the occurrence of a singularity which is the reason for numerical instability and demands for different methods in regions where $\frac{d\epsilon_2}{dz} \geq 0$ and $\frac{d\epsilon_2}{dz} < 0$ respectively. Also, the beam emission profile has to be recorded entirely such that an inner boundary condition of the form $N_2(z_{max}) \ll N_2(0)$ can be presumed. For brevity it shall be merely stated that the standard method can be applied only for medium and high density plasmas and typically does not exploit the full radial range covered by the diagnostics. In addition, for numerical reason a sufficient signal-to-noise ratio needs to be provided by averaging the raw data in time and thereby reducing the time resolution.

An alternative method for the reconstruction of $n_e(z)$ from $\epsilon_2(z_s)$ is the probabilistic data analysis described in [40]. The beam emission is modelled using a prescribed profile of electron density and other plasma parameters required, where to all input data uncertainties are considered. The most probable description of the electron density profile, which is characterised by a specific number of free parameters of a cubic spline polynomial, is obtained by an optimisation calculus in the framework of Bayesian probability theory which compares the modelled and measured (also including uncertainties from calibration etc.) emission profiles. Since no inversion of the measured data is performed, the approach can in principle be applied to experimental data without restrictions, ie using the total radial range and the maximum time resolution, independent of the shape of the emission profile related to the level of plasma density. This probabilistic

approach further can be conducted for the combination of different diagnostics in terms of an integrated data analysis [41]. Because of its universal character and consistent treatment of uncertainties of input parameters (including atomic data, geometry, etc.) and measurement errors, the standard Lithium beam analysis is being replaced by an integrated data analysis of Lithium beam emission and DCN-interferometry data. An important feature of Lithium beam emission is the instance that in the present range of plasma parameters, the problem is only weakly dependent on electron temperature and impurity content (Z_{eff}) and generic values for both can be set for these. This observation resembles the physics of the beam-plasma interaction, since it is obtained regardless of the method applied for resolving the n_e profile.

While profiles of electron density are taken from integrated data analysis and are believed to be a very precise description, the situation for electron temperature is more complicated. The first choice for edge resolved temperature measurements is the Thomson scattering system [42] which can be optionally configured to deliver core or edge profile data. However, for two reasons the Thomson diagnostics has not been considered. Firstly, the configuration for edge measurements has not been set for all experiments of interest and secondly, a strong scatter of data is nearly always observed and hampers the interpretation in terms of a smooth profile. Whether this character of data is related to issues of signal-to-noise ratio or the analysis technique applied, or if the wide vertical distribution of scattering volumes and the presence of a perturbation of flux surfaces might be problematic for flux mapping, cannot be answered at this place. From the point of view of $\varepsilon_{D\alpha}$ interpretation, which profile shape strongly depends on T_e , in particular in the vicinity of the excitation threshold, profiles of T_e with a reasonable, ie limited, uncertainty range need to be considered in order to be at all able to compare experimental and modelled emission profiles. A pragmatic procedure is chosen which refers to data obtained from the microwave heterodyne radiometer for measurement of electron cyclotron emission (ECE) and includes a forced exponential decay in the SOL.

The principle of ECE diagnostics is to record radiation emitted from electrons which are accelerated in the magnetic field. The gyromotion of the electrons is accompanied by emission at the gyrofrequency $\omega_g(\vec{x}) = e|\vec{B}(\vec{x})|/m_e$ and its harmonics. Given the spatial variation of the magnetic field, the measurement of ECE at certain frequencies can be exploited for a spatially resolved determination of n_e and T_e . The complex description of ECE involves to consider the magnitude of T_e (relativistic mass increase at high velocities), more generally the electron velocity distribution, the angle between the direction of emission and the magnetic field, and also issues of radiation transport for the path between the origin of emission and the position of the receiver [43]. In the standard setup at AUG, the receiver of the heterodyne radiometer is aligned perpendicularly to the magnetic axis and analysis of ECE is done for 48 frequencies corresponding to second harmonic emission according to the range of the magnetic field strength in the experiment. The choice of the harmonic number is motivated on the one hand by the necessity to use frequencies above plasma characteristics like the lower hybrid or plasma frequencies and on the other hand to avoid harmonic overlap (different harmonics in the same frequency range emerging from different locations) which becomes more relevant the higher the harmonic number. For a wide range of parameters, the plasma is optically thick for second harmonic ECE and taking into account the low photon energy in comparison to the electron kinetic energy the Rayleigh-Jeans approximation for the description of black-body radiance is applied for the interpretation of the calibrated diagnostics data: $L_{ECE} = \omega^2 T_e / (8\pi^3 c^3)$, ie T_e corresponds to the radiation temperature. At the plasma edge however, the assumption of optical thickness may not be fulfilled and the application of the standard procedure leads to an underestimation of electron

temperature. On the contrary, various other effects like the deviation of the electron velocity distribution from the presumed Maxwellian shape, eg a fraction of suprathermal electrons at the plasma edge due to enhanced fast particle transport, result in enhanced emission at the plasma edge and hamper the ECE interpretation in the framework of the basic treatment [44]. For the low and medium density discharges subject to $\varepsilon_{D\alpha}$ analysis, T_e data from ECE is typically reliable in the plasma core and close to the edge region. So the relevant part of the T_e profile in the edge and SOL remains to be specified.

The pragmatic procedure mentioned above uses ECE data as a core boundary condition. An important link between the core region and SOL is the value of T_e at the last closed flux surface. This fundamental quantity is determined from basic SOL-fluid considerations (see [45]). Except for very low density and high heating power applied, the plasma temperature at the target plates is considerably lower than the value at the midplane separatrix, ie the position usually referred to as the upstream ('u') location. The existence of a gradient of temperature along the magnetic field implies that heat transport is dominated by conduction rather than by plasma convection. For this so-called conduction limited regime an expression for the upstream temperature can be derived. For its formulation, the classical value for parallel heat conduction density $q_{\parallel cond}$ is adopted: $q_{\parallel cond} = -K_{\parallel} \frac{dT}{dx_{\parallel}} = -\kappa_0 T^{5/2} \frac{dT}{dx_{\parallel}}$, with the thermal conductivity K_{\parallel} being a strong function of T and the coefficient κ_0 containing parameters governing the collision process of charged particles. Since it is found that $\kappa_{0e} \gg \kappa_{0i}$, heat conduction by electrons is assumed to dominate. The heat flux density to be conducted can be expressed as the ratio of the power which enters the SOL from the core P_{SOL} and the total cross sectional area of the SOL power flow $A_{q\parallel}$ which can be expressed as $A_{q\parallel} = 4\pi R^2 \frac{\lambda_T}{r} (B_{\theta}/B)_u$, where λ_T denotes the radial temperature decay length (of the profile to be determined). Within a simplified picture of a 1D SOL flux tube to which power from the core enters at one end and is conducted to the target at the other end, a basic relationship for the upstream electron temperature reads: $T_{e,u} \approx \left(\frac{7}{2} \frac{P_{SOL}/A_{q\parallel}}{\kappa_{0e}}\right)^{2/7}$, obtained by integration of the expression for $q_{\parallel cond}$ from the target to the upstream position. Although this basic reasoning ([45]) neglects complications like volumetric power loss in the SOL by ionisation and excitation of recycling neutrals, its character matches the experimental observations: because of the strong electron heat conductivity the plasma edge temperature is a very robust quantity, depending only very little on the magnitude of power entering the SOL from the core - it is typically found that $T_{e,sep} \lesssim 100$ eV.

In actual practise a generic profile shape is fitted to the ECE data of the core and appended to an exponential decay part in the SOL. This profile is modified until a reasonable agreement is obtained for $T_{e,sep}$, for given P_{SOL} and $A_{q\parallel}$, and also for the resulting modelled $\varepsilon_{D\alpha}$ profile. For the latter it is predominantly the decay length in the SOL which determines the shape of the D_{α} excitation profile for a certain density profile delivered by integrated data analysis of density diagnostics.

The foundation of n_e and T_e data has been described in the preceding paragraphs. It is desirable to include an estimate on errors in the further calculus, but the integrated data analysis for n_e does not provide absolute values for deviations and the procedure for T_e is only partly based on direct measurements. For both parameters, deviations are thus defined to allow for a parameter scan for the application of KN1D. The deviations are prescribed in an inverse exponential relationship to the magnitude of the parameter in question, ranging from 30% (40%) in the SOL to 10% (20%) in the core region for n_e (T_e). Based on these uncertainties, the extreme profile values are combined to 4 different pairs as input sets for KN1D. The ion temperature which is not routinely

available from diagnostics, is always set to twice the electron temperature, due to the lack of better knowledge, but hints from experimental and modelling results (see eg [46]). However, T_i was not found to influence the resulting neutral parameters considerably in a range of about $T_i=1-3 \times T_e$ in dedicated test runs. The approach for obtaining neutral parameters from experimental determination of $\epsilon_{D\alpha}$ is to apply the KN1D code with input parameters such that a reasonable agreement of modelled and experimental $\epsilon_{D\alpha}$ profiles results (see fig. 5.2). As the matching criterion the radially integrated emission has been chosen which values are allowed to deviate by 1%. This criterion obviously does not contain measures for the detailed profile shape. While the shape of the $\epsilon_{D\alpha}$ profile is predominantly determined by the evolution of n_e and T_e in the SOL (increase of excitation rate) and in the near core region (high ionisation rate, strong reduction of neutral density), the magnitude of emission is related to the molecular flux density at the grid boundary. For the LFS, the n_e profile is well established by diagnostics and only the SOL decay length for T_e , λ_{T_e} , needs to be set appropriately which results in a consistent picture (fig. 5.2, middle). Deviations of modelled and experimental $\epsilon_{D\alpha}$ profiles are often observed in the core region which is attributed to the character of the Lorentzian shape of the profile fit.

The situation is much more complicated at the HFS. It is presumed that profile data (from the LFS) can be mapped to the HFS on flux surfaces of the plasma core. Both n_e and T_e are unknown in the HFS SOL and are described as exponentially decaying profiles with the decay lengths λ_{n_e} and λ_{T_e} as free parameters. The difficulty lies in the instance that both n_e and T_e have a similar impact on $\epsilon_{D\alpha}$ (see section 5.2.1), albeit with a pronounced difference for energies below the excitation threshold with a strong increase of the emissivity coefficient with T_e , and that gradients parallel to the magnetic field are present in the SOL (pressure drop towards the target). A remarkable mismatch of $\epsilon_{D\alpha}$ profiles was found when the plasma parameters had been simply flux-mapped to the HFS or poloidally constant decay lengths defined on the flux label or in real space had been introduced. Instead, for every single 1D grid at the HFS, decay lengths of n_e and T_e have been adjusted with an emphasis on a monotonic change along the p_{sc} coordinate (distance to the X-point). Different values concerning λ_{n_e} and λ_{T_e} were set according to the 'more linear' impact of n_e and the 'strongly nonlinear' influence of T_e on the shape of $\epsilon_{D\alpha}$.

Although large uncertainties of plasma parameters are assumed, the neutral parameters obtained from KN1D do not differ in the same range, since the SOL width is relatively small compared to the penetration depth of molecules and atoms, in particular at the HFS. The uncertainty of the separatrix position (see section 5.1.2) is another important aspect, but data of n_e and experimental $\epsilon_{D\alpha}$ depend on the same magnetic reconstruction and are thus consistently linked. A relative shift of the T_e profile would require to be compensated by different n_e data in order to model $\epsilon_{D\alpha}$ close to experimental observations. The discussion of the code results in the following sections, in particular the molecular flux density at the vessel wall compared to measurements by ionisation gauges, questions the applicability of a 1D code in the sense that the SOL flow towards the divertor cannot be considered. Taken all these issues into account, it is not straight forward to motivate reasonable error estimates for the neutral parameters derived. When parameters obtained from KN1D are presented, deviations are based on the range of input parameters. It is argued that the comparison of KN1D results might be sensible, although the SOL plasma might not be properly described. Since no alternative methods - except elaborate 2D modelling (see section 5.2.5) - for interpretation of $\epsilon_{D\alpha}$ are available, it has been omitted to guess error ranges. The comparison with data from ionisation gauges serves as a hint, but the description close to the separatrix is believed to be appropriate, because the KN1D approach could be replaced by the application of atomic data only (S/XB -coefficients [25]).

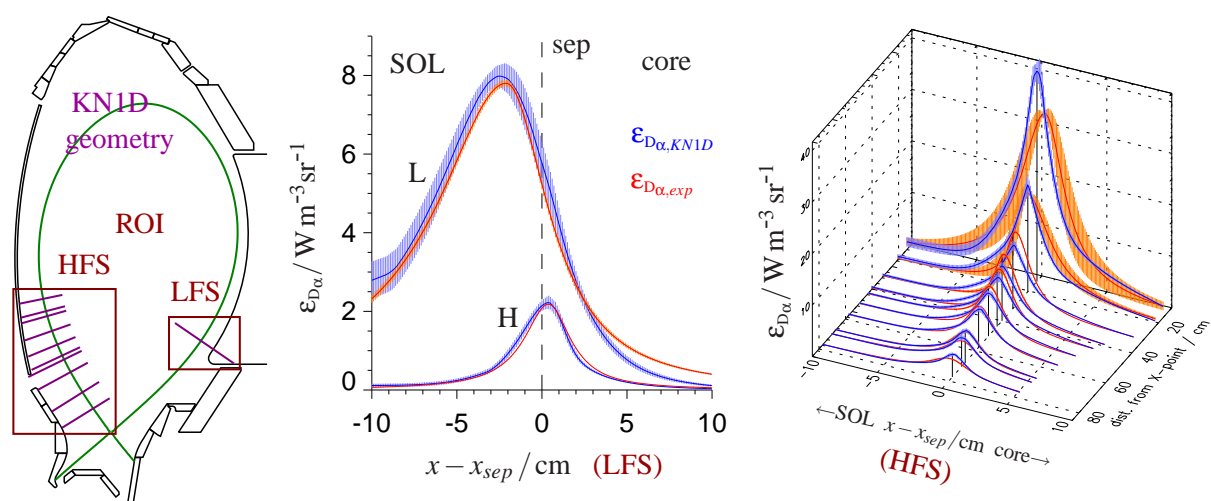


Figure 5.2: Left: Positions of the grids for KN1D modelling for the regions of interest at the high and low field sides. Middle: Match of experimental and modeled $\epsilon_{D\alpha}$ profiles at the LFS for two discharge scenarios (H- and L-mode, see section 5.2.2) obtained by adjusting the decay length of T_e in the SOL. Right: Match of $\epsilon_{D\alpha}$ profiles for the H-mode case on the HFS obtained by specifying SOL decay lengths for both T_e and n_e .

The measurement of $L_{D\alpha}$ and $\epsilon_{D\alpha}$ obtained from data deconvolution serves as a method of indirect determination of parameters of neutral particles. This approach is obviously influenced by the accuracy of measurements or estimates of plasma parameters and the level of complexity of the model for neutral-plasma interaction applied. Important constraints are delivered by diagnostics which are able to measure neutral pressure or flux density directly. In principle, for cases of low pressure gases, the pressure can easily be measured by ionisation gauges [47]. The harsh environment of a fusion plasma demands a dedicated design of such instruments. These need to operate in magnetic fields of strength 1-10T which might in addition change direction and magnitude in time, and be sensitive in a wide range of neutral flux densities: $\Gamma_{D_2} \in [10^{19}, 10^{23}] \text{ m}^{-2} \text{ s}^{-1}$ - corresponding to pressures at room temperature of $p_{D_2} \in [10^{-4}, 10^0] \text{ Pa}$. This task was met by the development of the ASDEX pressure gauge to which a detailed description can be found in [48]. Its basic principle relates to the standard hot cathode ionisation gauge setup (see fig. 5.3).

Electrons are emitted from a heated cathode wire which needs to be strong enough to resist $\vec{j} \times \vec{B}$ forces, and are accelerated towards the grid. Those electrons passing the grid may ionise neutrals in the volume between the grid and the maximum turning point where the potential equals that of the filament. Both the electron flux to the grid I_e and the ion flux to the collector plate I_i is measured. The sensitivity S of the gauge is expressed in the generally nonlinear relationship of normalised ion current and pressure: $I_i / (I_e - I_i) = S \cdot p$, where $S = S(p, \vec{B})$. S is found to be roughly constant for low pressure and increasing with the magnitude of the magnetic field which acts as to confine the electrons and thereby increasing the probability for ionisation for each emitted electron. Reliable operation is achieved, if $I_i \ll I_e$. In general, ionisation gauges saturate if the ionisation rate becomes too large - the actual maximum pressure level which can be measured for a fixed electron current depends on the confinement of the electrons, more precisely the electron velocity distribution, and the size of the ionisation volume. Operation at high pressure and magnetic field is discussed in [49].

For application in fusion experiments the gauges need to be properly shielded against charged particles. As a consequence, the conductance for neutrals to enter the gauge is too small such

that velocity distributions of neutrals outside and inside deviate. This prohibits to put the focus on measuring the neutral density directly which is related to the ion current. On the contrary, the conductance to the gauge is adjusted as to assure thermal equilibration of neutrals inside. The actual mean velocity inside the gauge may be unknown, but only needs to be reproducible. Using the flux density as a conserved quantity ($\Gamma_{in} = \Gamma_{out}$) the gauges are in practise calibrated for Γ in an environment of specified pressure, temperature and magnetic field.

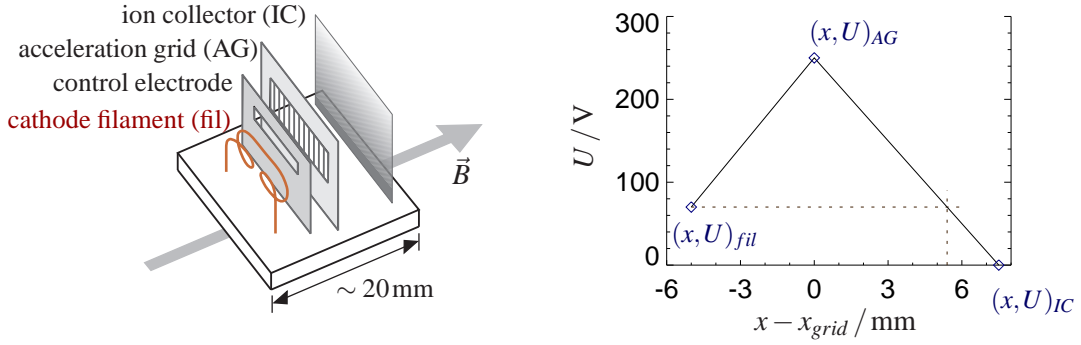


Figure 5.3: Basic scheme of the ASDEX pressure gauge and space potential in the arrangement [49]. Typical voltages applied are: $U_{fil} = 70 \text{ V}$, $U_{AG} = 250 \text{ V}$, $U_{IC} = 0 \text{ V}$. The control electrode is used for modulation of the emission current for suppression of large background in the ion collector current. The setup needs to be aligned to the magnetic field such that the acceleration of electrons in the electric field is barely influenced.

At AUG, several ionisation gauges are placed in different poloidal and toroidal locations in the far limiter shadow or behind plasma facing components. Three of these positions are referenced when comparing gauge data to estimates of the $\epsilon_{D\alpha}$ interpretation (KN1D), indicated in figure 5.1, delivering neutral flux densities behind the lower heatshield $\Gamma_{D, lhs}^G$, below the divertor roof baffle $\Gamma_{D, Div}^G$ and near the LFS midplane $\Gamma_{D, mp}^G$. In the case of one poloidal location being covered by gauges at different toroidal angles, the average value is used. Usually small deviations are observed which might be related to calibration accuracy or the toroidal distance to the pump duct. Data of gauges is discarded if obtained close to an active gas valve.

Electron density and temperature in the divertor region can be obtained from Langmuir probes which are integrated in the target plates. In order to withstand the high power and particle loads, the probe plates are flush mounted in the plasma facing components. The Langmuir probes are referenced only once in section 5.2.1 and for a detailed description the reader may refer to the explanations of [50] and [51].

The principle of these diagnostics is to record the electrical current between the plasma and a small plate exposed to the plasma which is biased against the plasma potential. A conducting surface in contact with the plasma is charged negatively, because of the high mobility of electrons. An ambipolar plasma flow to the wall is maintained by the acceleration of ions in an electric field formed in front of the wall and directed towards it. This electric field is generated in a narrow sheath of width in the order of the Debye length and is based on the deviation of the velocity distributions of ions and electrons compared to their expressions in the bulk of the plasma, usually assumed to be Maxwellian. The corresponding space potential in the sheath is also influenced by secondary electron emission which is a material property. The fundamental problem of the plasma sheath is reviewed in [52]. The simplest probe setup is to connect a probe to the surrounding wall components through an electrical circuit containing a power sup-

ply which is capable of maintaining a certain potential difference between probe head and wall. The electron velocity distribution is scanned by the variation of the potential difference between the probe plate and the vessel wall termed the floating potential. If the probe potential is strongly negative, all electrons will be rejected and only ions will reach the collecting surface. The corresponding current is termed the ion saturation current. At large positive bias voltage, electrons of the full range of the distribution function are attracted and the current reaches the electron saturation level. If the electron distribution function at the sheath entrance is known in principle, eg assumed to be Maxwellian, the shape of the U - I characteristics can be analysed in terms of electron temperature. The properties of the sheath imply that the ion saturation current density is related to the soundspeed and the plasma density. Assuming that ion temperature equals electron temperature or is related in some other fashion, the sound speed is determined and the ion saturation current density can be interpreted in terms of the plasma density. In order to translate the measured currents to current densities, obviously a detailed knowledge of the effective area of the probe head is required.

Actual saturation of currents is in fact encountered only for an unmagnetised plasma or a magnetic field orientation perpendicular to the probe surface. In the Tokamak configuration, magnetic field lines intersect the divertor targets at grazing incidence. The plasma sheath problem has to be revised for this case, resulting in the generation of a magnetic presheath in front of the Debye sheath [53]. This presheath marks a region, in which the particle trajectories are changing from the magnetic field bounded gyro motion to a electric field dominated path towards the wall in the Debye sheath. Because the thickness of the Debye sheath depends on the magnitude of the bias voltage, the effective collection area for ions is not constant for oblique angles of the magnetic field to the wall, hence the ion current cannot saturate and the simple reasoning mentioned above is not applicable [51]. Further complications are the uncertainties in the estimate of the ion temperature and the actual magnitude of the coefficient for secondary electron emission.

In section 5.2 several $\epsilon_{D\alpha}$ profiles are presented and discussed which were recorded during different types of plasma discharges. Although the $D\alpha$ emission is determined by the local values of neutral and plasma density and plasma temperature, it is tried to characterise each of the discharges by the reference of some global parameters. Among those is the 'L-factor' which requires some explanation. One of the fundamental parameters which needs to be optimised for fusion operation is the energy confinement time τ_E which characterises the quality of thermal insulation. In present Tokamak experiments without significant fusion power generation, this parameter can be derived from the known quantities of heating power applied to the core plasma P_{heat} and the plasma energy content W : $\tau_E := W/P_{heat}$. In order to compare different types of discharges including cross-machine comparison and due to the lack of complete analytical understanding of the Tokamak plasma, the experimental τ_E is gathered in data bases and analysed for dependencies on a set of basic plasma parameters. This set comprises heating power P_{heat} , toroidal magnetic field B_t , plasma current I_p , elongation of the plasma cross section k , major radius R , minor radius a , density n and isotopic mass M . The aim is to find scaling laws to be used for extrapolation such to motivate parameter ranges to be met by larger Tokamak devices. Considering global plasma parameters puts a limitation to the robustness of scaling laws, because actually different plasma scenarios, eg with distinct profiles of current density or density, are not treated separately. A scaling law to examine the correlation of these global plasma parameters for the L-mode scenario is the so-called ITER89-P which is a power law expression [54]:

$$\tau_E^{\text{ITER89-P}} = 0.048 \cdot M^{0.5} I_p^{0.85} R^{1.2} a^{0.3} k^{0.5} n^{0.1} B_t^{0.2} P_{heat}^{-0.5} .$$

The L-factor is the ratio of the actual τ_E and the one expected from the ITER89-P scaling. If this factor is around 1, the discharge can be regarded as L-mode type. Values of the L-factor in the range of 2 would be interpreted in terms of the presence of a much better energy confinement and attributed to an H-mode scenario. The latter characterisation is not straight forward, because the majority of discharges discussed are operated at rather low heating power and the level of edge perturbation (see section 5.1.3) is very low. During high power discharges these edge perturbations encountered are often used synonymous for the classification of the discharge. If parameter variations are performed during the discharge, eg plasma shaping or change in heating power, and a rapid change in the density profile, indicating reduced transport parameters at the edge, is observed, the distinction of two different regimes is more obvious, independent of the underlying τ_E .

5.1.2 MHD Equilibrium Reconstruction

The interpretation of D_α emission at the plasma edge relies on accurate data of plasma parameters, mainly n_e and T_e , but also n_i and T_i (charge exchange reactions) which need to be precisely prescribed in relation to the actual plasma position. It is the poloidal magnetic flux Ψ which is used to define a radial coordinate reflecting the magnetic topology: $\rho_p = \sqrt{(\Psi - \Psi_a)/(\Psi_s - \Psi_a)}$ (a : magn. axis, s : separatrix) which in ideal MHD serves as a label of flux surfaces identical to surfaces of constant plasma pressure inside the last closed flux surface. Diagnostics data given in certain spatial positions can be related to the flux coordinate and data obtained from different locations in the core region can be compared if the poloidal flux is known. If this mapping to the flux coordinate is sensible for regions in the SOL depends on the connection length (distance to limiting structures along the magnetic field) between the different locations, ie the variation of plasma parameters should not be too large. Taking the spatial extension of the plasma edge into account which for the AUG tokamak at the LFS is in the order of ~ 5 cm (steep gradient region of plasma pressure and region of interaction with neutral particles) a very high precision in the position of the separatrix is essential. The distinction if plasma parameters are valid in the core region or the SOL is particularly important for the issues of plasma fuelling because of the short ionisation length at the plasma edge. In this section the question of positioning accuracy is briefly mentioned in the framework of standard MHD equilibrium reconstruction.

One of the very basic tasks of experimental Tokamak physics is the reconstruction of the MHD equilibrium which is obtained by solving the Grad-Shafranov equation [55]:

$$-\frac{\partial^2 \Psi}{\partial R^2} + \frac{1}{R} \frac{\partial \Psi}{\partial R} - \frac{\partial^2 \Psi}{\partial z^2} = \mu_0 R^2 p'(\Psi) + \mu_0^2 f(\Psi) f'(\Psi) \equiv \mu_0 R j_\Phi(\Psi) \quad , \quad (5.1)$$

where the poloidal magnetic flux Ψ is determined by flux functions for pressure $p(\Psi)$ and current density $f(\Psi)$ defining the toroidal current density profile $j_\Phi(\Psi)$. The important aspect is that two functions (p, f) need to be specified in order to solve for Ψ . Constraints for Ψ exist in the form of experimental data for the magnetic flux or field components delivered by pickup coils placed in the periphery of the plasma column. Since these are positioned outside the plasma volume, the shape and position of the plasma boundary is reconstructed more accurately than the plasma interior. For the latter region it is necessary to include information related to the plasma pressure like electron density and temperature (and if not available from diagnostics, estimates on ion density and temperature) and the toroidal current density profile inferred from

the utilisation of the motional Stark effect [56, 57]. [58] gives an impression about the standard equilibrium reconstruction performed at the AUG Tokamak. There are two methods for different purposes. The first one is adapted to the requirements of plasma control. For online analysis of pickup coil data a large set of MHD equilibria and the corresponding simulated magnetic signals of the probes are prepared. A principal component analysis is applied to provide uncorrelated linear combinations of these signals. During the plasma discharge the set of actual magnetic measurements are projected to the eigenvectors defining the principal components such that the real MHD equilibrium is approximated as a linear combination of the prescribed ones. This procedure allows realtime control of plasma shape and position within a cycle time of 1-2 ms, but the resulting equilibria may not rigorously satisfy the Grad-Shafranov equation due to a small number (optimised for speed) of principal components considered. The accuracy of positioning (strike- and X-points, magnetic axis, separatrix) is typically in the order of 1-2 cm. This error estimate is based on the deviation of the results from the online reconstruction and the method sketched below.

The second method is a more elaborate interpretive equilibrium reconstruction performed after the plasma discharge. The CLISTE code [59] solves (5.1) by adjusting parameters of the parametrisations for the source profile functions p' , ff' such to obtain a minimum deviation of simulated and measured reference signals. For reference, magnetic flux and field strength data from the plasma periphery is included standardly and if available also information on the current density profile is considered. The character of the reconstruction is influenced by the type of parametrisation which is an expansion of p' and ff' in spline base functions with a selectable number of knots. This representation can lead to an underestimation of special aspects, eg in the case of a large density gradient at the plasma edge (H-mode) the contribution of the bootstrap-current. The latter is the basis of an elevated current density in the edge region, which might not be well accounted for by the typically applied monotonically increasing current density towards the core. Since the magnetic measurements outside the plasma are a constraint predominantly for the total toroidal or poloidal current components, the reconstructed flux topology strongly depends on assumptions on the shape of the source profile functions.

Some very basic details shall be mentioned to describe the accuracy of equilibria used as far as relevant for the interpretation of D_α emission. The output of the CLISTE code is the poloidal magnetic flux on a grid covering the cross section of the vacuum vessel. A standard grid size is 64×128 (figure 5.4) with $R \in [0.75, 2.67]$ m ($\Delta R = 3$ cm) and $z \in [-1.504, 1.504]$ m ($\Delta z = 2.35$ cm). For each discharge these equilibria are calculated for time intervals of 100 ms ($t_{CLISTE} = N \cdot 0.1$ s) where the reference signals are taken from single time slices corresponding to the sampling rate of the probe data ($\mathcal{O}(1$ kHz)) and no averaging over time is performed. For data analysis in this thesis normalised flux coordinates for arbitrary time and spatial position are obtained by referring to the poloidal flux matrix closest in time and applying quadratic interpolation on the spatial domain. Concerning the time intervals of MHD equilibria and the time points of D_α detector data, interpretation in terms of radial position is sensible only in phases of quasi constant plasma parameters, particularly of plasma position, volume and the current density profile.

From the point of view of grid resolution and interpolation schemes of which different ones may be applied, the precision of spatial parameters, eg radial position of the separatrix in the midplane, is clearly limited. Although this displays a critical issue for the analysis and interpretation of edge diagnostics data, CLISTE equilibria are commonly provided and used without estimates on uncertainty. A number reflecting this aspect often cited is (in the minor radius sense)

$\Delta r_{sep} \lesssim 5$ mm for the possible systematic displacement of the separatrix ([60]). An alternative is to use diagnostics data provided in spatial coordinates and to define the position of the separatrix by the magnitude of plasma parameters and to adjust the MHD reconstruction accordingly. With the knowledge of the power which enters the SOL from the core ($P_{loss} \approx P_{heat} - P_{rad,core}$) and the parallel heat conductivity of electrons $\chi_{e,\parallel}$ being a strong function of electron temperature ($\chi_{e,\parallel} \propto T_e^{5/2}$, [45]), a robust constraint can be established for the electron temperature at the separatrix (typically at AUG: $T_{e,sep} \sim 100$ eV).

In fact, the accuracy of MHD equilibrium reconstruction and apparent mismatches in position (in the flux coordinate) of radial profiles inferred from different plasma diagnostics are subject of a permanent discussion which goes along with Tokamak operation.

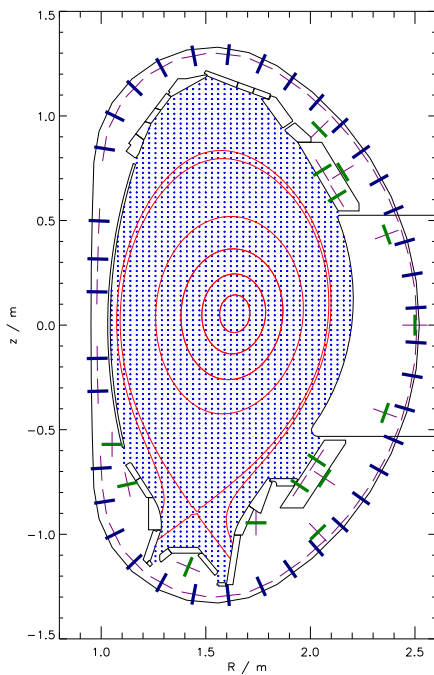


Figure 5.4: Cross section of the AUG vacuum vessel with contours of plasma facing components. Blue crosses mark the vertices of the poloidal flux matrix of the standard CLISTE-based equilibrium reconstruction - here indicated only inside the plasma chamber. Red lines are contours of the poloidal magnetic flux ($\rho_p \in \{0.2, 0.4, 0.6, 0.8, 1., 1.015\}$) from an arbitrarily chosen discharge. For the measurement of magnetic field components (thin pink lines) a large set of coils (blue and green bars) is placed in the plasma periphery. In addition, pairs of larger saddle coils which span parts of or the complete toroidal circumference deliver data for differences in Ψ (not included in the figure).

5.1.3 Edge Perturbation

Besides the uncertainty from magnetic equilibrium reconstruction regarding the position of the last closed flux surface, its shape may locally deviate from a smooth surface due to the impact of macro scale perturbations at the plasma edge. The fluxes of particles and energy perpendicular to the surfaces of constant pressure are determined by anomalous transport parameters which are larger than the one predicted by neoclassical theory. These transport properties are attributed to micro scale instabilities as the origin of plasma turbulence. If plasma transport was constant in time for steady state discharge operation, ie constant heating power, feedback control of density, current, shape and position of the plasma column, also a constant flux of energy and particles would cross the separatrix and the divertor conditions and geometry would be designed to handle the resulting flux densities. In many discharge scenarios with good confinement properties (H-mode) the plasma edge is found to lose its integrity frequently by the occurrence of so-called edge localised modes (ELMs) in which phases of $\sim 0(0.1 - 1$ ms) a certain fraction of the total stored energy of the plasma core is ejected to the SOL and distributed to the plasma facing components. The amount of energy transported to the divertor targets in such transient events can be up to 3%

of the total stored energy for AUG or even higher for larger machines like JET [61]. At the high power densities accompanied, impact limits of plasma facing components can be surpassed. For the development of a high performance discharge scenario which meets the requirements for economic operation of a future power plant, it is crucial to understand the nature of ELMs in order to avoid enhanced erosion of vessel components like the divertor target plates. According to the experimental characteristics of these modes, several types of ELMs are defined in the literature. The main features are the frequency of the edge perturbation and the related energy loss. Different ELM types are distinguished by the dependence of their frequency on heating power. ELMs of type I are the most critical modes in the framework of interaction with plasma facing components, and are easily identified by fast recording of D_α emission (diode setup) in the strike point region (optics similar to SPO) in the form of pronounced spikes indicating the excitation of neutrals during a short period of time, typically with a repetition rate of $\mathcal{O}(50\text{Hz})$ (AUG operation) depending on various parameters like heating power, plasma density and shape. Unfavourable scaling of type-I-ELMs to larger devices is expressed in decreasing ELM frequency and increasing power loads. The time averaged ELM losses of a certain discharge scenario are seen to be roughly constant (relative fraction of core energy content), while the ELM energy scales with the total stored energy and the ELM frequency $f_E \propto \tau_E^{-1}$ [62]. According to the properties of ELMs, the need for the development of operation scenarios compatible with machine safety is discussed in [63] and [64].

Efforts are being made to provide a detailed picture of the loss mechanism by the examination of the spatial distribution of power loads in the main chamber and the divertor [65, 66, 67]. The patterns of power deposition observed at the target plates suggest the energy from the core plasma being transported in filamentary structures through the SOL. With the availability of fast measurements of electron density and temperature like provided by the present day Thomson scattering systems, the dynamics and the spatial structure of the edge perturbation can be examined [68, 69]. Observations are compared to models in the framework of ideal and non-ideal MHD instabilities [70]. Stability analysis of the ideal MHD set of equations (zero resistivity) leads to a variety of mechanisms which are characterised by mode structures with positive growth rates, ie small perturbations from the equilibrium state enter an exponentially growing excursion and driving the system unstable. The energy integral of the perturbed plasma is negative corresponding to a relaxation of the system to a energetically lower, more stable state. Modes from ideal MHD analysis which are believed to be connected with the ELMs are the peeling and the ballooning instability. Driving terms of those are governed by edge current density and the pressure gradient respectively. The effect of the bootstrap current enforces the current density in regions of considerable pressure gradient and both parameters are thus coupled particularly at the plasma edge.

If the plasma edge is perturbed by some mode structure which is driven unstable until plasma from the near core region is ejected to the SOL, a significant change is also expected in the magnitude of line emission of those species which photon emissivity coefficients are different for the plasma parameters in the quiescent phase before and during the event. This is the case for D_α radiation (see section 5.2.1) and influx of neutrals from plasma recycling or gas puffing is excited in the edge region according to the spatial structure of elevated density and temperature. It is possible to resolve filamentary structures of D_α emission for exposure times of $t_{exp} \lesssim 100\mu\text{s}$ and if the detector is capable of high frame rates $\sim 10\text{kHz}$ an examination of the dynamics of these structures can be made with optical diagnostics [71]. The numbers regarding timing are clearly just reference values and are depending on transport times of hot and dense aggregations or fil-

aments in the SOL. With the diagnostics setup described in section 3.2 only an extremely slow (compared to edge dynamics) frame rate is provided ($f_{frame} < 12\text{Hz}$) but the detectors can be set to short exposure times in the order of $10\mu\text{s}$ which has been verified with test measurements. In the 2006 campaign the XPMC diagnostics has been operated for a couple of discharges without interference filter to collect as much emission as possible and at exposure times feasible in terms of signal-to-noise ratio. Despite the filter being removed the recorded light predominantly stems from Hydrogen radiation and only very little contribution from core bremsstrahlung is seen in cases of impurity accumulation and high plasma temperatures. The data obtained is very important for the interpretation of D_α emission at the plasma edge and is presented from two different discharge scenarios:

shot	time range / s	I_p/MA	q_{95}	\bar{n}_e/m^{-3}	P_{heat}/MW	gas feed / Ds^{-1}	L-fact.
20771	[3.0, 4.8]	1.	-3.1	$8 \cdot 10^{19}$	5.	$2 \cdot 10^{22}$	> 1.5
20784	[2.2, 5.5]	0.8	-4.7	$6 \cdot 10^{19}$	1.8	$1 \cdot 10^{22}$	1.

The basic parameters of the discharges are barely similar, #20771 belongs to the class of H-mode discharges which is established by a sufficient magnitude of heating power, while additional heating for #20784 is too low relative to the plasma density adjusted by gas puffing such that this discharge is of L-mode type. Another remarkable feature of the H-mode is a larger density gradient at the plasma edge based on reduced transport parameters commonly attributed to a specific edge transport barrier. In L-mode a higher density at the separatrix and in the SOL with a larger decay length is seen eg when comparing discharges with similar line averaged density, see section 5.2.2.

For both discharges filamentary structures at the LFS could be identified with the XPMC main chamber view, although a relatively large exposure time of $t_{exp} = 200\mu\text{s}$ was set. In this short presentation of basic observations the term 'filamentary structure' is used because of the patterns obtained for D_α emission. If plasma transport in the SOL parallel to the magnetic field is fast such that transit times are comparable with or even smaller than the integration time of the diagnostics, the details of the transport mechanism obviously cannot be resolved and no distinction is possible between the cases of core plasma being ejected to the SOL locally or over a large interval of the toroidal circumference. When looking at a series of frames the perturbation at the plasma edge is obvious, but here only single frames can be presented on the following figures.

The position of the plasma column is controlled to ensure a gap between the separatrix (its position being obtained from online reconstruction) and the vessel wall of about 5-10cm. If the distance is too close, enhanced line emission from plasma recycling is observed. In figures 5.5 and 5.6 this plasma-wall interaction is highly localised, indicating its origin being separate structures in the SOL. For larger exposure times, the detailed pattern at the limiters would be blurred and the resulting emission might be interpreted as unfavourable plasma positioning. The pictures also indicate that the structures at the plasma edge are apparent from line radiation only if a certain flux of neutrals is present in the SOL (see area of access-ports).

When analysing diagnostics data in consideration of the presence of ELMs, the latter is often assessed by the time traces of D_α emission in the divertor region. While for #20771 a modulation of divertor D_α is observed (in this case corresponding to a high frequency ELM-type: $f_{ELM} \approx 340\text{Hz}$), indicating a modulation of power deposition in the divertor, the same signal for #20784 appears less rich in contrast and rather noisy, although the edge perturbation is obvious from the video diagnostics. This raises the question of energy content and transport characteristics of filamentary structures in the SOL. Figure 5.8 gives an impression of D_α -filaments in the

SOL of an H-mode discharge close to the divertor. Detailed measurements and discussion on the propagation of filamentary structures in the SOL can be found in [72, 73]. A central mechanism for perpendicular motion is suspected to be the polarisation of plasma aggregations in the SOL by the action of curvature- and $\nabla\vec{B}$ -drifts and accompanied $\vec{E} \times \vec{B}$ -drift which accelerates the filaments towards the LFS wall. For #20784 it is suspected that either perpendicular transport is large enough, such that the filamentary structures do not enter the divertor but interact with the LFS wall, or it exists a mechanism which distributes the former localised energy to a greater volume during the transport time in the SOL, so no separate structures penetrate the divertor region.

The conclusion of the short exposure data is that a fine structure of D_α emission due to edge perturbation is marginally resolved with the XPMC diagnostics, albeit the speed of data acquisition is not appropriate for studies of SOL dynamics. The aspect aimed at is the impact of the spatial D_α modulation on the ansatz of data analysis presented in section 4.1 which is based on the assumption of toroidal symmetry and the existence of a smooth flux topology.



Figure 5.5: Main chamber view XPMC diagnostics: #20771, $t \in [3.7672; 3.7674]$ s in logarithmic scaling. D_α emission from plasma facing components (eg upper part of ICRH limiter frame) indicate enhanced plasma recycling in a few distinct areas. It is hardly possible to recognise filamentary structures highlighted by gas puffing in the large access-port (see also fig. 5.6).

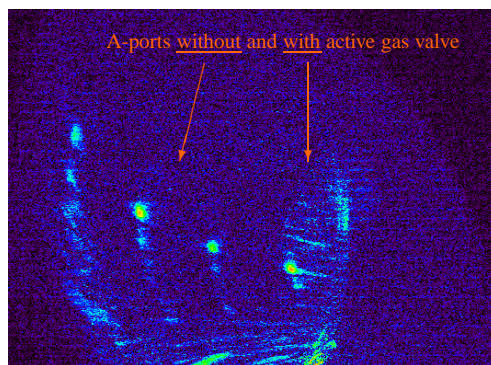
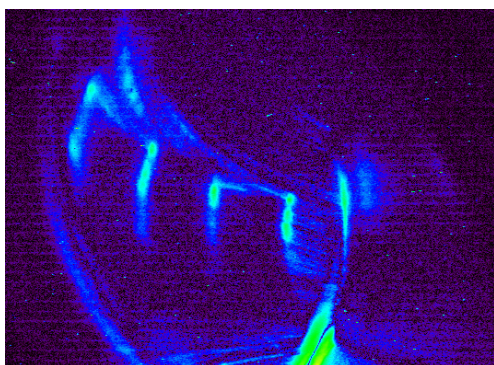


Figure 5.6: Filamentary structures in the LFS SOL become apparent from video diagnostics if two consecutive frames are subtracted to resolve the differences. For both discharges (left: #20771, right: #20784) contact of filaments with limiting structures is observed and also D_α emission in front of the access-port with an active gas valve for density control is recognised to be spatially modulated. The relationship of D_α emission and edge perturbation based on MHD instabilities is supported by the alignment parallel to the magnetic field (simple plasma-wall interaction by unfavourable positioning leads to emission patterns which are toroidally symmetric on the limiters).

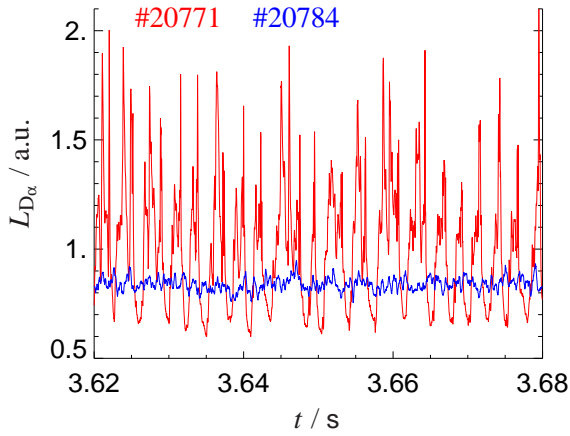


Figure 5.7: Time traces of outer divertor leg $L_{D_{\alpha}}$ from fast diode based diagnostics in an arbitrarily chosen interval with LFS edge perturbation present. Modulated excitation of neutrals is obvious for #20771. The situation for #20784 is not clear: the data might be interpreted in terms of the presence of small scale fluctuations or simply as a noisy radiance level. A possible reason for the latter observation might be a low recycling flux and a low application of modulated power.

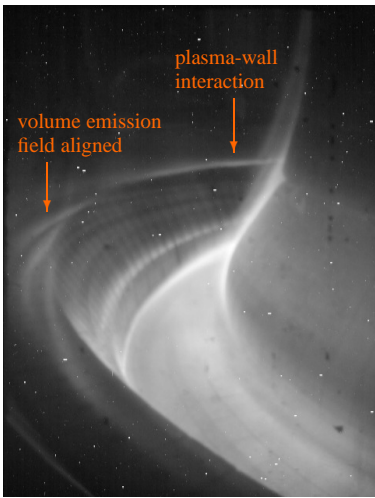


Figure 5.8: XPMC divertor view of H-mode #20733, $t \in [5.6283, 5.6284]$ s in logarithmic scaling. Some D_{α} filaments are field aligned close to the LFS divertor tiles but also wall contact is observed in the background (horizontally aligned) which has to be explained by considerable perpendicular transport of a few cm radially outwards during the motion in the SOL. Increased noise level is due to interaction of radiation (high neutron flux and related γ -radiation) with the CCD-sensor.

Corresponding to the situation in which the edge perturbation might not have been recognised, the ray-tracing-fit was applied to the frame series of both discharges to radiance data at the LFS. Since the region of interest is very small, the assumption of minor variation in the poloidal direction seems still to be justified, at least according to the signal-to-noise ratio obtained. The procedure was found to converge for most of the frames of the #20771-sequence, while only a few profile fits could be achieved for the series of #20784, indicating that the profile model is not well suited for this special case of filamentary structures. This kind of data analysis is based on the standard MHD equilibrium reconstruction and the results are summarised in figure 5.9. A possible interpretation is to relate the radial position of the $\epsilon_{D_{\alpha}}$ -profiles to perpendicular transport of hot and dense plasma aggregations or filamentary structures. The different radial positions might then be an indication for the evolution of these structures starting from the toroidally varying location of origin to the measurement location. This reasoning is likely to be wrong or at least only partly correct. The equilibrium reconstruction is done on a 2D grid whereas the perturbation of MHD instability is a 3D structure. A spatial modulation of plasma density and temperature at the edge implies that the shape of flux surfaces may deviate from a smooth, toroidally symmetric shape. In addition, filamentary structures in the SOL are suspected to be areas of increased current density [74] which also influences the poloidal magnetic flux locally. The variation in radial position may therefore be to some extent related to the simplified flux topology. Regarding the 3D character of the plasma edge, further interpretation of D_{α} -profiles is hampered, since the measurement of plasma parameters like n_e and T_e are done in a different area and the mapping on the basic ρ_p might be deficient.

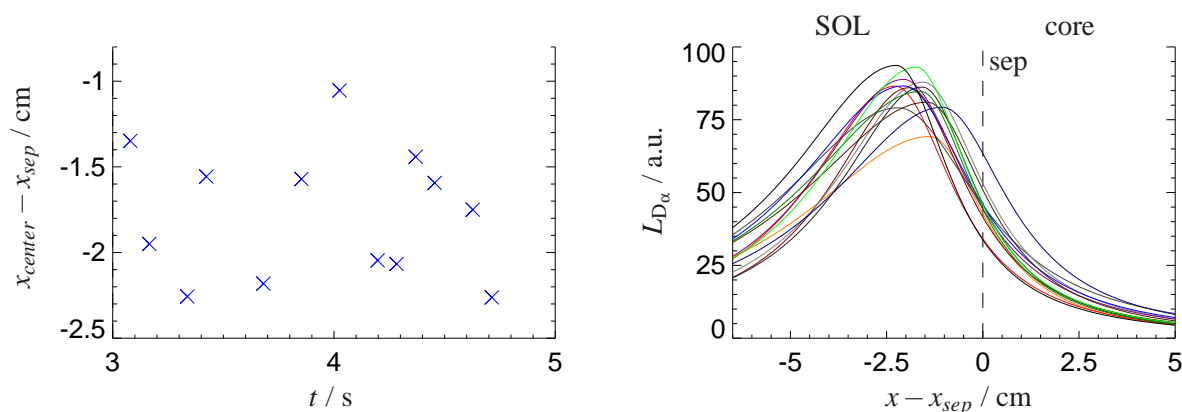


Figure 5.9: Ray-tracing-fit for XPMC LFS-ROI frame series of #20771, $t \in [3.0, 4.8]$ s. Left: Resulting center parameter in terms of distance to the CLISTE-separatrix position. Right: ϵ_{D_α} profiles of frame sequence. As the abscissa the x -coordinate displays the penetration of neutrals from the SOL towards the core plasma along an imaginary line perpendicular to the separatrix in the ROI (-volume).

In the standard XPMC diagnostics setup larger exposure times are set ($t_{exp} \gtrsim 1$ ms) and edge perturbations, if present, are no longer resolved. The effect is as if the profiles of figure 5.9 were merged to an average one. Plasma parameters from other diagnostics for interpretation of emission are time averaged on the exposure interval for consistency (usually XPMC exposure is larger than integration times of various edge diagnostics). To what extent the averaged values display effective profiles for the presence of significant edge perturbation is unknown. At least to consider an uncertainty in radial position seems to be reasonable. However, attention has to be paid that emission is related to plasma parameters in a nonlinear fashion which makes the 3D character of the plasma edge more problematic. The simulated emission profile based on average plasma parameters might not match the experimental one, if the emissivity coefficient is strongly affected during a time interval which is short compared to the integration time.

For most of the discharges discussed, edge perturbation is assumed not to be present, if no modulation of divertor D_α is seen, since mainly low density ohmic and L-mode scenarios are examined. Nevertheless, the example of #20784 shows that modulation of divertor parameters is not a sufficient criterion. If H-mode discharges are analysed the phase between pronounced ELMs is considered. This time interval is determined by reference of divertor radiance assuming the transit times of the SOL perturbation from upstream to downstream locations to be sufficiently fast.

5.2 Interpretation of D_α Emission

5.2.1 Dynamic Range of D_α Emission

Before discussing ε_{D_α} -profiles at the plasma edge and the distribution of emission in the divertor in more detail in the following sections, it is useful to recapitulate the relationship of plasma parameters and the magnitude of D_α emission. During Tokamak plasma operation a huge range of emission in the order of $1 : 10^2 - 10^3$ is observed, eg when comparing the divertor and mid-plane regions, which as the very basic consequence imposes a challenge to operate CCD-based diagnostics with optimised settings for exposure time. In the range of plasma parameters relevant for SOL and edge physics, collisional radiative modelling is required to establish the correlation of radiation and plasma density and temperature (see section 2.2). The magnitude of line radiation is connected to the reactants involved over photon emissivity coefficients ($\mathcal{P}EC$ s) which are equivalent to rate coefficients, eg

$$\varepsilon_{D_\alpha} = \mathcal{P}EC_{D_\alpha,exc}(n_e, T_e) \cdot n_D \cdot n_e \quad (+ \mathcal{P}EC_{D_\alpha,rec}(n_e, T_e) \cdot n_{D^+} \cdot n_e) \quad . \quad (5.2)$$

Although in principle both mechanisms are active simultaneously, often a classification of regimes into ionising or recombining plasmas is adequate. Figure 5.10 shows the D_α photon emissivity coefficients for electron impact excitation and radiative recombination. Only for very low electron temperatures ($T_e \sim 1.5$ eV) $\mathcal{P}EC_{D_\alpha,rec}$ becomes comparable to $\mathcal{P}EC_{D_\alpha,exc}$ and surpasses the latter for lower temperatures, however, for the comparison of emission from both reactions, the density of the species involved have to be considered.

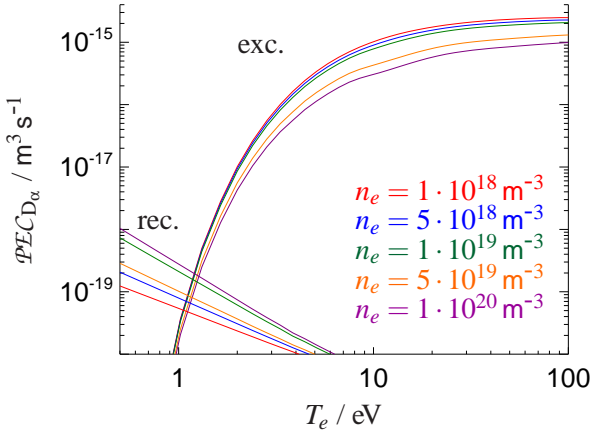


Figure 5.10: Photon emissivity coefficients for Deuterium Balmer- α radiation from excitation and recombination, taken from the ADAS data base [75]. These rate coefficients are functions of both electron density and temperature. One notes a large variation of $\mathcal{P}EC_{exc}$ for $1 \text{ eV} < T_e < 10 \text{ eV}$ (threshold energy $E_{D,exc}^{0,3} \approx 12.1 \text{ eV}$).

Radiance data and emission from tomographic reconstruction for two strongly differing discharge scenarios are presented in figures 5.11 and 5.12. Considering the magnitude of emission in the strike point region of inner and outer divertor target, ε_{D_α} for the high density H-mode discharge #21372 is found to be about 400 times larger than for the low density ohmic discharge #22061. In table 5.1 a set of fundamental parameters is given.

The Deuterium flux density measured by ionisation gauges below the central divertor components $\Gamma_{D,Div}^G$ is a direct measure of plasma recycling at the targets. Differences in the core line averaged density, the gas feed flux and the divertor neutral flux clearly demonstrate the nonlinear relationship of midplane edge and SOL plasma parameters on the one hand and the divertor parameters on the other hand. In order to achieve a higher core density (factor > 4) the gas puff for density control has to be increased by more than a factor of 10. This is explained by the large

SOL density of #21372 (even if the ratio of separatrix to core density might be lower for H- than for L-mode; estimate for $n_{e,sep}$: $n_{e,sep}(\#21372) \approx 2.5 \cdot 10^{19} \text{ m}^{-3}$, $n_{e,sep}(\#22061) \approx 7 \cdot 10^{18} \text{ m}^{-3}$) which is the reason for neutrals being ionised predominantly in the SOL equivalent to reduced fuelling efficiency. Dominant SOL fuelling results in a large recycling flux and is expressed in the factor of ~ 50 when comparing $\Gamma_{D,Div}^G$ of both discharges.

shot	time / s	$\bar{n}_e / \text{m}^{-3}$	P_{heat} / MW	gas feed / Ds^{-1}	$\Gamma_{D,Div}^G / \text{m}^{-2}\text{s}^{-1}$	L-fact.
22061	~ 2.1	$2.1 \cdot 10^{19}$	0.9	$1.2 \cdot 10^{21}$	$5.5 \cdot 10^{21}$	0.6
21372	~ 2.8	$8.8 \cdot 10^{19}$	7.5	$1.5 \cdot 10^{22}$	$2.5 \cdot 10^{23}$	1.4

Table 5.1: Basic parameters for the discharges to which D_α data is shown in figures 5.11 and 5.12. The flux density of neutrals in the divertor region $\Gamma_{D,Div}^G$ is one of the key parameters together with the data of plasma parameters presented in figures 5.13 and 5.14 to explain the large differences in the magnitude of ε_{D_α} . The data sets are representative for quasi steady state phases of the discharges and the Langmuir probe data is collected accordingly.

The aspect of neutral density in the divertor region marks one factor of the triple product of (5.2, excitation part) and it remains to specify n_e and T_e to determine ε_{D_α} . Direct measurements of plasma parameters in the divertor are routinely available only from Langmuir probes located at the target plates. These deliver parameters of the sheath entrance in front of the probes and might be interpreted as representative for the plasma in the divertor volume some distance along the magnetic field if the plasma is attached. In case of detachment, strong neutral plasma interaction leads to a partial shielding of the plasma flow to the targets and the probes at the surface of the plasma facing components merely recognise the remaining plasma which reaches the wall. Except for the attached regime it is difficult to obtain information on plasma parameters in the divertor volume, eg by probes mounted on reciprocating manipulators.

Profiles of n_e and T_e at the target plates deduced from the standard Langmuir probe diagnostics for both discharges are presented in figures 5.13 and 5.14. Since the probes are spatially fixed, strike point sweeps are performed to obtain target profiles of higher resolution than the number of probes. This procedure presumes that all major parameters are largely independent of the position of the plasma column in a small range of R - and z -shift.

The low density ohmic discharge #22061 displays an example for an attached divertor plasma. Although the ohmic heating power is rather low, plasma and neutral density in the SOL are too low to create significant parallel gradients of density and temperature. Low collisionality and neutral friction result in an effective transport of power from the core boundary to the divertor target. The acceleration of plasma to sonic speed at the sheath entrance results in the reduction of density to about half the value at the midplane separatrix. A very high electron temperature is observed at the target. The reduction of the peak value to about 50% compared to the midplane separatrix is partly due to the conversion of static to dynamic pressure and probably also influenced by low volumetric losses. These divertor parameters are predominantly generated by the properties of the sheath in front of the target and the state is called sheath-limited regime [45]. This example is very close to the ideal case of a isothermal SOL plasma. Transport in the SOL seems to be constant in time which is expressed by the distinct profile shape at the target with hardly any scatter of data points.

A different picture is obtained for the divertor state of high density H-mode #21372. The high neutral density in the divertor (high recycling) cools the incoming plasma from the core region

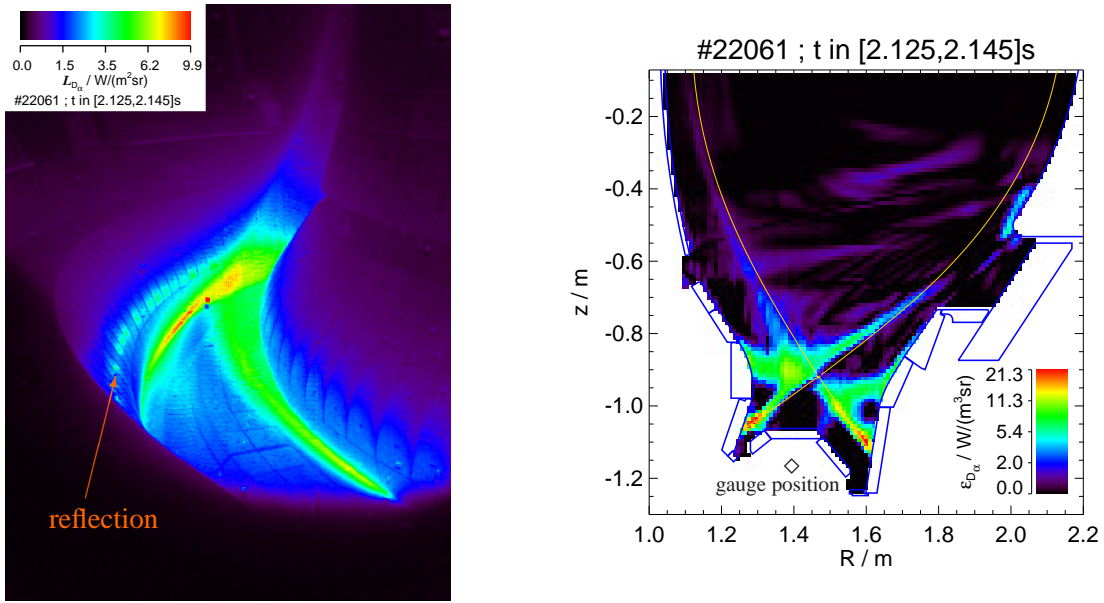


Figure 5.11: $L_{D\alpha}$ and $\epsilon_{D\alpha}$ deduced from one XPMC divertor view exposure of low density ohmic discharge #22061. The divertor state is found to be attached which is expressed in the localised emission at the strike points (see also target parameters of fig. 5.13). The impact of reflection is indicated by the pattern at the LFS tile surface on the $L_{D\alpha}$ -image and results in artefacts of the tomographic reconstruction in the form of apparent emission regions above the strike points. Emission at the target is similar for LFS and HFS.

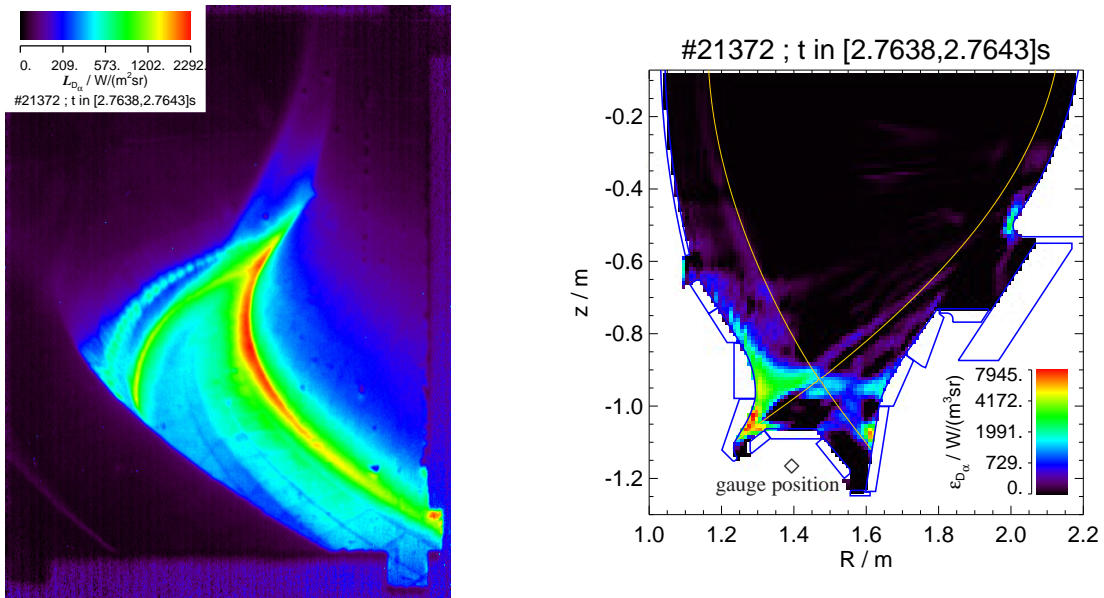


Figure 5.12: $L_{D\alpha}$ and $\epsilon_{D\alpha}$ deduced from one XPMC divertor view exposure of high density H-mode discharge #21372. High neutral density is suspected to result in partial detachment at the targets, eg at the LFS the maximum plasma flux is found above the strike point. An alternative explanation is the action of a strong $\vec{E} \times \vec{B}$ -drift pointing towards the LFS. At the LFS the zone of maximum emission is displaced with respect to the strike point position due to the shifted n_e - and T_e -profiles (see fig. 5.14). The emission pattern at the HFS is much larger and more intense which might be attributed to the action of drift mechanisms resulting in an increased plasma density in the HFS SOL, ie the commonly observed in/out asymmetry in plasma fluxes to the targets.

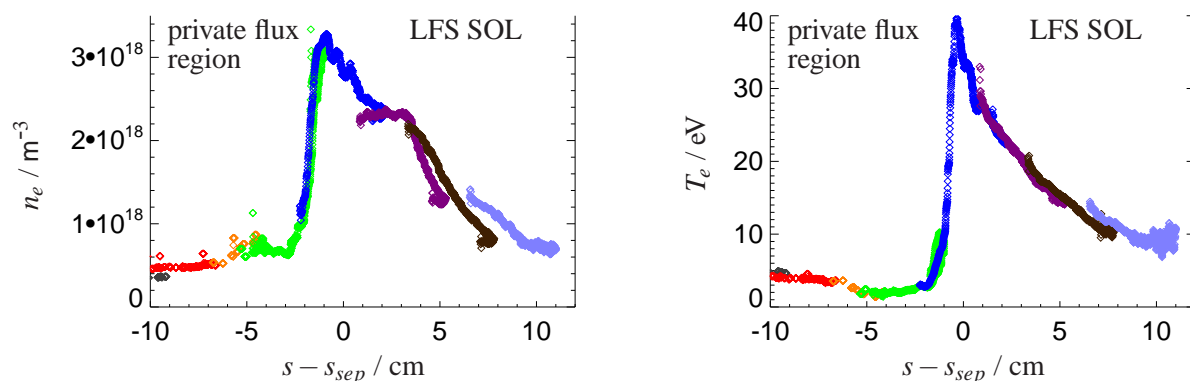


Figure 5.13: Profiles of n_e and T_e obtained from 8 Langmuir probes mounted in the LFS target plate during a strike point sweep for the low density ohmic discharge #22061. Low scatter of data points indicate a steady plasma flow to the divertor. Peak density similar to the midplane separatrix value and high T_e indicate the attached divertor state. The s -coordinate describes the position on the contour line of plasma facing components from bottom to top.

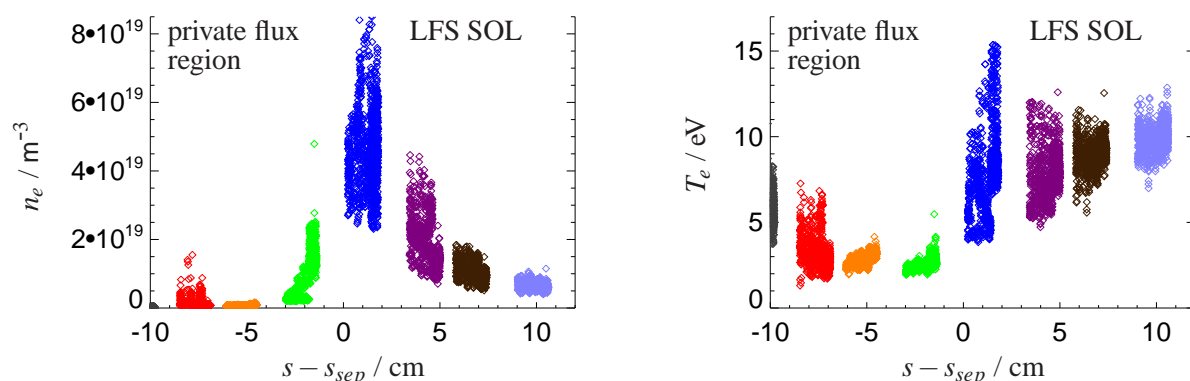


Figure 5.14: Profiles of n_e and T_e obtained from 8 Langmuir probes mounted in the LFS target plate during a strike point sweep (smaller Δs -range than for #22061) for high density H-mode discharge #21372. A large scatter of data points is observed which displays the fluctuations in the SOL plasma flow induced by ELM-activity. Compared to density and temperature at the midplane separatrix there is a significant change of plasma parameters. Neutral-plasma interaction in a high-recycling regime (large density, low temperature) causes gradients along the magnetic field. The s -coordinate describes the position on the contour line of plasma facing components from bottom to top.

by ionisation and excitation and charge exchange reactions are a mechanism of interception (parallel field momentum loss) of the plasma flow leading to a larger radial spread. As a consequence, target temperature profiles are strongly reduced and density is increased in amplitude compared to the values at the midplane separatrix and in the upstream SOL. The large scatter in the data due to modulated core losses to the SOL makes it difficult to deduce precise numbers eg for the ratio of upstream and downstream plasma pressure.

In summary, the huge difference in ϵ_{D_α} in the strike point region of the two discharges is motivated as follows. $\Gamma_{D,Div}^G$ and n_e are larger for #21372 by factors of about 50 and 15 respectively. Low density and high temperature of #22061 are the basis of a higher $\mathcal{P}EC_{D_\alpha,exc}$, due to the larger impact energy of reactants and reduced contribution of collisional deexcitation. A factor of about 0.1-0.2 might be reasonable for the ratio of the different divertor plasmas. This very simple es-

timation already gives a factor for emission in the order of 10^2 . For detailed comparison in the divertor volume, knowledge of the plasma parameters at each location is required but cannot be delivered by the diagnostics instrumentation.

5.2.2 Comparison of L- and H-mode Regimes at Medium Density

With data from the XPMC diagnostics basic features of the SOL and divertor can be deduced for different confinement regimes. The medium density discharges #21347 (*L*) and #21402 (*H*) (tab. 5.2) are examined with the ray-tracing-fit interpreted by KN1D and the tomographic reconstruction for the divertor. Data is taken from steady state phases and for the H-mode an inter-ELM phase has been selected. Parameters for the LFS are inferred from the main chamber view at time slices equivalent to the exposure of the divertor camera.

shot	time / s	\bar{n}_e / m^{-3}	P_{heat} / MW	L-fact.	$\Gamma_{D,Div}^G$ /	$\Gamma_{D,mp}^G$ /	$\Gamma_{D,lhs}^G$ /
					$\text{m}^{-2}\text{s}^{-1}$		
21347	~ 2.3	$4.8 \cdot 10^{19}$	1.9	1.15	$7.5 \cdot 10^{22}$	$1 \cdot 10^{22}$	$1.4 \cdot 10^{22}$
21402	~ 3.3	$6 \cdot 10^{19}$	3	1.9	$2 \cdot 10^{22}$	$5 \cdot 10^{20}$	$3 \cdot 10^{21}$

Table 5.2: Basic parameters of the discharges #21347 (L-mode) and #21402 (H-mode). Subscripts for flux densities are *Div*: divertor, *mp*: midplane and *lhs*: lower heat shield.

In figure 5.15 $\varepsilon_{D\alpha}$ -profiles from the analysis of the LFS-ROI are presented. The profile of $D\alpha$ emission in the L-mode case is larger in amplitude by about a factor of 3.5 and is radially more displaced towards the far SOL than observed for the H-mode case. For interpretation of the L-mode profile the discussion of section 5.1.3 should be kept in mind - the broad profile of emission might be due to the impact of radially displaced plasma aggregations created by edge perturbation. All profile parameters then reflect effective values which result in an $\varepsilon_{D\alpha}$ -profile corresponding to the exposure time averaged one.

Various parameters from the 1D-simulation of neutral-plasma interaction are summarised in figures 5.16 and 5.17. Given a certain flux density of molecules at the vessel wall, the SOL plasma parameters of this L-mode case would lead to a very weak core fuelling because of the large ionisation rate in the SOL, much less efficient than obtained for the H-mode SOL. The flux density of molecules at the midplane is determined by perpendicular particle losses from the core plasma and from neutral leakage of the divertor volume. Considering the ratio of atomic neutral flux densities in the divertor (~ 3.8 , see table 5.2) and the ratio of molecular flux densities at the wall in the 1D-simulation (~ 5.8 , see figure 5.17) the large spatial SOL decay lengths of n_e and T_e of the L-mode case consistently correspond to a strong perpendicular particle transport and a higher level of divertor neutral confinement.

The atomic neutral flux density at the midplane vessel wall is measured by an ionisation gauge (#21402: $\Gamma_{D,mp}^G \approx 5 \cdot 10^{20} \text{m}^{-2}\text{s}^{-1}$) which can be compared to the corresponding flux density of neutrals at the grid boundary of the simulation ($\Gamma_{D_{eq},wall} \equiv 2 \cdot \Gamma_{D_2,wall}$, #21402: $\Gamma_{D_{eq},wall} = 1.2 \cdot 10^{21} \text{m}^{-2}\text{s}^{-1}$). A difference of a factor of ~ 2.4 is obtained for the value deduced from the $\varepsilon_{D\alpha}$ -profile. Two aspects need to be considered in order to judge this deviation. Firstly, the grid boundary set for the KN1D code is somewhat arbitrarily fixed, 10cm in front of the edge of the limiter shadow and 20cm away from the separatrix position. The larger the distance

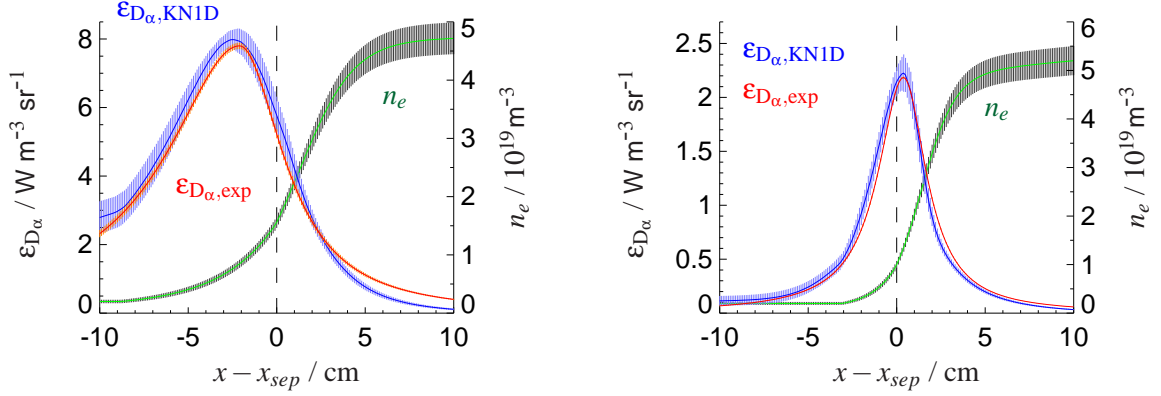


Figure 5.15: Profiles of ϵ_{D_α} and n_e for the LFS-ROI from the discharges #21347 (L, left) and #21402 (H, right). A good match of experimental and simulated emission profiles is achieved by adjusting the molecular flux density at the grid boundary Γ_{D_2} and SOL decay lengths of plasma parameters if not sufficiently determined by edge diagnostics. The obvious difference in the two scenarios is the magnitude, width and radial position of the ϵ_{D_α} -profiles.

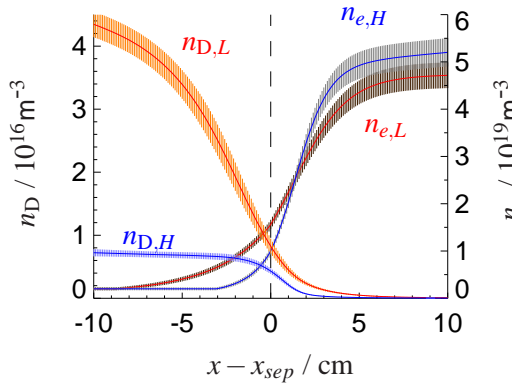


Figure 5.16: Comparison of atomic neutral and electron density profiles at the LFS for the discharges #21347 (L) and #21402 (H). In the far SOL $n_{D,L}$ is about 5 times larger than $n_{D,H}$ which reflects the difference in plasma recycling. The more dense SOL plasma in the L-mode case leads to an increased ionisation rate.

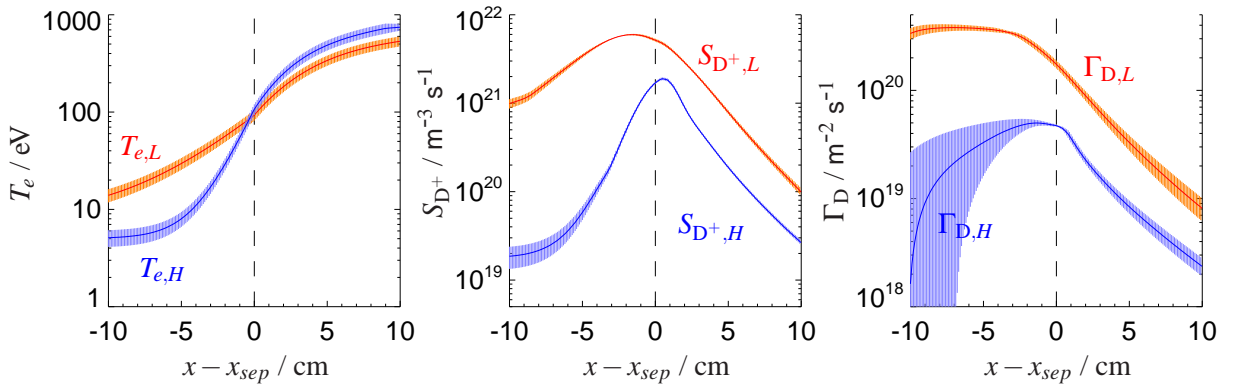


Figure 5.17: Comparison of electron temperature, ion source and atomic neutral flux density profiles at the LFS for the discharges #21347 (L) and #21402 (H). The SOL plasma is considerably more dense and hotter in the L-mode case and the ion source is sparsely distributed in the SOL and edge region, while in the H-mode case neutrals can penetrate to the separatrix more efficiently. The large D_α -emission in this L-mode scenario is established by a large flux density of molecules at the grid boundary (\equiv vessel wall) about 5.8 times the value of the H-mode ($\Gamma_{D_2, \text{wall}, L} = 3.5 \cdot 10^{21} \text{m}^{-2} \text{s}^{-1}$, $\Gamma_{D_2, \text{wall}, H} = 6 \cdot 10^{20} \text{m}^{-2} \text{s}^{-1}$). The different penetration of molecules in the SOL is expressed in the shape of the profiles for Γ_D .

of vessel wall and edge of the limiter shadow and the higher the plasma parameters in this region, which is not covered by diagnostics, the larger the molecular flux density at the wall to achieve the magnitude of atomic neutral flux density and accompanied profile of D_α emission. Secondly, the LFS-ROI is about 0.5 m below the midplane and neutrals from divertor leakage are ionised in upstream locations such that an exponential decay of neutral density from bottom to top of the plasma vessel is established. Assuming plasma parameters in the limiter shadow to be extremely low ($n_e < 10^{18} \text{ m}^{-3}$, $T_e < 5 \text{ eV}$), the latter aspect is more relevant and the value obtained for $\Gamma_{D_2, \text{wall}}$ seems to be reasonable in principle. For #21347 one finds the situation of $\Gamma_{D, \text{mp}}^G \approx 1 \cdot 10^{22} \text{ m}^{-2} \text{ s}^{-1}$ and $\Gamma_{D_{eq}, \text{wall}} \approx 7 \cdot 10^{21} \text{ m}^{-2} \text{ s}^{-1}$, opposite to the relationship of #21402. If as argued above the divertor leakage is less pronounced, then one would have to suppose larger plasma parameters in the limiter shadow to explain the deviation. Both examples show that the determination of neutral parameters in the far SOL and at the vessel wall is not straight forward and data from a few gauges placed in different segments of the torus may serve as a guideline.

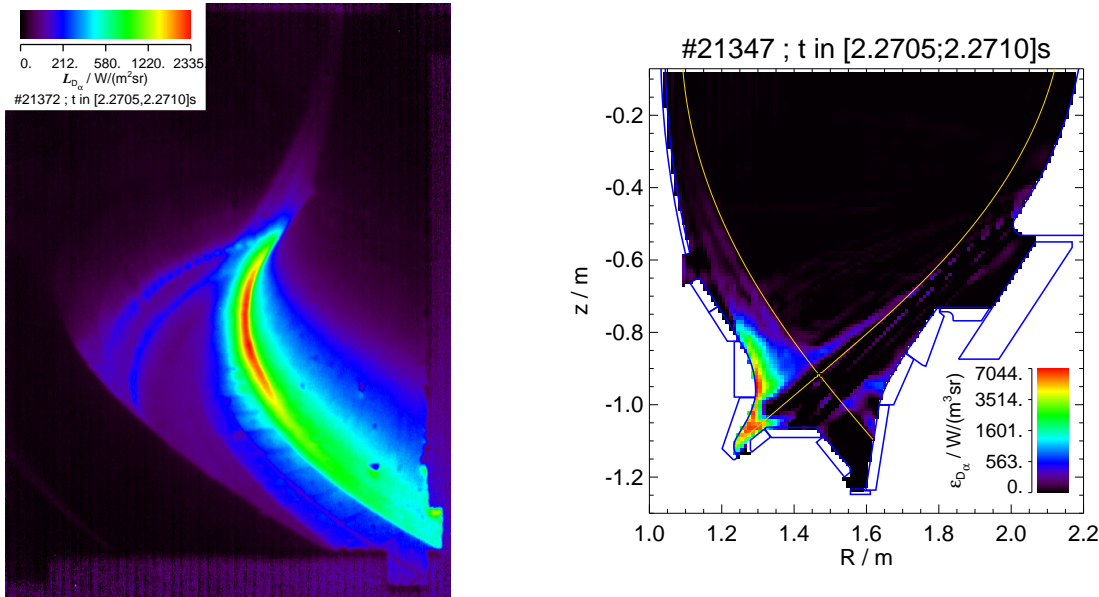


Figure 5.18: L_{D_α} and ϵ_{D_α} deduced from one XPMC divertor view exposure of medium density L-mode discharge #21347. Emission at the HFS dominates the data sets. In the tomographic reconstruction, the outer strike point is resolved in similar amplitude as the level of artefacts. The region of reflection at the LFS appears as bright as the outer strike line which indicates that the origin of the reflected signal is the HFS emission pattern. A remarkable feature is recognised at the HFS above the target where two separate sheaths of ϵ_{D_α} are present. The one close to the separatrix displays the excitation before ionisation at the plasma edge, while the second sheath closer to the wall might be recombination which could explain the spatial separation, but on the other hand requires a very low electron temperature.

Images of the divertor view and corresponding 2D emission profiles from tomographic reconstruction for the selected time slices of both discharges are presented in figures 5.18 and 5.19. Concerning the difference in the magnitude of ϵ_{D_α} , arguments like mentioned in section 5.2.1 apply. While the pattern at the LFS strike point seems to be similar in character, as far as the quality of the reconstruction allows to suggest, the situation at the HFS is quite different. For the inner target of #21402 the assumption of ionising conditions seems appropriate, since the emission is rather localised. The large volume of ϵ_{D_α} at the HFS wall in the case of #21347 and in particular the separate sheath of emission in the HFS SOL closer to the wall above the target area could be

indications for a recombining plasma. For the latter to be reasonable, high plasma density and low electron temperature are required of which parameters unfortunately are not available from diagnostics in the volume of the HFS SOL.

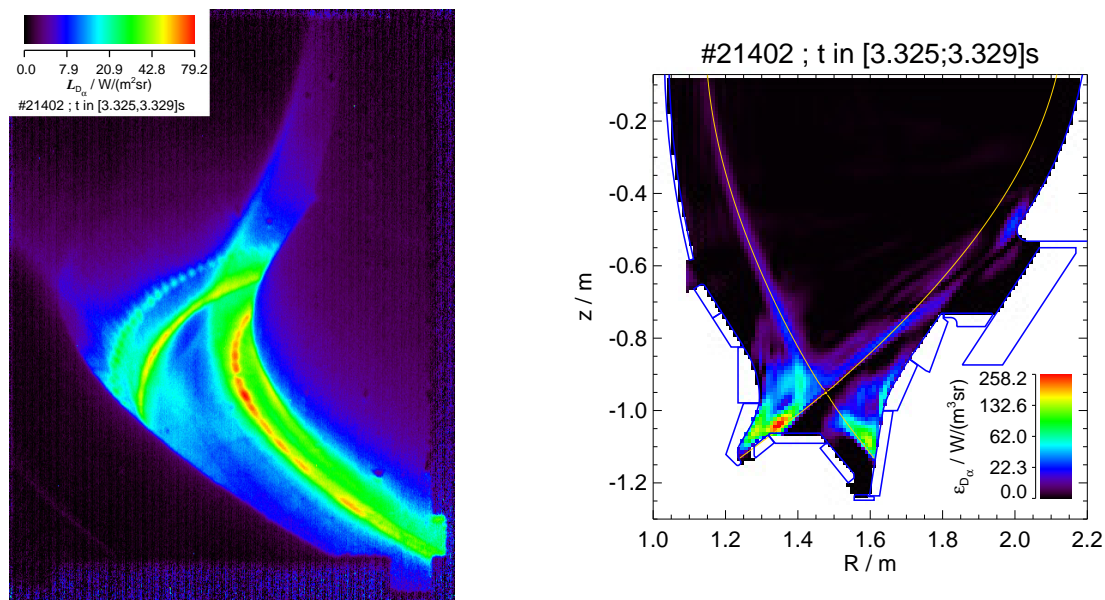


Figure 5.19: L_{D_α} and ϵ_{D_α} deduced from one XPMC divertor view exposure of medium density H-mode discharge #21402. This plasma equilibrium has its inner strike line on the central divertor components rather than the inner target plate. The fact, that the position of the inner strike zone is properly resolved in the reconstruction, supports the method for the verification of the viewing geometry. The localised emission patterns at the strike zones indicate ionising divertor conditions and the slight asymmetry is probably based on a higher electron density at the HFS or a larger recycling plasma flux onto the inner strike area. Good contrast is obtained for the L_{D_α} image in front of the heatshield such that the ray-tracing-fit can be applied.

The emission sheath of high contrast in front of the heatshield for #21402 allows to apply the ray-tracing-fit and to compare plasma fuelling at the HFS and LFS. Molecular flux density at the vessel wall and atomic neutral flux density at the separatrix are depicted in figure 5.20. With the experimental coverage of the separatrix contour it is hard to estimate the total fuelling rate of the core plasma, but from the emission patterns observed, it seems reasonable to claim that the dominant part of core fuelling is positioned at the HFS close to the divertor region which is the main source of neutral particles from plasma recycling. Because of the different wall structures and distances of wall and plasma edge, the comparison of atomic neutral flux density at the separatrix is more useful than the molecular counterparts at the wall. In this case the core fuelling is lower at the LFS than at the HFS for comparable p_{sc} -value including the ratio of the major radii at the relevant positions. This finding is surprising when comparing the molecular flux density which is higher at the LFS wall. However, the width of the (simulated) SOL is larger at the LFS and this aspect has a stronger impact on neutral penetration than the different spatial gradient lengths of plasma parameters due to the magnetic flux expansion (smaller gradient lengths at LFS). Generally, the range of neutral penetration from the divertor region towards the midplane depends on the parameters in the SOL which neutrals need to pass and the gap between the wall and the core plasma. Thus, different radial plasma positioning is likely to result in changes in the ratio of HFS and LFS fuelling (see section 5.2.4).

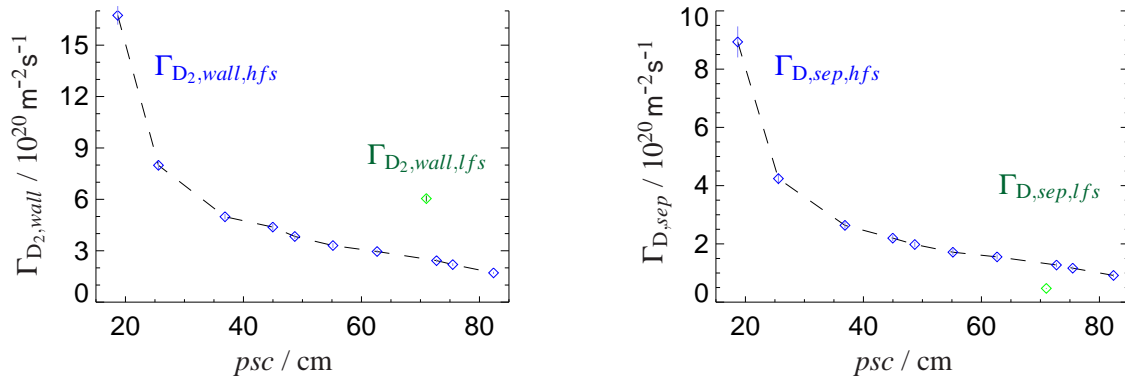


Figure 5.20: Flux densities of molecules at the vessel wall and atomic neutrals at the separatrix obtained from the KN1D-interpretation of the ray-tracing-fit $\varepsilon_{D\alpha}$ -profiles of #21402. The strong decay with increasing psc confirms the divertor as the dominant source of neutrals in the HFS SOL. The psc -coordinate represents the distance between the intersection of the KN1D grid line and the separatrix and the X-point position along the last closed flux surface in the poloidal plane.

As was done for the LFS, the flux density of molecules at the wall might be verified against gauge measurements. The position of the ionisation gauge to deliver $\Gamma_{D,lhs}^G$ is located behind the lower heatshield, corresponding to a psc -value of about $psc_{gauge,lhs} \approx 50 \text{ cm}$. While the agreement of flux densities at the LFS is promising, the situation at the HFS is more difficult. Concerning the factor of 2 for the equivalent atomic neutral flux density at the wall, a mismatch in the order of a factor of 5 is observed, indicating the value deduced from $\varepsilon_{D\alpha}$ being too low. The reason for this discrepancy is not clear. An elevation of estimated plasma parameters in the far SOL, sufficiently large to ionise molecules (reaction 2.R1 of section 2.3.1) but low enough not to create a large excitation rate of atomic neutrals would require a larger flux density of molecules at the wall to achieve the same emission profile at the plasma edge. Another aspect to consider is the simplified slab model of KN1D which does not account for a plasma flow perpendicular to the 1D grid. Elastic collisions among the plasma ions flowing towards the divertor and neutrals might result in an increased flow of neutrals in the same direction. Thus, a higher flux of neutrals starting at the vessel wall would be required to result in a certain emission profile than without this perpendicular displacement.

5.2.3 Recognition of Regime Change in L-mode Confinement

The low density L-mode discharge #21418 has been performed in the framework of core turbulence studies. Turbulent transport of heat and particles may be driven by various modes, eg trapped electron mode (TEM), electron temperature gradient mode (ETG) or ion temperature gradient mode (ITG) [76]. The electron cyclotron resonance heating (ECRH) allows to dominantly heat electrons and to accurately configure plasma conditions of different temperatures in the electron and ion channels. This type of plasma control was used for #21418 to investigate the transition of regimes characterised by the ITG and TEM instabilities respectively [77]. A different level of ECRH-power and presumably accompanied change in core turbulence was found also to lead to different confinement properties at the plasma edge. This situation of variation of edge and SOL parameters during one discharge is very useful to assess the sensitivity of the video diagnostics based analysis of $\varepsilon_{D\alpha}$. It should be emphasised that for the discussion of parameters in particular at the LFS, the remarks about the accuracy of magnetic equilibrium

reconstruction are highly relevant. Parts of the results presented are based on the assumption that the uncertainty in the radial position of the LFS separatrix is below 5 mm (± 2.5 mm). Furthermore, the existence of a significant perturbation of the plasma edge is excluded and the absence of fluctuation in divertor D_α might be taken as to support this (see section 5.1.3).

Two time slices of the discharge are analysed regarding radiance data of the main chamber and divertor views. For the LFS, ϵ_{D_α} profile parameters are time averaged to reflect the scatter of the ray-tracing-fit results, whereas for tomographic reconstruction single exposures are considered. Some basic parameters of the discharge for the relevant time intervals are collected in table 5.3. The difference in confinement properties is notably recognised in the relationship of heating power P_{heat} and stored energy W_{MHD} : for an increase in P_{heat} of $\sim 20\%$, W_{MHD} is raised by $\sim 45\%$.

shot	time / s	$\bar{n}_e /$ m^{-3}	$P_{heat} /$ KW	$W_{MHD} /$ KJ	L-fact.	$\Gamma_{D,Div}^G /$	$\Gamma_{D,lhs}^G /$ $m^{-2}s^{-1}$	$\Gamma_{D,mp}^G /$
21418	~ 2.3	$3.4 \cdot 10^{19}$	700	130	1.3	$1.4 \cdot 10^{22}$	$3.5 \cdot 10^{21}$	/*
21418	~ 3.4	$3.65 \cdot 10^{19}$	850	190	1.8	$1.2 \cdot 10^{22}$	$2.7 \cdot 10^{21}$	/*

Table 5.3: Basic parameters of the low density L-mode discharge #21418 for two time slices of interest. The important measurement of $\Gamma_{D,mp}^G$ (/*) unfortunately has to be discarded, because the position of the gauge coincides with the location of the gas feed valve and thus gives a measure of active fuelling rather than intrinsic recycling.

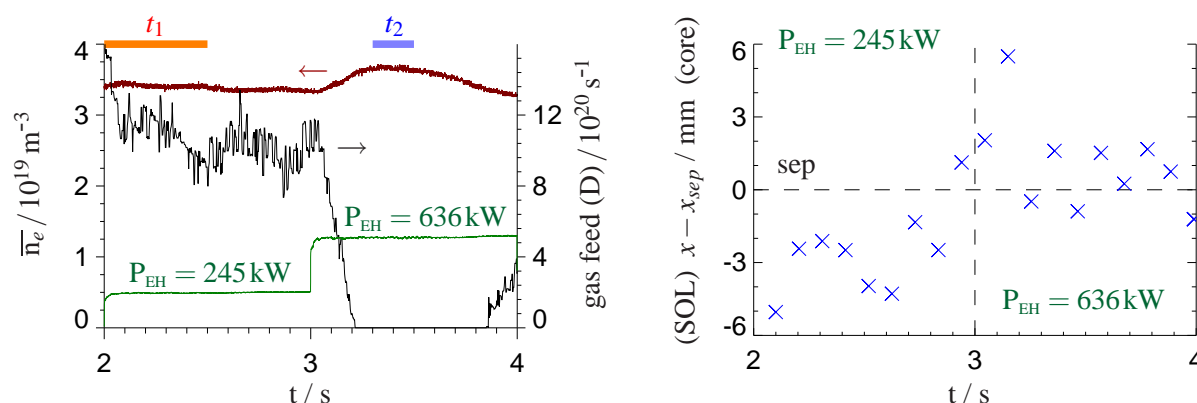


Figure 5.21: Left: Time traces of midplane line averaged density and gas feed flux related to the level of ECRH power. The gas valve is switched off at the onset of density rise imposed by the change of confinement properties due to enhanced electron heating. As with increasing electron temperature the resistivity of the plasma decreases, and the total plasma current being a control parameter, the ohmic heating power is reduced accordingly: $t < 3$ s, $P_{OH} : P_{EH} \approx 2 : 1$; $t > 3$ s, $P_{OH} : P_{EH} \approx 1 : 3$. For the time intervals t_1 and t_2 steady state conditions are assumed in order to use time averaged profile parameters. Right: Center position of the ray-tracing-fit for ϵ_{D_α} at the LFS. Due to the large number of grid points and the small number of fit-parameters, no significant error estimate is returned from the simple χ^2 -minimisation procedure. Even when taking the scatter into consideration, a significant difference in the radial separation of the ϵ_{D_α} profile center with respect to the last closed flux surface is observed for the two confinement regimes. The data point just before $t = 3$ s which is already shifted towards the core plasma is believed to display a misleading coincidence.

Time traces of midplane line averaged density, gas feed and level of ECRH are displayed in

figure 5.21 to motivate the time intervals chosen. Starting with the switching of additional ECRH power at $t = 3$ s, the density is seen to increase. Since the discharge is feedback controlled on density, the gas feed is stopped at recognition of the positive slope. Keeping in mind that the torus pumping system (cryo pump) is permanently active, the time interval $t \in [3, 3.5]$ s might be regarded as a period of enhanced particle pinch in which losses are surpassed by source terms. From about $t = 3.5$ s density drops, because the total particle inventory of the plasma vessel is reduced by pumping, while a steady state of confinement has been reached. However, the action of an inward pinch is probably not required and the situation might be explained by reduced transport coefficients at the edge and the density rise would be based on the particles in the SOL which recycle several times at the vessel wall before being pumped out. If the radial decay length of plasma pressure are reduced, then the fuelling efficiency is increased and neutral particles may enter the core region instead of being ionised in the SOL. The residence time of particles in the vessel would have to be known if to decide upon the impact of the two arguments.

The important observation of the XPMC diagnostics in this discharge is the change of shape and position of the ϵ_{D_α} profiles following the ECRH power level. Although the shift in radial position is small and the resolution of the main chamber view is not optimised, a consistent picture including all plasma parameters is obtained, even if ϵ_{D_α} -profile parameters are time averaged for intervals t_1 and t_2 . With the density profiles available from edge diagnostics, the T_e profile remains to be specified. For the more narrow ϵ_{D_α} -profile during t_2 (less excitation in the far SOL) also a shorter decay length of T_e is required which is believed to be compatible with the reduced parameters for particle transport (increased density gradient). The situation at the LFS is represented by figure 5.22.

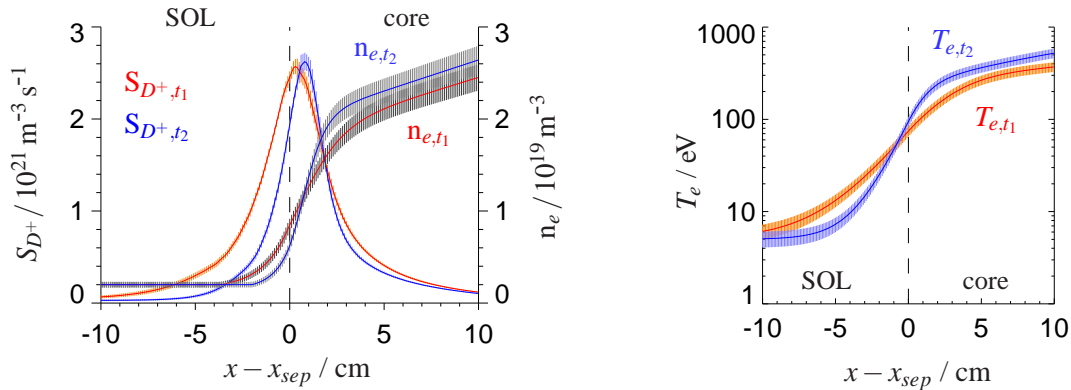


Figure 5.22: Left: Ion source and electron density profiles at the LFS for the two time intervals t_1 and t_2 . The core fuelling during t_2 is more efficient since fewer neutrals are ionised in the SOL and the peak source lies inside the core region. Right: A good match of experimental and KN1D ϵ_{D_α} profiles (not shown) is achieved by adjusting SOL decay lengths of electron temperature appropriately while the electron density profile is obtained from diagnostics. T_e in the SOL is the key parameter to influence the width of the ϵ_{D_α} profile.

Radiance data and reconstructed emission profiles of the two time slices are shown in figures 5.23 and 5.24. Results for the HFS-ROI which allows the analysis of a larger p_{sc} -interval are presented in figures 5.25 and 5.26. Taking the limitations of analysis imposed by the estimation of SOL parameters and the ROI-sizes into consideration, the lower part of the HFS above the X-point region is found to be the main location of core fuelling. The tomographic reconstructions reveal that there is no dedicated X-point fuelling, eg by penetration of neutrals from the private flux region - keeping in mind that the emission pattern around the X-point is distorted by an artefact.

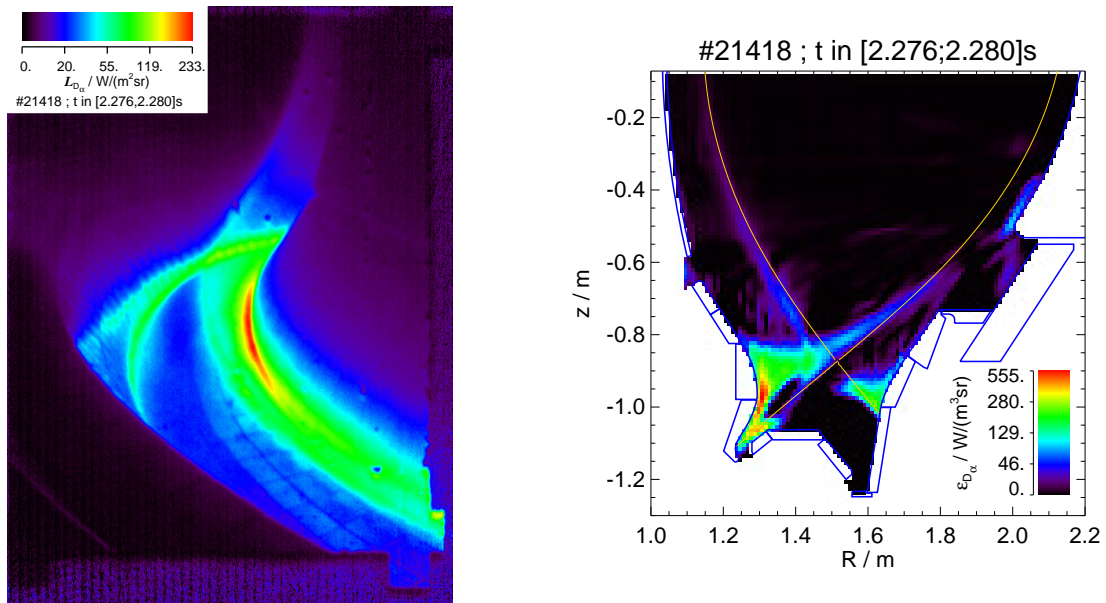


Figure 5.23: L_{D_α} and ϵ_{D_α} deduced from one XPMC divertor view exposure of low density L-mode discharge #21418 during time interval t_1 . Compared to the data of t_2 (figure 5.24) the maximum of emission is positioned at the HFS wall above the strike zone. It is assumed that this pattern is created by a rather high recycling flux and a broader particle and heat deposition profile at the inner target than for t_2 .

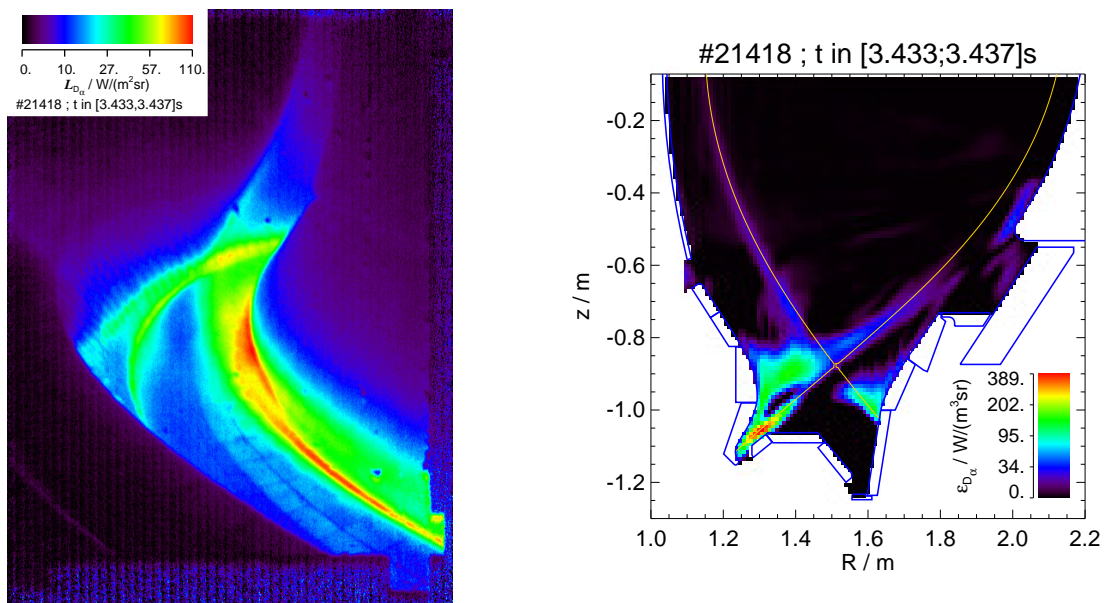


Figure 5.24: L_{D_α} and ϵ_{D_α} deduced from one XPMC divertor view exposure of low density L-mode discharge #21418 during time interval t_2 (according to the L-factor of this time interval one might also use the term H-mode phase). The emission pattern at the HFS is observed being decreased in amplitude and the peak emission placed at the strike point. Assuming fluxes of heat and particles to be lower (see eg gauge data) and the radial SOL decay lengths to be shorter, a more localised emission would result, while the region above the strike area might appear less bright.

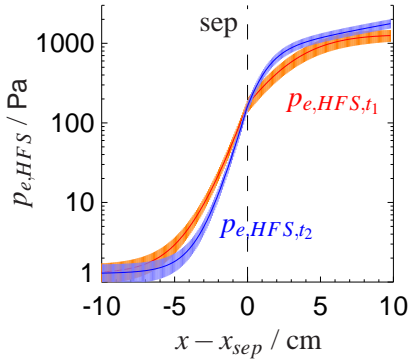


Figure 5.25: For the interpretation of $\varepsilon_{D\alpha}$ at the HFS, SOL decay lengths of both n_e and T_e have to be estimated. Since these have a similar impact on the shape of the emission profile and the values chosen cannot strictly be verified, it is more convenient to compare static electron pressure ($n_e \cdot T_e$). Data is presented from a p_{sc} -interval at the HFS corresponding to that valid for the LFS-ROI. The lower SOL pressure during interval t_2 allows a more efficient penetration towards the core plasma.

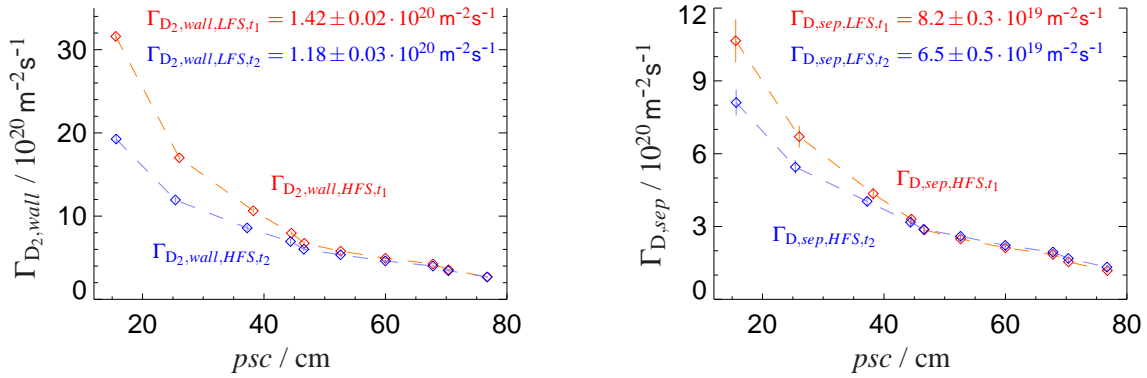


Figure 5.26: Flux densities of molecules at the vessel wall and atomic neutrals at the separatrix obtained from the KNID-interpretation of the ray-tracing-fit $\varepsilon_{D\alpha}$ -profiles of #21418 of time intervals t_1 and t_2 . The appearance of Γ_{D,sep,HFS,t_2} might indicate that more neutrals escape the divertor region (lower flux density closer to X-point) and reach locations further upstream (comparable flux further upstream, although the total flux during t_2 is lower). With these values for HFS and LFS a rough estimate on the core fuelling rate $F_{D,core}$ can be constructed. Using linear interpolation for the HFS data and considering the local toroidal circumference (see figure 5.27) it is obtained $F_{D,core,HFS,t_1} \approx 2.1 \cdot 10^{21} \text{ s}^{-1}$ and $F_{D,core,HFS,t_2} \approx 1.8 \cdot 10^{21} \text{ s}^{-1}$ for the limited p_{sc} -interval. The treatment for the LFS is more difficult, since only one data point is available: using $2\pi R \approx 13 \text{ m}$ and $\Delta p_{sc} = 0.5 \text{ m}$ it is obtained $F_{D,core,LFS,t_1} \approx 5.3 \cdot 10^{20} \text{ s}^{-1}$ and $F_{D,core,LFS,t_2} \approx 4.2 \cdot 10^{20} \text{ s}^{-1}$. These numbers obviously represent lower boundaries for the core fuelling rates, because a large part of the poloidal circumference is not covered, but nevertheless suggest the lower HFS being the most important fuelling location.

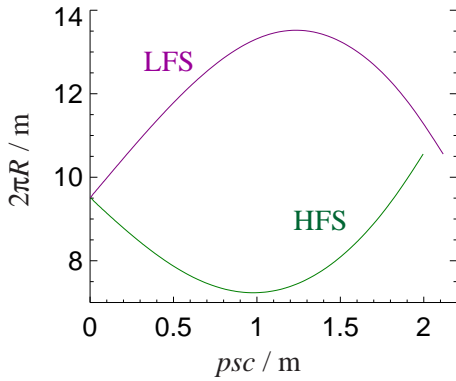


Figure 5.27: In order to calculate the actual fuelling rate F , the area at the last closed flux surface needs to be considered. Here, the toroidal circumference is given as a function of the p_{sc} -coordinate. A simple approximation is thus $F(p_{sc}, \Delta p_{sc}) \approx \Gamma(p_{sc}) \cdot \Delta p_{sc} \cdot 2\pi R(p_{sc})$. For comparison of flux densities at LFS and HFS the ratio of circumferences at specific locations has to be included.

Assuming the gauge positioned behind the lower heatshield to be properly calibrated, the level of agreement with respect to the equivalent atomic neutral flux density at the wall ($2 \cdot \Gamma_{D_2,wall}$) is moderate. At similar vertical position a discrepancy of a factor of about 3 is

observed. Changes in the SOL parameters which only marginally influence the emission profile to be compatible with the camera data and the simplification of the 1D treatment (radial penetration) for the torus shaped plasma chamber are found to only have a rather small impact on $\Gamma_{D_2,wall}$ in the order of 10%. One suspect might be that the parallel ($\parallel \vec{B}$) plasma flow towards the divertor acts as to confine neutrals in the divertor region by radiationless reactions like elastic collisions or charge exchange reactions. Since such a preferential direction is not contained in the simplified KN1D geometry, less neutrals starting from the wall are required to produce a certain emission profile at the plasma edge. Although the neutral parameters in the far SOL might be underestimated, the comparison of experimental and simulated emission at the plasma edge is a strong support for the magnitude of neutral parameters in that region and the uncertainty is then determined by calibration issues of the imaging diagnostics (and the accuracy of atomic data in general). However, even when relating to the basic KN1D picture it is apparent that a large fraction of the initial neutral flux is lost by ionisation in the SOL ($\sim 75\%$) before the core plasma is reached.

The data presented is based on the assumption of toroidal symmetry. During the action of a localised gas valve at the LFS this aspect is not fulfilled. Comparing the results for flux density at the vessel wall and considering at least part of the surface area with the valve flux, feed rates of about $F_{D,feed} \approx 10^{21} \text{ s}^{-1}$ are obtained. Thus it seems not unlikely that LFS fuelling is to a large extent determined by active means, but this reasoning is restricted by the fact that the gas flux is found not to change strongly when the valve is switched off. As already mentioned above, particle recycling and the efficiency of the pumping system leads to a residence time in the vessel and the total particle inventory is a rather slowly varying parameter. The actual magnitude of this residence time is unknown, but might be deduced from the change of plasma density that occurs when an additional small gas puff is applied to a discharge which is run at fixed gas feed and pumping rate. The temporal width of the density excursion from the steady state level might be defined as the residence time. With the KN1D estimate for the HFS the active flux is seen to contribute about 10% to the total flux. This fraction is the upper bound and will be significantly reduced if the factor of ~ 3 for the HFS gauge comparison and the parts of the surface area not considered are accounted for in the estimation.

5.2.4 Impact of Geometry Parameters on HFS Fuelling

For the 2007 AUG experimental campaign, experience from previous operation had been regarded and the best image definition and calibration accuracy had been achieved. The diagnostics equipment had been installed only for a couple of experimental sessions (84 discharges) and the radiation damage of image guides could be limited to a low level. Comparing the results based on the different calibration procedures (see appendix B) for similar discharges of the campaigns 2006 and 2007, the cross calibration used for 2006 is found to be well suited. On the other hand, the formation of the AUG device to a full Tungsten machine imposes a limitation of the XPMC diagnostics to the divertor region, since the contrast on the LFS is too low due to the impact of dominantly reflected emission. Thus, a series of dedicated discharges performed to examine the influence of geometry parameters on the distribution of fuelling can be analysed only in terms of tomographic reconstruction and the ray-tracing-fit on the HFS-ROI of the divertor view. In the following, the observations on HFS fuelling are presented from four discharges, including different radial and vertical position of the plasma column and also varied magnetic configuration at the plasma edge. A short notation of plasma position is expressed in the parameters of R_{in} , R_{out} and z_{XPT} which describe the radially most inward and outward extension of the last closed flux surface and the vertical position of the primary X-point respectively.

The discharge control of #22091 was configured to result in a low density plasma which is radially positioned in two different locations. Further, two different confinement regimes are established by additional heating: one ohmic phase and a second phase of electron cyclotron resonance heating (ECRH) which appears to be of H-mode type. An impression of the temporal evolution of control parameters (R_{out} , P_{ECRH}) can be gained from figure 5.35. In total, four different scenarios are obtained to which the basic parameters are summarised in table 5.4. Although the electron density is one of the control parameters, the density cannot strictly be forced to a certain level in an arbitrarily short time interval, since the complex interaction of particle confinement, plasma recycling, neutral gas puffing and pumping imposes a reaction time of the system. This is the reason for slightly different densities encountered.

shot	time / s	\bar{n}_e / m^{-3}	P_{heat} / MW	L-fact.	R_{out} / R_{in} / m	$\Gamma_{D,Div}^G$ / $\Gamma_{D,lhs}^G$ / $\text{m}^{-2}\text{s}^{-1}$
22091	$\sim 1.37 (t_1)$	$2.54 \cdot 10^{19}$	0.63	0.9	2.14 1.12	$6.25 \cdot 10^{21}$ $7 \cdot 10^{20}$
22091	$\sim 2.22 (t_2)$	$2.49 \cdot 10^{19}$	0.49	1.0	2.10 1.09	$4.65 \cdot 10^{21}$ $5 \cdot 10^{20}$
22091	$\sim 2.81 (t_3)$	$2.80 \cdot 10^{19}$	1.99	1.4	2.10 1.10	$6.70 \cdot 10^{21}$ $1.34 \cdot 10^{21}$
22091	$\sim 4.00 (t_4)$	$2.70 \cdot 10^{19}$	2.21	1.3	2.14 1.14	$8.11 \cdot 10^{21}$ $1.76 \cdot 10^{21}$

Table 5.4: Basic parameters of discharge #22091 for four time slices (the exact time intervals are given in figures 5.28 and 5.29). The radial position is defined by the control parameter R_{out} (two settings for (t_1, t_4) and (t_2, t_3)). Note that R_{in} does not tightly follow the R_{out} -shift, because of the reaction of the plasma cross section on the changes in the configuration of the control coils, which is not optimised for maintaining the cross section exactly. Two different confinement regimes are established by ohmic heating only (t_1, t_2) and ECRH (t_3, t_4): L- and H-mode phases.

Figure 5.28 presents the results of tomographic reconstruction of divertor view radiance data for the two ohmic time slices (t_1, t_2) of #22091 at the different radial positions of the plasma column.

At a first glance, both profiles are practically identical according to the resolution and the level of artefacts of each reconstruction. Merely, the inner strike zone appears slightly brighter in ϵ_{D_α} for t_1 than for t_2 . This situation is likely to be based on the reduced neutral flux density at the HFS and divertor ($\Gamma_{D,HS}^G, \Gamma_{D,Div}^G$) and the reduced heating power for t_2 (lower temperature at the target). The more detailed analysis of the HFS-ROI data confirms that the recycling flux is larger for t_1 than for t_2 (figure 5.30). The difference in plasma density is very small and the level of ohmic heating power is not believed to cause a significant change in particle confinement. Presumed that the particle losses of core to SOL are very similar for t_1 and t_2 , it seems that the reduced gap between plasma column and heatshield for t_2 changes the recycling pattern at the HFS. More particles recycle at the upper part of the heatshield outside the visual range and less are transported to the lower part and finally to the inner divertor. Surprisingly, $\Gamma_{D,sep}$ is similar for t_1 and t_2 in locations further upstream which - corresponding to the lower recycling flux in the inner divertor for t_2 as the source - might be based on slightly reduced plasma pressure in the HFS SOL such that neutrals can penetrate towards upper positions more efficiently, which would be consistent with the assumption of enhanced plasma-wall interaction at the upper part of the heatshield. Calculating the corresponding core fuelling rate at the lower heatshield, a reduction of $\sim 25\%$ is observed when shifting the inner plasma surface ~ 3 cm towards the center column. It should be noted that both radial positions are still regarded as displaying a large plasma-wall gap when compared to standard configurations.

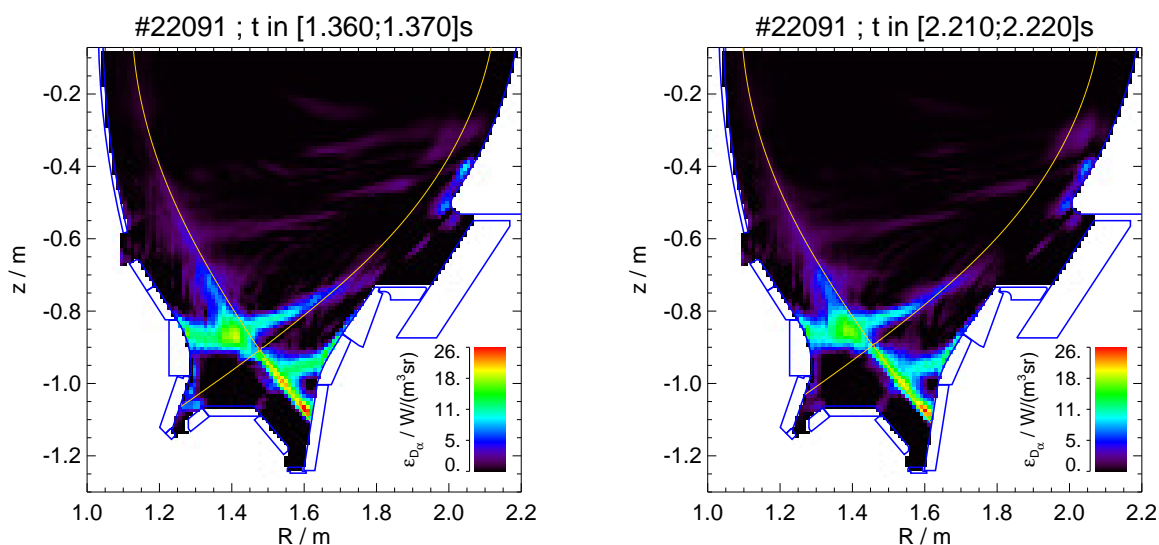


Figure 5.28: 2D profiles of ϵ_{D_α} from tomographic reconstruction of divertor view radiance data of discharge #22091 for the two ohmic time slices (t_1, t_2). Beside the different radial position of the plasma column the profiles seem to be identical. A closer look on the inner strike zone reveals a stronger emission in this region for t_1 which is related to the higher recycling flux indicated by the gauge measurements and probably also to an elevated target temperature due to an increased ohmic heating power.

Time slices t_3 and t_4 are taken from the phase of strong ECRH (~ 2 MW) which enhances the quality of particle confinement and according to the higher L-factor this time interval might be identified as an H-mode phase. The increase in density is based on the particle content in the SOL which is trapped in the core region when the auxiliary heating is applied and induces the new regime. Even the interruption of the active gas feed for density control is not sufficient to keep the plasma density at the requested level ($2.5 \cdot 10^{19} \text{ m}^{-3}$). In this case a transient density

level developed in time, because of a delayed reaction of the plasma on the active valve chosen. For the comparison of the data of t_3 and t_4 it is however more important that density is similar for these. The exact differences of ohmic and phases of higher confinement are secondary. The appearance of $\epsilon_{D\alpha}$ of the two scenarios is depicted in figure 5.29. Differences are encountered at the HFS where the peak emission is observed to be positioned above the inner strike point for t_3 (smaller R_{in}) and at the inner strike zone for t_4 (larger R_{in}). Since the magnitude of emission is closely related to electron temperature, the difficulty in this comparison is the change in P_{heat} by $\sim 10\%$ from t_3 to t_4 which is related to the conditioning of the heating system and the magnitude of ohmic heating. When arguing about the spatial distribution of $\epsilon_{D\alpha}$, the change on the HFS is significant, while the pattern at the LFS is fairly similar.

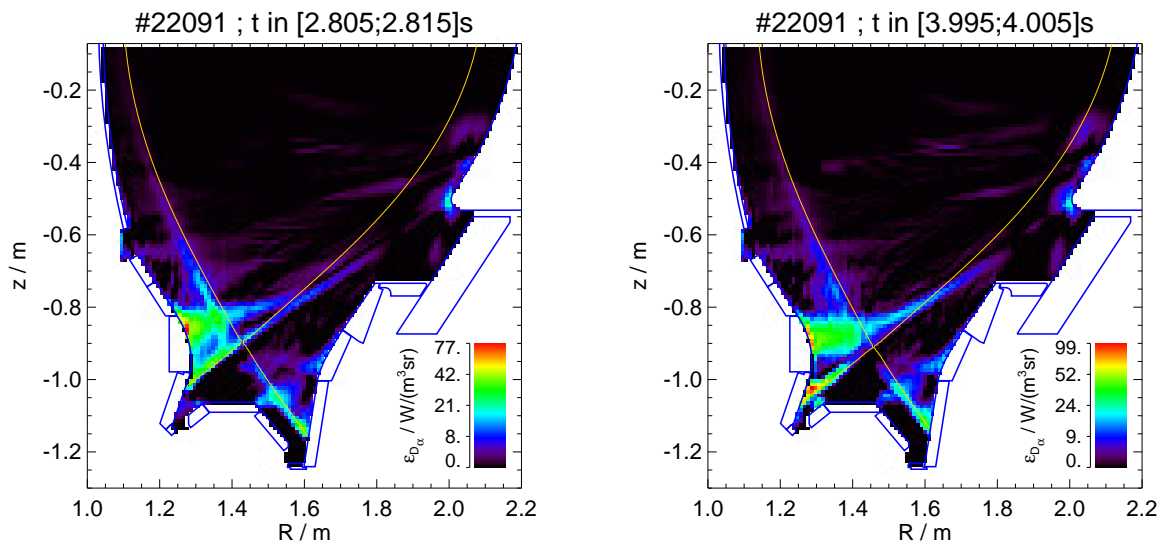


Figure 5.29: 2D profiles of $\epsilon_{D\alpha}$ from tomographic reconstruction of divertor view radiance data of discharge #22091 for the two time slices of enhanced confinement (t_3 , t_4). Accompanied with the radial shift of the plasma column is a change in the emission pattern at the HFS, while the LFS seems unaffected. Gauge data indicate a higher flux density of neutrals at the HFS and in the divertor region for t_4 which explains the increased emission in general (similar electron densities and temperatures presumed). The stronger emission at the inner strike zone for t_4 is likely to be related to an elevated power flux to the target which is either based on the radial shift (larger wall gap and less plasma-wall interaction in regions further upstream) or the increased heating power.

From analysis of the HFS-ROI it is found that the core fuelling in that region is higher for t_4 than for t_3 . Assuming that the total recycling flux scales with plasma density ($n_{e,t_3} > n_{e,t_4}$) the conclusion is thus - similar to the ohmic case (t_1, t_2) - that particle recycling during t_3 is positioned outside the lower HFS and divertor region to a larger extent than for t_4 . In this configuration, a change in core fuelling at the lower HFS of 45% is observed when the plasma-wall spacing is increased by ~ 4 cm. The radial decay length of plasma pressure in this region seems not to be altered, since the vertical penetration of neutrals appears to be similar for t_3 and t_4 , ie the flux density distribution is simply changed in magnitude, but not in shape.

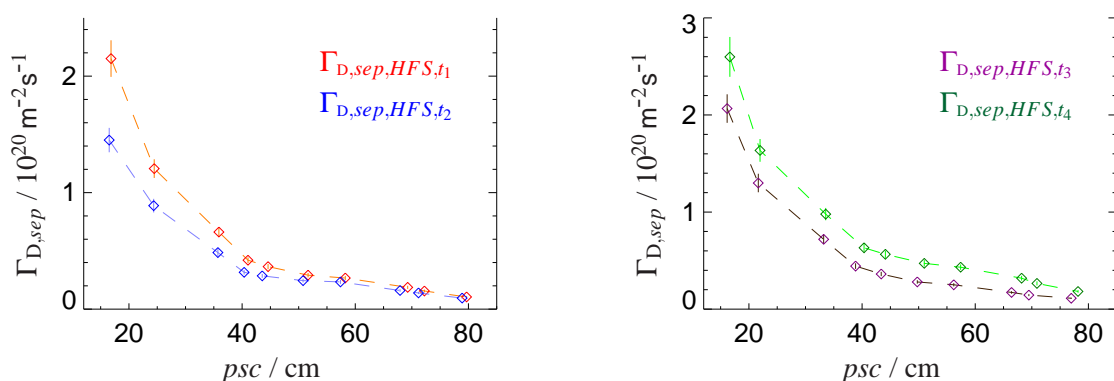


Figure 5.30: Atomic neutral flux density at the separatrix on the HFS for four time slices of #22091. Left: Comparison of $\Gamma_{D,sep}$ for the ohmic phase (t_1 , t_2). The corresponding fuelling rates are $F_{D,core,t_1} \approx 3 \cdot 10^{20} \text{ s}^{-1}$ and $F_{D,core,t_2} \approx 2.2 \cdot 10^{20} \text{ s}^{-1}$. A reduced plasma-wall gap for t_2 results in a lower recycling flux which is confirmed by $\Gamma_{D,lls}^G$ and $\Gamma_{D,Div}^G$ when comparing t_1 and t_2 . Regarding the source in the inner divertor, the penetration of neutrals to locations further upstream is more effective for t_2 , probably due to a reduced plasma pressure in the HFS SOL. Right: Distribution of $\Gamma_{D,sep}$ for the phase of enhanced confinement (t_3 , t_4). The corresponding fuelling rates are $F_{D,core,t_3} \approx 2.7 \cdot 10^{20} \text{ s}^{-1}$ and $F_{D,core,t_4} \approx 3.9 \cdot 10^{20} \text{ s}^{-1}$. Although the density is larger for t_3 , the recycling flux in the lower HFS SOL is elevated for t_4 which supports the idea of the radial position influencing the recycling pattern at the HFS vessel wall. However, the vertical penetration of neutrals from the target to locations further upstream is comparable (different magnitude, but similar shape of $\Gamma_{D,sep}(psc)$).

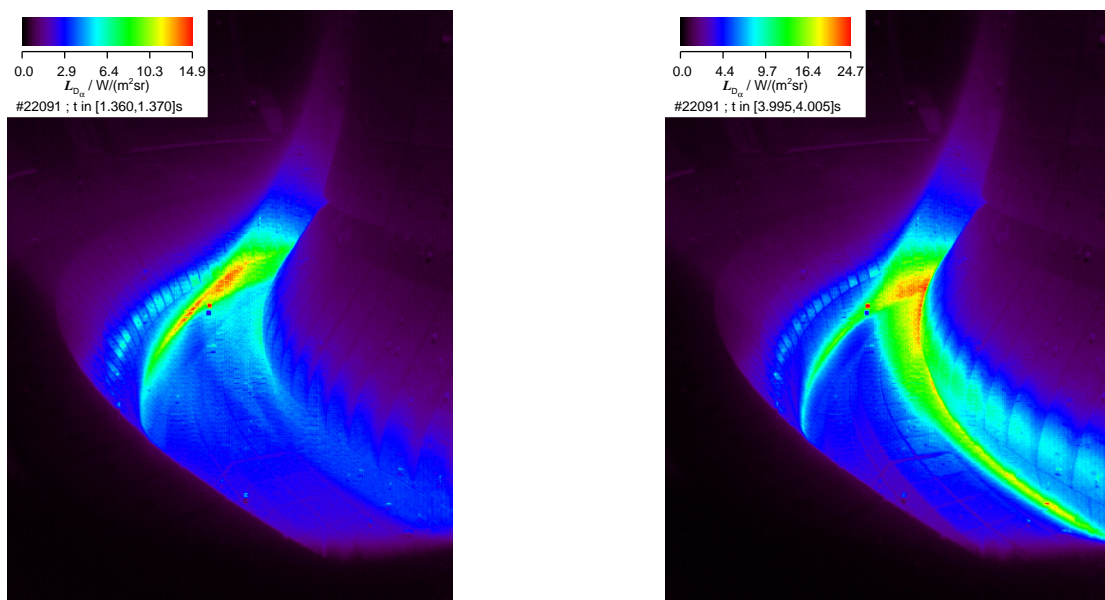


Figure 5.31: L_{D_α} from the XPMC divertor view of discharge #22091 for time slices t_1 and t_4 (large R_{out}). The feature immediately discovered is the change in position of peak emission from outer target (t_1) to inner target area (t_4), which is due to an increased SOL power flux being transported to the HFS. For a rough characterisation of the divertor state a similar density and neutral density might be assumed (based on similar gauge data as a measure for the recycling flux), leaving ϵ_{D_α} as an indicator for electron temperature. The weak dependence of PEC_{D_α} on T_e above a certain temperature level ($\sim 20 \text{ eV}$) may be the reason for the LFS emission to appear unchanged.

An impression of the actual radiance data for the two different levels of heating power can be gained from figure 5.31, which is useful to judge the quality of the 2D reconstructions. A more general observation is that at this low density level the increase of heating power also leads to an increase of D_α -emission. The origin of this enhanced ε_{D_α} obviously is the inner divertor leg. For t_1 and t_2 the power flux to the inner target is too low to generate a large $\mathcal{P}EC_{D_\alpha}$ while the gauge measurements indicate that neutrals are abundant. It is interesting to note that both targets appear equally bright for #22061 (see section 5.2.1) which is characterised by a larger ohmic heating power but also by a lower plasma density. The comparison shows that the HFS is more affected relatively than the LFS by the change of these parameters. Similarly, the increase of heating power for t_3 and t_4 seems to dominantly alter the plasma parameters in the inner divertor while the outer target appears in a comparable emission pattern.

The discharge #22097 was configured in the same manner as #22091, albeit with a higher target density of $n_{e,target} = 4 \cdot 10^{19} \text{ m}^{-3}$. Heating power and radial position were each set to two different values in order to obtain four different scenarios. One time slice of each configuration is addressed here, to which the basic parameters are collected in table 5.5.

shot	time / s	$\bar{n}_e /$ m^{-3}	$P_{heat} /$ MW	L-fact.	$R_{out} /$ $R_{in} /$ m	$\Gamma_{D,Div}^G /$ $\Gamma_{D,lhs}^G /$ $\text{m}^{-2}\text{s}^{-1}$
22097	$\sim 1.7 (t_1)$	$3.91 \cdot 10^{19}$	0.60	1.0	2.14 1.13	$3.3 \cdot 10^{22}$ $3.1 \cdot 10^{21}$
22097	$\sim 2.3 (t_2)$	$3.99 \cdot 10^{19}$	0.64	0.9	2.11 1.11	$3.4 \cdot 10^{22}$ $2.8 \cdot 10^{21}$
22097	$\sim 3.1 (t_3)$	$5.43 \cdot 10^{19}$	1.96	1.8	2.11 1.11	$6.6 \cdot 10^{21}$ $2.0 \cdot 10^{21}$
22097	$\sim 3.7 (t_4)$	$4.13 \cdot 10^{19}$	2.12	1.6	2.15 1.14	$6.8 \cdot 10^{21}$ $1.7 \cdot 10^{21}$

Table 5.5: Basic parameters of discharge #22097 for four time slices (the exact time intervals are given in figures 5.32 and 5.33). Like seen for #22091 the increased heating power induces enhanced particle confinement and a different density level results for the ohmic phase (t_1, t_2) and the phase with auxiliary heating by ECRH (t_3, t_4). The relationship of heating power level, gas feed flux and radial position is depicted with the time traces of these parameters in figure 5.35.

The higher core density in the ohmic phase (compared to #22091) is accompanied with a much higher SOL-plasma density, since neutrals are predominantly ionised in the SOL and the core fuelling is less efficient. As can be seen on figure 5.32, the level of ε_{D_α} is about a factor of 10 higher than for #22091 (see figure 5.28) which is basically due to the larger divertor neutral flux density ($\Gamma_{D,Div,22097}^G \approx 5 \cdot \Gamma_{D,Div,22091}^G$). Because of the similar ohmic heating power, the divertor plasma temperature will be lower for #22097, in which more plasma energy is lost to the interaction with neutrals. Although the temperature might be reduced, there must however exist a higher ionisation rate in the SOL to lead to an increased electron density to obtain the elevated radiation level in summary. This large radiation level in the ohmic phase (see also figure 5.36) is spatially more spread and results in a broad emission pattern obtained from tomographic reconstruction (figure 5.32). It is probably also the impact of reflection at the LFS in combination with the absence of dominant localised structures which leads to the horizontally distributed pattern that seems not to perfectly fit to the original radiance data. As was the case for #22091, the radial shift in the ohmic phase does not change the emission profile in the divertor region significantly. Merely a small change in magnitude at the inner and also outer target is observed which might well be related to the different \bar{n}_e and P_{heat} for t_2 relative to t_1 , rather than the result of the shift in radial position.

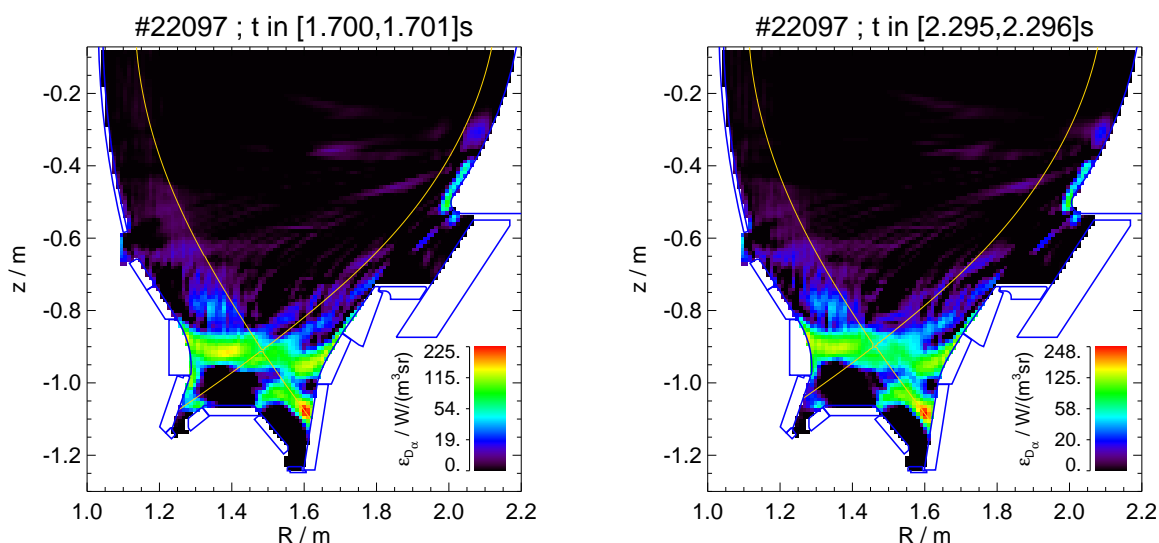


Figure 5.32: 2D profiles of ε_{D_α} from tomographic reconstruction of divertor view radiance data of discharge #22097 for the two ohmic time slices (t_1 , t_2). The large radial decay length of plasma pressure in the SOL and the accompanied radially spread excitation area leads to a less pronounced emission pattern. Together with the impact of reflection on the LFS, a horizontally smeared structure is obtained. The difference in magnitude of ε_{D_α} at the inner and outer target seems barely remarkable.

The more detailed analysis on the HFS-ROI concerning neutral flux density at the plasma edge is found to be hampered by the broad emission pattern. While the profile-fit converges for t_1 (fig. 5.34), the contrast is too low for this ansatz for t_2 and no result is gained. It seems that already for this medium density and low confinement scenario the plasma pressure in the SOL is large enough to result in a radially distributed emission to which the ansatz of a peaked profile is not adequate. Also the low signal-to-noise ratio for emission in front of the heatshield compared to the divertor region is relevant in that respect. Assuming that the recycling flux scales with line averaged density, the increase for $\Gamma_{D,Div}^G$ seems reasonable. Without knowledge of $\Gamma_{D,sep}(psc)$ for both t_1 and t_2 one may argue only by regarding the gauge measurement at the lower heatshield, that the recycling flux is differently distributed for the two time intervals. A smaller value for $\Gamma_{D,lhs}^G$ during t_2 , but at the same time a higher value for $\Gamma_{D,Div}^G$ suggests that a larger fraction of the SOL plasma flux is transported to the LFS and the recycling flux of neutrals being efficiently contained in the divertor region. Thus, like observed for #22091, the impact of the radial shift seems probable, but it appears less obvious in this ohmic phase.

In the phase of strong ECRH the confinement properties are enhanced, which is clearly recognised with the rise in core density when the heating is applied. While the level of ε_{D_α} was increasing for #22091, because of elevated electron temperature in the divertor region, it is the opposite for #22097, based on the strongly reduced SOL particle flux. The difference for ε_{D_α} of a factor of about 4-5 between the ohmic and ECRH phases is compatible with the values for $\Gamma_{D,Div}^G$, such that a change in temperature is suspected to be less pronounced. A very interesting feature of #22097 is the relationship of core density, heating power and radial position, which is indicated in figure 5.35. As has already been mentioned for #21418 (see section 5.2.3), transport coefficients are changed, when the heating power is increased and the particles from the SOL are trapped in the core region such that the target density is surpassed for a period of time depending on the residence time of particles in the plasma vessel. The astonishing aspect is that density

risers by about 20% from the start of ECRH ($t \approx 2.7$ s) and stays at this high level and only a very decent decay is observed for $t > 3.1$ s, although the gas feed is switched off. When the plasma column is shifted radially outwards ($\Delta R_{in} = 3$ cm), density drops immediately on a much shorter time scale and the decay has to be compensated by activation of the gas valve. Regarding the data listed in table 5.5, the values for $\Gamma_{D,Div}^G$ and $\Gamma_{D,lhs}^G$ are not varied as much as one might expect from the different core density level. The conclusion of this situation is that a certain fraction of the total recycling particle flux is not connected with the divertor region. Probably the small distance to the heatshield for the phase of low R_{in} prevents particles (emerging from core losses on the LFS or the top of the cross section) from being transported to the lower part of the vessel and a circular recycling flux is established at the upper part of the plasma chamber. Since the ionisation gauge positioned at the top of the vessel does not indicate any change during the discharge, it is assumed that neutrals are confined in front of the upper heatshield.

The results of tomographic reconstruction (fig. 5.33) indicate a change in the distribution of power flux at the HFS related to the different radial positions of the plasma column. For t_3 the emission at the inner strike point is very low and the peak of $\varepsilon_{D\alpha}$ is found to be located above the strike zone at the vessel wall. During t_4 obviously more power reaches the inner target and the maximum $\varepsilon_{D\alpha}$ is recognised in this region, while the emission in the area above the strike zone is still pronounced but reduced in magnitude. The level and shape of emission at the LFS target area is not affected by the radial shift.

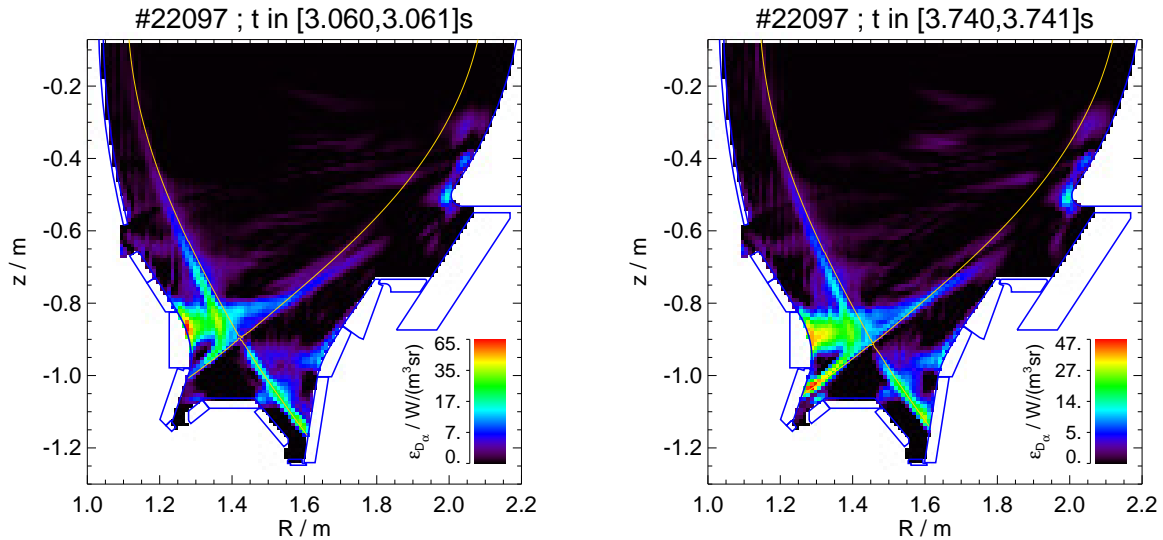


Figure 5.33: 2D profiles of $\varepsilon_{D\alpha}$ from tomographic reconstruction of divertor view radiance data of discharge #22097 for the time slices of enhanced confinement (t_3, t_4). The radial position obviously has an impact on the power flux to the inner target. While for t_3 a rather low target temperature is the reason for low emission, this area appears as the location of peak emission during t_4 . The region of pronounced emission at the vessel wall above the strike zone seems to receive more power during t_3 than t_4 . On the other hand, the emission pattern at the LFS target seems unaffected by the radial shift.

Both scenarios exhibit a very sharp sheath of $\varepsilon_{D\alpha}$ at the HFS plasma edge which can well be analysed with the profile-fit. The results for the distribution of neutral flux density at the separatrix are summarised in figure 5.34. The corresponding core fuelling rates in the limited p_{sc} -interval are identical, but differences in the poloidal distribution are observed. For t_4 the penetration of neutrals to higher p_{sc} -positions is more efficient due to the larger plasma-wall distance. A con-

siderable fraction of the total core fuelling rate must be located outside the visual range at the upper part of the plasma cross section, in order to maintain the high core density level (equal confinement properties for t_3 and t_4 presumed).

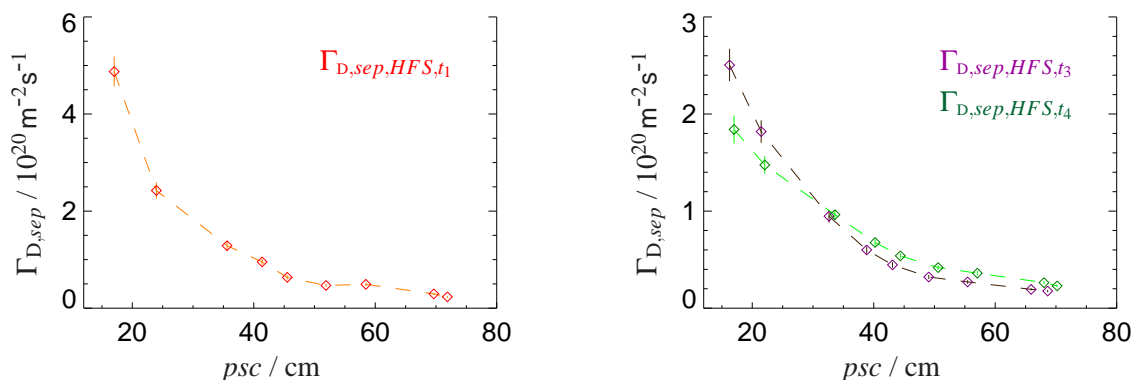


Figure 5.34: Atomic neutral flux density at the separatrix on the HFS for three time slices of #22097 (t_1 , t_3 , t_4). Left: $\Gamma_{D,sep}$ for the ohmic interval t_1 with a corresponding core fuelling rate of $F_{D,core,t_1} \approx 5.8 \cdot 10^{20} \text{ s}^{-1}$. The fuelling rate is nearly twice as large as observed for the interval t_4 which is characterised by a similar core density but better confinement properties. For t_2 the profile-fit failed to converge, because of the low contrast for data of the HFS-ROI. Right: $\Gamma_{D,sep}$ for the intervals of enhanced confinement (t_3 , t_4). The corresponding fuelling rates are $F_{D,core,t_3} \approx 3.3 \cdot 10^{20} \text{ s}^{-1}$ and $F_{D,core,t_4} \approx 3.3 \cdot 10^{20} \text{ s}^{-1}$. Presuming that the quality of confinement is very similar for both intervals, an increased core fuelling for t_3 must occur in areas in the upper part of the plasma chamber, since a higher core density is maintained without change of divertor neutral flux density. From the distribution of $\Gamma_{D,sep}(psc)$ a more efficient vertical penetration of neutrals during t_4 seems to be present which is reasonably connected to the larger wall gap.

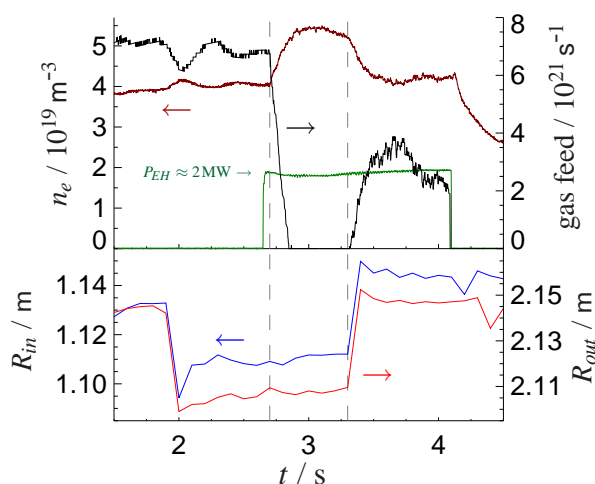


Figure 5.35: Collection of parameters related to particle confinement (top) and radial position (bottom) for #22097. The remarkable feature of this configuration is the density rise induced by additional heating and the higher density level being maintained without gas feed until the plasma column is shifted outwards. Together with the observation that neutral flux density does not change strongly in the divertor region during the ECRH phase, it is suspected that local recycling is present at the upper part of the heatshield.

Two examples of the actual radiance data for the phases of ohmic heating and ECRH are presented in figure 5.36. Besides the magnitude of radiance which is found to differ by a factor of about 5, the spatial distribution of emission is more diffuse in the ohmic phase and the origin from volume emission and reflection cannot easily be distinguished. Even at the reduced signal-to-noise ratio for the ECRH phase the peaked emission at the HFS plasma edge can be reliably interpreted with the profile ansatz. An important feature is emerging for the phase of increased heating power which is the development of two distinct patterns of localised emission at the inner target and above this region at the vessel wall.

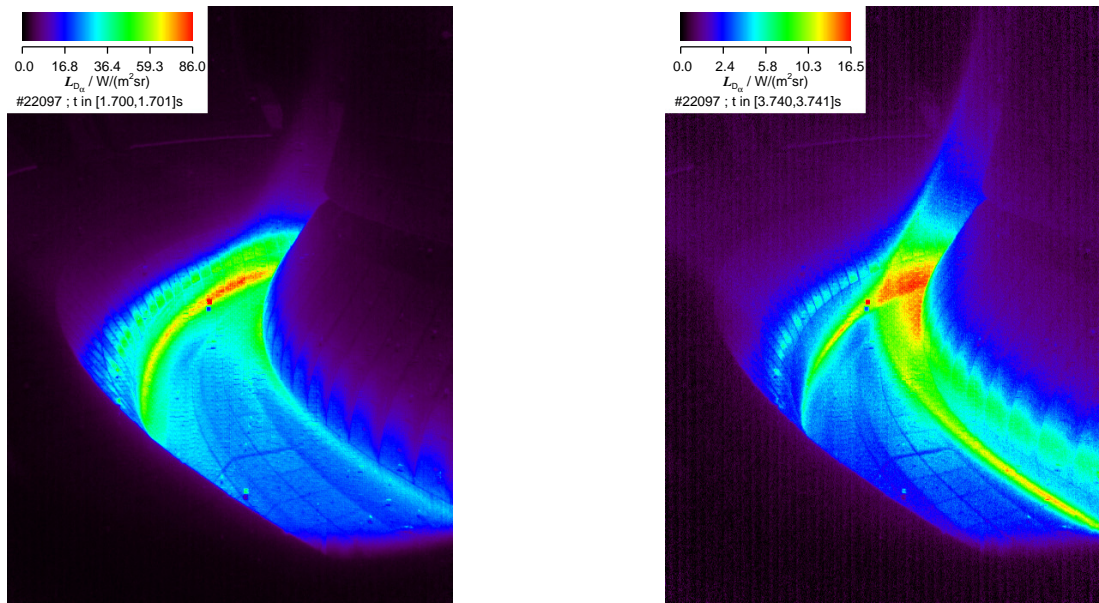


Figure 5.36: $L_{D\alpha}$ from the XPMC divertor view of discharge #22097 for time slices t_1 and t_4 (large R_{out}). Radiance in the ohmic phase (t_1) appears much more diffuse than in the phase of enhanced confinement (t_4). A small decay length of plasma pressure in the SOL results in a narrow sheath of $\epsilon_{D\alpha}$ close to the separatrix. While emission in the ohmic phase is located mainly in the target areas, the phase of increased heating power is accompanied by the development of two localised zones of emission at and near the HFS target.

A general problem of the divertor camera viewing geometry is that emission at the X-point (if present) is obscured by emission from the LFS target area. The region around the X-point might be suspected to be an effective area for fuelling, if neutrals enter the core plasma from the private flux region, ie from below the X-point between the targets. In order to gain a larger benefit in that respect from the fixed view, the plasma of discharge #22113 has been vertically shifted as far as feasible concerning the capacity of the control system. A low density, moderately heated configuration has been chosen to achieve reasonable contrast in $\epsilon_{D\alpha}$ and to keep the power flux to the wall at a low level, since the strike zones for the vertically lifted position are outside the surface area of the target plates. Some basic parameters are given in table 5.6 for two time intervals which are representative for the two phases of different vertical position (indicated by z_{XPT}).

Radiance data and results from tomographic reconstruction are displayed in figures 5.37 and 5.38. Two important results are obtained which have consequences for the interpretation of $L_{D\alpha}$ camera data in general. Firstly, the emission pattern at the LFS above the target plate can be clearly identified as originating from reflection. The change in shape and orientation of projected emission on these tiles during the vertical motion is attributed to the secondary viewing geometry. If this emission pattern was due to a radially separated plasma-wall interaction, its orientation would be independent of the plasma position, ie it would be aligned parallel to the strike zone. Secondly, the diagonally elongated pattern of emission of the reconstructed profile above the X-point in the core region can be rather convincingly be realised as an artefact, based on the line of sight integration in parts of the field of vision where the viewing chords are nearly parallel to the flux surfaces just beyond the separatrix intersecting the inner target. This pattern is the result of reduced radial resolution and the emission is thus smeared along the integration path. When the plasma column is shifted upwards, this feature is seen to change position relative to the X-point,

which would most probably not be the case if a real plasma-neutral interaction was observed.

shot	time / s	\bar{n}_e / m^{-3}	P_{heat} / MW	L-fact.	R_{in} / m	z_{XPT} / m	$\Gamma_{D,Div}^G$ / $\text{m}^{-2}\text{s}^{-1}$	$\Gamma_{D,lhs}^G$ / $\text{m}^{-2}\text{s}^{-1}$
22113	$\sim 2.6 (t_1)$	$2.43 \cdot 10^{19}$	1.03	1.0	1.12	-0.91	$6.7 \cdot 10^{21}$	$1.25 \cdot 10^{21}$
22113	$\sim 4.4 (t_2)$	$2.53 \cdot 10^{19}$	1.12	0.9	1.14	-0.81	$4.4 \cdot 10^{21}$	$1.33 \cdot 10^{21}$

Table 5.6: Basic parameters of discharge #22113 for two time slices (the exact time intervals are given in figures 5.37 and 5.38). The main purpose of this configuration is the change in vertical position of the plasma column ($\Delta z_{XPT} = 10\text{cm}$). Note that the actual shaping and positioning control scheme also leads to a different inner wall gap for the two scenarios ($\Delta R_{in} = 2\text{cm}$).

For t_1 a similar ε_{D_α} profile is obtained like for #22061. Both target areas exhibit considerable D_α radiation, but also the region above the inner strike zone is noticed. Although for t_2 heating power is larger by 10% and also the distance to the heatshield is increased which should result in enhanced particle and power flux to the inner target (compare to observations for #22091 and #22097), the inner strike point is much lower in ε_{D_α} and also the region above the target appears less bright. Concerning the strike point region, the more open divertor configuration might explain the different radiation level. During t_1 the inner strike point is placed inside the gap of target plate and bottom baffle tiles and recycling neutrals are more likely ionised than to escape after several collisions with the adjacent wall surfaces. In t_2 , recycling neutrals may more efficiently escape the inner target and exit the divertor to remote locations or be intercepted at the outer separatrix and target. For the different magnitude of emission at the inner vessel wall above the target, one may assume an equal radial decay length of plasma pressure in the HFS SOL such that the excitation of recycling neutrals is less strong at the more distant wall. Probably the temperatures at the inner target are close to the energy interval of strong change in $\mathcal{P}EC_{D_\alpha}$, ie small variations in power density have a significant impact on the radiation level (compare also appearance of #22091 (t_1, t_2)).

The distribution of core fuelling on the HFS (figure 5.39) gives an impression as gathered for #22091 (t_3, t_4), ie the recycling flux at the HFS being larger for the increased wall gap. This conclusion is supported by the gauge measurement for $\Gamma_{D,lhs}^G$. The vertical position is not believed to influence the HFS fuelling pattern, because the distance of the separatrix to the vessel top is quite large for both time intervals.

As a summary it may be stated that the z -shift experiment proved to be useful for the understanding of reflection and the identification of artefacts in the tomographic reconstruction. The limitation of the vertical range for plasma positioning excludes a configuration in which the X-point could be observed horizontally. However, taking all L_{D_α} images presented so far into consideration, it seems obvious that the main fuelling is located at the HFS and no significant contribution from the private flux region being present.

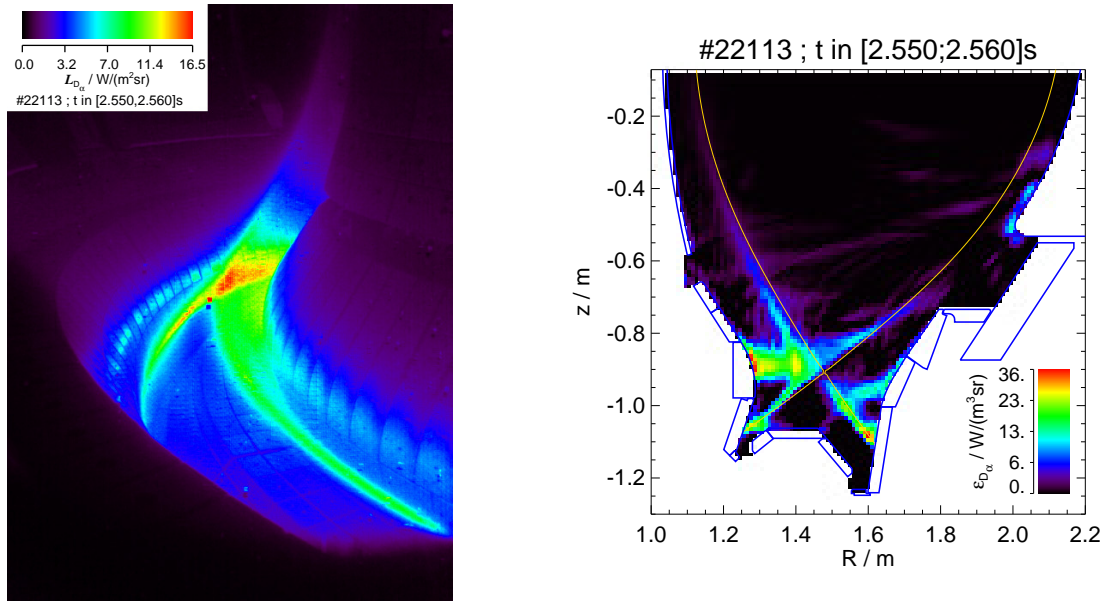


Figure 5.37: L_{D_α} and ϵ_{D_α} deduced from one XPMC divertor view exposure of discharge #22113 (t_1 , low z_{XPT}). The spatial distribution of radiation is very similar to #22061 with both target areas highlighted by D_α emission. Note the appearance of radiance on the LFS above the target plates as compared to t_2 (fig. 5.38).

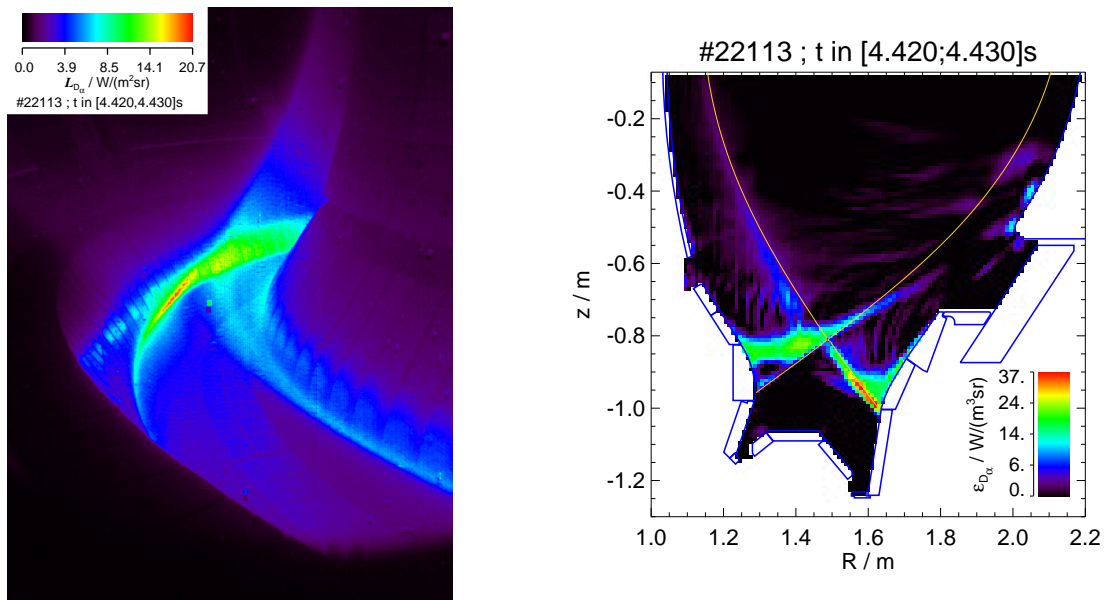


Figure 5.38: L_{D_α} and ϵ_{D_α} deduced from one XPMC divertor view exposure of discharge #22113 (t_2 , high z_{XPT}). The magnitude of D_α emission is seen to be reduced relative to t_1 in the region above the inner target due to the larger distance to the heatshield and also at the inner strike point which is probably based on the more open divertor configuration with more neutrals being able to escape the strike zones.

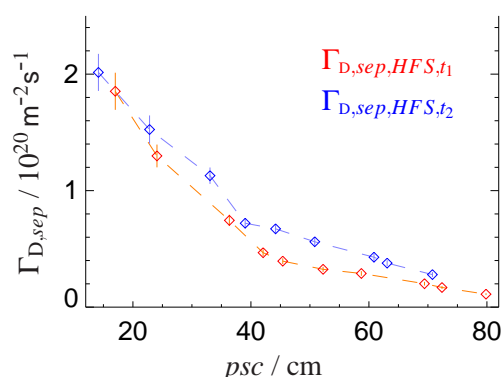


Figure 5.39: Atomic neutral flux density at the separatrix on the HFS for two time slices of #22113 (t_1 , t_2). The corresponding fuelling rates are $F_{D,core,t_1} \approx 3.1 \cdot 10^{20} \text{ s}^{-1}$ and $F_{D,core,t_2} \approx 4.3 \cdot 10^{20} \text{ s}^{-1}$. Variation of R_{in} is the reason for the different recycling flux on the HFS rather than the vertical position of the plasma column.

For the interpretation of ε_{D_α} from the profile-fit on the HFS-ROI, plasma parameters in the SOL have to be estimated. Radial decay lengths for n_e and T_e are defined for each of the KN1D grids such to obtain a reasonable agreement of experimental and modelled ε_{D_α} . The only restriction applied is the condition that these decay lengths should change monotonously along the psc -coordinate. Presuming that the distribution of plasma pressure in the SOL is established by the relative impact of parallel-field and perpendicular-field particle- and heat transport, a relationship concerning the connection length (distance between the targets following the direction of the magnetic field) might be suspected. In this framework the comparison of discharges with different rotational transform of the magnetic field at the plasma edge, indicated by the safety factor at the boundary surface of 95% of the poloidal magnetic flux at the separatrix, q_{95} , is motivated. The safety factor q describes the number of toroidal turns counted when following a magnetic field line for one poloidal turn, it can be approximately written as $q \approx rB_t / (RB_p)$. The parameters of the different scenarios are summarised in table 5.7.

shot	time / s	$\bar{n}_e /$ m^{-3}	$P_{heat} /$ kW	L-fact.	$ q_{95} $	$R_{in} /$ m	$\Gamma_{D,Div}^G /$ $\text{m}^{-2}\text{s}^{-1}$	$\Gamma_{D,lhs}^G /$
22091 (s_1)	~ 1.4	$2.53 \cdot 10^{19}$	630	0.9	4.8	1.12	$6.3 \cdot 10^{21}$	$7 \cdot 10^{20}$
22155 (s_2)	~ 2.8	$2.54 \cdot 10^{19}$	570	1.0	3.6	1.14	$7.9 \cdot 10^{21}$	$1.0 \cdot 10^{21}$

Table 5.7: Basic parameters for two ohmic scenarios which differ in the safety factor at the plasma edge. Different values for q_{95} are obtained by alternate magnitudes of the toroidal magnetic field: $B_{t,s_1} = 2.47 \text{ T}$, $B_{t,s_2} = 1.83 \text{ T}$. The neutral flux densities measured at the HFS wall and below the central divertor tiles indicate a higher recycling flux, ie weaker particle confinement for s_2 .

Figure 5.40 displays ε_{D_α} profiles which are characterised by the same spatial features. Merely, the larger neutral flux in the divertor for s_2 leads to an elevated radiation level. The profile analysis results in the neutral flux densities shown in figure 5.41. A variation in the edge safety factor is achieved by setting a smaller toroidal magnetic field B_T , while the plasma current and the accompanied poloidal magnetic field is kept at the same level. The change of quality in particle confinement by the different magnitude of B_T is consistent in the framework of a direct relationship of the magnetic field and transport coefficients, eg Bohm-like diffusion [78] (the correlation of magnetic field strength and perpendicular transport is actually not resolved yet [45]). The issue to be addressed here is the poloidal evolution of plasma pressure, which is obtained by the simple approach used to achieve a good match of experimental and modelled ε_{D_α} profiles. The resulting parallel profiles of static plasma pressure are depicted in figure 5.42 which

are encountered to be very similar for the two scenarios. A remarkable drop of static pressure along the flux surface is obtained. The probably underlying reduction of temperature could be partly attributed to the neutral-plasma interaction which cools the electron species the stronger the higher the neutral flux density towards the divertor. Also, the acceleration of plasma towards the inner target [79] results in a reduced static pressure while the dynamic pressure increases when following the field line, which would be compatible with the assumption that the total pressure is constant or decreasing along a flux tube in the SOL. If the drop of static pressure presented here was reasonable could only be checked by flow measurements at the HFS which are not available at AUG. Robust 2D SOL modelling would also be helpful (see section 5.2.5).

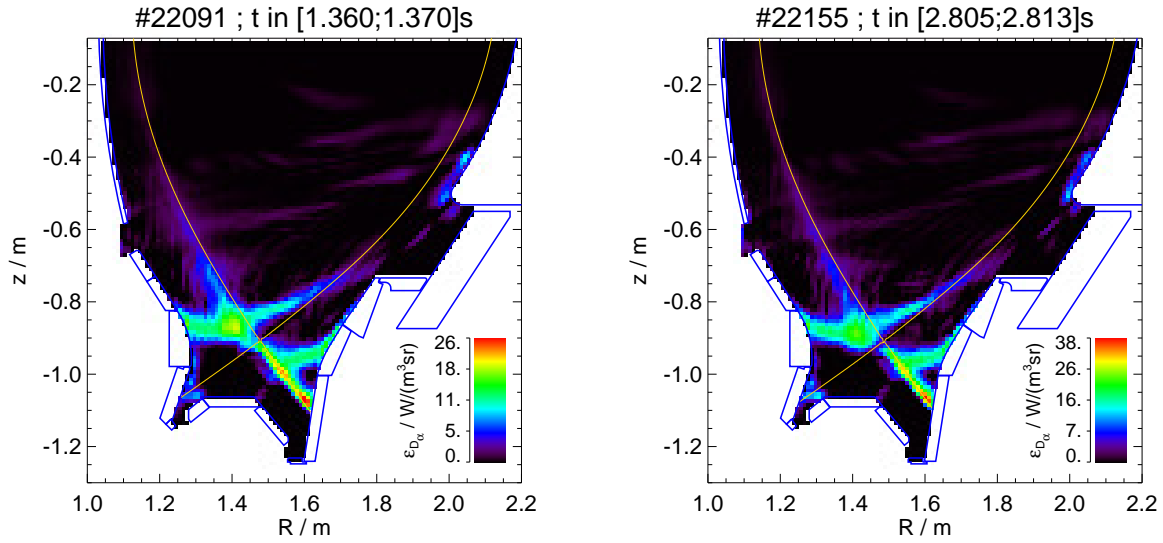


Figure 5.40: 2D profiles of $\epsilon_{D\alpha}$ from tomographic reconstructions of divertor view radiance data from two low density ohmic discharges at varied q_{95} . The only difference to be recognised is the enhanced radiation level for #22155 which relates to the higher recycling flux.

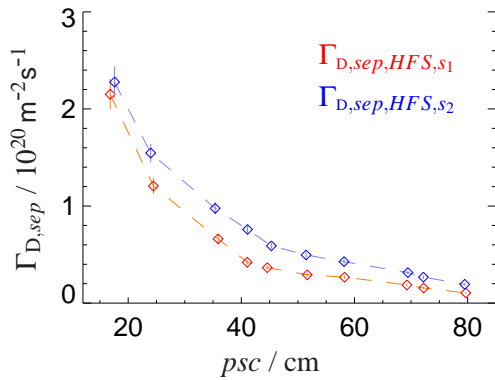


Figure 5.41: Atomic neutral flux density at the separatrix on the HFS for the two ohmic scenarios (see table 5.7). The corresponding fuelling rates are $F_{D,core,s1} \approx 3 \cdot 10^{20} \text{ s}^{-1}$ and $F_{D,core,s2} \approx 4 \cdot 10^{20} \text{ s}^{-1}$. It is suspected that the reduced strength of the magnetic field is the reason for the weaker core particle confinement and the higher related recycling flux for #22155.

In order to give an impression about the parallel-field extension of the SOL, an algorithm for field line tracing has been employed. As the starting point, the location of the closest distance of the separatrix to the heatshield has been considered and the radial position has been reduced by 0.5 cm to assure to be placed on an open flux surface. The distances along the magnetic field to the inner (d_i) and outer (d_o) target are for $q_{95} = 3.6$: $d_i \approx 23 \text{ m}$, $d_o \approx 38 \text{ m}$ and for $q_{95} = 4.8$: $d_i \approx 30 \text{ m}$, $d_o \approx 51 \text{ m}$. The connection length for s_2 is thus reduced by about a quarter compared to s_1 . Since no measurements for HFS SOL parameters exist for the discharges of interest, the

estimated values have to be regarded with caution. The marginally lower plasma pressure for s_2 at the same distance to the separatrix might be based on the varied extension of the SOL or simply be a coincidence, eg related to the uncertainty of the separatrix position. Considering the error margins, which are estimates as stated in section 5.1.1, the poloidal profiles cannot be distinguished. Omitting a clear statement about the comparison of s_1 and s_2 , the general observation of a static pressure drop along the magnetic field at the lower HFS displays an issue which might serve as fundamental characteristics to be reconstructed with SOL modelling codes.

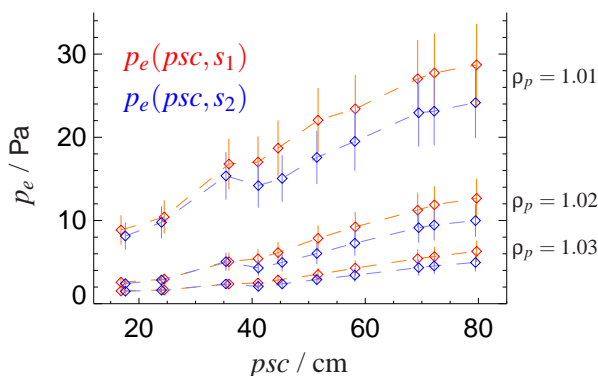


Figure 5.42: The p_{sc} -profiles of estimated static plasma pressure on the HFS for the two ohmic scenarios with different q_{95} . The flux labels correspond to surfaces which are positioned at a distance of about 1 cm, 2 cm and 3 cm to the separatrix in the midplane for both magnetic configurations. Flow measurements at the HFS or complex self-consistent SOL-modelling are required to judge if the reduction of static plasma pressure by more than a factor of three is reasonable at the lower HFS.

5.2.5 D_α Emission as Boundary Condition for SOL Modelling

The complexity of the processes which determine the state of the SOL, ie plasma transport, plasma-wall and neutral-plasma interaction, requires the use of extensive numerical modelling tools, in order to develop a detailed physical understanding. In a large area of the range of plasma parameters encountered in the SOL, a fluid description of the plasma species is justified. On the contrary, the mean free paths of neutral particles being large compared the gradient lengths of plasma parameters, in particular that of fast charge exchange neutrals, require a kinetic treatment of the neutral-plasma interaction. Plasma fluid codes and kinetic neutral codes need to be coupled for a self-consistent treatment of the SOL plasma. For modelling of the SOL in realistic Tokamak geometry a small number of codes exist, which are for the fluid part B2 [80], EDGE2D [81] and UEDGE [82], and for the kinetic part DEGAS2 [83], EIRENE [84] and NIMBUS [85]. The main aim of these codes is to provide a robust predictive modelling capability for the SOL plasma. Besides the general physical understanding such modelling is a prerequisite for the large next-step devices (eg ITER [86]), because the demand for a reasonable lifetime of plasma facing components in high power, long pulse discharges, does not allow for trial-and-error campaigns. At first, the modelling codes need to be verified and validated against experimental data. If the code contains a number of free parameters, these are varied such to obtain the best match to the experimental boundary conditions, which is known as interpretive modelling.

The numerical tool referenced in this section is the code package SOLPS 5.0 (scrape-off layer plasma simulator) [87], which is the combination of the fluid code B2.5 [88] and the Monte Carlo code EIRENE '99 [89], both running on a 2D grid covering (nearly) the complete SOL plasma cross section and plasma vessel respectively. As a hint for the practical setup of the code package, figure 5.43 shows a typical grid of B2.5. The grid cells are constructed as to be strictly aligned to the magnetic flux surfaces obtained from equilibrium reconstruction, such to avoid numerical diffusion, forming a curvilinear, quasi-orthogonal grid structure. It is important to note that the plasma is bound to the radially limited extension of the grid and plasma-wall

interaction is defined only at the contact area of the grid and the vessel components, ie the target plates. The standard procedure of grid generation requires to restrict the wall contact to the divertor and to ensure a poloidal connection between the LFS and HFS targets. Corresponding to the position of the vessel components and the shape of the flux surfaces, a small SOL width may result. At the grid boundary (except the targets) the plasma is reflected as neutral particles at the local ion temperature. It is known from experiment that the SOL fills the whole gap between the separatrix and plasma facing components, but this aspect is not implemented in the fluid code. For the kinetic code a grid is built such to cover the whole cross section bounded by the walls of the vacuum vessel. The vessel model also includes obstacles like the plasma facing components. At several of these surfaces permeabilities are defined which account for the gaps between components in the toroidal direction. Part of the kinetic code setup is also to define at various locations particle sources (gas puff) and sinks like adsorbing surfaces to simulate wall pumping or to mimic the efficiency of the pumping system.

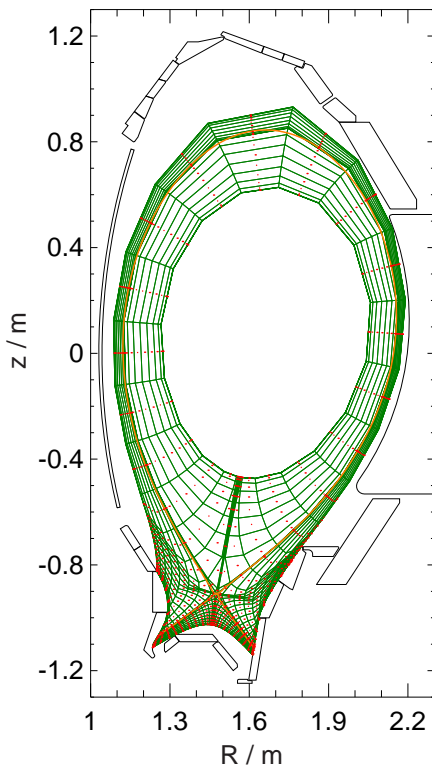


Figure 5.43: SOLPS fluid grid. Red dots indicate the cell centers and green lines the cell boundaries of a standard B2.5 grid of size 18(radial) \times 48(poloidal) cells. The orange line highlights the separatrix position at a higher resolution and shows the slight deviation of the grid structure and the actual shape of the SOL. Local poloidal gradient lengths which are assumed to be smallest in the divertor region and largest at the top of the plasma cross section determine the varying poloidal resolution of the grid, while the radial resolution relates to the shorter radial gradient lengths. The plasma is bound to this grid volume and reflected as neutrals of local ion temperature at the grid boundaries. Only at the target plates plasma-wall interaction is treated by the code.

There is a large number of modelling efforts at several Tokamak experiments which try to resolve crucial physics issues and to analyse the impact of various control parameters on the code result [90, 91, 92]. These control parameters are eg radial particle and heat diffusivities or chemical sputtering yields. One can imagine that with the presence of a set of free parameters due to the lack of experimental data or general understanding of physics details, a necessity of developing recipes arises. Clearly, such recipes can be considered robust only if reasonable agreement of code result and experimental data is achieved for similar plasma discharges in a routine manner. For the AUG device, discussions on modelling can be found in [46] concerning the properties of an H-mode discharge and in [93] which focusses on divertor detachment.

In previous modelling approaches at AUG, $L_{D\alpha}$ from the SPO diagnostics has been referenced as radiation data at the targets. The $\varepsilon_{D\alpha}$ data deduced from video diagnostics gives information

about the SOL state in a much larger area of the plasma cross section. The assumptions on n_e and T_e on the lower HFS, which are mandatory for the interpretation of ϵ_{D_α} in terms of neutral flux density, provide an additional indirect experimental boundary condition for the development of modelling recipes. In the following, plasma parameters deduced from two XMPC frames are compared with SOLPS results. The different modelling runs are like the plasma discharges labeled with a number and here, for brevity, indicated with an 'm'. Table 5.8 shows some basic parameters of the two ohmic discharges of interest. The main difference is the magnitude of heating power and the strength of the toroidal and poloidal (I_p) magnetic field components. Both discharges are operated practically at the same line averaged density and the larger value for the gasfeed of #22091 required to maintain the density level might be taken as a hint of a weaker particle confinement compared to #21303. In contrast to this interpretation the neutral flux in the divertor is larger for #21303 which is an indication for a higher recycling flux in the SOL than in #22091. Varying neutral flux and power levels are likely to result in slightly different divertor conditions. Despite these details, #21303 and #22091 are very similar and 'simple' discharges and should pose no major problems for SOLPS modelling within the standard recipe [94].

shot	time / s	\bar{n}_e / m^{-3}	I_p / MA	$ B_t $ / T	$ q_{95} $	W_{MHD} / KJ	P_{heat} kW	L-fact.
21303	~ 3.6	$2.55 \cdot 10^{19}$	1.04	1.9	3.3	130	750	1.2
22091	~ 1.4	$2.54 \cdot 10^{19}$	0.84	2.5	4.8	80	630	0.9

shot /	gasfeed / s^{-1}	$\Gamma_{\text{D,Div}}^{\text{G}}$ /	$\Gamma_{\text{D,lhs}}^{\text{G}}$ / $\text{m}^{-2}\text{s}^{-1}$	$\Gamma_{\text{D,mp}}^{\text{G}}$ /	R_{in} /	R_{out} / m
21303	$1.5 \cdot 10^{21}$	$1.0 \cdot 10^{22}$	$8 \cdot 10^{20}$	n.a.	1.12	2.17
22091	$3.7 \cdot 10^{21}$	$6.3 \cdot 10^{21}$	$7 \cdot 10^{20}$	$6 \cdot 10^{20}$	1.12	2.14

Table 5.8: Basic parameters of the ohmic AUG discharges #21303 and #22091 for which SOLPS modelling has been conducted.

Discharge #21303 is equivalent to #21305 which was part of the ohmic series discussed in [93]. In figure 5.44 the experimental ϵ_{D_α} of #21303 is shown in comparison with the code runs m17886 and m17797. The actual ϵ_{D_α} -profile is characterised by similar values for peak emission in the divertor legs with the outer strike zone being slightly brighter and more separated from the intersection of the separatrix and the target plate. For the simulated emission pattern the impact of the Carbon content is obvious by comparing m17886 ($Y_{\text{chem}} = 0.1$) and m17797 ($Y_{\text{chem}} = 0$). By excitation and ionisation of Carbon the divertor plasma is cooled and the lower T_e implies a lower D_α emissivity coefficient. Thus, with the increase of Y_{chem} a better match to the experimental ϵ_{D_α} in the radiation level can be achieved. From the two modelling results it is also obvious that with a larger Y_{chem} , the emission pattern changes such to be more spread in the SOL. The ϵ_{D_α} of m17886 in the inner divertor leg is more shifted towards the X-point and on the outer target it is more distributed between the target and X-point than observed for m17797 which ϵ_{D_α} is more peaked at the targets due to the larger temperature and reduced mean free path of neutrals. The asymmetry in divertor ϵ_{D_α} in the models is attributed to the drift-terms being activated. Keeping the uncertainties of the experimental determination of ϵ_{D_α} in mind, the agreement in shape and magnitude of the modelled ϵ_{D_α} -profiles seems fairly good. Here, Y_{chem} is used as a control parameter to influence the divertor state. The circumstance, that high values for Y_{chem}

need to be defined, indicates that it might not be the only issue which needs to be altered in order to approximate the actual conditions.

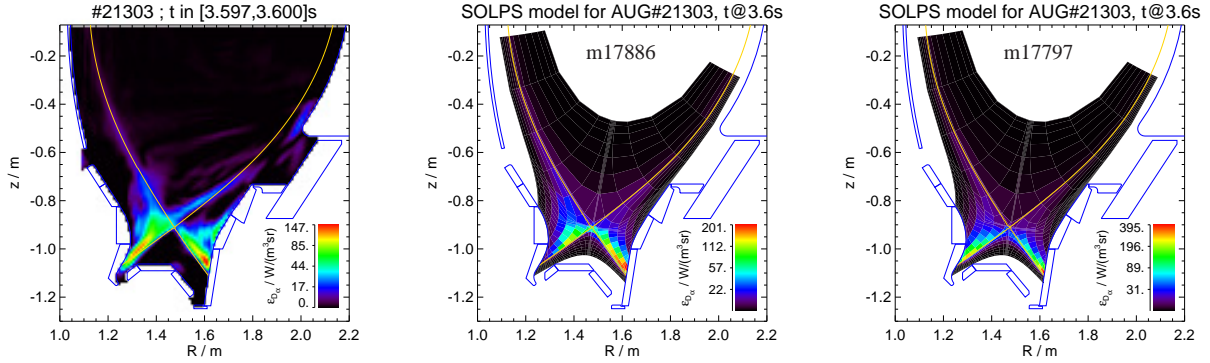


Figure 5.44: ε_{D_α} -profile of #21303 and those profiles obtained from SOLPS modelling (m17886/middle and m17797/right). For both code runs, drift-terms have been activated, but the chemical sputtering yield of Carbon is considered differently with $Y_{chem} = 0.1$ (m17886) and $Y_{chem} = 0$ (m17797).

The interpretation of ε_{D_α} on the HFS by the KN1D code allows to check SOLPS results in that region of the SOL. Of course, the plasma parameters used with KN1D display an estimate and are thereby only an indirect benchmarking criterion. Since two SOLPS runs of similar settings are available, results of both are combined to indicate a sensitivity range. Figure 5.45 shows the cells of the SOLPS grid which data values are compared with result or input data on the corresponding linear grids. The experimental ε_{D_α} -profiles from the ray-tracing-fit are somewhat distorted with a large decay length towards the plasma core. This is believed to be based on a poor signal-to-noise ratio which is often encountered for low contrast images of ohmic discharges. In this region of the HFS SOL the radiation level is much lower than in the divertor and the agreement of the emission profiles in amplitude, width and radial position seems quite good.

The appearance of ε_{D_α} is determined by the interplay of neutral density n_0 , electron density n_e and temperature T_e . Except in the temperature interval $T_e \in [1, 10]$ eV with a strong dependence of the emissivity coefficient on T_e , the influence of n_e and T_e is more similar at higher temperatures. There is some freedom in how to choose the corresponding profiles in the SOL for the KN1D interpretation in order to approximate ε_{D_α} and it is therefore more sensible to compare the electron static pressure p_e . In figure 5.46 n_0 and p_e from the different data sets are presented. According to the shape the ε_{D_α} -profiles no striking deviation is observed. Based on the iteration scheme to match $n_{e,sep}$, p_e at the separatrix is roughly the same for the SOLPS result and KN1D input data. The evolution of p_e is seen to be different in the core region but this does not influence the ε_{D_α} -profile, because the ionisation rate is already large enough for the neutral flux density to decay rapidly. This deviation of core pressure could be approached by analysing the impact of the detailed settings for the transport parameters including an asymmetry regarding HFS and LFS. An obvious difference of parameters in the SOL is the drop of p_e on the outer grid cells to very low values. This might be related to a drop of plasma density at the grid boundary where plasma is neutralised by definition (artificially thinned out zone). The profiles of n_0 , in particular for slices 2 and 3 are peculiar, because there is no continuous decay of density but a maximum at the grid boundary and a local maximum a few centimeter inwards. It is suspected that this feature is related to the small width of the modelled SOL. In the more realistic KN1D geometry a local maximum of n_0 is obtained due to the radially varying rates of molecular dissociation as the source and atomic ionisation as the sink term. The restriction on the SOL grid extension might

be the reason for an unrealistic distribution of plasma and neutral particles. For completeness it has to be noted that the indirect experimental p_e in the far SOL is arbitrarily forced to a low but nonzero value. Although there exists no direct measurement at the HFS, this assumption seems to be reasonable, because a radial shift of the plasma column by a few centimeter already results in a change of the recycling flux (see section 5.2.4). The actual magnitude of this p_e offset cannot be deduced from the ϵ_{D_α} profile, because the data analysis focusses on the peak emission and the magnitude of ϵ_{D_α} at the walls is not resolved precisely - in other words, the dynamic range of data deconvolution is not sufficient.

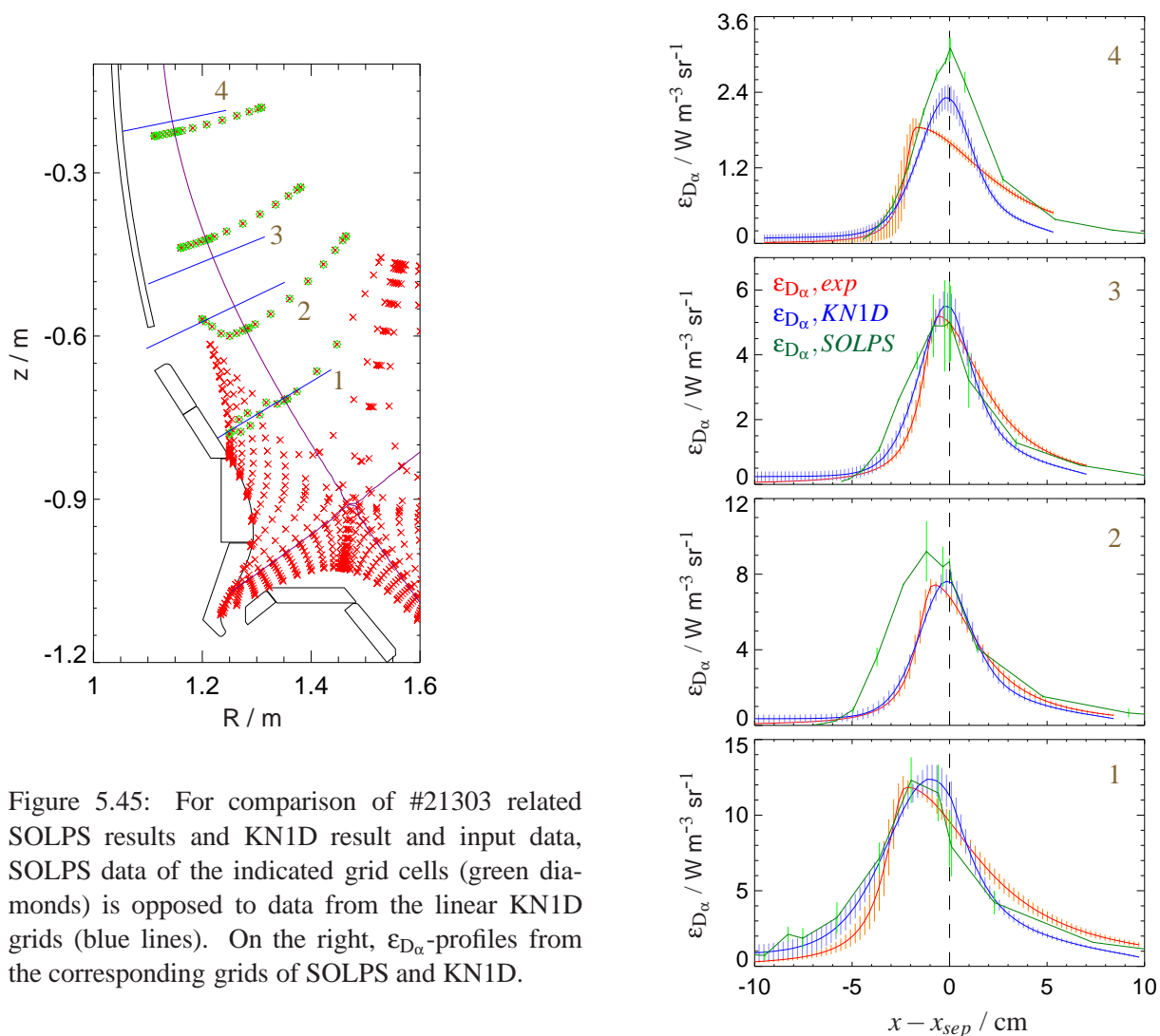


Figure 5.45: For comparison of #21303 related SOLPS results and KN1D result and input data, SOLPS data of the indicated grid cells (green diamonds) is opposed to data from the linear KN1D grids (blue lines). On the right, ϵ_{D_α} -profiles from the corresponding grids of SOLPS and KN1D.

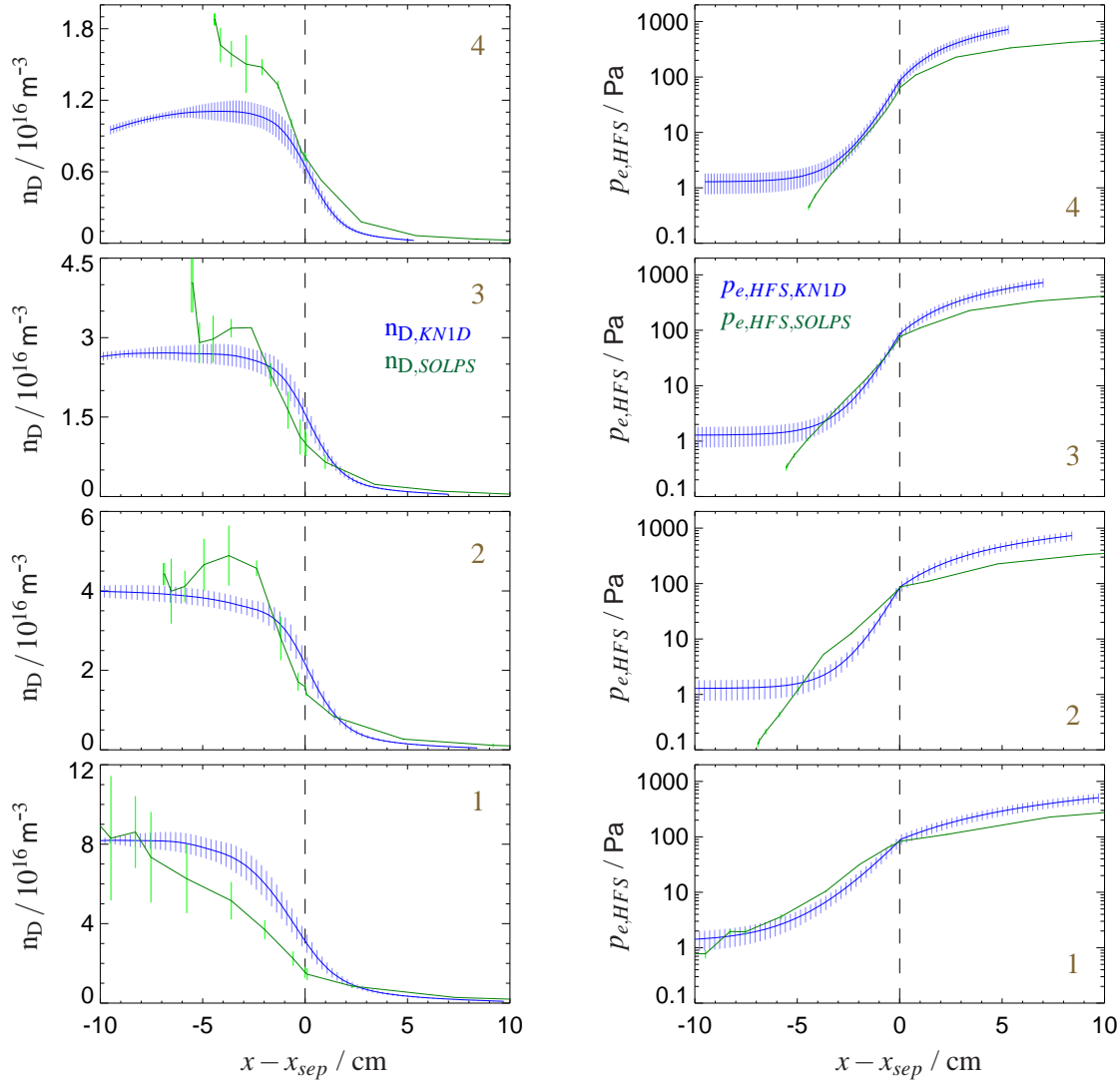


Figure 5.46: Comparison of neutral density n_0 and electron static pressure p_e at the HFS from SOLPS modelling and KN1D interpretation of experimental ϵ_{D_α} for #21303.

The AUG discharge #22091 was operated at the same line averaged density like #21303 but at a lower plasma current which also results in a lower ohmic heating power. Expressed in the edge safety factor q_{95} , the magnetic geometry differs in addition, because a larger toroidal magnetic field is set in combination with a smaller I_p . With the neutral density in the divertor being smaller, as indicated by $\Gamma_{D,Div}^G$, and the lower power level, the ϵ_{D_α} profile is considerably different. In particular the electron temperature at the inner target must have dropped to very low values ($T_e < 10\text{eV}$), since barely any emission is observed in that region. The D_α radiation level is in general very low compared to #21303 which is brighter by about a factor of five in peak emission. SOLPS modelling efforts using the same recipe as for #21303 resulted in three converged code runs (m21962, m21688, m21961) which differ in separatrix density according to the uncertainty of the edge density measurement. A fundamental drawback concerning the quality of the models is the need for deactivation of drift-terms to avoid numerical instability. The reason for this behaviour in contrast to the success in modelling of #21303 with drifts is unknown and to suspect the different magnetic configurations as a cause remains speculative. Figure 5.47 shows the ϵ_{D_α} -profiles for the XPMC deconvolution and the SOLPS models. Even

for m21962 with the lowest $n_{e,sep}$, the D_α radiation level surpasses the experimental data by nearly one order of magnitude. Both divertor targets are relatively hot (peaked emission at strike points) and no asymmetry in ϵ_{D_α} is obtained in the models. A number of aspects is suspected to cause this mismatch. The transport parameters might be too large such that the divertor particle flux is too high. Further, the impurity content is probably too low ($Y_{chem} = 0$, in agreement with the full Tungsten first wall of #22091), so the divertor plasma is not sufficiently cooled. With the absence of drifts in the model no asymmetry in particle and power fluxes to the targets is generated which would be required to establish a colder inner target. The strongly nonlinear dependence of the D_α emissivity coefficient on T_e for low temperatures makes the ϵ_{D_α} -profile a very sensitive plasma parameter in the divertor region and deviations of SOL models are easily discovered.

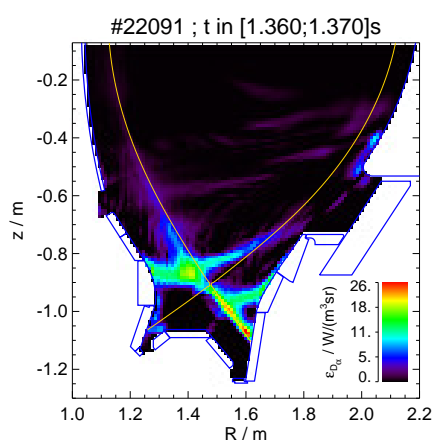
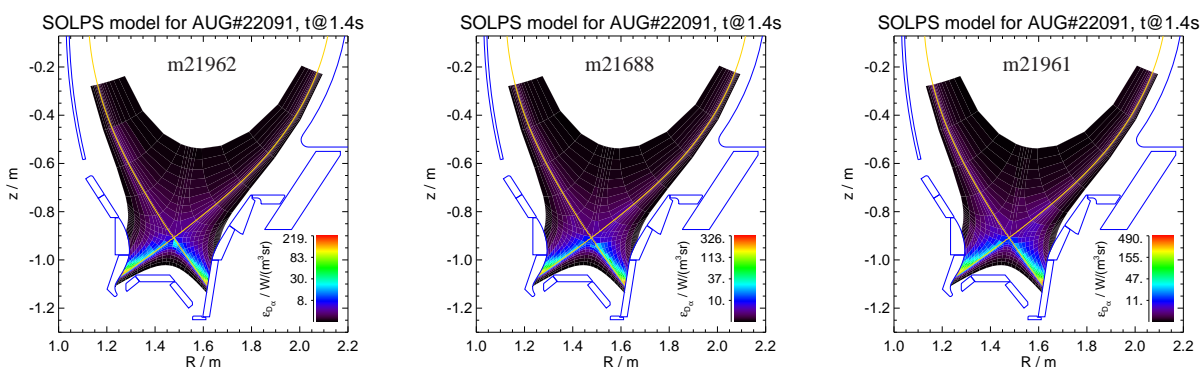


Figure 5.47: Experimental ϵ_{D_α} pattern for the low density ohmic discharge #22091 and three SOLPS models. The same recipe as for #21303 was used but drift-terms could not be activated due to numerical instability. A variation in the separatrix density was done to check its impact on the divertor conditions: m21962 ($n_{e,sep} = 5 \cdot 10^{18} \text{ m}^{-3}$), m21688 ($n_{e,sep} = 6 \cdot 10^{18} \text{ m}^{-3}$), m21961 ($n_{e,sep} = 7 \cdot 10^{18} \text{ m}^{-3}$). Slight changes of the inner target geometry have been ignored for the generation of the SOLPS grids (see inner target module).



The figures below concentrate again on the parameters ϵ_{D_α} , n_0 and p_e at the HFS as obtained from the experimental and modelling procedures. In figure 5.48 it is seen that the ϵ_{D_α} -profiles from SOLPS are basically centered at the separatrix, whereas the experimental profiles are more shifted towards the SOL. In the regions more distant from the divertor also a deviation in amplitude becomes obvious.

The profiles of n_0 and p_e shown in figure 5.49 readily explain the mismatch of the ϵ_{D_α} -profiles. While the core static pressure is identical with the experimental one, the deviation in the SOL is quite strong. It is in particular the difference of a few eV in electron temperature for $T_e \lesssim 10 \text{ eV}$ in the outer SOL which through the corresponding ionisation rate determines the radial position of the ion source profile. In the outermost grid cells the ionisation rate of neutrals is such that the probability to escape to the plasma free region at the HFS outside the fluid grid is increased. Consequently, the decay of neutral density along the flux surfaces with increasing

distance to the X-point is not of the same character as in the experimental/KN1D case. For slices 1-4 the peak neutral density level is comparable and only for slice 5 a drop in amplitude is noticed. In contrast, a continuous evolution for n_0 along the flux surfaces in the poloidal plane is observed for the experimental data.

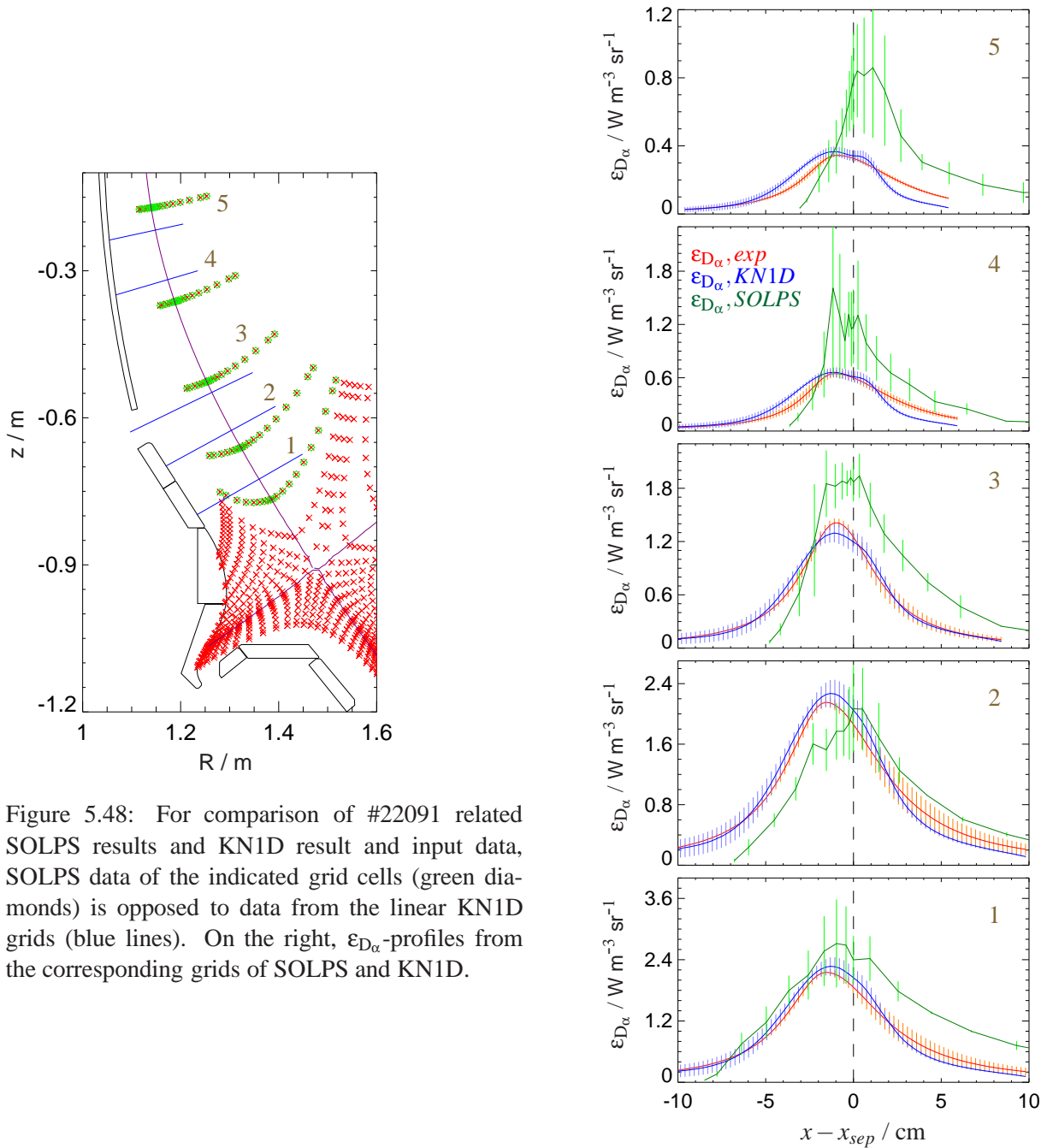


Figure 5.48: For comparison of #22091 related SOLPS results and KN1D result and input data, SOLPS data of the indicated grid cells (green diamonds) is opposed to data from the linear KN1D grids (blue lines). On the right, ϵ_{D_α} -profiles from the corresponding grids of SOLPS and KN1D.

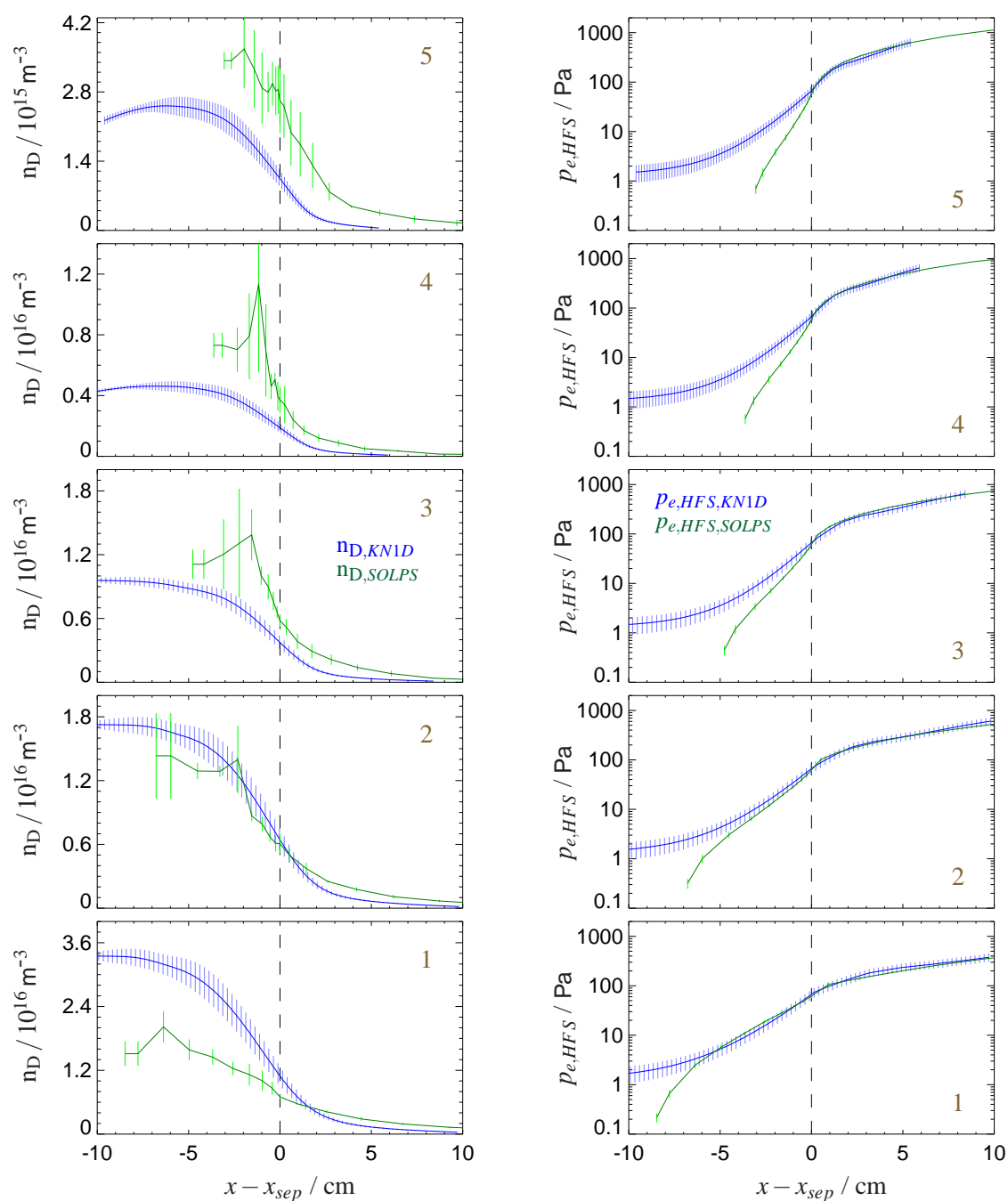


Figure 5.49: Comparison of neutral density n_0 and electron static pressure p_e at the HFS from SOLPS modelling and KN1D interpretation of experimental ϵ_{D_α} for #22091.

The deviation of ϵ_{D_α} in the divertor region marks the modelling results as unsatisfactory in quality. It is hard to guess the most appropriate change in code parameters offhand. One might think of using different values for perpendicular particle and heat diffusivities. The situation at the HFS suggests that a stronger radial flux of heat and/or particles is actually present. The larger radial spread of fluxes would also lead to a reduction of peak emission at the targets. In general, however, it is questionable if such modelling efforts should be continued when the aspects of particle drifts cannot be considered due to numerical restrictions.

To the knowledge of the author, up to now no straight forward scheme for predictive SOLPS modelling exists for a dedicated discharge type. With the variation of several code parameters it is in some cases possible to achieve a good match with experimental observations, eg #21303, but the recipe obviously cannot be translated to a similar discharge easily, eg #22091. Even for the simplest low density ohmic plasmas, modelling is not available routinely, instead each case poses a separate problem. In this respect, the usage of SOL codes for predictive modelling like that conducted for the ITER divertor design [95] requires special attention. This claim is in particular adequate if older versions of codes are applied, although several extensions and enhancements, like an increased complexity of the neutral-plasma interaction, have been included in more recent code packages. What seems disadvantageous in present kinetic/fluid code combinations is that the grid for neutrals contains a fraction of plasma-free area placed between the fluid grid boundary and the surface of the plasma facing components. Also, the area of plasma-wall interaction is restricted to the target plates. This poses the question if the detailed structure of the plasma vessel is required at all and if alternatively it might be beneficial to generate fluid grids with a large radial SOL width and to define material properties on the complete grid boundary. The latter approach does not exclude the definition of plasma shadowed regions for the neutral grid behind the plasma facing components which might be important for bypassing neutral fluxes. This ansatz would also offer the opportunity to examine the impact of separatrix-wall distance on SOL fluxes which is found in the experiment (see section 5.2.4).

5.2.6 Overview on Neutral Penetration Data

The parameters of neutrals which have been presented in the preceding sections are summarised in a condensed form in a series of tables (D.1 to D.4) to be found in appendix D. The idea is to provide a look-up-table of experimental results for approaches of modelling or theory. Neutral density and flux density, electron density and temperature and the ratio of neutral to electron densities are listed for three positions at the HFS and, as far as available, at one position at the LFS, each for two radial locations. The position of the separatrix is denoted as x_{sep} and the neutral penetration has been defined as the point at x_{pd} , where the neutral density is attenuated to the $\exp(-1)$ -fraction of its value at the separatrix. With this representation, however, details of the various profiles are lost. This issue becomes apparent when comparing the penetration depths $\Delta x_{pd} (=x_{pd}-x_{sep})$ obtained for the HFS and LFS. At the HFS, Δx_{pd} is found to be smaller the larger the p_{sc} -value. Since the spatial gradients of plasma pressure are larger with the more closely packed magnetic flux surfaces closer to the midplane, the decay length of neutral density becomes shorter. Consequently, an even smaller Δx_{pd} would be expected for the LFS, where the magnetic flux expansion is further reduced. Astonishingly, rather large values for Δx_{pd} are observed. The reason is, that the radial ion source profiles are different in shape and central position at the HFS and LFS and that the neutral density does not follow an exponential decay, because ionisation and charge exchange both influence the shape of the neutral density profile.

Chapter 6

Summary and Conclusion

The emission from excited neutrals at the plasma edge can be reasonably recorded with video diagnostics, such to cover large parts of the poloidal cross section. Unlike diagnostics which are based on a small number of sightlines and are typically interpreted in terms of flux densities at the vessel wall or close to the location of emission, the high spatial resolution of video optics allows for data deconvolution to resolve the radial profile of emission. The resolution of the radial position is mandatory for the distinction if the plasma of the core or scrape-off layer region is affected by neutral penetration. The ultimate goal of D_α video diagnostics is the determination of the radial and poloidal ion source profile. This parameter could serve as a boundary condition for SOL/edge modelling. If the plasma source term was known, the focus of analysis could be directed on the proper specification of transport parameters as to match the experimental plasma density profile shape.

At the ASDEX Upgrade Tokamak two cameras are attached to image guide based optics with a visual range covering the divertor and midplane region. Within the course of this project, the operation of video diagnostics has been carried out for the first time with an emphasis on accurate calibration of viewing geometry and radiance sensitivity. The deterioration of the fiber bundle transmission due to the impact of ionising radiation during plasma operation has been recorded for one complete experimental campaign. The now quantitative knowledge of this issue helps to improve future applications. A good accuracy of radiance calibration can be achieved only if the diagnostics is installed at the torus for a short period of time and calibration measurements are done before and after the radiation exposure.

A quantitative analysis of video diagnostics data has not been available so far. Two methods for data deconvolution have been prepared. A simple profile-fit can be used to analyse regions of high contrast at the low field and high field sides, including a poloidal variation of the radial emission profile. This approach is applicable only to image data from discharges of low and medium density, in which a separate sheath of emission can be identified at the plasma edge of the midplane. For radiance data of the divertor region, an algorithm for tomographic reconstruction is used. In general, the Tungsten coverage of the plasma facing components poses a severe complication for spectroscopy in the visible spectral range. The diffuse reflectivity of a Tungsten-coated tile has been measured solid angle resolved in order to generate an accurate model for secondary viewing geometry. This model has been successfully implemented in the tomographic algorithm and the improvement of the profile definition has been shown. Due to the asymmetric distribution of D_α emission in the poloidal plane, the analysis of the radiance recorded from the low field side, which is low in magnitude and contrast, is possible only, if no metallic surfaces are

positioned in the background. In an all-Tungsten machine, the data deconvolution is restricted to the high field side and divertor region.

The data presented on neutral penetration, such as density, flux density or fuelling rates, are based on the comparison of the experimental emission profile and the results obtained from 1D kinetic modelling using the code KN1D. For the specification of plasma parameters, estimates had to be made on the electron temperature in the low field side scrape-off layer and on both electron density and temperature in the high field side scrape-off layer, according to the edge diagnostics coverage and quality. Within the uncertainty of these estimates the agreement of experimental and modelled emission profiles seems fairly good. The flux density of neutrals at the vessel wall is reasonably matched, when taking the simplification of the 1D treatment, which does not include the impact of a parallel field plasma flow in the scrape-off layer, into account. The sensitivity of the experimental procedures is confirmed by the accurate recording of the emission profile at different configurations of the plasma edge. Changes of the fuelling profile in magnitude and radial position can be resolved, eg to distinguish between the actual core fuelling and ionisation in the scrape-off layer. Slight changes in the width of the separatrix-wall gap at the high field side have been observed to result in changes in the scrape-off layer recycling pattern, indicated by modifications of the poloidal profile of neutral flux density at the separatrix. The details of these profiles lead to the suspect that local recycling is present at the upper part of the high field side wall, resulting in a reduction of particle and power flux to the inner divertor, depending on the size of the wall gap. One example for a drop of core density accompanied by the radial displacement of the plasma column seems to confirm this interpretation. Another interesting observation is the reduction of static plasma pressure along the magnetic field towards the inner target at the high field side. Although obtained indirectly through the estimates on radial plasma profiles, this feature would be compatible with the expected acceleration of plasma in the scrape-off layer towards the divertor. From the deconvolution of divertor view data, separate emission patterns have been resolved. Besides the character of emission at the strike zones which can give a hint on the level of detachment, the occurrence of radiation above the inner target indicates that the distribution of plasma parameters is probably more complex than expected from simple radial decay lengths.

The essence of this thesis is described as follows. Calibrated D_α imaging diagnostics data has been exploited with elaborate methods for data deconvolution. A reflection-aware procedure for tomographic reconstruction has been presented which serves as a proof-of-principle in view of plasma spectroscopy in the vicinity of highly reflecting plasma facing components. The emphasis on geometry definition and radiance calibration and algorithms applied for deconvolution might be understood as a reference for quantitative video data analysis. Parameters describing the penetration of neutral particles have been deduced for low and medium density discharges.

The task of quantitative analysis of video diagnostics data has been met with considerable effort. However, the actual parameters of neutral particles have been discussed merely on a phenomenological level. The relative changes of emission pattern or magnitude of the recycling flux have been simply motivated in relation to measurements from ionisation gauges or the suspected impact of heating power on divertor temperature. Future work should therefore aim at the implementation of complex SOL models to which the experimental data could be compared. The use of emission data as a boundary condition for 2D modelling codes like SOLPS shows that also in this field improvements are required.

Appendix A

The ASDEX Upgrade Tokamak

The ASDEX Upgrade Tokamak (AUG) is a medium size machine operated at the Max-Planck-Institute for Plasma Physics [96] in Garching, Germany. It is the successor of the ASDEX (axial-symmetric divertor experiment) Tokamak which had gathered noticeable reputation, in particular in the framework of the discovery of the H-mode [97], a plasma regime of enhanced confinement induced by strong heating power. AUG started plasma operation in 1991 and an elaborate description of the experiment concerning the status as of 2003 can be found in [98]. The machine design of AUG (see also figure A.1) is related to conceptual studies for an experimental fusion reactor, namely ITER [86], which comprises eg an elongated plasma shape and the magnetic field coils to be positioned outside the vacuum vessel. A list of basic parameters of AUG is given in table A.1. Concerning the linear geometrical dimension, the AUG device is about a factor of 2 smaller than the JET Tokamak [99], being at present the largest facility for fusion research in plasma volume, which in turn is exceeded by the current ITER design by a factor of 2.

Although the poloidal field coils are placed rather distant from the plasma, the design allows for a variety of plasma cross sections (see figure A.2), including circular or elongated limiter plasmas, divertor configurations with lower (LSN), upper (USN) or doubly (DN) diverted poloidal field and different levels of lower and upper triangularity. Aspects related to these configurations are eg the impact of closed (lower) and open (upper) divertor or the relationship of plasma shape and stability/performance [100].

The AUG device is equipped with three different auxiliary heating systems, which are neutral beam injection (NBI), ion cyclotron resonance heating (ICRH) and electron cyclotron resonance heating (ECRH). Each of these systems in principle exhibits the capability of plasma current drive which is a crucial aspect when demanding long pulse plasma operation in a reactor based on nearly or completely non-inductively driven plasma current. Another aspect is the detailed configuration of the current density profile by localised current drive in order to establish a desired q -profile which in turn characterises the stability of the magnetic configuration [101]. One of the main issues pursued at AUG is the use of electron cyclotron current drive (ECCD) to influence the stability of those MHD modes which have a deteriorating impact on plasma confinement and need to be suppressed in reactor relevant scenarios [102, 103]. Another important application of heating systems is the use of ICRH for wall conditioning [104]. The problem not yet solved is to find effective methods which are operational at the presence of the toroidal magnetic field generated by superconducting coils, unlike the presently used glow discharges [105].

Another outstanding project of the AUG experiment is to investigate the applicability of Tungsten as a material for plasma facing components. Starting in 1996 [106] the surface of the plasma facing components has been changed stepwise from Carbon to Tungsten. In the 2007 experimental campaign, the complete coverage of the first wall has been reached (figure A.4). Some notes on this topic can be found in appendix C.

Major / minor plasma radius	R_0 / a	1.65 m / 0.5 m
Max. height / width of plasma cross section	$2a / 2b$	1.6 m / 1.0 m
Plasma volume / surface	V_p / S_p	$14 \text{ m}^3 / 42 \text{ m}^2$
Max. average triangularity	$\langle \delta \rangle$	0.5
Max. plasma current	I_p	1.6 MA
Max. toroidal field	B_t	3.9 T
Max. OH flux swing	Φ_{OH}	9 Vs
Max. discharge duration (current flat top)	t_{FT}	10 s
Min. discharge sequence	t_D	15 to 20 min
Max. plasma heating:		
ohmic	P_{OH}	1 MW
neutral beam injection (60 keV, Deuterium)	$P_{NBI(1)}$	$4 \times 2.5 \text{ MW}$
neutral beam injection (100 keV, Deuterium)	$P_{NBI(2)}$	$4 \times 2.5 \text{ MW}$
ion cyclotron resonance heating ($f \in [30, 120] \text{ MHz}$)	P_{ICRH}	$4 \times 2 \text{ MW}$
electron cyclotron resonance heating ($f = 140 \text{ GHz}$)	$P_{ECRH(1)}$	$4 \times 0.5 \text{ MW}$
($f \in \{105, 140\} \text{ GHz}$)	$P_{ECRH(2)}$	0.8 MW

Table A.1: Collection of a few basic parameters characterising plasma operation of the AUG Tokamak. A high amount of heating power related to the plasma volume is provided in order to permit studies of plasma-wall interaction with power loads at the divertor targets similar to values projected for a fusion reactor ($\sim 10 \text{ MWm}^{-2}$).

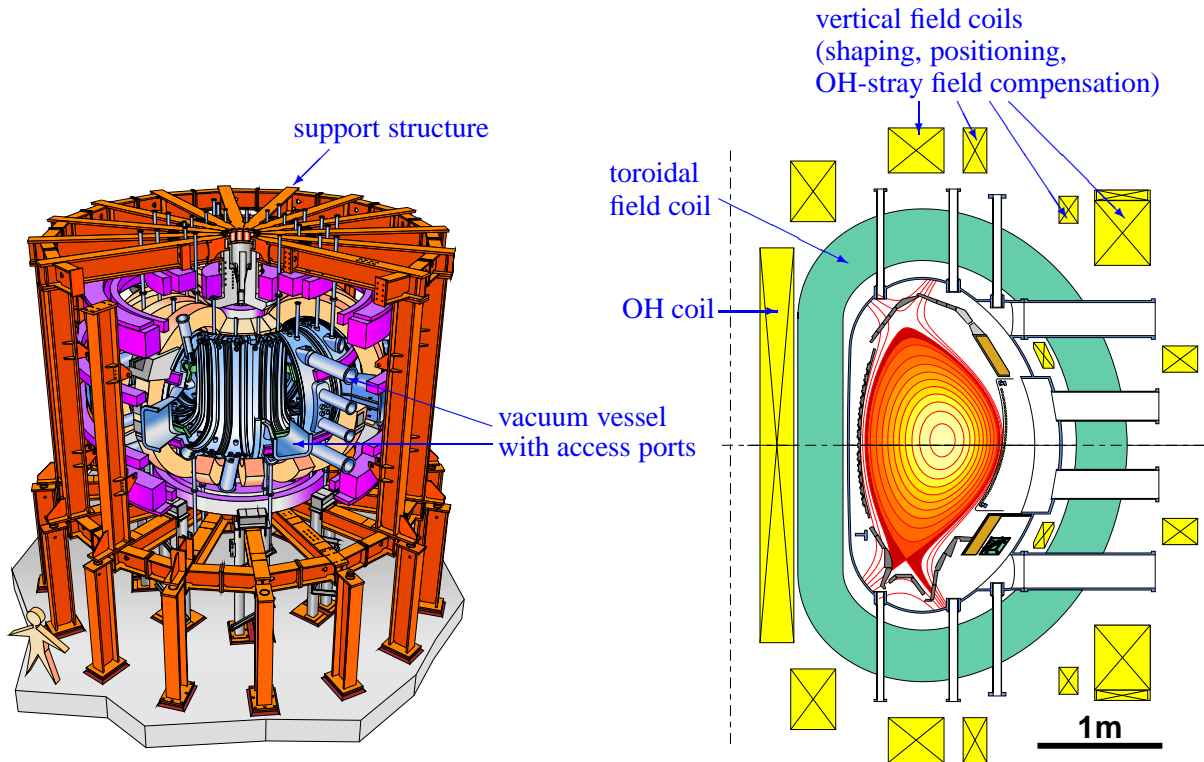


Figure A.1: General assembly of the AUG device. All magnetic field coils are positioned outside the vacuum vessel. The capability for positioning and shaping of the plasma cross section by the distant poloidal field coils is indicated in figure A.2.

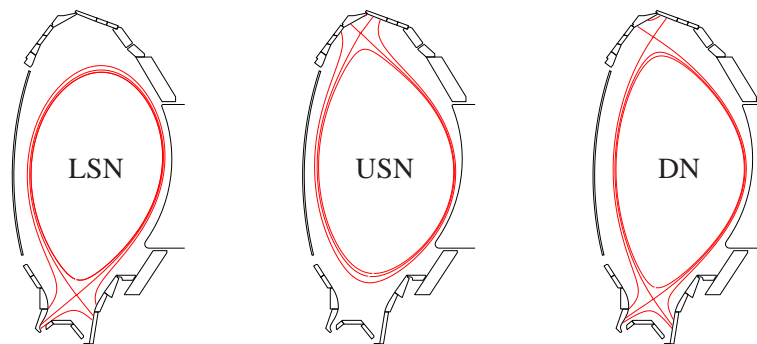


Figure A.2: Cross sections of poloidal magnetic flux surfaces from equilibrium reconstruction of three discharges: #20901, $t = 4.7$ s (lower single null LSN); #21283, $t = 3.8$ s (upper single null USN); #21148, $t = 3.7$ s (double null DN). The poloidal field coils are mandatory for the stabilisation of the radial and vertical position of the plasma column. In addition, they are used to divert the poloidal magnetic field in one or two locations inside the plasma vessel for active control of the areas of primary plasma-wall interaction.

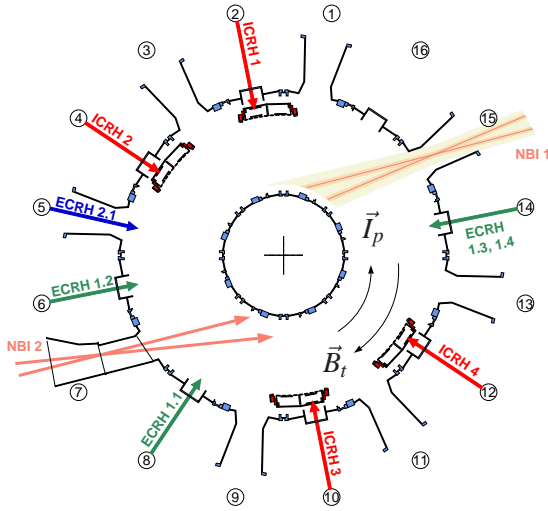


Figure A.3: The auxiliary heating systems of the AUG Tokamak comprise neutral beam injection (NBI), ion cyclotron resonance heating (ICRH) and electron cyclotron resonance heating (ECRH). One of the NBI boxes (NBI2) is configured such that 2 of 4 sources can be used for current drive studies. Also indicated in this figure is the standard configuration of the toroidal components of the magnetic field \vec{B}_t and the plasma current \vec{I}_p .

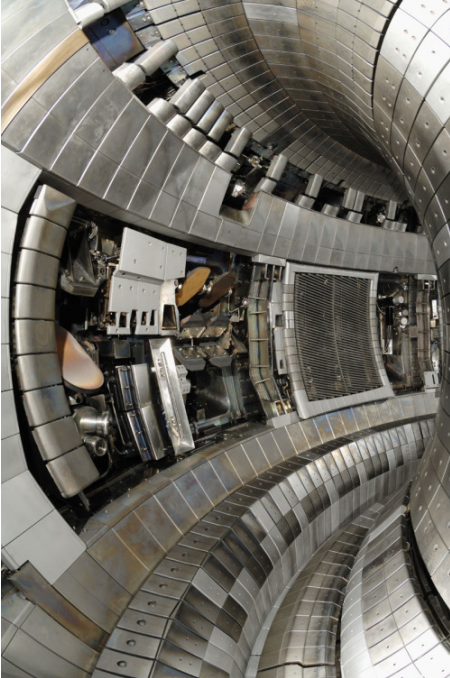


Figure A.4: Tangential view into the plasma vessel taken in the maintenance phase before the 2007 experimental campaign. After stepwise replacement of Carbon- with Tungsten-surfaces starting in 1996 [106] the complete coverage had been achieved. Besides the impact of Tungsten as an impurity species in the plasma in terms of dilution and radiation losses, the high reflectivity of metallic surfaces hampers the analysis of visible spectroscopy data which is further discussed in appendix C.

Appendix B

Calibration of D_α Diagnostics

In order to gather maximum information from diagnostics data, calibration procedures are performed before and eventually after data acquisition. At a first glance, the calibration of optical diagnostics in the visible spectral range does not seem to pose severe problems, since calibrated light sources are available and the properties of the diagnostics components should be well characterised. In this section, efforts taken for radiance calibration of the H_α -diagnostics are summarised.

The strike point observation SPO and the tangential cameras XPMC are very similar in assembly. Collecting optics are placed close to the plasma boundary and light is transmitted to the detector at a distance of a few meters to the vacuum vessel by fiber guides. Line emission from the plasma is selected by using narrow band pass filters which are mounted in the center of relay optics to reduce beam divergence. SPO collecting optics and fibers are located inside the vacuum vessel like most of the optical diagnostics and calibration measurements can be done only before and after the experimental campaign. In the case of the XPMC diagnostics, the whole setup is mounted in an entry port separated from the vacuum vessel by a window and is accessible also during plasma operation. If calibration measurements are made on the entry mounting separately, the impact of the port window on sensitivity of the diagnostics has to be estimated, which may be a difficult task if during operation the window pane is successively coated with thin layers originating mainly from wall conditioning glow discharges (see also appendix C).

The principle of radiance calibration is simple: the diagnostics is operated with the settings valid for plasma experiments, which comprise eg focal length, aperture, filter type, detector parameters like CCD-binning etc., and is exposed to a light source of specified spectral radiance L_λ . For this purpose an integrating sphere is used which provides light equally distributed in solid angle from a small cut in the surface of the sphere. Care has to be taken that the diagnostics is exposed to full aperture. Brightness of the light source is set by controlling the electric current of the halogen bulbs of the lamp accurately. The spectrum L_λ of the source is depicted in figure B.1 which is the result of a cross calibration with a commercial spectral radiance norm and probably containing a systematic uncertainty in the order of 5% [107]. When calibrating spectrally dispersing diagnostics (wavelength calibration presumed), incident spectrum and detector response can be directly related to yield calibration factors regardless of the spectral composition of the measured signal during later operation. If the diagnostics is integrating in its spectral range like it is the case for simple filter setups, the relative spectral sensitivity needs to be known as well as the spectral profile of the light to be recorded.

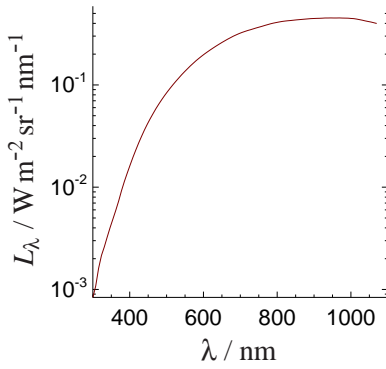


Figure B.1: Spectral radiance L_λ of calibration light source.

The spectral transmission of the various optical components (lenses, panes, etc.) may vary across a large spectral range, but is assumed to be constant on the small interval imposed by the narrow band pass (here $fwhm \sim 1 - 2$ nm) filter which makes this filter the central part of investigation. Figures B.2 and B.3 show spectral transmission of one filter sample to illustrate several important aspects.

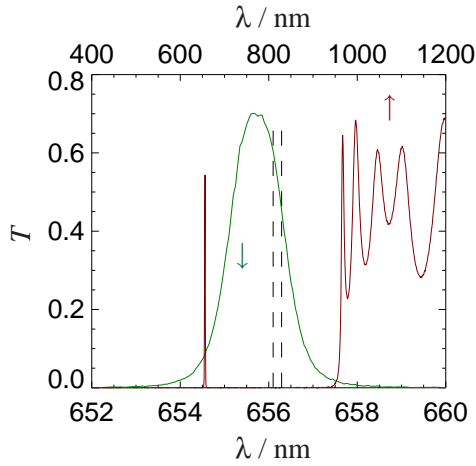


Figure B.2: H_α -filter curve on two wavelength scales of a new sample; dashed lines indicate H_α and D_α spectral lines.

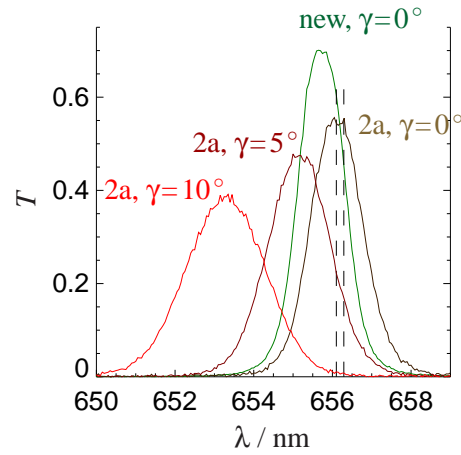


Figure B.3: Filter curves of one sample for different age (new, two years old '2a') and pitch angles γ .

The band pass transmission is obtained by a multilayer system characterised by number, thickness and refractive indices of alternating layers which results in selective transmission based on interference effects. A single transmission peak of a periodic pattern is picked by combining the multilayer stack with appropriate edge filters, eg to block UV and IR photons. When discussing filter transmission curves one has to bear in mind that the optical properties of a multilayer system might not be homogeneous throughout the sample due to the layer growth process of manufacturing. Profiles obtained by spectroscopic measurements are thus a local or an area-averaged description of the transmission depending on the geometry of the probing beam. Figure B.2 shows the properties of a filter sample shortly after fabrication. The peak transmission is placed closely to the desired values of the Hydrogen Balmer- α lines (H_α : 656.28 nm; D_α : 656.1 nm) and the $fwhm$ has been kept rather small (~ 1.5 nm). The magnitude of peak transmission is very good, however presumably achieved at the cost of blocking capability which is expressed in the high IR transmission for $\lambda > 950$ nm. An additional IR filter has to be attached which also reduces transmission in the visible spectral range. Narrow peaks are not resolved with high

precision in the survey measurement because of low wavelength resolution set for a reasonably fast recording of the profile.

One important issue regarding interference filters is long term stability. These types of filters are observed to age and alter optical properties. It is suspected that chemical reactions involving water or Oxygen from the surrounding atmosphere if not properly sealed or from contamination of the multilayer stack lead to a red-shift and a broadening accompanied with reduced peak transmission of the filter curve like shown in figure B.3. The time period of change seems to be large enough in relation to the duration of an experimental campaign of about 6-7 months at AUG. Usually it is tried to avoid maintenance work like filter monitoring at diagnostics in operation if it is impossible to perform calibration measurements. The reason is that the filter would have to be removed from the configured system and reinserted without the possibility to check for variations of the optical properties of the whole setup.

As already mentioned, the filter is placed in the center of relay optics which map the light source - here the exit plane of several fibers - to the detector. The object to be mapped being placed in the focal plane of the collimating lens, light from each point is transmitted through the filter with very low divergence, but with an angle of pitch γ to the optical axis depending on radial displacement d_r and focal length f_c involved: $\tan \gamma = d_r / f_c$. With $d_r < 5$ mm and $f_c = 55$ mm like employed in the XPMC X-point view, pitch angles of $\gamma < 5^\circ$ are found. The impact of pitch angle on the transmission profile is apparent from the measurements shown in figure B.3. Regarding the position of the H_α and D_α lines, the system is most sensitive for light collected from the optical axis and becomes less sensitive for increasing pitch angle γ . In this example the system becomes insensitive for large angles $\gamma \approx 10^\circ$. To consider the impact of pitch angle for arbitrary filter geometry, two measured profiles can be used as boundary values for interpolation. Filter curves of figure B.3 can be approximated with Gaussian profiles with very good accuracy. Parameters determining the profile shape can be interpolated linearly in $\cos \gamma$ to give a reasonable description. It should be noted that pitch angles for these measurements were set with an uncertainty of about 0.5° .

Obviously, position and shape of the spectral line to be recorded needs to be known in order to provide accurate calibration factors. In general, line emission from a magnetised plasma is influenced by various effects. The width is determined by Doppler-broadening due to the temperature of the species and Stark-broadening depending on electron density. Zeeman splitting related to the strength of the magnetic field results in an increased spectral spread. This influence of the magnetic field comprises the dependence of the spectral profile on viewing geometry relative to the field direction (Zeeman σ - and π -components). For observation of nearby lines the relative intensities would have to be known in advance, eg the ratio of Hydrogen isotopes in case of recording both H_α and D_α . An additional complication arises if line emission becomes comparable in amplitude to background radiation like the Bremsstrahlung continuum. An example of a D_α profile obtained from a high resolution spectrometer attached to a radial line of sight in the divertor region is given in figure B.4. The major part of the spectrum is determined by the Zeeman-components of the Deuterium line and only a small contribution from Hydrogen is seen at the long wavelength wing. For the purpose of interpretation of so-called D_α data it is assumed that the plasma consists purely of Deuterium, which is realistic in view of a typical isotope ratio of $H/D \approx 5\%$.

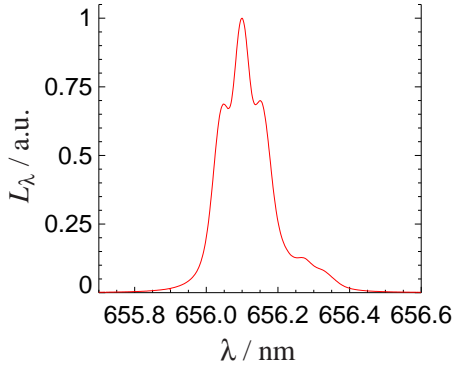


Figure B.4: Example of spectrally resolved D_α emission from the divertor region integrated along a radial line of sight. The width of the separate Zeeman components is due to temperature- and Stark-broadening and the apparatus function of the spectrometer. The long wavelength part of the spectrum stems from the small Hydrogen content of the plasma.

Taking all aspects mentioned so far into consideration, calibration factors f_{cal} would be established as follows. The diagnostics setup is exposed to the calibration source for an exposure time of $t_{exp,c}$ and the detector response is preprocessed like in the actual diagnostics operation which might include detector offset subtraction and basic data reduction like profile fitting of mapped fibers. This data is denoted as $D_{c,i}$, with i identifying a single detector element or mapped fiber. This index also stands for a certain viewing geometry and corresponding plasma parameters to influence the spectral profile $P_{\lambda,i}$ of the line observed. With the filter curve denoted as $F_{\lambda,i}$, here i now determining pitch angle γ_i , the calibration factor is:

$$f_{cal,i} = \left[\int L_\lambda(\lambda') F_{\lambda,i}(\lambda', \gamma_i) d\lambda' \cdot t_{exp,c} \right]^{(a)} \cdot \left[\left(\frac{\int F_{\lambda,i}(\lambda', \gamma_i) P_{\lambda,i}(\lambda') d\lambda'}{\int P_{\lambda,i}(\lambda') d\lambda'} \right)^{-1} \right]^{(b)} \cdot \left[(D_{c,i})^{-1} \right]^{(c)} .$$

Since the spectral transmission appears in numerator and denominator and other optical components are presumed to have constant transmission in the spectral interval of interest, only the filter profile is considered and may be used in arbitrary scaling. The first term (a) describes the relative amount of energy (per solid angle and area) which was delivered to the system and the second term (b) is the fraction of the line to be observed which reaches the detector in the same transmission scaling. Term (c) stands for the detector response given in units of counts ct. Recalling that $[L_\lambda] = \text{W m}^{-2} \text{sr}^{-1} \text{nm}^{-1}$, the unit of the calibration factor becomes $[f_{cal,i}] = \text{J sr}^{-1} \text{m}^{-2} \text{ct}^{-1}$. This factor is applied to the (preprocessed) raw data of diagnostics measurements M_r obtained at exposure time $t_{exp,m}$ to give calibrated data M_c :

$$M_{c,i} = M_{r,i} \cdot f_{cal,i} \cdot t_{exp,m}^{-1} \quad ; \quad [M_{c,i}] = \text{W sr}^{-1} \text{m}^{-2} .$$

So far the spectral sensitivity of the detectors has not been regarded. SPO and XPMC employ standard silicon CCD-sensors. The quality of these is characterised among other aspects by the probability of the production of a hole-electron-pair in the semiconductor by an incident photon. This so-called quantum efficiency (QE, see fig. B.5) is a measure of the principal sensitivity of the sensor but does not give an absolute ratio of detected and incident photon flux density, since the sensor area usually is only partly sensitive depending on the detailed CCD design. With a broad range of spectral sensitivity an emphasis is put on the blocking capability of filter setups. Taking the accuracy of separate transmission measurements (noise $\sim 0.1\%$) into account, calibration factors are afflicted with an uncertainty which is hard to quantify. Outside the wavelength intervals of remarkable transmission, the light emitted from the calibration source is assumed to be blocked completely, although only a very small amount of passing photons

distributed over a large spectral range would have a considerable impact on the detector response and would lead to an underestimation of line radiation.

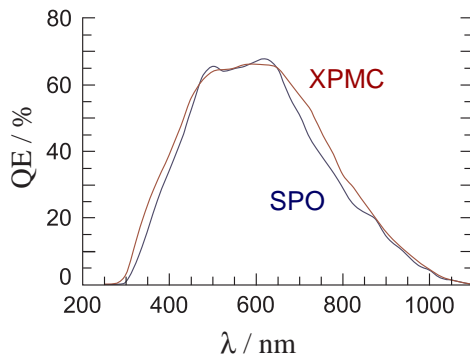


Figure B.5: Quantum efficiency of CCD-sensors employed [108].

Strike Point Observation SPO

The setup of the SPO diagnostics contains two beam paths established with a dichroitic beam splitter, such that two different lines can be recorded with the same detector simultaneously. D_{α} ($\lambda=656.1$ nm) and CIII ($\lambda \approx 465$ nm) are the standard pair (see also section 3.1). A grey filter is used to adjust the brightness of the D_{α} -channel to ensure a comparable recording level for the different lines. This additional filter is removed for calibration measurements to improve the signal-to-noise ratio, but has to be considered for the actual calibration factors. The array of fibers is mapped to the CCD which is operated such to exploit the full horizontal resolution (fiber position) and to collect the fiber transmitted radiance in a one dimensional data array by vertical binning. An example is shown in figure B.6 (SPO outer divertor array: 69 fibers). Decreasing sensitivity towards the edges of the mapped area are due to the vignetting effect of the collecting lens. The spectrally integrated transmission profile of the filter does not strongly depend on pitch angle of the incident photons to the optical axis.

Because the diagnostics setup is mounted close to the vacuum vessel it is partly affected by vibrations which result in a shallow shift of the CCD position relative to the mapped image of the fibers. The fiber image is observed to shift on a pixel scale in arbitrary direction. Consequently, it is not perfectly safe to use the calibration data in full resolution to prepare calibration factors for each detector element. The more adequate treatment is to characterise the mapping of each fiber by applying a fit function. A function which was found to model the fiber image quite well, including fiber cross-talk, is $f(i) = \sum_{j=0}^N a_j \exp\left[\frac{-8|i-b_j|^3}{c_j \ln 2}\right]$, with i the detector array column index as the variable, j the index of the fiber and $\{a, b, c\}$ parameters describing amplitude, position and width of a single peak. If these parameters are properly adjusted (see figure B.6), the amplitude is used as a measure for line radiance. For analysis of experimental data, the same fit function is employed with the same width, the position being slightly corrected if required, and the amplitude remaining as the free parameter. For the preparation of calibration factors for each fiber, the transmission curve of the interference filter has been measured for normal beam geometry and the sensitivity to the D_{α} -line is considered by using the average transmission for $\lambda \in [656.0, 656.2]$ nm. The impact of pitch angle on filter transmission as discussed above is not treated since these angles are unknown and could be determined only by a complete reconfiguration of the diagnostics. For larger pitch angles for fibers radially more distant to the optical axis, higher calibration factors would result, probably similar in magnitude like obtained due to the vignetting effect of the collecting lens.

Figure B.7 displays the calibration factors for the same fiber array obtained from calibration measurements before and after the 2006 experimental campaign. The deviation is extremely low and suggests that the diagnostics setup is largely unaffected by plasma operation. Slightly higher values for the after-campaign factors might be related to reduced transmission in silica fibers or to aging effects of the interference filter. A much simpler explanation would be a thin coating on the surface of the collecting lens formed during operation, predominantly of wall conditioning glow discharges.

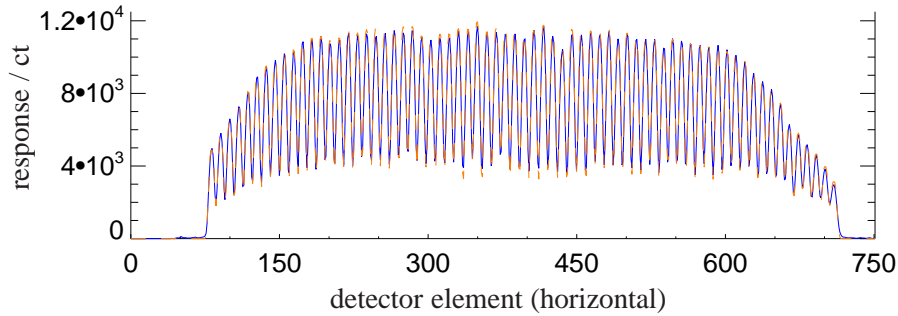


Figure B.6: SPO outer divertor array: offset subtracted detector response to calibration source illumination (blue solid line); fit function to characterise fiber mapping (orange dashed line).

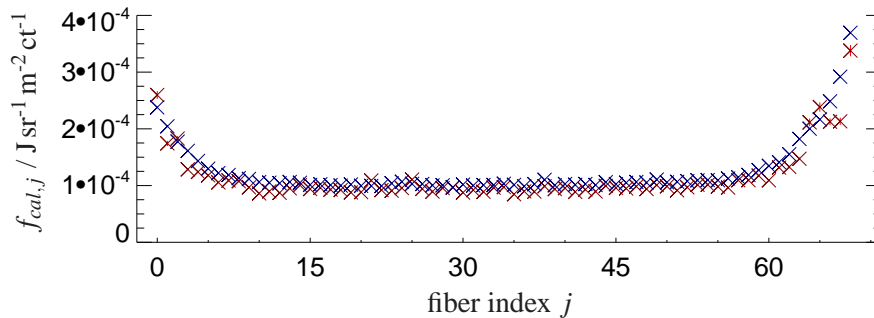


Figure B.7: SPO outer divertor array: calibration factors obtained from measurements before (red) and after (blue) the 2006 experimental campaign.

In present day fusion experiments, optical fibers are commonly used to transmit light from collecting optics near the plasma to spectrometers and detectors installed far from the machine hall to keep a safe distance to sources of electromagnetic interference and mechanical vibrations. These fibers exhibit low transmission losses, are easy to handle and are sufficiently heat proof to resist baking procedures performed on the vacuum vessel. However, optical fibers are not immune to ionising radiation [109] which can result in strong impact on calibration efforts and hamper the interpretation of the recorded signal.

Neutrons produced in fusion reactions penetrate all surrounding materials and accompanied nuclear reactions are the source of γ -radiation and high energetic electrons originate from subsequent ionisation processes. Ionising radiation penetrating the fiber causes radio luminescence which is supposed to consist mainly of Cherenkov-radiation and emission from defects of the glass structure like non-bridging Oxygen which might have been caused by radiation impact

[110]. These photons emerging from the fiber volume create an offset to the signal collected from the plasma which is proportional to the fusion reaction rate. Aside from this disturbing effect, the deterioration of fiber transmission is a major concern for the long term availability of plasma diagnostics. The formation of structural defects and color centers results in increased scatter of former passing photons to angles outside the margin of total reflection at the boundary of core and cladding of the fiber. This issue of radiation induced attenuation is complex and comprises different mechanisms leading to transient or permanent damage. It is observed that transmission may recover at room temperature, by photo bleaching or be annealed by heat treatment [111]. Radiation resistance is found to depend on fiber material composition, ie dopants, and temperature of operation. Information about optical fibers in an ionising environment have to be gathered from experimental efforts and cannot be deduced from first principles. Regarding the experience obtained from D-T operation so far (eg [112]), the use of optical fibers for large Q (high fusion gain) devices like ITER (Tritium phase) has to be excluded and more complicated optical arrangements have to be considered for diagnostic access.

Deuterium operation of the ASDEX Upgrade device creates dose rates and fluences which do not seem to have a deleterious effect on fiber based diagnostics. At least this is the case for the commonly used pure silica fibers with high concentration of hydroxide. Color centers formed due to the destruction of chemical bonds by radiation impact are supposed to be neutralised by the saturation of dangling bonds by the hydroxyl group which is highly mobile in the glass structure. A very different behaviour is observed when glass fibers are exposed to radiation which is discussed in the next subsection.

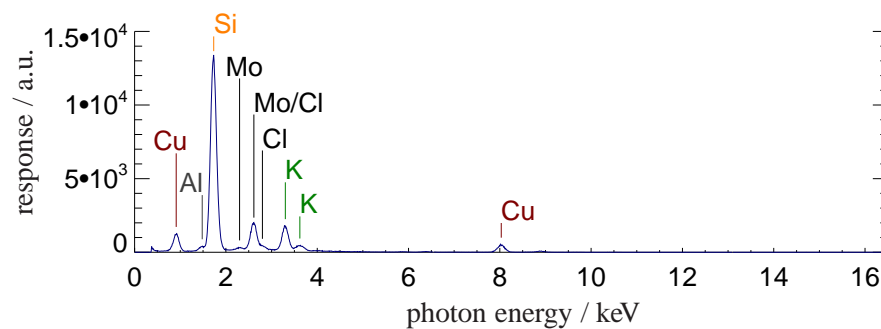


Figure B.8: Spectrum of proton induced X-ray emission from a silica fiber.

Concerning the striking difference of silica and glass fibers used for the D_α -diagnostics, the composition of each fiber material was examined. A proton induced X-ray spectrum (not calibrated on ordinate) is depicted in figure B.8. High energetic protons (here $E_p = 3$ MeV) ionise electrons of the K or L-shell and the line radiation of the shell relaxation is recorded. The recording and analysis of such spectra for fiber samples is non-standard regarding the in-house expertise. Particle induced X-ray emission (PIXE) spectra are usually interpreted by comparison to reference samples [113]. Nevertheless, a basic X-ray spectrum like of figure B.8 might be discussed qualitatively. The aspect to mention here shall be simply to confirm the high purity in composition of the fiber sample. Beside Copper which is the bulk material of the sample holder, the appearance of Potassium most probably relates to the use of potash (K_2CO_3) as flux melting agent in the manufacturing process. The assignment of Molybdenum and Chlorine is not perfectly convincing regarding the energy of the characteristic photons and it is unclear whether these elements

should be thought of as contamination or ingredient. It should be emphasised that this kind of interpretation is sensible only in comparison to the spectrum obtained for the glass fiber. This topic is followed up in the discussion on optical properties of the XPMC image guide below.

XPMC Diagnostics During the 2006 Campaign

Without prior experience in the operation of the tangential cameras, the goal was to perform one calibration measurement before the experimental campaign and keep the diagnostics installed, in particular to reduce efforts in the determination of viewing geometry which was planned to be based on exposures of the empty and illuminated vacuum vessel. A calibration procedure as described for the SPO was employed differing from the latter only in the instance that pre-processing of CCD data is restricted to offset subtraction. Illumination of the collecting optics results in a detector signal like shown in figure B.12. The structure of the image guide is recognised by small gaps between multi-fibers (5×5 single fibers of $10 \mu\text{m}$ diameter) and defects of the fiber bundle of reduced transmission. If the setup was unchanged for experimental operation, these effects would be corrected for by the calibration factors. For practical reason the detector mounting has to be disconnected from image guide and port mounting before the diagnostics is installed at the plasma vessel. Minimal differences in adjustment ($\sim 10 \mu\text{m}$ would be sufficient) affect the appearance of calibrated data which is expressed by systematic scatter of data points due to imperfections of the image guide. Taking the quality and dynamic range of experimental data into account, which is strongly influenced by detector noise and hard radiation (n, γ) impact, this shift of calibration factors is not easily compensated. The more important aspect of correcting for the vignetting effect of the collecting lens is however met.

Interpretation of D_α emission inferred from data deconvolution in terms of atomic neutral flux density suggested the calibration factors being about one order of magnitude too low and in addition, sensitivity of the diagnostics seemed to decrease steadily during the campaign.

The reason for the large discrepancy in radiance obtained was found to be insufficient IR-blocking of the interference filters used. Transmission of one of the XPMC filters is depicted in figure B.2 which was checked before the calibration measurement only for $\lambda < 800 \text{ nm}$. Consequently, the detector was predominantly exposed to IR radiation during calibration and factors valid only for the D_α spectral interval cannot be deduced since the sensitivity of the whole optical setup and sensor would have to be known to high accuracy in the IR range relative to the interval of interest.

A continuous drop in sensitivity of the diagnostics can be attributed to radiation damage. This aspect is documented by the detector response to a well defined time interval of a standard discharge (here ohmic discharge with a phase of additional heating) which is a frequently performed part of the experimental campaign. The execution of such an experiment on a regular basis serves as an inspection of reliable machine operation and as a diagnostic survey of plasma performance, eg in terms of impurity content or isotope ratio. In this case the diagnostics setup itself was focussed on. Figure B.9 illustrates the approach and the result obtained. Three regions of interest (ROI) were defined to monitor different parts of the viewing geometry. Data of these ROI was averaged over detector area and time to provide a robust measure largely unaffected by small deviations in plasma position or density on a short time scale. A series of 31 discharges has been analysed and the radiance obtained by applying the pre-campaign calibration factors is related to the total neutron production as the primary origin of fiber degradation. Although there is quite some scatter, the general trend seems to be robust. This series has been adopted to model the relative decay of image guide transmission as a function of neutron fluence, for which monotonic characteristics have been assumed.

In order to obtain suitable factors for absolute radiance calibration, a cross-calibration was performed regarding the data of radially viewing D_α -diagnostics which was operated for a couple of discharges about half time of the experimental campaign. Comparison of diagnostics data is complicated by the fact that the viewing geometries are practically perpendicular to each other. Radial integration of volume emission based on tangential camera image data deconvolution inherently contains systematic uncertainties imposed by data analysis. Due to this inaccurate procedure a systematic error for the calibration factors within a factor of 2 cannot be excluded.

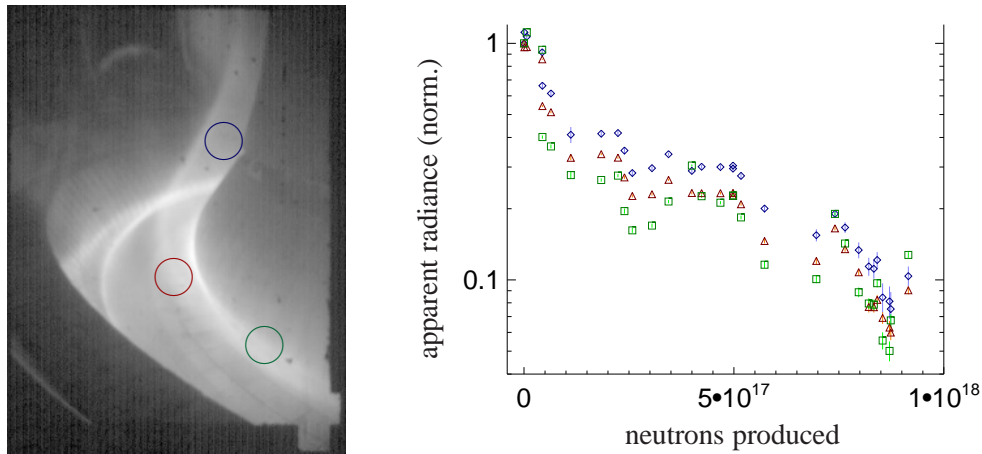


Figure B.9: Left: Image of reference discharge to monitor the image guide transmission (#20861, $t \in [3.977, 3.978]$ s); circles indicate ROI-definitions. Right: Detector response multiplied by pre-campaign calibration factor for each ROI, averaged for a certain time interval of steady plasma conditions and normalised to the first data point of the series. The neutron production relates to a total number of 497 discharges.

At this place, the discussion about the impact of ionising radiation on optical fibers started in the previous subsection shall be continued. It has been tried to document the status of the image guide by spectrally resolved transmission measurements (see figure B.10) by using a basic spectrometer-diode setup. The new sample shows a reasonable magnitude in transmission about 50% over a wide range of the visible spectrum which would be hard to achieve with periscope optics at reduced flexibility. The transmission is seen to drop in the blue part of the wavelength interval. The larger error bars for the measurement of the new sample compared to the other two are based on an improved setup for those. Degradation of the fiber transmission is observed to predominantly affect shorter wavelengths and is less pronounced for the near IR part. A closer look reveals that the reduction of transmission found for the H_α/D_α lines is not compatible with the impression gained from the reference discharge series presented in figure B.9. The reason is the impact of white light (3000 K) which was used to illuminate the spectrometer for reference and the fiber bundle connected to the spectrometer during the measurement. The fiber was placed in front of the entrance slit of the spectrometer and therefore exposed to the full spectrum. This setup was chosen in order to illuminate the fiber to full aperture which would not have been the case if put to the exit slit. The left part of figure B.10 shows the appearance of the photo bleached image guide when exposed to white light. Obviously the central part of the bundle which was illuminated during the transmission measurement is capable of transmitting a higher amount of photons of lower wavelengths. A striking observation is that photo bleaching of this sample

could not be reproduced, eg by illuminating the edge parts of the bundle cross section. Although identical experimental conditions were applied, the glass structure had lost its sensitivity to photon impact which indicates the occurrence of some process changing the properties of the fiber material on a larger time scale.

Reduction of fiber defects by thermal annealing has been successfully demonstrated by baking of the fiber in a vacuum oven. A few tests showed that the more and longer heat treatment is applied, the more pronounced the recovery of fiber transmission, eventually reaching original values. Probably very slow diffusion or reconfiguration processes in the glass matrix supported by thermal motion of its constituents are responsible for this behaviour. Maximum settings tested so far are a temperature of 190°C and a baking time of 48h. This procedure is restricted by the thermal flow limit of the cement which fixes the fibers in the end pieces.

It is highly desired to recover transmission properties of the fiber bundles, because of the high purchase costs. Unfortunately, no silica fiber bundles of comparable image resolution are available on the fiber market. These would be even more expensive, but also robust against radiation levels encountered at AUG. An alternative scheme would be to operate imaging diagnostics with heated fiber bundles. The technical effort might be rewarded by an improved resistance of the system against ionising radiation.

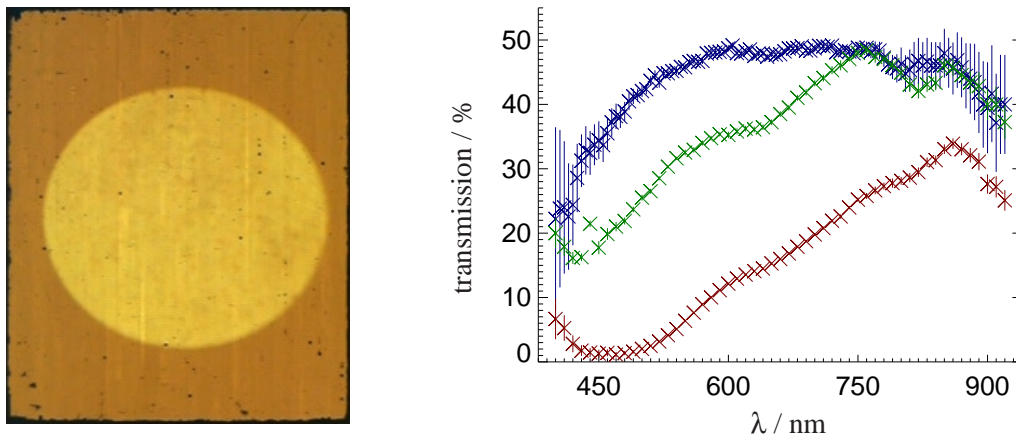


Figure B.10: Left: Image guide after illumination with white light for transmission measurement (photo bleaching). Right: Image guide transmission of one sample (length $108''$): new (blue), after 2006 operation (red) and the latter after baking at 180°C for 24 hours in vacuum (green).

Proton induced X-ray emission (fig. B.11, compare to fig. B.8) indicates the very different composition of the glass fiber compared to the pure silica fiber. Except Copper as part of the sample holder, Potassium, Barium, Cerium, Zinc, Zirconium and Lead are reasonable ingredients from flux melting agents or as dopants to influence the refractive indices of core and cladding. The occurrence of the elements K, Ba, Zn, Zr and Pb have been confirmed by a separate X-ray fluorescence analysis. Given the additional components it is supposed that a much higher effective cross section for the production of defects and color centers by the impact of γ -radiation and fast electrons exists. Also the nuclear reaction rate involving neutrons at a certain flux density in the fiber volume is likely to be larger compared to pure silica and this way directly depositing sources of γ -radiation in the fiber material.

The generation of radioactive isotopes due to neutron activation was examined on a simplified basis using the activation code FISPACT [114]. Since the composition of the glass is not known

quantitatively, merely fixed masses of the single elements where exposed to a neutron fluence typical to the one present in the periphery of the AUG plasma for one discharge. This way, it was hoped to identify those isotopes which deposit the majority of heat by γ - and β -radiation. For each element, the isotope with the largest integrated decay heat for a time interval of several half lives was picked. This simple calculus was done only for isotopes characterised by a half life reasonably short with respect to the duration of the experimental campaign. It was found that this decay heat was comparable to the one from the natural K-40 which is present in both silica and glass fibers, albeit in different concentrations. Obviously it is necessary to examine the detailed energy spectrum of the radiators in relation to the absorption mechanisms of the glass structure. A problem, which to the knowledge of the auther has not been addressed so far and unfortunately exceeds the capacity of this thesis.

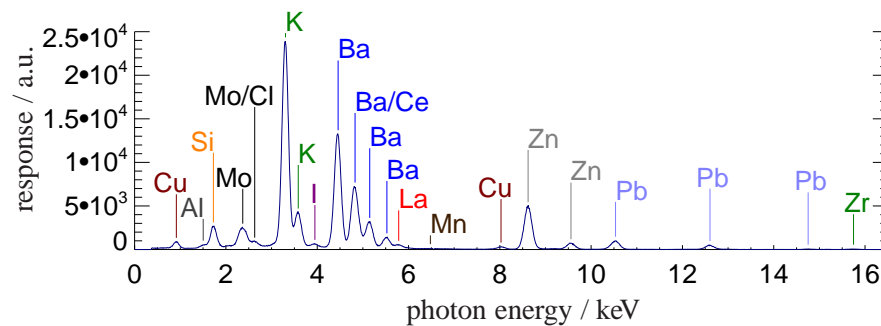


Figure B.11: Spectrum of proton induced X-ray emission from the glass fiber.

XPMC Diagnostics During the 2007 Campaign

Regarding the experience of the 2006 campaign the following measures were taken for experiments in 2007. Additional IR blocking of D_α -filters was implemented and checked over the full range of spectral detector sensitivity. Calibration measurements were performed before and after a short phase of dedicated plasma discharges to minimise radiation induced deterioration of image guide transmission. The diagnostics setup was installed for a total number of 104 plasma discharges with an estimated neutron production of $N_n \approx 7.7 \cdot 10^{16}$ which lead to a decrease of sensitivity of about 20%. For each discharge of interest a set of calibration factors is deduced by linear interpolation on neutron production between the boundary values.

Figure B.12 illustrates the calibration factors of one CCD-column obtained by disregard and consideration of the impact of pitch angle on the filter transmission profile. For the latter the actual filter curve has been measured for several pitch angles and values for arbitrary pitch angles are obtained by interpolation of Gaussian fit functions. For this example, the transmission for the D_α line has been inferred from the average value for $\lambda \in [656.0, 656.2]$ nm.

Because the spectral integral of the transmission profile is only weakly dependent on the pitch angle (variation of a few percent) the blue curve of figure B.12 represents the vignetting effect of the collecting lens only. If in addition the impact of pitch angle is included (red curve), a strong variation is found for increasing radial distance to the optical axis. The more the wavelength interval of consideration is displaced from the center of the transmission profile, the larger the deviation emerges. Although this strong impact is known in principle, it is not considered for the calibration factors and the pragmatic procedure as described for the SPO diagnostics is applied,

since the actual H_α/D_α spectrum is unknown and the calibration factors should be regarded with an uncertainty of magnitude in the order of a factor of 2, likely increasing towards the edges of the image, induced by the large wavelength interval chosen.

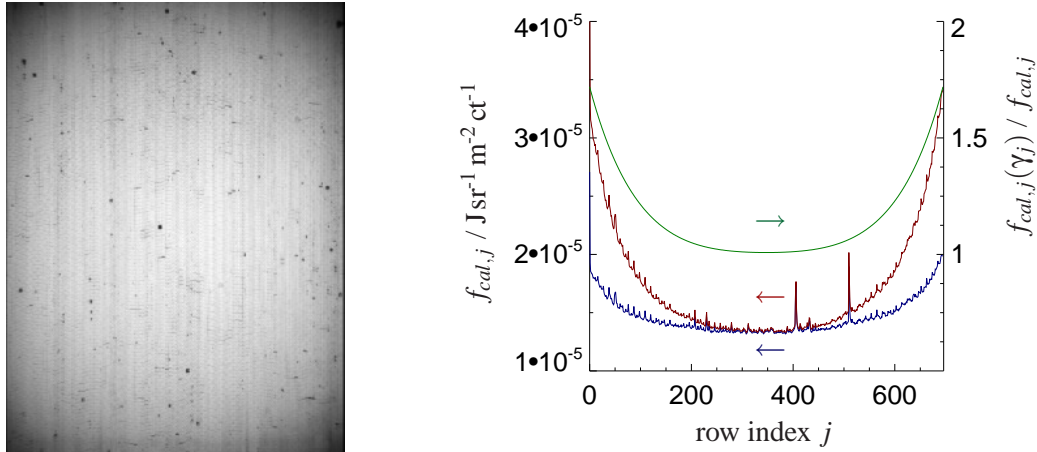


Figure B.12: Left: CCD raw data of calibration exposure. Right: Calibration factors for one CCD-column with (red) and without (blue) the consideration of the impact of pitch angle on filter transmission.

Appendix C

Reflection Properties of Tungsten Surfaces

One of the basic tasks for fusion research is to find integrated configurations regarding plasma and machine parameters which ensure compatibility of plasma performance and integrity of plasma facing components to allow for economic power generation. The contribution of the ASDEX Upgrade Team in this field is the characterisation of Tungsten as a first wall material. Besides the impact on plasma operation, the presence of metallic surfaces in the plasma vessel displays a drawback for diagnostics in the visible spectral range, since reflected light becomes part of the detected signal which in the first place is considered to originate from the volume of primary viewing geometry. A detailed knowledge of the reflection properties is required to judge the relevance of this issue for a particular diagnostic application. In the framework of the analysis of D_α video diagnostics data, diffuse reflection at Tungsten surfaces of the AUG vessel has been characterised for the first time and considered in ray-tracing for image deconvolution. In this section, after some remarks about the choice for plasma facing materials and the situation at AUG, the measurement of diffuse reflectivity at a Tungsten covered tile of the AUG Tokamak is presented.

The materials used for plasma facing components can be divided into two main groups: low-Z materials for which examples are Beryllium (Be, JET Tokamak [115]) or Carbon (C, DIII-D Tokamak [116]) and high-Z materials like Molybdenum (Mo, Alcator C-Mod Tokamak [117]) and Tungsten (W, AUG Tokamak [106]). An elaborate description of motivation and results of the Tungsten-programme at the AUG Tokamak, in which the first wall has been successively converted from Carbon to Tungsten over several experimental campaigns and experience has been gathered for both elements, can be found in [118].

Atoms from the first wall are released through physical and chemical sputtering imposed by the impinging plasma ions. Physical sputtering is characterised by a threshold energy which is determined by the surface binding energy of the wall material and the mass ratio of projectile and target particle. Considering protons, deuterons and tritons the sputtering yield for a given impact energy is larger for the low-Z elements. Aside from chemical reactions of Oxygen or other elements which might be present as impurities with the first wall, chemical sputtering is relevant predominantly for reactions of Hydrogen and Carbon. Hydrocarbons released from the wall display an impurity source for the plasma and on the other hand might be redeposited in areas of low or vanishing plasma-wall interaction. This latter aspect is in particular important with respect to the Tritium operation of a power plant, where the total Tritium inventory is restricted by radiation safety regulations.

Once particles from the wall penetrate the plasma volume, they act as a sink for plasma energy in the electron channel in terms of radiation and cause in addition a dilution of the fusion reactants Deuterium and Tritium. Radiation losses are due to line radiation originating from electron excitation of the ion stages of the impurity species and Bremsstrahlung resulting from acceleration of electrons in the strong Coulomb potentials of impurity nuclei. The electron shell of low-Z elements is fully stripped in the plasma core, whereas high-Z elements are only partly ionised and remain a source of line emission even in the hot core region. This and the aspect of dilution - for an ion stage Z an equal number of fuel ions is replaced - pose severe restrictions on the tolerable impurity concentration for scenarios of plasma operation relevant for energy production. Maximum concentrations are in the order of 10^{-2} for Carbon and 10^{-5} for Tungsten. Although high-Z materials are demanding in terms of impurity content, high erosion rates for light elements and in particular the problem of chemical sputtering of Carbon, they are thought of as being the better choice with respect to the lifetime requirements of plasma facing components.

An additional aspect regarding the first wall with impact on reflection properties shall be mentioned, namely wall conditioning. The general goal is to prevent impurities at the surface of the first wall to interact with the fusion plasma, either by removal from the plasma vessel, eg by conversion to the gas phase and pumping, or by enforced binding to the surface by the growth of surface layers incorporating or simply covering the impurity atoms. A review about various techniques can be found in [105]. Here, only the so called boronisation is mentioned briefly, since it is relevant for the discussion below. Boron layers, or more precisely layers containing boron, are grown on the surface of the vessel wall in a dedicated glow discharge. Anodes are placed at several locations in the plasma chamber and the vessel wall acts as the cathode. A typical procedure like operated at AUG is to perform a Helium glow discharge with a seed of diborane (B_2D_6), resulting in the production of borane layers eventually containing Carbon if involved, termed a-C/B:H, with a thickness of several 10nm. The primary interest of these boronised surface layers is to getter Oxygen which is present in experimental plasma devices due to water from air humidity attached to or incorporated in the vessel components during vented maintenance phases.

D_α -measurements discussed in section 5.2 were recorded in the AUG experimental campaigns of the years 2006 and 2007. In 2006 nearly the whole plasma facing surface area was coated with Tungsten, except upper and lower row of the limiter frame of the ICRH-antennas and lower divertor target modules consisted of pure Graphite. These components are indicated in figure C.1. Frequent boronisations were part of the experimental campaign which can be seen in the upper right picture of figure C.1 from the brown shade on the light grey Tungsten surface. These layers are residues of the previous campaign. The Tungsten coverage of the first wall had reached 100% in the campaign 2007, an example of which is shown in the lower right picture of figure C.1. During the campaign of 2007 no boronisations were performed in order to emphasise the operation being conducted with a clean Tungsten wall such to avoid speculation about the first wall being replaced by a low-Z material due to wall conditioning. First experience gathered with the all-Tungsten plasma facing components are described in [119]. An important detail is that the Tungsten coating on Graphite tiles is done in variable thicknesses depending on the tile position and using different techniques. These procedures, like physical vapor deposition or plasma vacuum spray, also result in different surface roughness and optical properties.

All these details are mentioned in order to provide means of understanding the difficulties faced when trying to characterise the surface of the first wall in terms of reflection properties. The model used for ray-tracing is based on a measurement of reflection at a newly manufactured

and clean Tungsten surface. However, a look on the images of figure C.1 reveals that obviously each part of the plasma facing components is different, either because of surface layers or simply by the plasma-wall interaction which seems to result in a surface more glazed compared to the appearance before the exposure. In addition, surface properties are subject to transient change during an experimental phase depending on position in the vessel. Further, surface layers might be oxidised during vent of the machine, so the actual state in the vacuum chamber remains unknown without in situ examination.

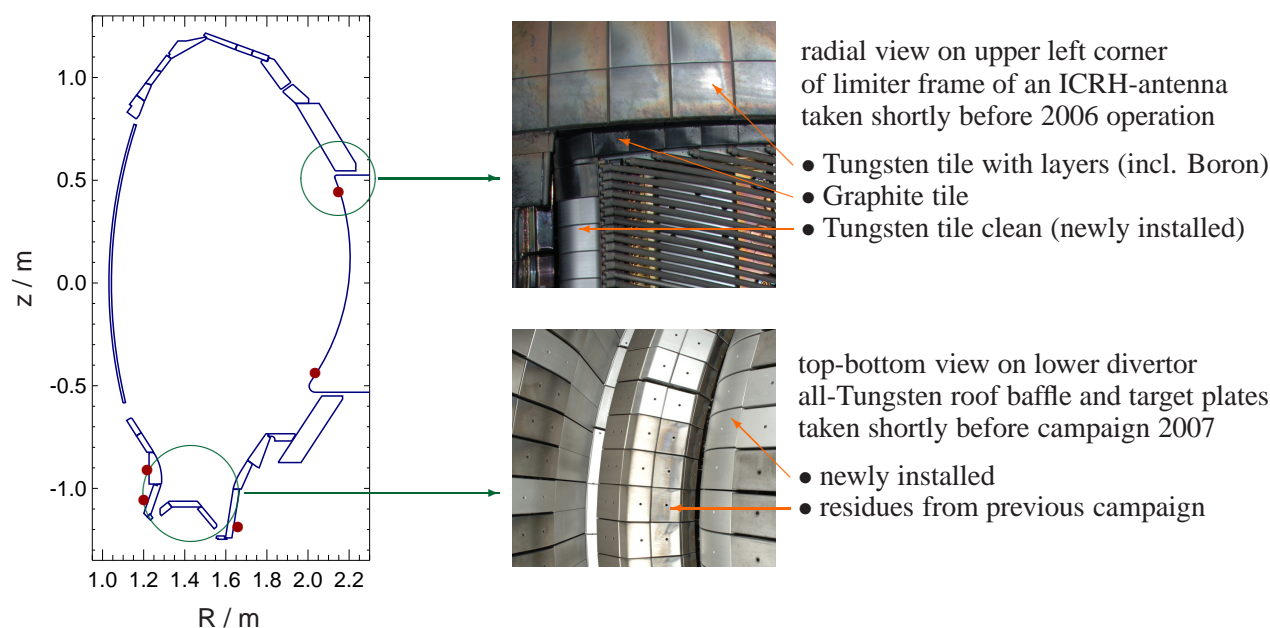


Figure C.1: Left: Scheme of the AUG cross section of plasma facing components. In the 2007 campaign all parts were coated with Tungsten. In the previous 2006 campaign, only components indicated with ● were pure Graphite. Right: Closeup views of indicated areas.

The Tungsten coated tiles used at AUG exhibit a diffuse kind of reflectivity such that a simple measurement limited to zero order geometry, ie as if presuming a specular model, is not sufficient. Scattering of light to a large solid angle requires an intense radiation source and a sensitive detector. In addition, high precision is desired for the geometric arrangement and the result of the measurement should be applicable for D_α image data analysis. These aspects have been met in the setup sketched in figure C.2. The beam of a laser is directed onto the surface of an original tile and the cone of scattered light is probed with optics attached to a detector in a goniometric mounting.

An optical parametric oscillator (OPO), in combination with a powerful pump laser, is used to deliver light close to the D_α -line. Related to issues of long term stability, the wavelength valid for the measurement can be stated to be $\lambda_{\text{OPO}} = 656.2 \pm 0.1$ nm, however at a fluctuating pulse energy in the order of 1 mJ ($\pm 50\%$). Repetition rate and pulse length are 10 Hz and 10 ns respectively. For light detection, avalanche diodes are adopted for sensitive and fast recording. The diode circuit used is characterised by a bandwidth of 50 MHz such that the detector output signal cannot fall below a pulse length of 20 ns, which has to be kept in mind when discussing this signal in the following.

The test sample (fig. C.4) is mounted on a rotary table placed in the beam path such that

the angle of incidence α can be adjusted easily. A mounting which allows to set turn and pitch angles β and γ - see also fig. C.3 - is placed in the direction of specular reflection. The vertex of the cone which is probed coincides with the point of light incidence at the surface of the sample. In order to obtain absolute values for solid angle resolved reflectivity, light intensity of the incident beam has to be measured simultaneously with the scattered beam. Only if the light source was perfectly stable in intensity, one single reference measurement would suffice for a series of (α, β, γ) -triplets. To meet this issue, a beam splitter is introduced. Prior to the reflectivity measurements a relative detector calibration is performed by placing the diodes in the primary and deflected beam path. With this preparation, the signal in the deflected path is a measure of the primary beam intensity, which can be related to the signal obtained from the detector placed in the reflection cone.

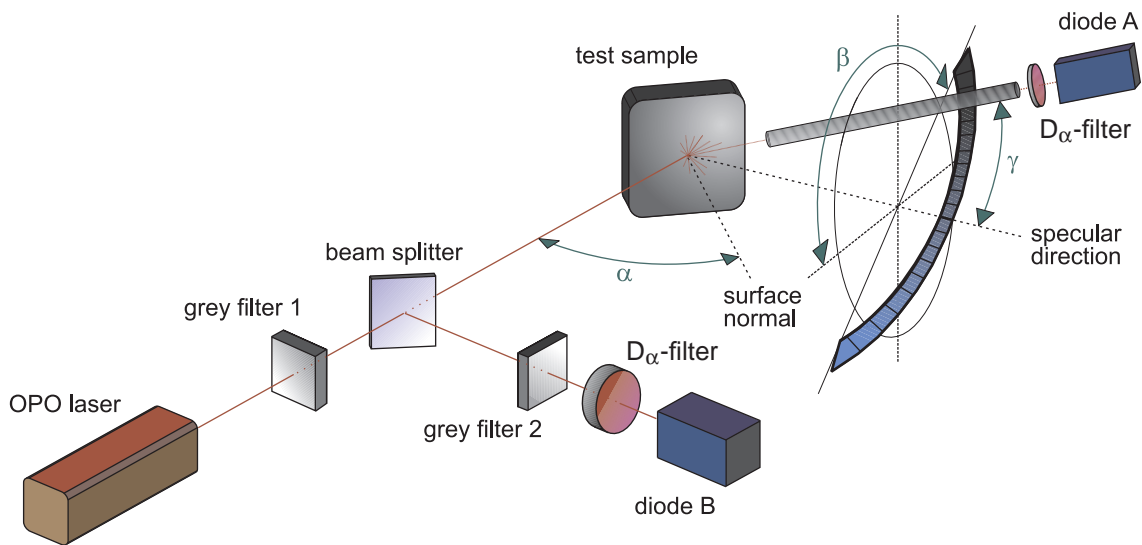


Figure C.2: Scheme of the setup to measure diffuse reflectivity, solid angle resolved.



Figure C.3: The goniometric mounting used to probe the cone of reflection.

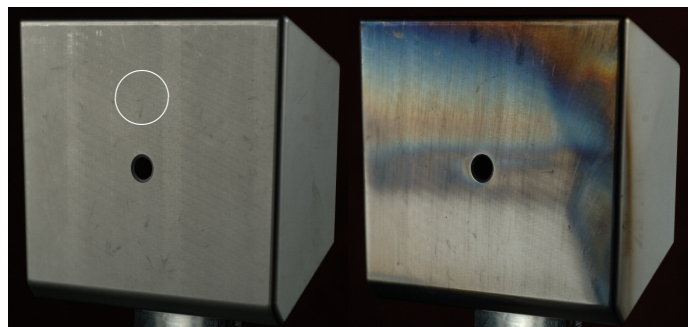


Figure C.4: Samples of original tiles. Left: clean, right: surface layers. The position of the measurement is indicated with \bigcirc , valid for both parts.

Each of the optics involved are configured to have an aperture larger than the beam cross section. In the case of the reflection cone, a sufficiently large part of the surface is mapped such to include the whole area of incident light which coincides with the beam cross section only for the specular direction and otherwise is a function of α , β and γ . With A_0 denoting the cross section of the incident beam, the beam spot on the sample appears from an arbitrary direction as $A'_0 = A_0 \cdot (\cos \alpha \cos \gamma - \sin \alpha \sin \beta \sin \gamma) / \cos \alpha$. Narrow band pass filters are used to avoid perturbation by other light sources. A small tube which is blackened on the inside is used to define the aperture of the reflection viewing geometry to avoid recording of light scattered from various locations which occurs easily when working with intense laser sources. An emphasis is put on the issue to operate the detectors at good signal-to-noise ratio while preventing saturation. This is achieved by introducing grey filters GF1 and GF2. While GF1 simply reduces the overall intensity, GF2 changes the reference signal and therefore its transmission has to be determined in advance. A very high primary intensity might be necessary if γ is large, but as a consequence the reference detector needs to be protected.

Taking the relative calibration into consideration, the relationship of the output signals of the detectors, together with transmission of GF2 and the aperture size of observation, yields the desired solid angle resolved reflectivity.

An example of the detector signals inferred from is shown in figure C.5. The oscilloscope used to record the time traces of output voltages of the diode circuits has a bandwidth of 500 MHz and also a maximum sampling rate of 500 MS/s. A single laser pulse is not resolved accurately, since the impact of electromagnetic interference from high voltage switching, eg from driving of the Pockels cell as a part of the resonator of the pump laser, in conjunction with the time resolution of 2 ns leads to profile shapes hard to interpret. Averaging over 50 pulses reduces the impact of noise to a tolerable level and the output is visualised with 10 GS/s. The amplitudes of the time traces are taken as a measure of intensity and the contribution from spurious signals expressed in the zigzag part of the profile is recognised as a degree of uncertainty for data analysis.

A couple of examples for measurement series are depicted in figures C.6 and C.7. Corresponding to the mechanical setup, the angle of incidence is restricted to $\alpha \in [30, 85]^\circ$ and the polar angle $\gamma \leq 38^\circ$. The three parameters α , β and γ have been chosen from the sets $\alpha \in \{30, 37.5, 45, 52.5, 60, 67.5, 75, 80, 85\}^\circ$, $\beta \in [0, 180]^\circ$ ($\Delta\beta = 15^\circ$) and $\gamma \in \{0., 2.5, 5, 10, 15, 20, 25, 30, 35, 38\}^\circ$. The range of β was fixed after first series supported the assumption of symmetry about the plane of incidence within the margin of uncertainty. All possible combinations of the three angles, if applicable in the present setup, were examined, just for the two largest values of α only the zero order direction was measured, resulting in a total number of 768 single measurements for the construction of a model for diffuse reflection.

The series of zero order reflection is the only one where both a clean and a coated tile were examined. In this particular case reflectivity for the impure surface is reduced in the specular direction for $\alpha < 65^\circ$ and higher for $\alpha > 70^\circ$ than observed for the clean surface. The characterisation of tiles with surface layers is however an unrealistic purpose since even each tile exhibits a variety of reflection properties (see figure C.4). Therefore the measurements were focussed on the clean surface which is assumed to give a good estimate for reflectivity of these type of Tungsten tiles in the framework of plasma operation without wall conditioning like the AUG campaign 2007.

Figure C.7 gives an impression about the functional dependencies for β if α and γ are fixed. Fit functions have been chosen such to be symmetric in β about $\beta = 0^\circ$ and $\beta = 180^\circ$. These series are combined for all α and γ and the parameter space is well resolved for $\alpha \in [30, 75]^\circ$.

Linear interpolation is used to obtain $dR/d\Omega$ for an arbitrary (α, β, γ) -triplet. No data is available for $\alpha < 30^\circ$ and the model is extrapolated by applying the result for $\alpha = 30^\circ$ which is found not to contain a β -dependence. Extrapolation for $\alpha > 75^\circ$ is based on the two values for reflection in the zero order direction and a dependence on γ is introduced to achieve a reasonable value for total reflection which must not exceed unity. The solid angle integrated $dR/d\Omega$, where $\gamma \leq 38^\circ$, is shown in figure C.8. Shape and magnitude of this quantity is considered as a support for the experimental approach. Figure C.9 gives a three dimensional depiction of the reflectivity model with color coding on the surface of a sphere centered at the point of incidence. One interesting feature of the observed reflectivity is the deviation of the peak value from the zero order direction which is tilted towards the surface normal by several degrees depending on α . The accuracy of the goniometric setup is sufficient to exclude a systematic error in that respect. For larger values of α , the model is restricted to a γ -dependence (see fig. C.10).

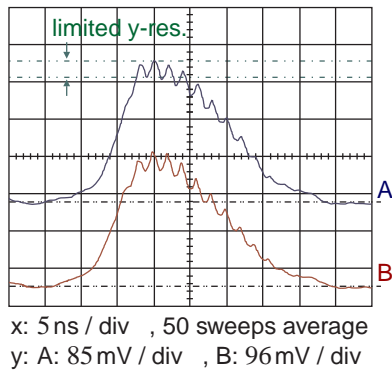


Figure C.5: Time traces of detector response: reflection (A), reference (B).

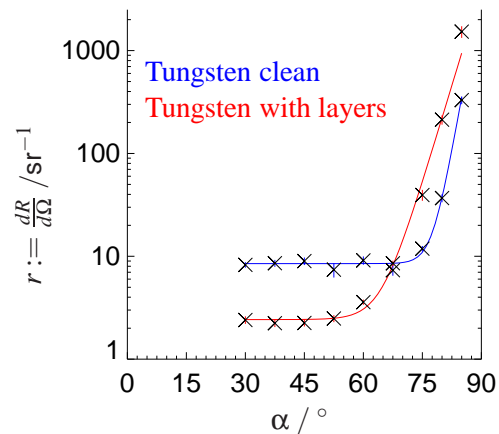


Figure C.6: Data series $r(\alpha, \gamma = 0^\circ)$.

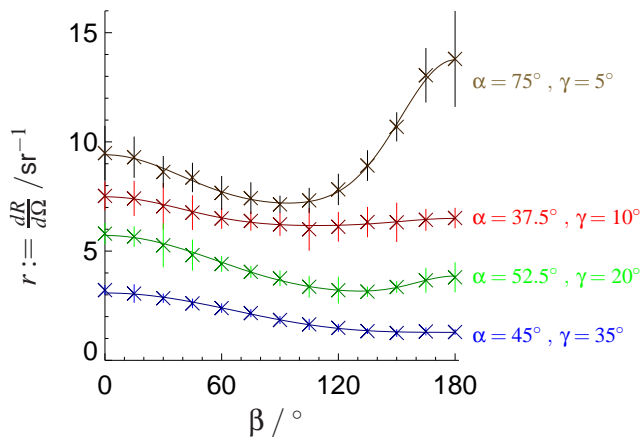


Figure C.7: r -series on β for fixed α and γ .

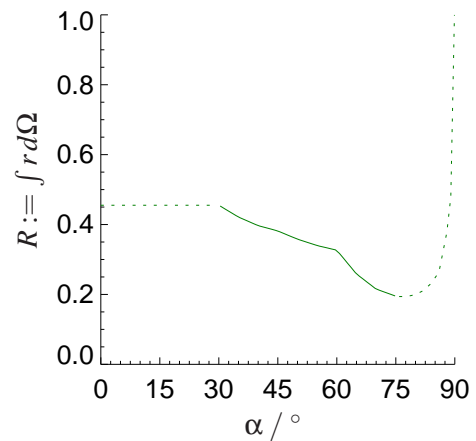


Figure C.8: Total reflectivity R of the r -model ($\gamma \leq 38^\circ$), measured (solid), extrapolated (dotted).

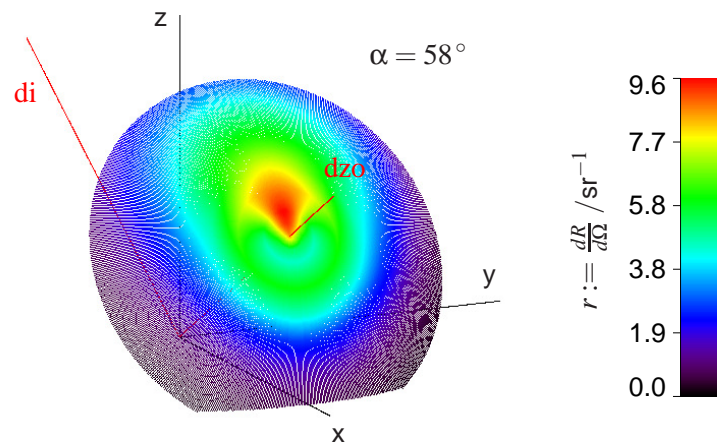


Figure C.9: $r(\alpha = 58^\circ, \beta, \gamma)$ color coded on spherical surface centered at point of incidence. Surface coordinate system (x, y, z) , with z -axis denoting the surface normal. Direction of incidence 'di' and direction of zero order 'dzo' in x - z -plane.

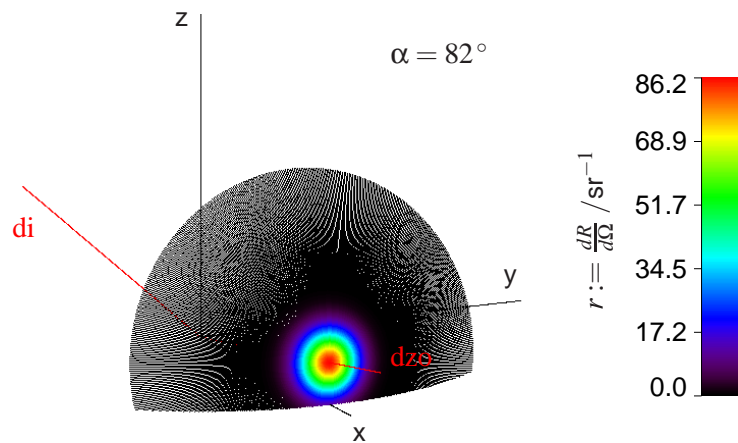


Figure C.10: $r(\alpha = 82^\circ, \beta, \gamma)$ color coded on spherical surface centered at point of incidence. Surface coordinate system (x, y, z) , with z -axis denoting the surface normal. Direction of incidence 'di' and direction of zero order 'dzo' in x - z -plane. A simple γ -dependence is introduced for the parameter space outside the range of high measurement density where only $r(\alpha, \gamma = 0)$ is known.

Appendix D

Overview on Neutral Penetration Data

As announced in section 5.2.6 the following pages contain tables D.1 to D.4 which summarise edge plasma and neutral parameters discussed earlier in a condensed form.

#21303, $t \sim 3.6$ s, ohmic (L-fact=1.2), $\bar{n}_e = 2.6 \cdot 10^{19} \text{ m}^{-3}$										
p_{sc} / cm	θ	$x_{sep} - x_{pd} / \text{cm}$	$\Gamma_D / \text{m}^{-2}\text{s}^{-1}$	n_D / m^{-3}	n_e / m^{-3}	n_D / n_e	n_D / n_e	T_e / eV	n_D / n_e	T_e / eV
25	-11	1.9	$x_{sep} : 3.2 (+/-0.2) \cdot 10^{20}$ $x_{pd} : 2.2 (+/-0.2) \cdot 10^{20}$	$x_{sep} : 3.1 (+/-0.5) \cdot 10^{16}$ $x_{pd} : 1.1 (+/-0.2) \cdot 10^{16}$	$x_{sep} : 7.3 (+/-0.7) \cdot 10^{18}$ $x_{pd} : 9.2 (+/-0.7) \cdot 10^{18}$	$x_{sep} : 4 (+/-1) \cdot 10^{-3}$ $x_{pd} : 1.3 (+/-0.3) \cdot 10^{-3}$	$x_{sep} : 4 (+/-1) \cdot 10^{-3}$ $x_{pd} : 1.3 (+/-0.3) \cdot 10^{-3}$	$x_{sep} : 75 (+/-10)$ $x_{pd} : 106 (+/-13)$	$x_{sep} : 4 (+/-1) \cdot 10^{-3}$ $x_{pd} : 1.3 (+/-0.3) \cdot 10^{-3}$	$x_{sep} : 75 (+/-10)$ $x_{pd} : 122 (+/-15)$
50	-26	1.5	$x_{sep} : 1.39 (+/-0.06) \cdot 10^{20}$ $x_{pd} : 9.9 (+/-0.7) \cdot 10^{19}$	$x_{sep} : 1.7 (+/-0.2) \cdot 10^{16}$ $x_{pd} : 6 (+/-1) \cdot 10^{15}$	$x_{sep} : 7.2 (+/-0.7) \cdot 10^{18}$ $x_{pd} : 1.01 (+/-0.08) \cdot 10^{19}$	$x_{sep} : 2.4 (+/-0.5) \cdot 10^{-3}$ $x_{pd} : 6 (+/-1) \cdot 10^{-4}$	$x_{sep} : 2.4 (+/-0.5) \cdot 10^{-3}$ $x_{pd} : 6 (+/-1) \cdot 10^{-4}$	$x_{sep} : 75 (+/-10)$ $x_{pd} : 122 (+/-15)$	$x_{sep} : 2.4 (+/-0.5) \cdot 10^{-3}$ $x_{pd} : 6 (+/-1) \cdot 10^{-4}$	$x_{sep} : 75 (+/-10)$ $x_{pd} : 122 (+/-15)$
75	-46	1.4	$x_{sep} : 6.5 (+/-0.4) \cdot 10^{19}$ $x_{pd} : 4.6 (+/-0.4) \cdot 10^{19}$	$x_{sep} : 8 (+/-1) \cdot 10^{15}$ $x_{pd} : 2.8 (+/-0.4) \cdot 10^{15}$	$x_{sep} : 7.2 (+/-0.6) \cdot 10^{18}$ $x_{pd} : 1.08 (+/-0.08) \cdot 10^{19}$	$x_{sep} : 1.1 (+/-0.3) \cdot 10^{-3}$ $x_{pd} : 2.7 (+/-0.6) \cdot 10^{-4}$	$x_{sep} : 1.1 (+/-0.3) \cdot 10^{-3}$ $x_{pd} : 2.7 (+/-0.6) \cdot 10^{-4}$	$x_{sep} : 74 (+/-9)$ $x_{pd} : 133 (+/-16)$	$x_{sep} : 1.1 (+/-0.3) \cdot 10^{-3}$ $x_{pd} : 2.7 (+/-0.6) \cdot 10^{-4}$	$x_{sep} : 74 (+/-9)$ $x_{pd} : 133 (+/-16)$
70	41	1.8	$x_{sep} : 3.4 (+/-0.3) \cdot 10^{19}$ $x_{pd} : 2.5 (+/-0.2) \cdot 10^{19}$	$x_{sep} : 4.4 (+/-0.4) \cdot 10^{15}$ $x_{pd} : 1.6 (+/-0.3) \cdot 10^{15}$	$x_{sep} : 7.2 (+/-0.6) \cdot 10^{18}$ $x_{pd} : 1.29 (+/-0.09) \cdot 10^{19}$	$x_{sep} : 6 (+/-1) \cdot 10^{-4}$ $x_{pd} : 1.3 (+/-0.3) \cdot 10^{-4}$	$x_{sep} : 6 (+/-1) \cdot 10^{-4}$ $x_{pd} : 1.3 (+/-0.3) \cdot 10^{-4}$	$x_{sep} : 74 (+/-10)$ $x_{pd} : 168 (+/-21)$	$x_{sep} : 6 (+/-1) \cdot 10^{-4}$ $x_{pd} : 1.3 (+/-0.3) \cdot 10^{-4}$	$x_{sep} : 74 (+/-10)$ $x_{pd} : 168 (+/-21)$
#21347, $t \sim 2.3$ s, L-mode (L-fact=1.2), $\bar{n}_e = 4.8 \cdot 10^{19} \text{ m}^{-3}$										
p_{sc} / cm	θ	$x_{sep} - x_{pd} / \text{cm}$	$\Gamma_D / \text{m}^{-2}\text{s}^{-1}$	n_D / m^{-3}	n_e / m^{-3}	n_D / n_e	n_D / n_e	T_e / eV	n_D / n_e	T_e / eV
71	41	1.6	$x_{sep} : 1.8 (+/-0.1) \cdot 10^{20}$ $x_{pd} : 1.0 (+/-0.1) \cdot 10^{20}$	$x_{sep} : 8 (+/-1) \cdot 10^{15}$ $x_{pd} : 3.1 (+/-0.4) \cdot 10^{15}$	$x_{sep} : 1.6 (+/-0.1) \cdot 10^{19}$ $x_{pd} : 2.7 (+/-0.2) \cdot 10^{19}$	$x_{sep} : 6 (+/-1) \cdot 10^{-4}$ $x_{pd} : 1.2 (+/-0.2) \cdot 10^{-4}$	$x_{sep} : 6 (+/-1) \cdot 10^{-4}$ $x_{pd} : 1.2 (+/-0.2) \cdot 10^{-4}$	$x_{sep} : 93 (+/-12)$ $x_{pd} : 164 (+/-20)$	$x_{sep} : 6 (+/-1) \cdot 10^{-4}$ $x_{pd} : 1.2 (+/-0.2) \cdot 10^{-4}$	$x_{sep} : 93 (+/-12)$ $x_{pd} : 164 (+/-20)$
#21402, $t \sim 3.3$ s, H-mode (L-fact=1.9), $\bar{n}_e = 6 \cdot 10^{19} \text{ m}^{-3}$										
p_{sc} / cm	θ	$x_{sep} - x_{pd} / \text{cm}$	$\Gamma_D / \text{m}^{-2}\text{s}^{-1}$	n_D / m^{-3}	n_e / m^{-3}	n_D / n_e	n_D / n_e	T_e / eV	n_D / n_e	T_e / eV
20	-8	1.3	$x_{sep} : 8.0 (+/-0.5) \cdot 10^{20}$ $x_{pd} : 5.6 (+/-0.4) \cdot 10^{20}$	$x_{sep} : 8 (+/-1) \cdot 10^{16}$ $x_{pd} : 3.1 (+/-0.4) \cdot 10^{16}$	$x_{sep} : 9.8 (+/-0.7) \cdot 10^{18}$ $x_{pd} : 1.29 (+/-0.09) \cdot 10^{19}$	$x_{sep} : 9 (+/-2) \cdot 10^{-3}$ $x_{pd} : 2.5 (+/-0.5) \cdot 10^{-3}$	$x_{sep} : 9 (+/-2) \cdot 10^{-3}$ $x_{pd} : 2.5 (+/-0.5) \cdot 10^{-3}$	$x_{sep} : 105 (+/-13)$ $x_{pd} : 127 (+/-16)$	$x_{sep} : 9 (+/-2) \cdot 10^{-3}$ $x_{pd} : 2.5 (+/-0.5) \cdot 10^{-3}$	$x_{sep} : 105 (+/-13)$ $x_{pd} : 127 (+/-16)$
45	-21	1.3	$x_{sep} : 2.2 (+/-0.1) \cdot 10^{20}$ $x_{pd} : 1.5 (+/-0.1) \cdot 10^{20}$	$x_{sep} : 2.3 (+/-0.3) \cdot 10^{16}$ $x_{pd} : 8 (+/-1) \cdot 10^{15}$	$x_{sep} : 9.8 (+/-0.8) \cdot 10^{18}$ $x_{pd} : 1.6 (+/-0.1) \cdot 10^{19}$	$x_{sep} : 2.4 (+/-0.5) \cdot 10^{-3}$ $x_{pd} : 5 (+/-1) \cdot 10^{-4}$	$x_{sep} : 2.4 (+/-0.5) \cdot 10^{-3}$ $x_{pd} : 5 (+/-1) \cdot 10^{-4}$	$x_{sep} : 105 (+/-13)$ $x_{pd} : 144 (+/-18)$	$x_{sep} : 2.4 (+/-0.5) \cdot 10^{-3}$ $x_{pd} : 5 (+/-1) \cdot 10^{-4}$	$x_{sep} : 105 (+/-13)$ $x_{pd} : 144 (+/-18)$
70	-38	1.1	$x_{sep} : 1.39 (+/-0.08) \cdot 10^{20}$ $x_{pd} : 9.2 (+/-0.7) \cdot 10^{19}$	$x_{sep} : 1.4 (+/-0.2) \cdot 10^{16}$ $x_{pd} : 5.2 (+/-0.7) \cdot 10^{15}$	$x_{sep} : 1.00 (+/-0.08) \cdot 10^{19}$ $x_{pd} : 1.7 (+/-0.1) \cdot 10^{19}$	$x_{sep} : 1.4 (+/-0.3) \cdot 10^{-3}$ $x_{pd} : 3.1 (+/-0.6) \cdot 10^{-4}$	$x_{sep} : 1.4 (+/-0.3) \cdot 10^{-3}$ $x_{pd} : 3.1 (+/-0.6) \cdot 10^{-4}$	$x_{sep} : 107 (+/-13)$ $x_{pd} : 153 (+/-19)$	$x_{sep} : 1.4 (+/-0.3) \cdot 10^{-3}$ $x_{pd} : 3.1 (+/-0.6) \cdot 10^{-4}$	$x_{sep} : 107 (+/-13)$ $x_{pd} : 153 (+/-19)$
72	38	1.3	$x_{sep} : 4.72 (+/-0.09) \cdot 10^{19}$ $x_{pd} : 3.2 (+/-0.3) \cdot 10^{19}$	$x_{sep} : 4.3 (+/-0.4) \cdot 10^{15}$ $x_{pd} : 1.6 (+/-0.2) \cdot 10^{15}$	$x_{sep} : 9.9 (+/-0.8) \cdot 10^{18}$ $x_{pd} : 2.4 (+/-0.1) \cdot 10^{19}$	$x_{sep} : 4.4 (+/-0.8) \cdot 10^{-4}$ $x_{pd} : 7 (+/-1) \cdot 10^{-5}$	$x_{sep} : 4.4 (+/-0.8) \cdot 10^{-4}$ $x_{pd} : 7 (+/-1) \cdot 10^{-5}$	$x_{sep} : 106 (+/-13)$ $x_{pd} : 196 (+/-24)$	$x_{sep} : 4.4 (+/-0.8) \cdot 10^{-4}$ $x_{pd} : 7 (+/-1) \cdot 10^{-5}$	$x_{sep} : 106 (+/-13)$ $x_{pd} : 196 (+/-24)$
#21418, $t \sim 2.3$ s, L-mode (L-fact=1.3), $\bar{n}_e = 3.4 \cdot 10^{19} \text{ m}^{-3}$										
p_{sc} / cm	θ	$x_{sep} - x_{pd} / \text{cm}$	$\Gamma_D / \text{m}^{-2}\text{s}^{-1}$	n_D / m^{-3}	n_e / m^{-3}	n_D / n_e	n_D / n_e	T_e / eV	n_D / n_e	T_e / eV
20	-10	2.1	$x_{sep} : 9.0 (+/-0.7) \cdot 10^{20}$ $x_{pd} : 5.9 (+/-0.5) \cdot 10^{20}$	$x_{sep} : 6 (+/-1) \cdot 10^{16}$ $x_{pd} : 2.3 (+/-0.3) \cdot 10^{16}$	$x_{sep} : 9.0 (+/-0.7) \cdot 10^{18}$ $x_{pd} : 1.10 (+/-0.08) \cdot 10^{19}$	$x_{sep} : 7 (+/-2) \cdot 10^{-3}$ $x_{pd} : 2.1 (+/-0.4) \cdot 10^{-3}$	$x_{sep} : 7 (+/-2) \cdot 10^{-3}$ $x_{pd} : 2.1 (+/-0.4) \cdot 10^{-3}$	$x_{sep} : 82 (+/-10)$ $x_{pd} : 99 (+/-12)$	$x_{sep} : 7 (+/-2) \cdot 10^{-3}$ $x_{pd} : 2.1 (+/-0.4) \cdot 10^{-3}$	$x_{sep} : 82 (+/-10)$ $x_{pd} : 99 (+/-12)$
45	-26	1.4	$x_{sep} : 3.2 (+/-0.2) \cdot 10^{20}$ $x_{pd} : 2.2 (+/-0.2) \cdot 10^{20}$	$x_{sep} : 2.8 (+/-0.4) \cdot 10^{16}$ $x_{pd} : 1.0 (+/-0.1) \cdot 10^{16}$	$x_{sep} : 9.9 (+/-0.8) \cdot 10^{18}$ $x_{pd} : 1.33 (+/-0.09) \cdot 10^{19}$	$x_{sep} : 2.9 (+/-0.6) \cdot 10^{-3}$ $x_{pd} : 8 (+/-1) \cdot 10^{-4}$	$x_{sep} : 2.9 (+/-0.6) \cdot 10^{-3}$ $x_{pd} : 8 (+/-1) \cdot 10^{-4}$	$x_{sep} : 89 (+/-11)$ $x_{pd} : 117 (+/-15)$	$x_{sep} : 2.9 (+/-0.6) \cdot 10^{-3}$ $x_{pd} : 8 (+/-1) \cdot 10^{-4}$	$x_{sep} : 89 (+/-11)$ $x_{pd} : 117 (+/-15)$
70	-46	1.3	$x_{sep} : 1.6 (+/-0.1) \cdot 10^{20}$ $x_{pd} : 1.08 (+/-0.08) \cdot 10^{20}$	$x_{sep} : 1.4 (+/-0.2) \cdot 10^{16}$ $x_{pd} : 5.1 (+/-0.7) \cdot 10^{15}$	$x_{sep} : 1.07 (+/-0.08) \cdot 10^{19}$ $x_{pd} : 1.5 (+/-0.1) \cdot 10^{19}$	$x_{sep} : 1.3 (+/-0.3) \cdot 10^{-3}$ $x_{pd} : 3.4 (+/-0.7) \cdot 10^{-4}$	$x_{sep} : 1.3 (+/-0.3) \cdot 10^{-3}$ $x_{pd} : 3.4 (+/-0.7) \cdot 10^{-4}$	$x_{sep} : 96 (+/-12)$ $x_{pd} : 133 (+/-17)$	$x_{sep} : 1.3 (+/-0.3) \cdot 10^{-3}$ $x_{pd} : 3.4 (+/-0.7) \cdot 10^{-4}$	$x_{sep} : 96 (+/-12)$ $x_{pd} : 133 (+/-17)$
65	40	1.6	$x_{sep} : 8.2 (+/-0.3) \cdot 10^{19}$ $x_{pd} : 5.5 (+/-0.4) \cdot 10^{19}$	$x_{sep} : 8 (+/-1) \cdot 10^{15}$ $x_{pd} : 3.0 (+/-0.4) \cdot 10^{15}$	$x_{sep} : 8.4 (+/-0.7) \cdot 10^{18}$ $x_{pd} : 1.5 (+/-0.1) \cdot 10^{19}$	$x_{sep} : 1.0 (+/-0.2) \cdot 10^{-3}$ $x_{pd} : 2.0 (+/-0.4) \cdot 10^{-4}$	$x_{sep} : 1.0 (+/-0.2) \cdot 10^{-3}$ $x_{pd} : 2.0 (+/-0.4) \cdot 10^{-4}$	$x_{sep} : 74 (+/-10)$ $x_{pd} : 131 (+/-16)$	$x_{sep} : 1.0 (+/-0.2) \cdot 10^{-3}$ $x_{pd} : 2.0 (+/-0.4) \cdot 10^{-4}$	$x_{sep} : 74 (+/-10)$ $x_{pd} : 131 (+/-16)$

Table D.1: Collection of neutral penetration data; refer to caption of table D.4.

#21418, $t \sim 3.4$ s, H-mode (L-fact.=1.8), $\bar{n}_e = 3.7 \cdot 10^{19} \text{ m}^{-3}$							
psc / cm	θ / °	$X_{\text{sep}} - X_{\text{pd}} / \text{cm}$	$\Gamma_{\text{D}} / \text{m}^{-2}\text{s}^{-1}$	$n_{\text{D}} / \text{m}^{-3}$	n_e / m^{-3}	n_{D}/n_e	T_e / eV
20	-10	1.8	$X_{\text{sep}} : 6.9(+/-0.4) \cdot 10^{20}$ $X_{\text{pd}} : 4.8(+/-0.4) \cdot 10^{20}$	$X_{\text{sep}} : 7(+/-1) \cdot 10^{16}$ $X_{\text{pd}} : 2.4(+/-0.4) \cdot 10^{16}$	$X_{\text{sep}} : 7.1(+/-0.6) \cdot 10^{18}$ $X_{\text{pd}} : 1.02(+/-0.08) \cdot 10^{19}$	$X_{\text{sep}} : 9(+/-2) \cdot 10^{-3}$ $X_{\text{pd}} : 2.4(+/-0.5) \cdot 10^{-3}$	$X_{\text{sep}} : 105(+/-13)$ $X_{\text{pd}} : 136(+/-17)$
45	-26	1.3	$X_{\text{sep}} : 3.1(+/-0.2) \cdot 10^{20}$ $X_{\text{pd}} : 2.2(+/-0.2) \cdot 10^{20}$	$X_{\text{sep}} : 3.3(+/-0.4) \cdot 10^{16}$ $X_{\text{pd}} : 1.2(+/-0.2) \cdot 10^{16}$	$X_{\text{sep}} : 8.0(+/-0.7) \cdot 10^{18}$ $X_{\text{pd}} : 1.32(+/-0.09) \cdot 10^{19}$	$X_{\text{sep}} : 4.2(+/-0.9) \cdot 10^{-3}$ $X_{\text{pd}} : 9(+/-2) \cdot 10^{-4}$	$X_{\text{sep}} : 113(+/-14)$ $X_{\text{pd}} : 165(+/-20)$
70	-45	1.3	$X_{\text{sep}} : 1.7(+/-0.1) \cdot 10^{20}$ $X_{\text{pd}} : 1.17(+/-0.09) \cdot 10^{20}$	$X_{\text{sep}} : 1.8(+/-0.2) \cdot 10^{16}$ $X_{\text{pd}} : 6.5(+/-0.9) \cdot 10^{15}$	$X_{\text{sep}} : 8.4(+/-0.7) \cdot 10^{18}$ $X_{\text{pd}} : 1.5(+/-0.1) \cdot 10^{19}$	$X_{\text{sep}} : 2.1(+/-0.4) \cdot 10^{-3}$ $X_{\text{pd}} : 4.3(+/-0.9) \cdot 10^{-4}$	$X_{\text{sep}} : 115(+/-14)$ $X_{\text{pd}} : 186(+/-23)$
65	40	1.5	$X_{\text{sep}} : 6.5(+/-0.5) \cdot 10^{19}$ $X_{\text{pd}} : 5.1(+/-0.4) \cdot 10^{19}$	$X_{\text{sep}} : 8.1(+/-0.8) \cdot 10^{15}$ $X_{\text{pd}} : 3.0(+/-0.5) \cdot 10^{15}$	$X_{\text{sep}} : 6.2(+/-0.6) \cdot 10^{18}$ $X_{\text{pd}} : 1.7(+/-0.1) \cdot 10^{19}$	$X_{\text{sep}} : 1.3(+/-0.2) \cdot 10^{-3}$ $X_{\text{pd}} : 1.8(+/-0.4) \cdot 10^{-4}$	$X_{\text{sep}} : 95(+/-12)$ $X_{\text{pd}} : 209(+/-25)$
#22091, $t \sim 1.4$ s, ohmic (L-fact.=0.9), $\bar{n}_e = 2.5 \cdot 10^{19} \text{ m}^{-3}$							
psc / cm	θ / °	$X_{\text{sep}} - X_{\text{pd}} / \text{cm}$	$\Gamma_{\text{D}} / \text{m}^{-2}\text{s}^{-1}$	$n_{\text{D}} / \text{m}^{-3}$	n_e / m^{-3}	n_{D}/n_e	T_e / eV
20	-8	2.3	$X_{\text{sep}} : 1.8(+/-0.1) \cdot 10^{20}$ $X_{\text{pd}} : 1.2(+/-0.1) \cdot 10^{20}$	$X_{\text{sep}} : 1.4(+/-0.2) \cdot 10^{16}$ $X_{\text{pd}} : 5.1(+/-0.8) \cdot 10^{15}$	$X_{\text{sep}} : 6.4(+/-0.6) \cdot 10^{18}$ $X_{\text{pd}} : 9.6(+/-0.7) \cdot 10^{18}$	$X_{\text{sep}} : 2.2(+/-0.6) \cdot 10^{-3}$ $X_{\text{pd}} : 5(+/-1) \cdot 10^{-4}$	$X_{\text{sep}} : 69(+/-9)$ $X_{\text{pd}} : 84(+/-11)$
45	-23	1.7	$X_{\text{sep}} : 3.6(+/-0.2) \cdot 10^{19}$ $X_{\text{pd}} : 2.5(+/-0.2) \cdot 10^{19}$	$X_{\text{sep}} : 3.7(+/-0.6) \cdot 10^{15}$ $X_{\text{pd}} : 1.3(+/-0.2) \cdot 10^{15}$	$X_{\text{sep}} : 6.2(+/-0.6) \cdot 10^{18}$ $X_{\text{pd}} : 1.18(+/-0.08) \cdot 10^{19}$	$X_{\text{sep}} : 6(+/-2) \cdot 10^{-4}$ $X_{\text{pd}} : 1.1(+/-0.3) \cdot 10^{-4}$	$X_{\text{sep}} : 68(+/-9)$ $X_{\text{pd}} : 95(+/-12)$
70	-42	1.5	$X_{\text{sep}} : 1.8(+/-0.1) \cdot 10^{19}$ $X_{\text{pd}} : 1.3(+/-0.1) \cdot 10^{19}$	$X_{\text{sep}} : 1.8(+/-0.3) \cdot 10^{15}$ $X_{\text{pd}} : 7(+/-1) \cdot 10^{14}$	$X_{\text{sep}} : 6.2(+/-0.6) \cdot 10^{18}$ $X_{\text{pd}} : 1.23(+/-0.09) \cdot 10^{19}$	$X_{\text{sep}} : 3.0(+/-0.8) \cdot 10^{-4}$ $X_{\text{pd}} : 6(+/-1) \cdot 10^{-5}$	$X_{\text{sep}} : 67(+/-9)$ $X_{\text{pd}} : 102(+/-13)$
#22091, $t \sim 2.2$ s, ohmic (L-fact.=1), $\bar{n}_e = 2.5 \cdot 10^{19} \text{ m}^{-3}$							
psc / cm	θ / °	$X_{\text{sep}} - X_{\text{pd}} / \text{cm}$	$\Gamma_{\text{D}} / \text{m}^{-2}\text{s}^{-1}$	$n_{\text{D}} / \text{m}^{-3}$	n_e / m^{-3}	n_{D}/n_e	T_e / eV
20	-10	2.0	$X_{\text{sep}} : 1.20(+/-0.08) \cdot 10^{20}$ $X_{\text{pd}} : 8.0(+/-0.7) \cdot 10^{19}$	$X_{\text{sep}} : 1(+/-0.2) \cdot 10^{16}$ $X_{\text{pd}} : 3.7(+/-0.5) \cdot 10^{15}$	$X_{\text{sep}} : 8.3(+/-0.7) \cdot 10^{18}$ $X_{\text{pd}} : 1.04(+/-0.08) \cdot 10^{19}$	$X_{\text{sep}} : 1.2(+/-0.3) \cdot 10^{-3}$ $X_{\text{pd}} : 3.6(+/-0.8) \cdot 10^{-4}$	$X_{\text{sep}} : 64(+/-8)$ $X_{\text{pd}} : 76(+/-10)$
45	-25	1.8	$X_{\text{sep}} : 2.8(+/-0.2) \cdot 10^{19}$ $X_{\text{pd}} : 1.9(+/-0.2) \cdot 10^{19}$	$X_{\text{sep}} : 2.9(+/-0.5) \cdot 10^{15}$ $X_{\text{pd}} : 1.1(+/-0.2) \cdot 10^{15}$	$X_{\text{sep}} : 6.8(+/-0.6) \cdot 10^{18}$ $X_{\text{pd}} : 1.10(+/-0.08) \cdot 10^{19}$	$X_{\text{sep}} : 4(+/-1) \cdot 10^{-4}$ $X_{\text{pd}} : 1.0(+/-0.2) \cdot 10^{-4}$	$X_{\text{sep}} : 56(+/-7)$ $X_{\text{pd}} : 80(+/-10)$
70	-45	1.8	$X_{\text{sep}} : 1.5(+/-0.1) \cdot 10^{19}$ $X_{\text{pd}} : 9.7(+/-0.9) \cdot 10^{18}$	$X_{\text{sep}} : 1.6(+/-0.2) \cdot 10^{15}$ $X_{\text{pd}} : 5.7(+/-0.9) \cdot 10^{14}$	$X_{\text{sep}} : 6.0(+/-0.6) \cdot 10^{18}$ $X_{\text{pd}} : 1.18(+/-0.08) \cdot 10^{19}$	$X_{\text{sep}} : 2.7(+/-0.6) \cdot 10^{-4}$ $X_{\text{pd}} : 5(+/-1) \cdot 10^{-5}$	$X_{\text{sep}} : 52(+/-7)$ $X_{\text{pd}} : 85(+/-11)$
#22091, $t \sim 2.8$ s, H-mode (L-fact.=1.4), $\bar{n}_e = 2.8 \cdot 10^{19} \text{ m}^{-3}$							
psc / cm	θ / °	$X_{\text{sep}} - X_{\text{pd}} / \text{cm}$	$\Gamma_{\text{D}} / \text{m}^{-2}\text{s}^{-1}$	$n_{\text{D}} / \text{m}^{-3}$	n_e / m^{-3}	n_{D}/n_e	T_e / eV
20	-9	1.6	$X_{\text{sep}} : 1.5(+/-0.1) \cdot 10^{20}$ $X_{\text{pd}} : 9.7(+/-0.8) \cdot 10^{19}$	$X_{\text{sep}} : 9(+/-1) \cdot 10^{15}$ $X_{\text{pd}} : 3.2(+/-0.4) \cdot 10^{15}$	$X_{\text{sep}} : 1.5(+/-0.1) \cdot 10^{19}$ $X_{\text{pd}} : 1.7(+/-0.1) \cdot 10^{19}$	$X_{\text{sep}} : 6(+/-1) \cdot 10^{-4}$ $X_{\text{pd}} : 1.9(+/-0.3) \cdot 10^{-4}$	$X_{\text{sep}} : 97(+/-12)$ $X_{\text{pd}} : 120(+/-15)$
45	-24	1.2	$X_{\text{sep}} : 3.4(+/-0.2) \cdot 10^{19}$ $X_{\text{pd}} : 2.2(+/-0.2) \cdot 10^{19}$	$X_{\text{sep}} : 2.5(+/-0.3) \cdot 10^{15}$ $X_{\text{pd}} : 9(+/-1) \cdot 10^{14}$	$X_{\text{sep}} : 1.44(+/-0.09) \cdot 10^{19}$ $X_{\text{pd}} : 1.8(+/-0.1) \cdot 10^{19}$	$X_{\text{sep}} : 1.8(+/-0.3) \cdot 10^{-4}$ $X_{\text{pd}} : 5.1(+/-0.9) \cdot 10^{-5}$	$X_{\text{sep}} : 95(+/-12)$ $X_{\text{pd}} : 134(+/-17)$
70	-43	1.1	$X_{\text{sep}} : 1.4(+/-0.1) \cdot 10^{19}$ $X_{\text{pd}} : 9.4(+/-0.8) \cdot 10^{18}$	$X_{\text{sep}} : 1.0(+/-0.1) \cdot 10^{15}$ $X_{\text{pd}} : 3.9(+/-0.5) \cdot 10^{14}$	$X_{\text{sep}} : 1.44(+/-0.09) \cdot 10^{19}$ $X_{\text{pd}} : 1.9(+/-0.1) \cdot 10^{19}$	$X_{\text{sep}} : 7(+/-1) \cdot 10^{-5}$ $X_{\text{pd}} : 2.0(+/-0.4) \cdot 10^{-5}$	$X_{\text{sep}} : 95(+/-12)$ $X_{\text{pd}} : 147(+/-18)$

Table D.2: Collection of neutral penetration data; refer to caption of table D.4.

#22091, $t \sim 4.0$ s, H-mode (L-fact.=1.3), $\bar{n}_e = 2.7 \cdot 10^{19} \text{ m}^{-3}$										
p_{sc} / cm	θ	$x_{sep} - x_{pd} / \text{cm}$	$\Gamma_D / \text{m}^2 \text{s}^{-1}$	n_D / m^{-3}	n_e / m^{-3}	n_D / n_e	T_e / eV			
20	-8	1.9	$x_{sep} : 2.0 (+/-0.1) \cdot 10^{20}$ $x_{pd} : 1.3 (+/-0.1) \cdot 10^{20}$	$x_{sep} : 1.4 (+/-0.2) \cdot 10^{16}$ $x_{pd} : 5.2 (+/-0.7) \cdot 10^{15}$	$x_{sep} : 8.4 (+/-0.7) \cdot 10^{18}$ $x_{pd} : 1.21 (+/-0.08) \cdot 10^{19}$	$x_{sep} : 1.7 (+/-0.4) \cdot 10^{-3}$ $x_{pd} : 4.4 (+/-0.9) \cdot 10^{-4}$	$x_{sep} : 96 (+/-12)$ $x_{pd} : 124 (+/-15)$			
45	-23	1.4	$x_{sep} : 5.5 (+/-0.4) \cdot 10^{19}$ $x_{pd} : 3.7 (+/-0.3) \cdot 10^{19}$	$x_{sep} : 4.9 (+/-0.7) \cdot 10^{15}$ $x_{pd} : 1.8 (+/-0.3) \cdot 10^{15}$	$x_{sep} : 8.2 (+/-0.7) \cdot 10^{18}$ $x_{pd} : 1.42 (+/-0.09) \cdot 10^{19}$	$x_{sep} : 6 (+/-1) \cdot 10^{-4}$ $x_{pd} : 1.3 (+/-0.3) \cdot 10^{-4}$	$x_{sep} : 95 (+/-12)$ $x_{pd} : 144 (+/-18)$			
70	-42	1.3	$x_{sep} : 2.8 (+/-0.2) \cdot 10^{19}$ $x_{pd} : 1.9 (+/-0.2) \cdot 10^{19}$	$x_{sep} : 2.5 (+/-0.4) \cdot 10^{15}$ $x_{pd} : 9 (+/-1) \cdot 10^{14}$	$x_{sep} : 8.3 (+/-0.7) \cdot 10^{18}$ $x_{pd} : 1.6 (+/-0.1) \cdot 10^{19}$	$x_{sep} : 3.1 (+/-0.7) \cdot 10^{-4}$ $x_{pd} : 6 (+/-1) \cdot 10^{-5}$	$x_{sep} : 95 (+/-12)$ $x_{pd} : 158 (+/-19)$			
#22097, $t \sim 1.7$ s, ohmic (L-fact.=1.0), $\bar{n}_e = 3.9 \cdot 10^{19} \text{ m}^{-3}$										
p_{sc} / cm	θ	$x_{sep} - x_{pd} / \text{cm}$	$\Gamma_D / \text{m}^2 \text{s}^{-1}$	n_D / m^{-3}	n_e / m^{-3}	n_D / n_e	T_e / eV			
20	-9	2.4	$x_{sep} : 3.8 (+/-0.2) \cdot 10^{20}$ $x_{pd} : 2.1 (+/-0.2) \cdot 10^{20}$	$x_{sep} : 1.6 (+/-0.2) \cdot 10^{16}$ $x_{pd} : 5.9 (+/-0.7) \cdot 10^{15}$	$x_{sep} : 1.5 (+/-0.1) \cdot 10^{19}$ $x_{pd} : 1.9 (+/-0.1) \cdot 10^{19}$	$x_{sep} : 1.1 (+/-0.2) \cdot 10^{-3}$ $x_{pd} : 3.1 (+/-0.5) \cdot 10^{-4}$	$x_{sep} : 72 (+/-9)$ $x_{pd} : 88 (+/-11)$			
45	-24	1.5	$x_{sep} : 6.7 (+/-0.5) \cdot 10^{19}$ $x_{pd} : 4.2 (+/-0.3) \cdot 10^{19}$	$x_{sep} : 3.9 (+/-0.6) \cdot 10^{15}$ $x_{pd} : 1.5 (+/-0.2) \cdot 10^{15}$	$x_{sep} : 1.46 (+/-0.09) \cdot 10^{19}$ $x_{pd} : 1.9 (+/-0.1) \cdot 10^{19}$	$x_{sep} : 2.7 (+/-0.6) \cdot 10^{-4}$ $x_{pd} : 8 (+/-1) \cdot 10^{-5}$	$x_{sep} : 70 (+/-9)$ $x_{pd} : 93 (+/-12)$			
70	-43	1.3	$x_{sep} : 2.8 (+/-0.2) \cdot 10^{19}$ $x_{pd} : 1.8 (+/-0.1) \cdot 10^{19}$	$x_{sep} : 1.8 (+/-0.3) \cdot 10^{15}$ $x_{pd} : 6.6 (+/-0.8) \cdot 10^{14}$	$x_{sep} : 1.5 (+/-0.1) \cdot 10^{19}$ $x_{pd} : 2.0 (+/-0.1) \cdot 10^{19}$	$x_{sep} : 1.2 (+/-0.3) \cdot 10^{-4}$ $x_{pd} : 3.4 (+/-0.6) \cdot 10^{-5}$	$x_{sep} : 71 (+/-9)$ $x_{pd} : 99 (+/-12)$			
#22097, $t \sim 3.1$ s, H-mode (L-fact.=1.8), $\bar{n}_e = 5.4 \cdot 10^{19} \text{ m}^{-3}$										
p_{sc} / cm	θ	$x_{sep} - x_{pd} / \text{cm}$	$\Gamma_D / \text{m}^2 \text{s}^{-1}$	n_D / m^{-3}	n_e / m^{-3}	n_D / n_e	T_e / eV			
20	-9	1.4	$x_{sep} : 2.0 (+/-0.1) \cdot 10^{20}$ $x_{pd} : 1.3 (+/-0.1) \cdot 10^{20}$	$x_{sep} : 1.4 (+/-0.2) \cdot 10^{16}$ $x_{pd} : 5.1 (+/-0.7) \cdot 10^{15}$	$x_{sep} : 1.26 (+/-0.09) \cdot 10^{19}$ $x_{pd} : 1.6 (+/-0.1) \cdot 10^{19}$	$x_{sep} : 1.1 (+/-0.2) \cdot 10^{-3}$ $x_{pd} : 3.2 (+/-0.6) \cdot 10^{-4}$	$x_{sep} : 101 (+/-13)$ $x_{pd} : 111 (+/-14)$			
45	-24	1.2	$x_{sep} : 4.1 (+/-0.3) \cdot 10^{19}$ $x_{pd} : 2.7 (+/-0.2) \cdot 10^{19}$	$x_{sep} : 3.1 (+/-0.4) \cdot 10^{15}$ $x_{pd} : 1.1 (+/-0.1) \cdot 10^{15}$	$x_{sep} : 1.23 (+/-0.09) \cdot 10^{19}$ $x_{pd} : 1.9 (+/-0.1) \cdot 10^{19}$	$x_{sep} : 2.6 (+/-0.5) \cdot 10^{-4}$ $x_{pd} : 6 (+/-1) \cdot 10^{-5}$	$x_{sep} : 99 (+/-12)$ $x_{pd} : 120 (+/-15)$			
68	-41	1.1	$x_{sep} : 1.8 (+/-0.1) \cdot 10^{19}$ $x_{pd} : 1.19 (+/-0.09) \cdot 10^{19}$	$x_{sep} : 1.4 (+/-0.2) \cdot 10^{15}$ $x_{pd} : 5.0 (+/-0.7) \cdot 10^{14}$	$x_{sep} : 1.24 (+/-0.09) \cdot 10^{19}$ $x_{pd} : 2.1 (+/-0.1) \cdot 10^{19}$	$x_{sep} : 1.1 (+/-0.2) \cdot 10^{-4}$ $x_{pd} : 2.4 (+/-0.5) \cdot 10^{-5}$	$x_{sep} : 100 (+/-13)$ $x_{pd} : 126 (+/-16)$			
#22097, $t \sim 3.7$ s, H-mode (L-fact.=1.6), $\bar{n}_e = 4.1 \cdot 10^{19} \text{ m}^{-3}$										
p_{sc} / cm	θ	$x_{sep} - x_{pd} / \text{cm}$	$\Gamma_D / \text{m}^2 \text{s}^{-1}$	n_D / m^{-3}	n_e / m^{-3}	n_D / n_e	T_e / eV			
20	-7	2.0	$x_{sep} : 1.6 (+/-0.1) \cdot 10^{20}$ $x_{pd} : 1.08 (+/-0.09) \cdot 10^{20}$	$x_{sep} : 1.2 (+/-0.2) \cdot 10^{16}$ $x_{pd} : 4.3 (+/-0.6) \cdot 10^{15}$	$x_{sep} : 8.0 (+/-0.7) \cdot 10^{18}$ $x_{pd} : 1.20 (+/-0.08) \cdot 10^{19}$	$x_{sep} : 1.5 (+/-0.4) \cdot 10^{-3}$ $x_{pd} : 3.7 (+/-0.8) \cdot 10^{-4}$	$x_{sep} : 86 (+/-11)$ $x_{pd} : 93 (+/-12)$			
45	-21	1.5	$x_{sep} : 5.3 (+/-0.3) \cdot 10^{19}$ $x_{pd} : 3.5 (+/-0.3) \cdot 10^{19}$	$x_{sep} : 4.9 (+/-0.7) \cdot 10^{15}$ $x_{pd} : 1.8 (+/-0.3) \cdot 10^{15}$	$x_{sep} : 7.7 (+/-0.7) \cdot 10^{18}$ $x_{pd} : 1.5 (+/-0.1) \cdot 10^{19}$	$x_{sep} : 7 (+/-2) \cdot 10^{-4}$ $x_{pd} : 1.2 (+/-0.2) \cdot 10^{-4}$	$x_{sep} : 83 (+/-11)$ $x_{pd} : 98 (+/-12)$			
70	-39	1.3	$x_{sep} : 2.3 (+/-0.1) \cdot 10^{19}$ $x_{pd} : 1.6 (+/-0.1) \cdot 10^{19}$	$x_{sep} : 2.2 (+/-0.3) \cdot 10^{15}$ $x_{pd} : 8 (+/-1) \cdot 10^{14}$	$x_{sep} : 7.8 (+/-0.7) \cdot 10^{18}$ $x_{pd} : 1.7 (+/-0.1) \cdot 10^{19}$	$x_{sep} : 2.8 (+/-0.7) \cdot 10^{-4}$ $x_{pd} : 5 (+/-1) \cdot 10^{-5}$	$x_{sep} : 85 (+/-11)$ $x_{pd} : 101 (+/-13)$			

Table D.3: Collection of neutral penetration data; refer to caption of table D.4.

#22113, $t \sim 2.6$ s, L-mode (L-factor=1.0), $\bar{n}_e = 2.4 \cdot 10^{19} \text{ m}^{-3}$		#22155, $t \sim 2.8$ s, ohmic (L-factor=1.0), $\bar{n}_e = 2.5 \cdot 10^{19} \text{ m}^{-3}$					
$p_{sc} /$ cm	θ °	$x_{sep} - x_{pd} /$ cm	$\Gamma_D /$ $\text{m}^{-2}\text{s}^{-1}$	$n_D /$ m^{-3}	$n_e /$ m^{-3}	n_D/n_e	$T_e /$ eV
20	-8	2.4	$x_{sep} : 1.6(+/-0.1) \cdot 10^{20}$ $x_{pd} : 1.1(+/-0.1) \cdot 10^{20}$	$x_{sep} : 1.1(+/-0.2) \cdot 10^{16}$ $x_{pd} : 4.0(+/-0.6) \cdot 10^{15}$	$x_{sep} : 7.7(+/-0.7) \cdot 10^{18}$ $x_{pd} : 9.5(+/-0.7) \cdot 10^{18}$	$x_{sep} : 1.4(+/-0.4) \cdot 10^{-3}$ $x_{pd} : 4(+/-1) \cdot 10^{-4}$	$x_{sep} : 81(+/-10)$ $x_{pd} : 100(+/-13)$
45	-23	1.7	$x_{sep} : 4.0(+/-0.3) \cdot 10^{19}$ $x_{pd} : 2.8(+/-0.2) \cdot 10^{19}$	$x_{sep} : 3.6(+/-0.6) \cdot 10^{15}$ $x_{pd} : 1.3(+/-0.2) \cdot 10^{15}$	$x_{sep} : 7.7(+/-0.7) \cdot 10^{18}$ $x_{pd} : 1.04(+/-0.08) \cdot 10^{19}$	$x_{sep} : 5(+/-1) \cdot 10^{-4}$ $x_{pd} : 1.3(+/-0.3) \cdot 10^{-4}$	$x_{sep} : 81(+/-10)$ $x_{pd} : 113(+/-14)$
70	-41	1.6	$x_{sep} : 1.9(+/-0.2) \cdot 10^{19}$ $x_{pd} : 1.4(+/-0.1) \cdot 10^{19}$	$x_{sep} : 1.7(+/-0.3) \cdot 10^{15}$ $x_{pd} : 6(+/-1) \cdot 10^{14}$	$x_{sep} : 7.7(+/-0.7) \cdot 10^{18}$ $x_{pd} : 1.09(+/-0.08) \cdot 10^{19}$	$x_{sep} : 2.3(+/-0.6) \cdot 10^{-4}$ $x_{pd} : 6(+/-1) \cdot 10^{-5}$	$x_{sep} : 82(+/-10)$ $x_{pd} : 125(+/-15)$
#22113, $t \sim 4.4$ s, L-mode (L-factor=0.9), $\bar{n}_e = 2.5 \cdot 10^{19} \text{ m}^{-3}$		#22155, $t \sim 2.8$ s, ohmic (L-factor=1.0), $\bar{n}_e = 2.5 \cdot 10^{19} \text{ m}^{-3}$					
$p_{sc} /$ cm	θ °	$x_{sep} - x_{pd} /$ cm	$\Gamma_D /$ $\text{m}^{-2}\text{s}^{-1}$	$n_D /$ m^{-3}	$n_e /$ m^{-3}	n_D/n_e	$T_e /$ eV
20	-10	3.1	$x_{sep} : 1.7(+/-0.1) \cdot 10^{20}$ $x_{pd} : 1.1(+/-0.1) \cdot 10^{20}$	$x_{sep} : 1.2(+/-0.2) \cdot 10^{16}$ $x_{pd} : 4.3(+/-0.7) \cdot 10^{15}$	$x_{sep} : 6.6(+/-0.6) \cdot 10^{18}$ $x_{pd} : 7.4(+/-0.7) \cdot 10^{18}$	$x_{sep} : 1.8(+/-0.5) \cdot 10^{-3}$ $x_{pd} : 6(+/-1) \cdot 10^{-4}$	$x_{sep} : 75(+/-10)$ $x_{pd} : 102(+/-13)$
45	-26	2.0	$x_{sep} : 6.6(+/-0.4) \cdot 10^{19}$ $x_{pd} : 4.7(+/-0.4) \cdot 10^{19}$	$x_{sep} : 6(+/-1) \cdot 10^{15}$ $x_{pd} : 2.4(+/-0.4) \cdot 10^{15}$	$x_{sep} : 6.7(+/-0.6) \cdot 10^{18}$ $x_{pd} : 8.8(+/-0.7) \cdot 10^{18}$	$x_{sep} : 1.0(+/-0.2) \cdot 10^{-3}$ $x_{pd} : 2.7(+/-0.7) \cdot 10^{-4}$	$x_{sep} : 76(+/-10)$ $x_{pd} : 115(+/-14)$
70	-46	1.8	$x_{sep} : 2.9(+/-0.2) \cdot 10^{19}$ $x_{pd} : 2.1(+/-0.2) \cdot 10^{19}$	$x_{sep} : 2.8(+/-0.5) \cdot 10^{15}$ $x_{pd} : 1.0(+/-0.2) \cdot 10^{15}$	$x_{sep} : 6.7(+/-0.6) \cdot 10^{18}$ $x_{pd} : 1.01(+/-0.08) \cdot 10^{19}$	$x_{sep} : 4(+/-1) \cdot 10^{-4}$ $x_{pd} : 1.0(+/-0.3) \cdot 10^{-4}$	$x_{sep} : 76(+/-10)$ $x_{pd} : 126(+/-16)$
#22155, $t \sim 2.8$ s, ohmic (L-factor=1.0), $\bar{n}_e = 2.5 \cdot 10^{19} \text{ m}^{-3}$		#22155, $t \sim 2.8$ s, ohmic (L-factor=1.0), $\bar{n}_e = 2.5 \cdot 10^{19} \text{ m}^{-3}$					
$p_{sc} /$ cm	θ °	$x_{sep} - x_{pd} /$ cm	$\Gamma_D /$ $\text{m}^{-2}\text{s}^{-1}$	$n_D /$ m^{-3}	$n_e /$ m^{-3}	n_D/n_e	$T_e /$ eV
20	-9	2.4	$x_{sep} : 2.0(+/-0.1) \cdot 10^{20}$ $x_{pd} : 1.4(+/-0.1) \cdot 10^{20}$	$x_{sep} : 1.7(+/-0.3) \cdot 10^{16}$ $x_{pd} : 6(+/-1) \cdot 10^{15}$	$x_{sep} : 6.5(+/-0.6) \cdot 10^{18}$ $x_{pd} : 9.3(+/-0.7) \cdot 10^{18}$	$x_{sep} : 2.6(+/-0.7) \cdot 10^{-3}$ $x_{pd} : 7(+/-2) \cdot 10^{-4}$	$x_{sep} : 64(+/-8)$ $x_{pd} : 72(+/-9)$
45	-24	1.7	$x_{sep} : 6.0(+/-0.3) \cdot 10^{19}$ $x_{pd} : 4.3(+/-0.4) \cdot 10^{19}$	$x_{sep} : 7(+/-1) \cdot 10^{15}$ $x_{pd} : 2.5(+/-0.4) \cdot 10^{15}$	$x_{sep} : 6.5(+/-0.6) \cdot 10^{18}$ $x_{pd} : 1.12(+/-0.08) \cdot 10^{19}$	$x_{sep} : 1.0(+/-0.3) \cdot 10^{-3}$ $x_{pd} : 2.2(+/-0.5) \cdot 10^{-4}$	$x_{sep} : 64(+/-8)$ $x_{pd} : 77(+/-10)$
70	-43	1.5	$x_{sep} : 3.1(+/-0.2) \cdot 10^{19}$ $x_{pd} : 2.2(+/-0.2) \cdot 10^{19}$	$x_{sep} : 3.3(+/-0.5) \cdot 10^{15}$ $x_{pd} : 1.2(+/-0.2) \cdot 10^{15}$	$x_{sep} : 6.4(+/-0.6) \cdot 10^{18}$ $x_{pd} : 1.20(+/-0.08) \cdot 10^{19}$	$x_{sep} : 5(+/-1) \cdot 10^{-4}$ $x_{pd} : 1.0(+/-0.2) \cdot 10^{-4}$	$x_{sep} : 63(+/-8)$ $x_{pd} : 80(+/-10)$

Table D.4: Collection of neutral penetration data. Definition of x_{pd} : $n_D(x_{pd}) = \exp(-1) \cdot n_D(x_{sep})$. θ is the angle on the poloidal plane between the lines defined by the connections magnetic axis to X-point and magnetic axis to separatrix denoted by the p_{sc} -value (the symmetry axis of the torus is to the left of the cross section and the poloidal angle is followed counter-clockwise).

Bibliography

- [1] World Energy Council, Energy End-Use Technologies for the 21st Century, World Energy Council, London, 2004. URL: <http://www.worldenergy.org/documents/et2104.pdf> .
- [2] E. Teller (ed.), Fusion (Vol 1), Academic Press, London, 1981.
- [3] J. Wesson, Tokamaks (2nd ed.), Oxford University Press, Oxford, 1997.
- [4] R. L. Boivin et al, Phys. Plasmas **7** (5), 1919-1926, 2000.
- [5] R. J. Groebner et al, Plasma Phys. Control. Fusion **44** (2002), A265-A272.
- [6] M. A. Mahdavi, Phys. Plasmas **10** (10), 3984-3991, 2003.
- [7] A. Kallenbach et al, J. Nuc. Mat. 337-339 (2005), 381-385.
- [8] T. Fülöp et al, Phys. Plasmas **5** (11), 3969-3973, 1998.
- [9] P. Helander et al, Phys. Plasmas **10** (11), 4396-4404, 2003.
- [10] Ph. Mertens et al, Plasma Phys. Control. Fusion **43** (2001), A349-A737.
- [11] S. Brezinsek et al, Plasma Phys. Control. Fusion **47** (2005), 615-634.
- [12] M. F. A. Harrison, Atomic and Molecular Collisions in the Plasma Boundary, CLM-P746, UKAEA Culham Lab. Abingdon, 1985.
- [13] R. K. Janev, W. D. Langer, K. Evans Jr., D. E. Post Jr., Elementary Processes in Hydrogen-Helium Plasmas, Springer, Berlin, 1987.
- [14] A. G. Gaydon, Dissociation Energies and Spectra of Diatomic Molecules, Chapman + Hall, London, 1968.
- [15] T. Fujimoto, Plasma Spectroscopy, Clarendon Press, Oxford, 2004.
- [16] D. R. Bates et al, Proc. Roy. Soc. A **267**, 297-312, 1961.
- [17] H. R. Griem, Principles of Plasma Spectroscopy, Cambridge Univ. Press, Cambridge, 1997.
- [18] K. Behringer, Escape Factors for Line Emission and Population Calculations, IPP 10/11, Max-Planck-Institut für Plasmaphysik, Garching, Germany, 1998.

- [19] D. Reiter, S. Wiesen, M. Born, *Plasma Phys. Control. Fusion* **44** (2002), 1723-1737.
- [20] B. LaBombard, KN1D: A 1-D Space, 2-D Velocity, Kinetic Transport Algorithm for Atomic and Molecular Hydrogen in an Ionizing Plasma, PSFC/RR-01-3, Plasma Science and Fusion Center, Massachusetts Institute of Technology, Cambridge, 2001.
URL: http://www.psfc.mit.edu/~labombard/KN1D_Source_Info.html .
- [21] K. Sawada, T. Fujimoto, *J. Appl. Phys.* **58** (5), 2913-2924, 1995.
- [22] R. K. Janev, *Atomic and Molecular Processes in Fusion Edge Plasmas*, Plenum Press, New York, 1995.
- [23] P. L. Bhatnagar, E. P. Gross, M. Krook, *Phys. Rev.* **94** (3), 511-525, 1954.
- [24] L. C. Johnson, E. Hinnov, *J. Quant. Spectrosc. Radiat. Transfer* **13**, 333-358, 1973.
- [25] K. Behringer, et al, *Plasma Phys. Control. Fusion* **31** (1989), 2059-2099.
- [26] J. Gafert et al, *Proc. of the 29th EPS Conference on Plasma Phys. and Contr. Fusion Montreux, ECA Vol. 26B*, P-1.123, 2002.
- [27] A. Kallenbach et al, *Nucl. Fusion* **48**, 085008, 2008.
- [28] L. C. Ingesson, *Visible-Light Tomography of Tokamak Plasmas*, PhD-thesis, Technische Hogeschool Eindhoven, 1995.
- [29] L. C. Ingesson et al, *Fusion Sci. Tech.* **53**, No 2, 528-576, 2008.
- [30] A. M. Cormack, *J. Appl. Phys.* **34**, 2722-2727, 1963.
- [31] J. C. Fuchs et al, *Europhysics Conference Abstracts (Proc. of the 21th EPS Conference on Controlled Fusion and Plasma Physics, Montpellier, 1994)* , (Ed.) E. Joffrin, P. Platz, P. E. Stott (EPS, Geneva), Vol. 18B, part III, 1308-1311.
- [32] Numerical Algorithms Group, URL: <http://www.nag.co.uk> .
- [33] URL: <http://www.nag.com/numeric/fl/manual20/pdf/F07/f07mdf.pdf> .
- [34] URL: <http://www.nag.com/numeric/fl/manual20/pdf/F07/f07mef.pdf> .
- [35] URL: <http://www.nag.com/numeric/fl/manual20/pdf/E04/e04ncf.pdf> .
- [36] G. Braithwaite et al, *Rev. Sci. Instrum.* **60** (9), 2825-2834, 1989.
- [37] K. McCormick et al, *Rev. Sci. Instrum.* **56** (5), 1063-1065, 1985.
- [38] K. McCormick et al, *Fusion Engineering and Design* 34-35 (1997), 125-134.
- [39] J. Schweinzer et al, *Plasma Phys. Control. Fusion* **34** (1992), 1173-1183.
- [40] R. Fischer et al, *Plasma Phys. Control. Fusion* **50** (2008) 085009 (26pp).
- [41] R. Fischer et al, *Plasma Phys. Control. Fusion* **45** (2003), 1095-1111.

- [42] H. Murmann et al, *Rev. Sci. Instrum.* **63** (10), 4941-4943, 1992.
- [43] M. Bornatici et al, *Nucl. Fusion* **23** 1153, 1983.
- [44] W. Suttrop, A. G. Peeters et al, *Practical Limitations to Plasma Edge Electron Temperature Measurements by Radiometry of Electron Cyclotron Emission*, IPP 1/306, Max-Planck-Institut für Plasmaphysik, Garching, Germany, 1997.
- [45] P. C. Stangeby, *The Plasma Boundary of Magnetic Fusion Devices*, IOP Publishing, Bristol, 2000.
- [46] A. V. Chankin et al, *Plasma Phys. Control. Fusion* **48** (2006), 839-868.
- [47] G. J. Schulz, *J. Appl. Phys.*, **28** (10), 1149-1152, 1957.
- [48] G. Haas and H.-S. Bosch, *Vacuum*, **51** (1), 39-46, 1998.
- [49] A. Scarabosio and G. Haas, *AIP Varenna Conference Proceedings*, 998(238), 2008.
- [50] M. Weinlich, IPP 5/64, Max-Planck-Institut für Plasmaphysik, Garching, Germany, 1995.
- [51] M. Weinlich and A. Carlson, *Phys. Plasmas* **4** (6), 2151-2160, 1997.
- [52] K. U. Riemann, *J. Phys. D: Appl. Phys.* **24** (1991), 493-518.
- [53] R. Chodura, *Phys. Fluids* **25**(9), 1982.
- [54] P. N. Yushmanov et al, *Nucl. Fusion* **30** (10), 1999-2006, 1990.
- [55] V. D. Shafranov, *Plasma equilibrium in a magnetic field*, *Reviews of Plasma Physics*, Vol. 2, Consultants Bureau, New York, 1966.
- [56] F. M. Levinton et al, *Rev. Sci. Instrum.* **61** (10), 2914-2919, 1990.
- [57] D. W. Roberts, R. Kaita, F. M. Levinton, *Rev. Sci. Instrum.* **61** (10), 2932-2934, 1990.
- [58] W. Schneider et al, *Fusion Engineering and Design* **48** (2000), 127-134.
- [59] P. J. McCarthy, P. Martin, W. Schneider, *The CLISTE interpretive equilibrium code*, IPP 5/85, Max-Planck-Institut für Plasmaphysik, Garching, Germany, 1999.
- [60] W. Schneider, private communication, 2/2008.
- [61] A. W. Leonard et al, *J. Nuc. Mat.* 266-269 (1999), 109-117.
- [62] A. Herrmann, *Plasma Phys. Control. Fusion* **44** (2002), 883-903.
- [63] A. Loarte et al, *Plasma Phys. Control. Fusion* **44** (2002), 1815-1844.
- [64] L. D. Horton et al, *Plasma Phys. Control. Fusion* **46** (2004), B511-B525.
- [65] A. Herrmann et al, *Plasma Phys. Control. Fusion* **46** (2004), 971-979.
- [66] T. Eich et al, *Plasma Phys. Control. Fusion* **47** (2007), 815-842.

- [67] T. Eich et al, Plasma Phys. Control. Fusion **49** (2007), 573-604.
- [68] B. Kurzan et al, Phys. Rev. Lett. **95** (2005).
- [69] R. Scannell et al, Plasma Phys. Control. Fusion **49** (2007), 1431-1446.
- [70] H. R. Wilson et al, Plasma Phys. Control. Fusion **48** (2006), A71-A84.
- [71] B. Koch et al, J. Nuc. Mat. 363-365 (2007), 1056-1060.
- [72] A. Schmid et al, Plasma Phys. Control. Fusion **50** (2008) 045007 (16pp).
- [73] A. Herrmann et al, J. Nuc. Mat. 363-365 (2007), 528-533.
- [74] A. Schmid, Characterization of Type-I ELM Induced Filaments in the Far Scrape-off Layer of ASDEX Upgrade, PhD thesis, Technische Universität München, 2008.
- [75] ADAS - Atomic Data and Analysis Structure, URL: <http://adas.phys.strath.ac.uk> .
- [76] C. Angioni et al, Phys. Plasmas **10** (8), 3225-3239, 2003.
- [77] F. Ryter et al, Plasma Phys. Control. Fusion **48** (2006), B453-B463.
- [78] D. Bohm, The Characteristics of Electrical Discharges in Magnetic Fields, McGraw-Hill, New York, 1949.
- [79] N. Asakura et al, J. Nuc. Mat. 363-365 (2007), 41-51.
- [80] B. J. Braams, A multi fluid code for simulation of the edge plasma in tokamaks, EUR-FU/XII-80/87/68, 1987.
- [81] G. J. Radford et al, Contrib. Plasma Phys. **36** (1996), p187.
- [82] T. D. Rognlien et al, Contrib. Plasma Phys. **34** (1994), p362.
- [83] D. P. Stotler and C. F. F. Carney, Contrib. Plasma Phys. **34** (1994), p392.
- [84] D. Reiter, Randschicht-Konfiguration von Tokamaks: Entwicklung und Anwendung stochastischer Modelle zur Beschreibung des Neutralgastransports. PhD-thesis, Heinrich-Heine Universität Düsseldorf, Germany, 1984. KFA-Report, Jül-1947.
- [85] E. Cupini et al, NIMBUS - Monte Carlo simulation of neutral particle transport in fusion devices, EUR-FU/XII-324/9, 1984.
- [86] International Thermonuclear Experimental Reactor (ITER), URL: <http://www.iter.org> .
- [87] R. Schneider et al, Contrib. Plasma Phys. **40** (2000), p328.
- [88] V. A. Rozhansky et al, Nucl. Fus. **41**(4), p387, 2001.
- [89] EIRENE manual, 2004, URL:<http://www.eirene.de> .
- [90] W. Fundamenski et al, Contrib. Plasma Phys. **48** (2008), 190-195.

- [91] S. K. Erents et al, *J. Nuc. Mat.* 363-365 (2007), 565-569.
- [92] A. Huber et al, 32th EPS Conference on Plasma Physics Tarragona, 2005, ECA Vol.29C, P-2.112.
- [93] M. Wischmeier et al, *Contrib. Plasma Phys.* **48** (2008), 249-254.
- [94] M. Wischmeier, private communication, 10/2007.
- [95] A. S. Kukushkin et al, *Nucl. Fus.* **45** (2005), 608-616.
- [96] Max-Planck-Institut für Plasmaphysik, URL: <http://www.ipp.mpg.de> .
- [97] F. Wagner et al, *Phys. Rev. Lett.* **49** (19), 1408-1412, 1982.
- [98] A. Herrmann (ed.), Special Issue on ASDEX Upgrade, Fusion Science and Technology, Vol.44, No.3, 2003.
- [99] Joint European Torus (JET), URL: <http://www.jet.efda.org> .
- [100] P. Dumortier et al, *Plasma Phys. Control. Fusion* **44** (2002), 1845-1861.
- [101] T. J. J. Tala et al, *Plasma Phys. Control. Fusion* **44** (2002), 1181-1202.
- [102] A. Mück et al, *Plasma Phys. Control. Fusion* **47** (2005), 1633-1655.
- [103] H. Zohm et al, *Plasma Phys. Control. Fusion* **49** (2007), B341-B347.
- [104] E. de la Cal, *Plasma Phys. Control. Fusion* **48** (2006), 1455-1468.
- [105] J. Winter, *Plasma Phys. Control. Fusion* **38** (1996), 1503-1542.
- [106] R. Neu et al., *Plasma Phys. Control. Fusion* **38** (1996), A165-A179.
- [107] H. W. Meister, private communication, 10/2007.
- [108] Theta System, URL: <http://www.theta-system.de> .
- [109] E. J. Friebele et al, *Nucl. Instrum. Methods Phys. Res. B* **1** (1984), 355-369.
- [110] A. T. Ramsey, K. W. Hill, *Rev. Sci. Instrum.* **63** (10), 4735-4737, 1992.
- [111] A. T. Ramsey et al, *Rev. Sci. Instrum.* **68** (1), 632-635, 1997.
- [112] A. T. Ramsey, *Rev. Sci. Instrum.* **66** (1), 871-876, 1995.
- [113] M. Mayer, private communication, 11/2007.
- [114] Manual to the neutron activation code FISPACT, URL: <http://www.fusion.org.uk/techdocs/ukaea-fus-534.pdf> .
- [115] A. Loarte et al, *J. Nuc. Mat.* 337-339 (2005), 816-820.
- [116] P. M. Anderson et al, *Fusion Engineering and Design* 9 (1989), 9-13.

- [117] B. Lipschultz et al, J. Nuc. Mat. 220-222 (1995), 967-970.
- [118] R. Neu, Tungsten as a Plasma Facing Material in Fusion Devices, IPP 10/25, Max-Planck-Institut für Plasmaphysik, Garching, Germany, 2003.
- [119] R. Neu et al., Plasma Phys. Control. Fusion **49** (2006), B59-B70.

Acknowledgement

Each scientific investigation related to a large experimental undertaking like the projects for magnetic confinement fusion requires a well organised environment in order to be successful and effective. I would like to express my gratitude for the existence of the extraordinary technical infrastructure of the ASDEX Upgrade Tokamak and the engagement of the staff of technicians, engineers and scientists who put life into it: the ASDEX Upgrade Team.

The workshop under leadership of Mr G. Schultheiss and Mr K. Eismann later on has proven to be the reliable partner for physicists with demanding wishes but also with poor technical drawings. Mr P. Bischoff is the specialist at hand, if light guide connections for purposes of control and data acquisition need to be established. Problems regarding the organisation of electronics equipment for large scale as well as for small scale applications is well managed by the electronics workshop, in particular the immediate readiness for action of Mr C. Aubanel and Mr T. Pirsch shall be mentioned. The vessel maintenance team under management of Mr M. Ebner is capable of keeping the interior of the plasma chamber in the desired configuration within a tight time schedule, while at the same time handling technical requests of diagnosticians inside and outside the torus hall.

Very special thanks are devoted to Mr J. Fink, Mr. M. Hien and Mr R.-T. Seth together with whom I was able to organise the operation of the standard video diagnostics and who in addition assisted me in many technical problems. The convenient character of our teamwork is in particular to be emphasised, since we belong to different generations.

A heavy load is put on the staff which organises the equipment of information technology and data acquisition and transfer to storage of the AUG project and which needs to assist single users for special requests as well. This highly acknowledged work is done by Dr K. Behler, Mr H. Blank, Mrs A. Buhler, Dr R. Drube, Mr R. Merkel and Mr A. Lohs.

During the startup phase of my work, helpful advice was given by Mr E. Oberlander, whose technical organisation turned out to be a robust backbone in the field of video diagnostics, and by Dr J. Gafert who assisted in understanding the operation of the diagnostics and discussed approaches in data analysis and physical interpretation. Often enough, useful hints and explanations were found in discussions with Dr habil. R. Dux, Dr J. Hobirk, Dr H. Meister, Dr R. Pugno, Dr T. Pütterich, Dr W. Schneider and Dr habil. J. Stober. I'm indebted to Dr W. Schustereder who spend considerable time in order to obtain PIXE spectra of unusual specimens and to Mrs B. Gmeiner who provided answers to many questions about neutron activation of various elements. Dr M.-G. Adamov, Dr B. Kurzan and Dr H. Murmann who constitute the core of the Thomson-team deserve attention for granting me to occupy one of their labs for several weeks and to use a couple of sensitive parts of their equipment.

Plasma parameters adopted for interpretation of ε_{D_α} are predominantly based on diagnostics operated by and data analysis done by Dr G. Haas, Dr N. Hicks, Dr R. Fischer, Dr K. McCormick, Dr H.-W. Müller, Dr A. Scarabosio, Dr W. Suttrop and Dr habil. Wolfrum. The level of understanding of the algorithm for tomographic reconstruction I could achieve is based on the ideal documentation by Dr J. C. Fuchs.

Feedback to my efforts was given by Dr M. Groth from the DIII-D Team who also was so kind to advertise my poster presentation on the EPS conference in 2007 which contributed to a positive atmosphere during the session. Dr P. Lang didn't hesitate to acknowledge my part in the organisation of the standard video diagnostics which often gave useful data related to pellet injection experiments. Furthermore, he tried several times to convince me of heading for

an engagement in fusion science. I'm encouraged by the interest of Dr K.-D. Zastrow in the background for tomography in secondary viewing geometry I gathered, which he is going to apply in visible spectroscopy studies on the JET Tokamak. Dr M. Wischmeier contributed to my thesis in an outstanding way by identifying the relevant issues of SOL physics and by investing a considerable amount of time for the preparation of a series of SOLPS models.

Crucial assistance in resolving bureaucratic obstacles and organising conference trips is provided by Mrs A. Bauer, Mrs G. Daube, Mrs M. Jung and Mrs L. Scoones.

I wish to thank the second referee of my thesis Prof Dr H. Lesch and the examiners in the final exam Prof Dr D. Habs, Prof Dr A. Schenzle and Prof Dr R. Bender for their attendance.

During the past years I was glad to be member of the department lead by Prof Dr K. Behringer and I'm grateful for support concerning issues of plasma spectroscopy. Prof Dr H. Zohm is the official advisor of this PhD project and his engagement shall be acknowledged.

For proof-reading of the manuscript and general encouragement I would like to thank my friend Dr T. Lunt. I want to express my recognition of support received from my group leader Dr habil. R. Neu in terms of appraisal of my contribution to his group and my scientific efforts, and also to his comprehension of my view on certain aspects outside the purely scientific focus. Finally, there can be no doubt that my personal supervisor Prof Dr A. Kallenbach deserves to be acknowledged for his eminent contribution in the development of this PhD project. Not only did he assist in dedicated problems and helped to find a sensible route for dealing with the general subject, but also he stood out being patient and persistent during the phase of writing up.

